The molecular content of star-forming galaxies

Penelope Ann Smith

Ph.D. Thesis

University of Edinburgh

1992

This thesis has been composed of my own work, except where specifically noted in the text.

Penelope Smith

March 1992

'How *did* it go, Pooh?' said Rabbit.
Pooh gave a little cough and began.

LINES WRITTEN BY A BEAR OF VERY LITTLE BRAIN

On Monday, when the sun is hot
I wonder to myself a lot:
'Now is it true, or is it not,
That what is which and which is what?'

On Tuesday, when it hails and snows,
The feeling on me grows and grows
That hardly anybody knows
If those are these or these are those.

On Wednesday, when the sky is blue,
And I have nothing else to do,
I sometimes wonder if its true
That who is what or what is who.

On Thursday, when it starts to freeze
And hoar-frost twinkles on the trees,
How very readily one sees
That these are whose – but whose are these?

On Friday –

'Yes, it is, isn't it?' said Kanga, not waiting to hear what happened on Friday.

Milne, A.A., 1926. *Winnie-the-Pooh*, Methuen & Co. Ltd, London.

Acknowledgments

I would first like to thank my supervisors, Matt Mountain and Peter Brand, for their support and encouragement over the last four-and-a-half years, even after I crashed through all their deadlines. I am also indebted to Phil Puxley, my 'unofficial' supervisor, who guided me through many of the complexities of observational astronomy, and whose enthusiasm, advice and encouragement were much valued.

Of the many people who made me feel welcome and contributed to the (varying) success of my nine observing runs, I single out David Brock, Thomas Walker, Goran Sandell and Tim Hawarden in Hawaii, Hans Steppe and Dave John in Spain and Naomasa Nakai in Japan, although all the support staff at Nobeyama, IRAM and the JCMT deserve a mention. I am particularly grateful to Tim for his enthusiastic assistance with several of my JCMT runs and for his skydiving anecdotes, and to Nakai-san, who on my two visits to Nobeyama was simultaneously collaborator, support scientist, interpretor, chauffeur, tour guide and restaurant menu translator. Toby Moore and Phil P. did one of my IRAM observing runs for me when scheduling demanded that I be in two places at once. I should also mention Amanda at Amex who was landed with organizing my convoluted itineraries, all the friends who put me up, sometimes at very short notice, and Harley Thronson, who organized the excellent Wyoming conference in 1989 and then had to put up with the vegetarians winging about the food.

In Edinburgh, Claire Chandler was an office-mate and friend for three years, as well as a source of all knowledge on dust emission and FORTRAN. Phil Puxley, Lance Miller and Phil James bravely volunteered to read drafts of the thesis and made helpful comments. John Richer sent me his invaluable program for reading IRAM data into SPECX, David Hughes, Wolfgang Wild, Patrick McCarthy and Naomasa Nakai all made available unpublished data, Brian Williams found lots of bugs in my programs, Marjorie Fretwell drew Fig. 2.1 and Richard Dixon created the dots in Fig. 3.2.

Life at ROE over the last eight months would have been considerably more unpleasant and stressful without the other members of the 'Late Shift' – Brian, Rijdat, Phil and Dave, who provided friendship, late-night company, moral support and scones, thus helping me retain my sanity while writing up on top of a full-time job. Many other people helped make my stay at ROE a (mostly) pleasant one – among them are my fellow portacabin inmates (who put up with the overflowing desk), Maureen (for organizing Matt), Jocelyn (for advice and encouragement while I was job hunting), David, Alan (for the bad jokes), Lance, Pippa, Karl (for discovering the aurora), the Visitor Centre team, Drew, Bill, Jack and Scott, and the other MSc/PhD students.

Financial support came in the form of an SERC studentship for the first three years, and sales assistantships from Marks & Spencer and Capital Foods thereafter.

Outside ROE, thanks are due to my flatmates (Kris & Jane, Howard, Dave, Pete, Lydia & Dougs) and the mice (for the company), Blackwell Scientific Publications (for giving me a job and teaching me the correct spelling of Acknowledgments), Müller (for the fruit corners), Rachel, the Edinburgh Womens' Science Forum, and, especially, everybody at the Scottish Parachute Club, particularly Buzby, Kevin and Sam, for their friendship, for reminding me that there is life outside astronomy and for letting me throw myself out of a Cessna whenever the PhD got too much.

Last, but certainly not least, I thank my Mum and Dad for their love and support, for always being there when I needed them, for always backing me in whatever I wanted to do, and for not complaining (too much) about the massive phone bills.

Abstract

An exciting development in observational astronomy over the last 15 years has been the opening up of the submillimetre and millimetre atmospheric windows, to the extent that observations of external galaxies are now possible. This thesis presents the results of a millimetre/submillimetre-wave study of several nearby, infrared-bright, vigorously star-forming galaxies, in an attempt to investigate their molecular hydrogen content. In particular, it seeks to evaluate the relative merits of the two most commonly adopted molecular hydrogen 'tracers' – millimetre-wave transitions of the CO molecule and its isotopes, and submillimetre continuum emission from warm dust grains. Observational and theoretical evidence suggests that the effects of active star formation (in the form of intense UV fields, supernovae, etc.) on the CO emission may render it unreliable as a tracer of H_2 in such galaxies. Dust continuum emission offers the potential for an independent probe of the interstellar molecular gas in starburst systems.

The first part of the thesis concerns 450 μm mapping of the nearby starburst galaxy M82. In contrast to what might be expected if the CO and dust were both reliably tracing molecular hydrogen, the 450 μm map shows striking spatial dissimilarities to ^{12}CO line maps of the same region. Consideration of isotopic CO data suggests that optical depth effects may in part explain the discrepancy, while the effect of the vigorous nuclear star formation on the excitation state of the CO may also be an important factor. The optically thin 450 μm continuum emission shows no strong evidence for dust temperature gradients across the galaxy and appears to trace reliably the distribution of the grains and hence the gas with which they are associated.

As a follow-up to the M82 observations, 800 μm dust continuum maps were made of three more nearby star-forming galaxies, Maffei 2, M83 and IC342. Together with 450–1100 μm photometry, these data fill an important gap in the long-wavelength spectra of such galaxies, enabling a study of the molecular material with which the dust is mixed. It is found that a single-temperature, modified blackbody dust spectrum cannot fit the observed submillimetre fluxes, unless the emissivity spectral index β=1 all the way to 1100 μm, with corresponding dust temperatures $\sim$45 K. While this scenario cannot be ruled out by current grain models, a multitemperature dust grain population seems more plausible for a composite object such as a galaxy. A two-temperature spectral fit suggests that $\sim$90% of the dust may be cool ($\sim$20–25 K), somewhat surprising in a galaxy exhibiting observational evidence of vigorous nuclear star formation. Possible reasons for this, as well as the effect of a large cool-dust fraction on the derived gas column densities and masses, are discussed.

In the final section of the thesis, ^{12}CO and ^{13}CO observations are presented of the infrared-bright, gas-rich galaxy Maffei 2. The CO emission from this galaxy is characterized by high main-beam brightness temperatures ($\sim$ 2 K) and very wide lines (approaching 160 km s^{-1} FWHM at the centre). A simple rotating disc model shows that beam smearing of a steeply rising rotation curve fails to reproduce the observed linewidths, and that cloud velocity dispersions of $\sim$100 km s^{-1} may be present in the central regions. Possible energy sources behind such large velocity dispersions are discussed. The ^{12}CO and ^{13}CO J=2–1 and 1–0 antenna temperature ratios are compared point by point to investigate any large-scale variation of cloud excitation across the starburst region. It is found that a simplistic, single-temperature LTE analysis cannot reconcile the high observed 2–1/1–0 ratios with the low values of $T_{\rm mb}(^{12}{\rm CO})/T_{\rm mb}(^{13}{\rm CO})$ that imply optically thick gas in the nuclear region. Non-LTE excitation effects in a multicomponent interstellar medium may conspire to make reliable interpretation of CO line data very difficult without detailed modelling.

Contents

Chapter 1

Introduction

1.1 Enhanced star formation in galaxies

Galaxies can be divided into two broad classes in terms of their star formation: (i) 'normal' – slowly using up their gas on time-scales of $\sim 10^9$–10^{10} yr, to form a normal stellar population, and (ii) 'enhanced' – vigorous star formation, often concentrated in the central kiloparsec, at an apparent rate too large to be sustained for more than a small fraction of the galaxy lifetime, and therefore episodic unless the gaseous 'fuel' is somehow replenished. Such galaxies are characterized by mass-to-light ratios $\ll 1$, which cannot be sustained by a 'normal' stellar population and star-formation rate (e.g. Joseph 1990).

This latter group has become known in the literature as 'starburst' galaxies, although the term is not universally popular. As pointed out by Puxley (1988), the assumptions that go into the derivation of fundamental burst parameters like star formation rate or efficiency mean that these quantities are rather uncertain. J. Young, in Wynn-Williams (1987) has queried whether, for example, a galaxy that has both a high star-formation rate and rich reserves of gas is any more a starburst (as opposed to a 'scaled-up Milky Way') than a smaller, less gas-rich galaxy that may be forming stars very efficiently. In this thesis, by 'starburst', or 'star-forming galaxy' I mean one whose properties are consistent with a significant fraction of its emission arising from vigorous, near-nuclear star formation.

The first systematic studies of 'starburst' activity in galaxies were made in the

visible, using strong blue continuum from hot young stars as a sign of prolific star formation (e.g. Balzano 1983). However, as many extragalactic star-forming regions are deeply embedded in dust which both efficiently absorbs optical light and reradiates it at longer wavelengths, it is perhaps not surprising that it was in the infrared, particularly with the *IRAS* mission, that the study of starburst galaxies really began to take off. As well as the 'classical' examples (such as M82) of nearby galaxies containing vigorous nuclear star formation (e.g. Rieke *et al.* 1980), *IRAS* discovered a whole population of galaxies emitting $\sim 95\%$ of their bolometric luminosity at infrared wavelengths (Soifer, Houck & Neugebauer 1987; Telesco 1988).

Starburst activity is associated with three main types of object that can be broadly classified in terms of their far-infrared emission. The group with which this thesis will be concerned are the relatively nearby, usually isolated galaxies (although often possessing a nuclear bar) whose infrared luminosity (a few $\times\ 10^{9-10}\,L_{\odot}$) and appearance at other wavelengths are consistent with vigorous star formation in the central kiloparsec. Examples of this class include M82 and IC342. The first part of this introduction will discuss the observational characteristics of such galaxies, and their interpretation. The peculiar galaxy M82, which due to its proximity has been particularly well studied at all wavelengths, is used as an example.

Further up the scale ($L_{\rm IR} \sim 10^{10-12}\ L_{\odot}$) are interacting galaxies, in which it seems that a close tidal encounter between two gas-rich spirals has triggered an extensive episode of prolific star formation (e.g. Joseph & Wright 1985). Most extreme of all are the so-called ultraluminous galaxies ($L_{\rm IR} \geq 10^{12}\ L_{\odot}$) which are, almost without exception, merger systems (e.g. Sanders *et al.* 1988). It is at this end of the scale, from infrared luminosities of about $10^{11-12}\ L_{\odot}$ upwards, that the boundary between 'star formation' and 'active galactic nucleus' begins to blur – what fuels these immensely powerful systems – starburst or embedded 'monster'? What is the evolutionary link between them, if any – do starbursts evolve to black holes or does accretion onto a massive object trigger circumnuclear star formation? Is a compact source needed at all to explain the observed properties of active galaxies? Detailed consideration of such questions is beyond the scope of this introduction and they will be mentioned only briefly.

1.1.1 Emission mechanisms in star-forming galaxies

The first systematic studies of large-scale extragalactic star formation – for example, the study of Markarian galaxies by Balzano (1983) – were performed in the visible wavelength region, utilizing the strong blue photospheric continuum emission from young hot stars. In addition to a blue continuum, the visible spectrum of star-forming regions is characterized by emission lines from ionized H, Ne, Ar and other species, the line ratios of which can be used to constrain properties of the stellar population. Extensive emission nebulae in some star-forming galaxies have been interpreted as galactic-scale outflows driven by the high supernova rate associated with the starburst (e.g. Heckman *et al.* 1987).

The principal drawback of visible-wavelength data is the effect of uncertain dust extinction, making optical observations suitable only for relatively evolved starbursts which have begun to dispel their obscuring layers of dust. Very young star-formation regions, still deeply embedded in the dust and gas of their creation, remain effectively hidden to optical studies.

With the opening up of the infrared window, particularly after the *IRAS* mission, came the realization that active star formation in galaxies is a widespread phenomenon. Not only does infrared radiation pass relatively unhindered through dust, allowing even deeply buried near-nuclear starbursts to be observed, but the UV emission from young stars is efficiently absorbed and reradiated, making the infrared continuum a powerful tracer of global starburst properties. The fraction of the total galactic luminosity emerging in the far-infrared ranges from a few per cent for quiescent spirals such as M31, to 84% for the starburst M82, and 98% for the merger system Arp 220, which may be powered by an active nucleus (Telesco 1988).

Extragalactic star-forming regions display a wealth of spectral and continuum emission at near- (1–5 μm), mid- (5–30 μm) and far-infrared (30–300 μm) wavelengths. Near-infrared continuum emission from the photospheres of cool stars is a useful tracer of the underlying stellar mass distribution, particularly if the optical appearance of the galaxy is heavily extinguished or disturbed. In several cases, a bar-like morphology has been revealed by near-infrared mapping of an apparently unbarred galaxy (e.g. M82, Telesco *et al.* 1991). A CO photospheric absorption feature at 2.3 μm is a signature of

supergiants and can be used to constrain the age of the starburst, although it can be contaminated by a contribution from the underlying stellar population, or by continuum emission from very hot dust. At wavelengths longer than $\sim 2\,\mu$m, thermal emission from very hot (>150 K) dust in HII regions starts to take off, and dominates after about $5\,\mu$m as the stellar continuum dies away. Near-infrared hydrogen recombination lines (e.g. Brα, Brγ, Paβ) are powerful starburst diagnostics, being less affected by extinction than optical recombination lines like Hα, and can be used to estimate the ionizing stellar photon emission rate. Quadrupole line emission from molecular hydrogen, excited by UV pumping or by shocks, also features in the near-infrared spectrum. The very small wavelength differences between some of these near-infrared lines are useful as the effects of differential reddening are minimized. Molecular and ionized hydrogen line ratios can be a powerful probe of the stellar UV that is both exciting the H_2 and ionizing the HII, although there is still debate about whether the H_2 lines are predominantly UV-pumped or shock excited (Puxley 1988; Lester *et al.* 1990), and the presence of atmospheric and stellar absorption features makes this a difficult wavelength region to work in. Puxley (1988) uses the Brγ/v=1–0 $S(1)$ ratio in a sample of nearby star-forming galaxies to model the UV continuum in terms of emission from massive stars in clusters, well mixed with the molecular clouds and ionized gas. In some of the brighter galactic nuclei, near-infrared spectral lines from species such as SiIV can be detected (e.g. Blanco 1991).

Thermal reradiation by hot dust dominates the continuum emission at mid-infrared wavelengths, although there may also be a contribution from very small grains or large molecules undergoing non-equilibrium heating by absorption of single UV photons (e.g. Leger & Puget 1984). These small grains are also thought to be responsible for a cluster of mid-infrared emission features at 3–11 μm. As well as dust features, mid-infrared emission lines from ionized species such as [NeII], [ArIII] and [SIV] are observed. Cool silicate dust in star-forming regions additionally reveals itself via an absorption feature at $9.7\,\mu$m. The depth of this feature can be used to estimate the $9.7\,\mu$m opacity of the dust, and, where detected, provides a useful independent method of calculating the visual extinction, although the calibration between $\tau_{9.7}$ and A_V is uncertain by about a factor of 2. It is interesting to note that the extinction derived from observation of spectral features often increases with the wavelength employed, indicating that greater

depths of dust are being probed by longer wavelength lines and therefore that the emitting sources are probably well mixed with the dust. In M82, for example, visual extinctions of 5–6 are deduced from near-infrared recombination lines (Lester *et al.* 1990), while the H53α transition at 43 GHz gives $A_V \sim 27$ (Puxley 1988). This mixing of emitting sources and dust can affect parameters derived from line ratios when the two lines involved are far apart in wavelength (e.g. Puxley 1991).

Dust is such an efficient absorber and reradiator of the stellar emission that dusty star-forming galaxies characteristically emit the bulk of their bolometric luminosity in the far-infrared. Dust in molecular clouds, heated to equilibrium temperatures of 20–50 K, emits a modified blackbody spectrum peaking at $\sim 100\,\mu$m, with a spectral energy distribution characteristic of Galactic star-forming-region/molecular-cloud complexes. The far-infrared to millimetre continuum emission is also a powerful tracer of the molecular hydrogen content of those galaxies and this property is discussed in detail in Section 1.3. As well as the thermal dust continuum, fine-structure lines of ionized elements such as [OII], [OIII] and [CII] are emitted at far-infrared wavelengths. In particular the $158\,\mu$m transition of [CII] is strong in star-forming galaxies. It has been modelled as arising from 'photodissociation' regions at UV-illuminated molecular-cloud/HII-region interfaces. This line can contribute up to $\sim 0.5\%$ of the bolometric luminosity and in some cases it appears that a significant fraction of the neutral interstellar medium of a starburst galaxy may reside in these warm, dense regions (Crawford *et al.* 1985).

The submillimetre/millimetre region is one of the last to have opened up to extragalactic studies, primarily because of the observational difficulties involved (see Appendix A). The rewards for overcoming the technical hurdles are significant. As well as the long-wavelength tail of the dust continuum emission, the submillimetre/millimetre region contains a wealth of emission lines from cool (15–50 K) molecular gas – primarily ^{12}CO, but increasingly, transitions of other species such as ^{13}CO, C^{18}O, CS, HCN and HCO$^+$ are being detected outside the Milky Way. Apart from their use as a diagnostic of the physical and excitation state of the gas (although interpretation is not straightforward – see Section 1.2 and Chapter 5), these lines offer an extinction-free probe of the dynamics of near-nuclear star-forming regions, with the potential for insight into how the starburst was initially triggered, and its effect on the surrounding clouds.

Star-forming galaxies are characterized by bright, extended emission at radio wave-

lengths (Condon *et al.* 1982). The radio emission appears principally as a thermal, free–free contribution from ionized gas in HII regions, and a non-thermal synchrotron component, either from individual supernova remnants, or from the interaction of supernova-generated cosmic rays with the galactic magnetic field. The relative contributions of free–free and synchrotron emission vary from system to system and spatially within a galaxy. In M82, for example, a population of ~100 discrete non-thermal radio sources in the central 600 pc has been identified with young (10–300 yr) supernova remnants, embedded in a background of diffuse non-thermal emission (Kronberg, Biermann & Schwab 1985; Bartel *et al.* 1987; Kronberg 1988). The relative contributions of thermal and non-thermal emission give an idea of the age of a starburst – a lack of non-thermal emission indicates that the starburst is too young to have produced supernovae. Radio-wavelength recombination lines have been detected from a few of the brightest galaxies, for example H53α at 43 GHz from M82 and NGC 2146 (Puxley 1988; Puxley *et al.* 1991). These are valuable for starburst modelling, as they provide an extinction-free diagnostic of the ionizing UV continuum and the stellar population that produces it. 21-cm atomic hydrogen line emission is also detected (e.g. Brinks 1990), although the ratio of atomic to molecular gas decreases markedly towards the nuclei of these galaxies, with H_2 dominating over HI inside the central few kpc (Young 1990).

As well as the optical–radio properties described above, emission in the UV (from massive stars and ionized gas) and at X-ray energies (from hot gas, X-ray binaries and supernova remnants) are features of starburst spectra (e.g. Watson, Stanger & Griffiths 1984; Courvoisier *et al.* 1990). Fig. 1.1 shows the morphology of M82 as observed in near-infrared, mid-infrared, 3-mm and radio continuum, and the ^{12}CO J=1–0 2.6-mm line, tracing, respectively, the underlying stellar mass distribution, hot dust, ionized gas, young supernova remnants and the molecular interstellar medium.

One particular feature that has emerged from multiwavelength observations of galaxies is a remarkably tight correlation, both spatially and in flux, between the infrared and non-thermal radio continuum emission in spiral galaxies. This correlation extends over three orders of magnitude in luminosity, from the quiescent spiral M31 to the most powerful merger systems (Rieke *et al.* 1980; de Jong *et al.* 1985; Helou, Soifer & Rowan-Robinson 1985). Although the reason behind such a correlation

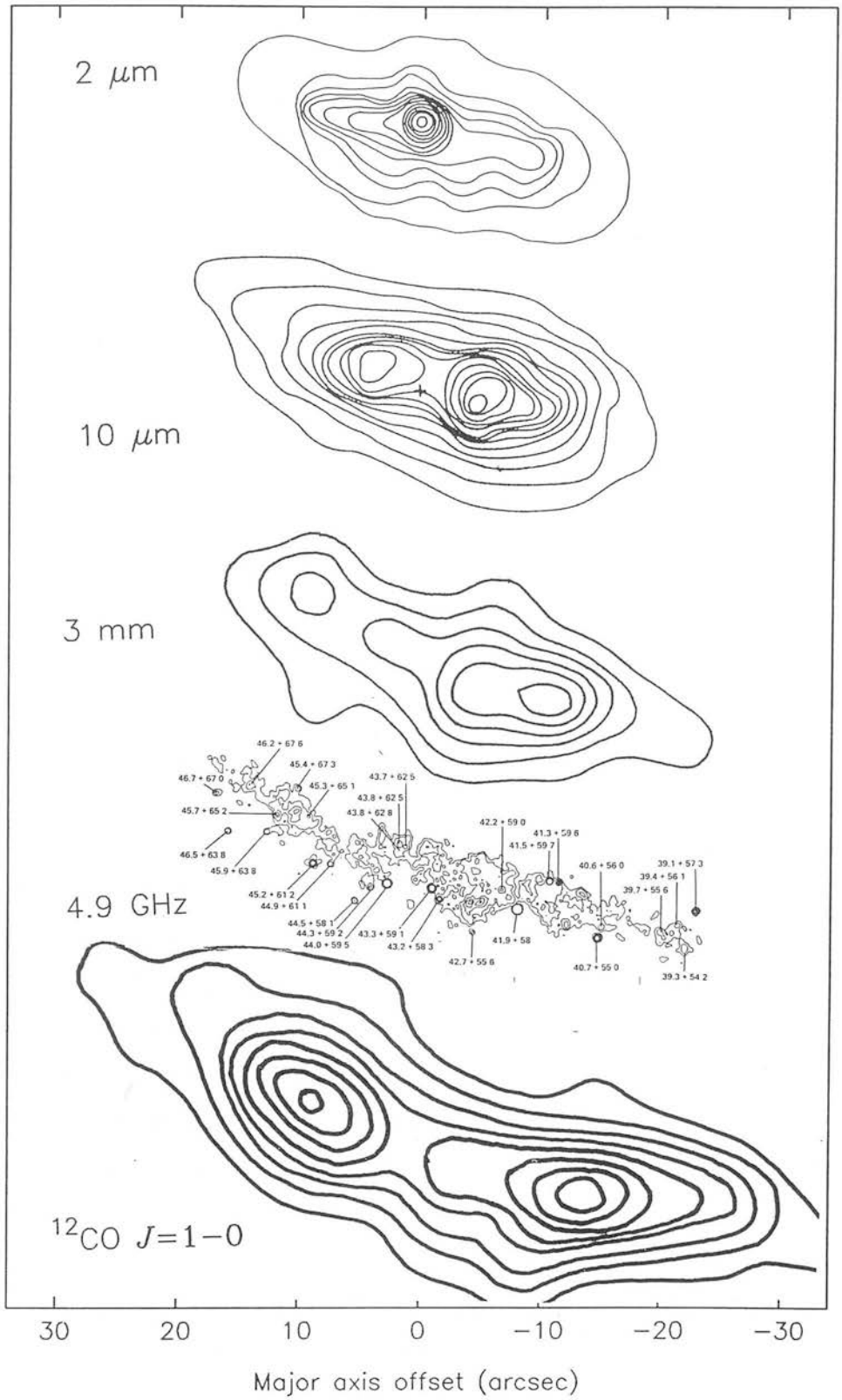

Figure 1.1: The morphology of M82 as seen in the near-infrared (Rieke *et al.* 1980), mid-infrared (Telesco *et al.* 1991), millimetre and radio continuum (Carlstrom & Kronberg 1991; Kronberg *et al.* 1985) and ^{12}CO (Lo *et al.* 1987), each tracing a different component of the star formation process – see text for more details.

might appear obvious (both infrared – via reradiation of UV – and radio emission – via supernovae – trace massive star formation), the reality is more complex. Derived supernova rates and observed discrete remnants can account for only a fraction of the non-thermal radio flux from a galaxy such as M82 (Helou *et al.* 1985), but introducing the diffuse cosmic-ray synchrotron component into the equation would involve the galactic magnetic field, and it is not immediately obvious how this would be correlated with massive star formation. The infrared emission, too, is composed of several components, including cool diffuse dust heated by the general stellar radiation field, as well as grains directly associated with massive star formation. The astrophysics underlying the infrared–radio correlation is still a topic of debate.

1.1.2 Starburst modelling

The physical dimensions of even nearby extragalactic starburst regions (1 kpc $\sim 20''$ at a distance of 10 Mpc), coupled with the available resolution (typically $5'' - 20''$ at infrared–radio wavelengths) means that, in general, only global properties of star-forming galaxies can be measured, and so it is global starburst characteristics (e.g. total ionizing photon flux) that are modelled. The parameters that we might hope to extract from such modelling include, for example, star formation rate, starburst age, and the distribution, upper and lower limits of stellar temperatures, masses and spectral types. Evaluating these would be a significant step towards finding out what triggered the starburst in the first place, investigating how it might evolve, and what effect it has already had, and will have, on the rest of the galaxy.

Several methods can be used to estimate the star formation rate [see, for example, the review by Kennicutt (1990)]. In the optical, recombination lines such as Hα can be used to calculate the emission rate of ionizing photons, but such lines are sensitive principally to more massive stars, and are affected by even small amounts of extinction. More useful tracers are infrared recombination lines, although in deeply embedded nuclear star formation regions, differential extinction can be a problem even at near-infrared wavelengths. Radio recombination lines are too weak to be detected in any but the nearest and brightest starbursts. Puxley (1988) detected the 43-GHz H53α transition in M82, and deduced a Lyman continuum photon rate of 1.1×10^{54} s^{-1} for the central $40''$ (2 kpc), equivalent to approximately 5×10^6 B0 stars (Chapter 2).

Radio free–free continuum emission is another tracer of ionized gas, but is prone to uncertain degrees of contamination by non-thermal synchrotron processes.

Far-infrared continuum emission can also be used to estimate the recent star formation rate, under the assumptions that (i) the long-wavelength radiation comes exclusively from the starburst, and not from the underlying old stellar population, and (ii) all the stellar emission is absorbed and reradiated – none escaping out of the plane of the galaxy, for example, in an edge-on system. Condition (i), in particular, requires more knowledge than we currently possess about the contribution to far-infrared emission of a cool, diffuse 'cirrus' component, produced by the general interstellar radiation field, rather than by OB-star/HII-region/molecular-cloud complexes (e.g. Cox & Mezger 1989). By assuming that the far-infrared *is* all from young stars, and by making some additional assumptions about the distribution of stellar masses, Telesco (1988) estimates a star formation rate of ~2–12 $M_\odot$ yr^{-1} for a far-infrared luminosity of around 0.4–3 $\times$ 10^{10} $L_\odot$. This compares to ~2 $M_\odot$ yr^{-1} for the entire Milky Way. The most luminous mergers ($L_{\rm IR} \sim 10^{11-12}$ $L_\odot$) can have star formation rates of up to several hundred $M_\odot$ yr^{-1}. If these rates are constant, then for nuclear molecular gas concentrations of a few $\times$ 10^8–10^9 $M_\odot$, it is clear that such a starburst cannot be maintained for more than ~10^8 yr. Of course, such estimates are subject to a variety of assumptions, such as the exact range of stellar masses involved, the contribution to the far-infrared luminosity of of non-starburst components, the time evolution of the star formation rate, and return of material to the interstellar medium via mass loss and supernovae. The ratio of far-infrared luminosity to molecular gas mass, $L_{\rm IR}/M({\rm H_2})$, is often interpreted as a 'star formation efficiency' (e.g. Young 1990), and is higher in interacting and merging galaxies than in isolated ones. However, given the current uncertainties in interpreting $L_{\rm IR}$ as arising purely from massive young stars, and in measuring $M({\rm H_2})$, the use of this ratio as a star formation 'efficiency' is not universally accepted.

Another approach to starburst modelling is to take properties of the star formation as deduced from multiwavelength studies, for example, ionization rate or near-infrared stellar luminosity, and model these in terms of power-law functions of stellar mass integrated over some initial mass function with parameters such as star formation rate and burst age being varied to find the best fit to the data (Telesco 1988). An important

consideration in such studies is the stellar initial mass function (IMF), defined by its slope, and upper and lower mass limits. A powerful constraint on the lower mass cut-off is the total (i.e. dynamical) mass of the system, since low-mass stars contribute principally mass to the integrated properties of a galaxy, while high-mass stars produce the bulk of the luminosity and ionization. A starburst model must be able to produce the observed emission without exceeding this mass constraint, including mass contained in the form of interstellar material and disc stars.

Rieke *et al.* (1980) adopted a multiwavelength approach in their study of M82. They modelled the bolometric and K luminosities, near-infrared CO band depth and Brγ emission in terms of an exponentially decaying starburst with a power-law IMF. They deduced a burst age of a few $\times$ 10^7 yr, a supernova rate of $\sim$ 0.3 yr^{-1} (10 times that of the entire Milky Way), and a high conversion efficiency of gas into stars, $\sim$30–50% . Significantly, they also found that the burst must be biased towards the formation of massive ($\geq$3 $M_{\odot}$) stars, if it is to stay within the limits imposed by the dynamical mass of the system. This finding – that bursts of star formation are deficient in low-mass stars, or that the IMF is 'top-heavy' (Scalo 1990) – have been mirrored by other studies. Wright *et al.* (1988) modelled the 10 μm luminosity of a sample of merging galaxies, assuming a solar neighbourhood IMF slope and upper mass limit of $\sim$30–60 $M_{\odot}$. Constraining the total mass of the starburst to be no more than 10% of the dynamical mass of the system, they concluded that stars less massive than $\sim$3–6 $M_{\odot}$ are not present. Such findings clearly have consequences for the effect of the starburst on its surroundings – massive stars are more likely to end their lives as supernovae, for example, and are more prolific emitters of UV radiation – and ultimately on the physical and chemical evolution of the galaxy. But, as pointed out by Scalo (1990), such conclusions are dependent on the exact form assumed for the IMF, as well as the extinction adopted (affecting observed fluxes) and assumptions concerning the time evolution of the star formation rate.

Information on the high-mass end of the stellar population can be obtained by observing emission features whose relative strengths are sensitive to the shape of the exciting radiation spectrum. For example, the infrared lines from species such as NeII, ArIII and SIV arise from different levels of excitation and so are sensitive to the effective temperature of the exciting stars. Similarly, the ratios of hydrogen and

helium recombination lines in the near-infrared depend on the shape of the ionizing UV continuum and hence the stellar population at the upper end of the IMF. The Brγ(2.166 μm)/HeI(2.058 μm) ratio in the merger NGC 3256, for example, has been modelled in terms of an IMF with an upper bound at 25–30 $M_{\odot}$ (Joseph 1991). Ho, Beck & Turner (1990a) adopt a slightly different approach, using Brγ and Brα observations to estimate the luminosity of young stars in several bright starbursts, then equating this with the observed infrared luminosity to deduce an upper mass limit of 30–60 $M_{\odot}$.

1.1.3 Starbursts in isolated galaxies

A number of studies have linked active star-forming activity with the presence of a bar or oval gravitational distortion in an otherwise apparently isolated galaxy. Puxley (1988) studied a sample of *IRAS*-selected galaxies and found that a significant fraction of the barred galaxies have 'warm' *IRAS* colours and extended central radio continuum sources indicative of active nuclear star formation. Devereux (1987) made 10 μm observations of over 100 infrared-bright, nearby, non-interacting galaxies and found that almost half of the early-type barred spirals showed enhanced luminosity in their central kiloparsec regions. Hummel (1981) concluded that the central radio sources in barred spirals are typically twice as strong as those in ordinary spirals.

Some of the nearest barred galaxies exhibit kiloparsec-sized rings of star-forming regions delineated by 'hotspots' seen in the radio, Hα and infrared, as well as in molecular tracers such as CO (e.g. NGC 1097, Telesco & Gatley 1981). Millimetre-wave CO observations often reveal the presence of bars in galaxies which optically appear unbarred, but which exhibit other signs of starburst activity such as intense infrared emission, for example NGC 6946 (Weliachew, Casoli & Combes 1988). Such galaxies frequently display highly non-circular motions of gas near their nuclei, seen in millimetre CO lines, suggesting infall or outflow, while the appearance of the rings suggests a build-up of star-forming 'fuel' near the nucleus. Numerical simulations of barred galaxies (e.g. Combes 1988) show that the effect of a bar is to produce a rotating non-axisymmetric gravitational potential. Gas encountering this potential loses angular momentum and flows inwards. The accumulation of gas at the centre of the galaxy may trigger high-mass star formation via an increase in cloud–cloud collisions. Combes

(1988) showed that the same effect (non-axisymmetric potential and gas inflow) can result from a mild tidal interaction. Such a model may therefore explain both the high incidence of star formation in barred and mildly interacting galaxies and the nuclear rings often associated with them. A related explanation for the formation of rings was proposed by Nakai *et al.* (1987) in their model for the origin of the M82 starburst. Nakai *et al.* suggest that a tidal interaction between M82 and the nearby (36 kpc distant) giant spiral M81, some 10^8 yr ago, triggered the development of a bar-like potential in M82 with subsequent gas flow to the centre, precipitating a starburst. The rapid star formation, via stellar winds and a supernova rate of $\sim$0.3 yr^{-1} in the starburst region, created the ring by evacuating the central cavity of gas, blowing it away from the plane in the form of an outflow of ionized gas seen in Hα and X-rays (Rieke *et al.* 1980; Watson *et al.* 1984; McCarthy, Heckman & van Breugel 1987). The starburst will be exhausted in a few $\times$ 10^8 yr, unless the molecular fuel is replenished, perhaps via infall of HI from M81 (Nakai *et al.* 1987).

1.1.4 Starbursts in interacting and merging galaxies

Closely interacting and merging galaxies are another class of object in which the signatures of vigorous massive star formation are observed. This class of galaxy ranges from the moderate- to high-luminosity (10^{11-12} $L_\odot$) interacting systems studied by Joseph and collaborators (e.g. Joseph & Wright 1985) to the 'ultraluminous galaxies' (L $>10^{12}$ $L_\odot$), many of which are mergers (Sanders *et al.* 1988). While in infrared-bright galaxies such as M82 and IC342 all the observational evidence points towards star formation powering the infrared emission, for these more violent systems the dominant energy source producing the observed spectrum may be an active nucleus.

Observationally, starburst activity may be distinguished by narrow, HII-region-like emission lines and extended emission at mid-infrared to radio wavelengths, while an AGN displays broad lines and a compact ($\leq$1 pc) nuclear source. The observational evidence is conflicting. Joseph & Wright (1985) studied nine advanced merging systems (where the two galaxies had coalesced into a single object) and found extended mid-infrared emission and HII-region line spectra, which they interpreted as evidence for extensive 'super-starbursts'. Sanders *et al.* (1988), on the other hand, studying 'ultraluminous' *IRAS* galaxies, found their data to be more consistent with an active

nucleus and suggested that these objects are the dust-embedded early stages of quasars. More recently, however, a VLA study of 40 ultraluminous galaxies by Condon *et al.* (1991) found only one with a $\leq$1 pc, 'monster-like' radio morphology, while most of the others were extended sources lying on the infrared–radio correlation. In the case of the double-nucleus merger NGC 6240, extended 2 and 10 μm emission, as well as the presence of a 2.3 μm CO absorption band and mid-infrared emission features, are evidence of star formation (Rieke *et al.* 1985). Andreasian & Khachikian (1987) found emission-line ratios characteristic of an HII region in one nucleus, and an AGN in the other. The merger Arp 220 displays an infrared luminosity of 10^{12} $L_{\odot}$ from a 20 μm source less than 500 pc across, an unresolved 2 μm source and broad (600–1300 km s^{-1}) Hα and Brα lines, all leading to its interpretation as a dust-embedded quasar (Norris 1985; Becklin & Wynn-Williams 1987; DePoy, Becklin & Geballe 1987; Neugebauer *et al.* 1987).

The interplay between starburst and central 'monster' in classical active galaxies is also not well understood. In the nearby Seyfert NGC 1068, for example, a 3-kpc 'starburst disc' appears to coexist with a compact active nucleus, both producing an equal share of the infrared luminosity of 1–2$\times10^{11}$ $L_{\odot}$ (Telesco *et al.* 1984; Lester *et al.* 1987). A few authors have even suggested that the observed properties of some 'active' nuclei do not require a compact 'monster' at all. Heckman *et al.* (1987) argue that a supernova-driven 'superwind' could reproduce the observed line characteristics, while Terlevich (1990) models active nuclei in terms of a population of very high-temperature ($\geq$100 000 K) massive young Wolf–Rayet-type stars ('warmers') produced in a young, high-metallicity starburst.

The question of an evolutionary link between starbursts and AGN is also actively debated. Sanders *et al.* (1988) interpret their ultraluminous galaxies as being the initial, dust-enshrouded stages of quasars, surrounded by a starburst which has been triggered by the huge nuclear gas concentrations resulting from the merger. As the AGN sheds its obscuring dust, and starts to dominate the decaying starburst, it becomes an optically visible quasar. An alternative view, presented by Scoville (1990), is that the large mass concentration in the central kiloparsec of a starburst galaxy causes any mass loss during stellar evolution to sink into the resulting deep potential well, leading to the formation of a compact nuclear 'monster'.

1.2 The interstellar medium of star-forming galaxies: the CO molecule as a tracer of molecular hydrogen

The most important constituents of the interstellar medium of a galaxy are atomic and molecular hydrogen (HI and H_2). Atomic hydrogen has been well studied via its 21-cm line (e.g. see van der Kruit & Allen 1976). The study of the spatial distribution, mass, physical condition and kinematics of molecular hydrogen in galaxies is vital, as it is the raw material for star formation, and the dominant component of the interstellar medium in the star-forming regions of a galaxy. In galaxies which show enhanced star formation, its relation to other tracers such as HI and far-infrared continuum may shed light on the past history and possible future evolution of the galaxy in terms of star-formation rate, efficiency and duration, as well as the effect that the high temperatures, intense UV fields and elevated energy input of a starburst may have on the molecular clouds when compared to those in the disc of the Milky Way.

Unfortunately, H_2 is very difficult to detect. Being a homonuclear molecule, it has no easily detectable rotational transitions, electric dipole transitions being forbidden, and the lowest quadrupole transition occuring 510 K above ground level, making it unsuitable for tracing relatively cool (<100 K) clouds. Rotation–vibration transitions in the near-infrared can be excited by shocks or UV fields, but such conditions are generally not representative of the bulk of the cool interstellar medium. Because of these difficulties, it has become common practice to observe a tracer, something that can be considered to be intimately mixed with the H_2, and then use some conversion factor to obtain $N(H_2)$, the column density of molecular hydrogen. The most widely used tracers for both Galactic and extragalactic observations have been rotational transitions of the CO molecule, and continuum emission from UV-heated dust, both mechanisms operating in the millimetre and submillimetre wavelength regions.

The use of CO as a tracer of the excitation, column density and kinematics of H_2 in star-forming regions, especially in extragalactic starbursts, has had perhaps more than its fair share of controversy over the last decade or so. Many excellent review papers exist, such as those by van Dishoeck & Black (1986), Israel (1988), Maloney (1990a), Young & Scoville (1991) and Henkel, Baan & Mauersberger (1991).

CO is the next most abundant molecule after H_2, being $\sim 10^5$ times less abundant. It has a rotational ladder with transitions in the millimetre and submillimetre region, all but one of the seven lowest transitions being in atmospheric windows observable from the ground under good conditions (van Dishoeck & Black 1986). In addition, the transitions correspond to temperatures easily attained in molecular clouds (e.g. $h\nu/k =$ 5.5 K for the J=1–0 and 11.1 K for the J=2–1 lines) and are excited, by collisions with hydrogen molecules, at densities $n(H_2)\sim$100–300 cm^{-3}, again typical of Galactic giant molecular clouds. The Milky Way has been extensively observed in $^{12}C^{16}O$ (^{12}CO) and most of the major isotopes, such as ^{13}CO, $C^{18}O$ and $C^{17}O$. Since the first extragalactic detection of ^{12}CO in five galaxies, including M82, over 15 years ago (Rickard *et al.* 1976), several hundred galaxies have been detected and many have been mapped in at least ^{12}CO J=1–0. Published work ranges from multiline, multitransition studies of individual objects (*e.g.* Eckart *et al.* 1990, for IC342) to global properties of large samples (*e.g.* Young & Scoville 1991).

All these studies require a reliable conversion factor to transform observed CO integrated intensities (where $I_{CO} = \int T_b \, dv$, the integral of observed brightness temperature over the line profile) to H_2 column densities. The following sections outline the methods usually employed, together with their possible pitfalls, in particular relating to the application of a 'constant conversion factor' $N(H_2)/I_{CO}$, to extragalactic starbursts in which conditions in the clouds are liable to be quite different to those in the disc of the Milky Way.[1]

1.2.1 Converting from ^{13}CO to $N(H_2)$

In Galactic molecular clouds, the ^{12}CO molecule is always very optically thick (Lada 1985), and so the ^{13}CO isotope is often used instead ([^{12}CO]:[^{13}CO]$\sim$89 in the solar neighbourhood, Wannier 1980). The column density of ^{13}CO is obtained by observations of both ^{13}CO and ^{12}CO (see Appendix C). This is then converted to $N(H_2)$ by applying a conversion factor, $N(H_2)/N(^{13}CO)$.

The accepted calibration of $N(H_2)/N(^{13}CO)$ was provided by Dickman (1978), who observed ^{12}CO and ^{13}CO at 100 locations towards 38 dark clouds, using a Local Ther-

[1] Here, I_{CO} always refers to the integrated intensity of the J=1–0 transition of ^{12}CO .

modynamic Equilibrium (LTE) analysis to obtain $N(^{13}\mathrm{CO})$. Measurement of the visual extinction, A_V, from star counts, and application of the 'standard' gas-to-extinction ratio (Bohlin, Savage & Drake 1978) then lead to $N(\mathrm{H_2}) = 5 \times 10^5\ N(^{13}\mathrm{CO})$ (Dickman 1978). Some possible uncertainties of this method were highlighted by Frerking, Langer & Wilson (1982) who used isotopic CO observations together with star counts and infrared photometry to deduce $N(\mathrm{H_2})/N(^{13}\mathrm{CO})$ for clouds in Taurus and ρ Oph. They found order-of-magnitude variations on small scales, attributing these to the effect of temperature, density and UV field on the ^{13}CO emission.

1.2.2 ^{12}CO as a tracer of H_2 in galaxies

Unfortunately, ^{13}CO is generally far too weak in extragalactic systems to be of use as a global tracer of H_2. The ^{12}CO line, on the other hand, is strong in many galaxies, but if, as in the Milky Way, it is very optically thick, it is not immediately apparent that it will trace $N(\mathrm{H_2})$. However, individual molecular clouds are unresolved by the large beams of millimetre-wave telescopes (for example $10'' = 500$ pc at a distance of 10 Mpc) and so extragalactic CO observations consist of an ensemble of unresolved clouds within the beam. If cloud–cloud shadowing in position–velocity space is not significant (because of the effects of galaxy rotation and large cloud–cloud velocity dispersions, compared to the small internal velocity dispersion of an individual cloud) then an observed CO profile is in effect just 'counting the number of clouds in the beam' and, if the clouds do not vary too widely in their physical properties, I_{CO} will be correlated with $N(\mathrm{H_2})$, with some conversion factor X, where

$$X = N(\mathrm{H_2})/I_{\mathrm{CO}}. \tag{1.1}$$

This approach has been widely developed, both empirically and theoretically, with the different methods giving results which are encouragingly within a factor ~2–3 of each other. This has led to a so-called 'constant conversion factor' which has been widely applied to nearly all extragalactic CO observations so far (e.g. Young & Scoville 1991). However, doubts have recently been voiced over the applicability of this calibration to environments such as those of high star formation or low metallicity, in which the molecular clouds may be expected not to resemble those in the disc of the Milky Way (e.g. Sanders, Solomon & Scoville 1985). Before considering the reliability of X in

such environments and its dependence on the physical parameters of the gas, it may be useful to review briefly its calibration in the Milky Way.

The four methods used to obtain $N(H_2)$ and hence calibrate the I_{CO}–$N(H_2)$ conversion are extinction measurements, LTE analysis of ^{12}CO and ^{13}CO, virial equilibrium in clouds, and high-energy γ-ray observations. These techniques and their possible pitfalls are outlined below.

Extinction measurements

Visual extinction, A_V, can be measured (via star counts or infrared photometry) for a sample of clouds for which ^{12}CO data also exist, and the standard Galactic gas-to-extinction ratio (Bohlin *et al.* 1978) applied to give $N(H_2)$ as a function of I_{CO}. The main problem with this method is that the $N(H_2)/A_V$ ratio comes from regions of low extinction (A_V <1.5) and must be assumed to hold also for the higher extinctions present in molecular clouds.

LTE analysis

LTE analysis of ^{12}CO and ^{13}CO observations (see Appendix C) can be used to obtain a ^{13}CO column density, $N(^{13}CO)$, which can then be combined with an $N(H_2)$:$N(^{13}CO)$ abundance ratio (e.g. Dickman 1978) to yield $N(H_2)$. The possibility of non-LTE effects, or the effect on the ^{13}CO:H_2 abundance of massive star formation (intense photodissociating UV radiation, etc.) should be considered, however (e.g. Frerking *et al.* 1982).

γ-ray analysis

The diffuse, high-energy γ-rays (E_γ >300 MeV) observed from the Galactic plane result from the decay of π^0 mesons produced by the interaction of a uniform distribution of cosmic ray particles with atomic and molecular hydrogen nuclei. The intensity of γ-rays can be related to the column density of molecular hydrogen in a way that is independent of CO/H_2 abundance, temperature, optical depth, and excitation of the clouds. The major work in this area has been done by comparing data from the *COS-B* satellite with large-scale HI and CO surveys of the Galactic plane (e.g. Bloemen *et al.* 1986).

The only pitfalls are the rather low resolution ($\sim 1°$) of the *COS-B* surveys, and the possibility of contamination of the diffuse γ-ray emission by point sources. For this reason, values of X that emerge are generally upper limits.

Virial theorem analysis

All the methods outlined above are essentially empirical – that is, although they provide a value for the conversion factor, they do not explain why there should be a correlation between $N(\mathrm{H_2})$ and I_{CO} in the first place, nor what its physical dependencies might be. The virial theorem, on the other hand, offers both a method of calculating $N(\mathrm{H_2})$ in a cloud, and also some physical insight into where the correlation comes from (e.g. Dickman, Snell & Schloerb 1986; Maloney 1990a).

Consider (for simplicity) a uniform top-hat beam profile of angular diameter θ being used to observe an unresolved ensemble of molecular clouds in a galaxy at distance D. Then the area covered by the beam on the galaxy is

$$A_{\mathrm{b}} = \frac{\pi}{4} (\theta\ D)^2. \tag{1.2}$$

It can be shown (Dickman *et al.* 1986; Maloney 1990a), that the observed integrated intensity of CO can be represented by the sum of the contributions from the individual clouds, which, if cloud–cloud shadowing is not important and the physical properties of the clouds do not vary too greatly, is given by

$$< I_{\mathrm{CO}} > \simeq\ A_{\mathrm{b}}^{-1}\ N\ \frac{\pi}{4}\ T_0\ < l^2\ \Delta v(l)\ >, \tag{1.3}$$

where N is the total number of clouds in the beam, T_0 is the area-averaged radiation temperature of a cloud (assumed the same for all clouds), l is the diameter of a cloud and Δv the FWHM of the individual cloud profile. Similarly, the average column density of molecular hydrogen in the beam can be expressed as

$$< N(\mathrm{H_2}) > = A_{\mathrm{b}}^{-1}\ N\ \frac{\pi}{6}\ < l^3\ n(l) >, \tag{1.4}$$

where n is the molecular hydrogen number density. Then the conversion factor X [$= N(\mathrm{H_2})/I_{\mathrm{CO}}$] is given by

$$X = \frac{2}{3}\ \frac{< l^3\ n(l) >}{T_0\ < l^2\ \Delta v(l) >}. \tag{1.5}$$

For virialized clouds, the observed linewidth is governed by the cloud size, and the one-dimensional velocity dispersion Δv is given by

$$\begin{aligned} \Delta v &= (2\alpha\, GM/3l)^{1/2} \\ &= (\alpha\, G\pi\, n\, \overline{m}_{\mathrm{H_2}} l^2/9)^{1/2}, \end{aligned}$$

where α is a constant related to the physical structure of the cloud and $\overline{m}_{\mathrm{H_2}}$ is the mean mass per hydrogen molecule (including the contribution from helium and other elements). Hence

$$X = \frac{N(\mathrm{H_2})}{I_{\mathrm{CO}}} \propto \frac{n^{1/2}}{T_0}. \tag{1.6}$$

Therefore the virial theorem provides a theoretical basis for a correlation if the cloud physical conditions are similar, and predicts its dependence on cloud conditions.

A large number of papers have been published over the last decade, utilizing one or more of the above methods to evaluate X. Perhaps the most comprehensive work on the subject is that of Young & Scoville (1982). Using extinction measurements, LTE analysis and the virial theorem on observations of cloud cores, dark clouds and disc Giant Molecular Clouds (GMCs), they derived a value for X of

$$X = 4 \times 10^{20}\ \mathrm{cm^{-2}}\ (\mathrm{K\ km\ s^{-1}})^{-1}. \tag{1.7}$$

Encouragingly, all the methods (empirical and theoretical) in the literature seem to converge on a value for X, for disc clouds in the Milky Way, within a factor ~2–3 of the Young & Scoville value, although values derived from γ-ray observations are consistently lower (e.g. see Table 1.1) than those arrived at by other methods (Young & Scoville 1982; Sanders, Solomon & Scoville 1984; Kutner & Leung 1985; Bloemen *et al.* 1986; Dickman *et al.* 1986; Scoville *et al.* 1987; Solomon *et al.* 1987; Strong *et al.* 1988).

Table 1.1 summarizes values of X derived from the various studies.

1.2.3 X in extreme extragalactic environments

The 'constant conversion factor', as it has become known, has been widely applied to nearly all extragalactic CO observations, whether single-object studies or multi-object

Reference	X $[\mathrm{cm}^{-2}\ (\mathrm{K\ km\ s}^{-1})^{-1}]$	Notes
Young & Scoville 1982	4×10^{20}	1
Sanders *et al.* 1984	3.9×10^{20}	2
Kutner & Leung 1985	2×10^{20}	3
Blitz *et al.* 1985	3×10^{19}	4
Dickman *et al.* 1986	2.8×10^{20}	5
Bloemen *et al.* 1986	$<2.8 \times 10^{20}$	6
Scoville *et al.* 1987	3.6×10^{20}	7
Solomon *et al.* 1987	3.0×10^{20}	7
Strong *et al.* 1988	$<2.3 \times 10^{20}$	6

(1) Extinction measurements, LTE and virial theorem analyses of hot cores, dark clouds and GMCs. (2) $N(\mathrm{H_2})$ versus $I(^{13}\mathrm{CO})$ correlations of Dickman (1978) and Frerking *et al.* (1982), plus the assumption that $I(^{12}\mathrm{CO})/I(^{13}\mathrm{CO}) \simeq$constant$\simeq 5.5$. (3) Theoretical, non-LTE cloud models. (4) γ-rays in the central 400 pc of the Galaxy. (5) Virial theorem modelling of a cloud ensemble. (6) γ-rays in the Galactic disc. (7) Virial analysis of UMass/Stony Brook Galactic Plane CO Survey.

Table 1.1: The Galactic value of X.

statistical surveys, over the last 10 years (Young & Scoville 1991). Radial variations of I_{CO}, and variations from one galaxy to another, have all been interpreted in terms of differing amounts of molecular hydrogen, and the studies have been used to infer global properties of star formation in galaxies (Young & Scoville 1991). In the discs of normal spiral galaxies it probably does give a reliable measure of the quantity of molecular gas. However, doubts have recently been raised as to its applicability in galactic nuclei, 'starburst' galaxies and low-metallicity irregular galaxies, where conditions are likely to differ from those in the disc of the Milky Way. The conversion factor X, having been calibrated in the Galactic disc, is as such strictly valid only in regions where the physical conditions are the same [$T \simeq 10$ K, $n(\mathrm{H_2}) \simeq 200\ \mathrm{cm}^{-3}$].

Even in the disc of the Milky Way, the $^{12}\mathrm{CO}/^{13}\mathrm{CO}$ ratio varies from $\simeq$3–20 on scales of individual clouds, indicating that molecular cloud properties vary. The $^{13}\mathrm{CO}/N(\mathrm{H_2})$ ratio varies by up to an order of magnitude on small scales (Solomon, Sanders & Scoville 1979; Frerking *et al.* 1982) due to the effects of UV field and temperature on the ^{13}CO emission. The assumption of virial equilibrium in molecular clouds has also been questioned. Injection of energy into the clouds via stellar winds, HII regions and supernovae may result in linewidths greater than virial and consequent overestimation of $N(\mathrm{H_2})$ (Maloney 1990b).

Could the central concentration of CO emission seen in many infrared-bright galax-

ies be merely an artefact of increased CO excitation at their centres? There are many reasons to believe that in vigorously star-forming galaxies the molecular clouds will be very different from those in the disc of the Milky Way, with high temperatures (>40 K), gas densities (10^3 cm^{-3}) and UV field intensities (100–1000χ, where χ is the solar neighbourhood UV field).

It has already been shown (equation 1.6) that X varies with the physical conditions of the gas; specifically, $X \propto n^{1/2}/T$. Maloney & Black (1988; see also Maloney 1990a) have carried out extensive modelling of the CO emission from ensembles of clouds in spiral galaxies, investigating the effect on X of changing physical conditions. Their results are of particular relevance to two important classes of extragalactic environment – galactic nuclei and starbursts, and low-metallicity galaxies.

The conversion factor in galactic nuclei and starbursts

Molecular clouds in the nuclei of spiral galaxies like the Milky Way, and in actively star-forming galaxies such as M82 and IC342, can be dramatically influenced by the intense UV fields, high temperatures and energy input from stellar winds and supernovae that result from the star formation within and among them. In such environments, can the conversion factor X, calibrated on relatively quiescent Galactic disc molecular clouds, be reliably tracing molecular hydrogen?

The models of Maloney & Black (1988) indicate that the Galactic value of X can overestimate $N(H_2)$ by factors of ~5 in galaxies with enhanced nuclear temperatures, such as may be expected for starbursts, or the central few hundred parsecs of normal spirals. In the Milky Way, too, γ-ray observations of the Galactic Centre have produced striking results. While the integrated intensity of ^{12}CO peaks sharply in the central few hundred parsecs, implying a central concentration of molecular gas, the high-energy γ-rays show no such enhancement (Blitz *et al.* 1985). By converting γ-ray intensity to $N(H_2)$, Blitz *et al.* conclude that the 'constant conversion factor' may be overestimating $N(H_2)$ by a factor of 7 in the centre of the Milky Way. It has been suggested that the central concentrations of H_2 inferred from CO observations of the Milky Way and other galaxies (e.g. Young 1990) may be partially an artefact of the physical conditions found there, and that the CO integrated intensity may in reality be tracing a complicated combination of gas excitation and mass. There is ample evidence of high temperatures,

densities and UV fields in galactic nuclei and starbursts. Rotation–inversion transitions of the ammonia molecule imply temperatures $\geq$50 K over large scales, both in the Galactic Centre and in the starburst galaxy IC342 (Morris *et al.* 1983; Mauersberger *et al.* 1986; Martin & Ho 1986), while high-resolution interferometer observations of M82 reveal gas temperatures of 40 K or more (Lo *et al.* 1987). Single-dish ^{12}CO J=1–0/J=2–1 antenna temperature ratios of $\geq$2 in M82 and Maffei 2 have been interpreted as arising from warm, partially optically thin gas (Knapp *et al.* 1980; Sargent *et al.* 1985), whereas use of the constant conversion factor relies on the assumption that the molecular gas is both cool and optically thick. Dust temperatures of >30 K in infrared-bright galaxies such as M82 and Maffei 2 are common (Telesco & Harper 1980; Rickard & Harvey 1983, 1984; Thronson *et al.* 1987; Hughes, Gear & Robson 1990). Improving millimetre-wave receiver technology has enabled the detection of molecules such as HCN, CS and HCO^+ in galaxies, requiring the presence of moderate amounts of dense [$n(H_2)\sim10^4$ cm^{-3}] gas, far in excess of the $n(H_2)\sim200$ cm^{-3} typical of galactic GMCs (e.g. Sanders *et al.* 1985). Observation of the extinction-free H53α radio recombination line from the centre of M82 (Puxley *et al.* 1989) suggests that the molecular clouds there are subject to UV fields 100–1000 times more intense than in the solar neighbourhood, resulting in increased gas heating and photodestruction of CO.

An indication of the extent to which molecular clouds in star-forming galaxies are affected by the hot young stars within them comes from far-infrared spectroscopy. The 158 μm transition of singly ionized carbon arises in photodissociation regions (PDRs) at the interfaces between HII regions and molecular clouds, illuminated by intense UV fields from hot young O and B stars. The [CII] line has been detected from $\sim$15 infrared-bright, gas-rich galaxies, and accounts for up to 0.5% of the far-infrared luminosities of these systems (Crawford *et al.* 1985; Stacey *et al.* 1991). There is a striking correlation, in intensity, line profile and spatial distribution, between the [CII] and ^{12}CO J=1–0 transitions in these galaxies, implying that the CO- and [CII]-emitting regions are intimately associated. The correlation in intensity extends over nine orders of magnitude and includes both Galactic star formation regions and extragalactic starbursts (Crawford *et al.* 1985; Stacey *et al.* 1991). Wolfire, Hollenbach & Tielens (1989) explain the correlation by a common origin of both the CO and [CII] emission in PDRs. They conclude that a significant fraction of the ^{12}CO J=1–0 emission in galaxies may arise

from the warm (>50 K), partly photodissociated cloud layers at A_V=2–5, and that up to 40% of the interstellar medium of a star-forming galaxy may reside in these regions. Under such circumstances, the Galactic disc calibration of X is unlikely to be valid, and the CO emission may be tracing a complex combination of UV field and mass (Crawford *et al.* 1985).

The conversion factor in low-metallicity galaxies

Dwarf irregular galaxies, which are actively forming stars and which might therefore be expected to have rich reserves of molecular gas, are unexpectedly weak in CO emission (Israel & Burton 1986; Israel *et al.* 1986). If the Galactic conversion factor is considered to hold in these galaxies, then the mass of molecular hydrogen must be very low, and the star formation very efficient. Maloney & Black (1988), however, interpret the observations as a result of the lower metallicity of irregular galaxies, leading to clouds that are smaller, when 'seen' in CO, than in H_2. In addition, if low metallicity is linked to a low gas-to-dust ratio, then the penetration of UV radiation into molecular clouds will be increased. While H_2 is quite strongly self-shielding to dissociating UV, CO is less so, and the CO:H_2 ratio will decrease still further. Thus, the weakness of CO emission in irregulars is explained quite naturally as a result of the lower metallicity in these systems, and adoption of the Galactic value of X will lead to underestimates of the H_2 mass in these galaxies.

1.3 Dust continuum emission

An alternative tracer of the molecular interstellar medium, which has already been widely used in the Milky Way and, more recently, as receiver technology improves, in external galaxies as well, is thermal continuum emission from dust.

Grains, mixed with gas and illuminated by the interstellar radiation field (ISRF), or by discrete sources (young stars), are very efficient absorbers of UV/optical radiation, attaining equilibrium temperatures of 10–40 K. This energy is then reradiated as blackbody emission (modified by the grain optical depth), peaking in the far-infrared at $\sim$100 μm. That the far-infrared/submillimetre emission is a powerful signature of the star-forming ISM in galaxies is illustrated by the success of the *IRAS* mission, un-

covering a whole new class of infrared-bright galaxies radiating most of their luminosity longward of 10 μm.

Dust is optically thin to submillimetre radiation and so long-wavelength emission samples all the material equally, making the submillimetre thermal continuum a potentially powerful tracer of the gas with which the grains are mixed. In addition, unlike molecular line emission, the dust continuum is relatively unaffected by the increased UV fields and gas excitation which accompany active star formation, and so is useful as an independent handle on H_2 mass, as well as a check on the reliability of using ^{12}CO as a tracer of molecular hydrogen.

1.3.1 Optically thin dust continuum spectra

The observed spectrum of optically thin dust emission can be described in the simplest case, that of a uniform isothermal source, by a modified blackbody spectrum at a dust temperature T_d, via

$$F(\nu) = \Omega_s \, B(\nu, T_d) \, [1 - e^{-\tau(\nu)}] \simeq \Omega_s \, \tau(\nu) \, B(\nu, T_d), \tag{1.8}$$

where the submillimetre continuum optical depth is given by

$$\tau(\nu) = \tau_0 \left(\frac{\nu}{\nu_0}\right)^{\beta}, \tag{1.9}$$

and $\beta \simeq$1–2 at submillimetre wavelengths (Hildebrand 1983). In general, this equation only applies for wavelengths $\geq$40 μm , since the shorter wavelengths normally exhibit an excess of emission indicating a contribution from hotter dust in the source. Furthermore, the optically thin assumption may start to break down at short wavelengths in the densest clouds [column densities $N(H+H_2) \geq 10^{25}$ cm^{-2}, e.g. Mezger (1990)].

For optically thin material, then,

$$F(\nu) = \frac{2h\nu^3}{c^2} \left(\frac{\nu}{\nu_0}\right)^{\beta} \frac{(\tau_0 \Omega_s)}{(e^{h\nu/kT_d} - 1)}. \tag{1.10}$$

A least-squares fit (e.g. Bevington 1969) to the observed far-infrared-to-millimetre spectrum will therefore yield values for β, T_d and $(\tau_0 \Omega_s)$. If observations have been made at two or more wavelengths on the Rayleigh–Jeans tail of the emission ($\lambda \gg$ 480 μm for $T_d \sim$ 30 K) then it is possible to estimate the value of β and hence reduce the number of free parameters in the fit, since in the Rayleigh–Jeans region:

$$F(\nu) \propto B(\nu, T_d) \, \nu^{\beta} \propto \nu^{2+\beta}.$$

1.3.2 Molecular hydrogen masses from dust continuum observations

Consider a cloud of hydrogen (atomic and molecular) containing a population of N spherical dust grains mixed with the gas and heated, by absorption of stellar radiation, to a common temperature $T_{\rm d}$. The total flux density emitted by the grains at frequency ν will be

$$F(\nu) = N \, \frac{\pi a^2}{D^2} \, Q(\nu) \, B(\nu, T_{\rm d}),$$

where a is the radius of a grain, $Q(\nu)$ its emissivity at frequency ν, $B(\nu, T_{\rm d})$ the Planck function at frequency ν and temperature $T_{\rm d}$, and D the distance to the source. For a grain mass density ρ, the mass of dust in the source is

$$M_{\rm d} = \frac{F(\nu) D^2}{B(\nu, T_{\rm d})} \, \frac{4a\rho}{3Q(\nu)}. \tag{1.11}$$

If a gas-to-dust ratio, $M_{\rm g}/M_{\rm d}$, is then assumed, the mass of gas in the source is simply

$$M_{\rm g} = \frac{F(\nu) D^2}{B(\nu, T_{\rm d})} \, C, \tag{1.12}$$

where

$$C = \frac{4a\rho}{3Q(\nu)} \, \frac{M_{\rm g}}{M_{\rm d}}. \tag{1.13}$$

The effect on the above relations of grain size distribution, shape and composition is discussed by Hildebrand (1983), from which this sequence of equations is largely derived. Equation (1.12) requires knowledge of grain parameters and assumption of a gas-to-dust ratio. It is possible, however, to calibrate this relationship observationally, without the need to explicitly input values for a, ρ, $M_{\rm g}/M_{\rm d}$, etc., since the equation for gas mass can also be written

$$M_g = \Omega_{\rm s} \, D^2 \, N({\rm H} + {\rm H_2}) \, m_{\rm H} \, \mu, \tag{1.14}$$

where $\Omega_{\rm s}$ is the source solid angle, N(H+H_2) the total hydrogen column density (atomic + molecular), $m_{\rm H}$ the mass of a hydrogen atom and μ the ratio of total gas mass to hydrogen mass ($\mu \simeq$1.36).

In the submillimetre/millimetre region, the dust continuum emission is optically thin and the total flux density from the grain population is given by equation (1.8):

$$F(\nu) \simeq \Omega_{\rm s} \, \tau(\nu) \, B(\nu, T_{\rm d}), \tag{1.15}$$

where the optical depth $\tau(\nu)$ follows a power law, $\tau(\nu) \propto \nu^{\beta}$, with $\beta \sim$1–2. Adopting a standard extinction law, $R = A_V/E(B-V)$ (Rieke & Lebofsky 1985), and assuming that the ratio of column density to colour excess, $N(\mathrm{H+H_2})/E(B-V)$, as measured in the intercloud medium, applies (Bohlin *et al.* 1978) gives the ratio of hydrogen column density to visual extinction, $N(\mathrm{H+H_2})/A_V$. Determination of $\tau(\nu)$ and A_V in a calibration object then yields a value for $N(\mathrm{H+H_2})/\tau(\nu)$. Combining this with equation (1.14) and substituting for Ω_s in equation (1.15) then gives

$$M_g = \frac{F(\nu)D^2}{B(\nu,T_d)} \frac{N(\mathrm{H}+\mathrm{H_2})}{\tau(\nu)} m_H \mu \tag{1.16}$$

and, from comparison with equation (1.12), it can be seen that

$$C = \frac{4a\rho}{3Q(\nu)} \frac{M_g}{M_d} = \left[\frac{N(\mathrm{H}+\mathrm{H_2})}{\tau(\nu)}\right] m_H \mu \ . \tag{1.17}$$

Note that equation (1.17) does not require explicit knowledge of grain parameters and a gas-to-dust ratio if $N(\mathrm{H+H_2})/\tau(\nu)$ is calibrated observationally. It does, however, require the assumption that grain parameters and excitation conditions are similar in both the source and the calibration object used to determine $N(\mathrm{H+H_2})/\tau(\nu)$.

The foregoing equations, as derived by Hildebrand (1983), assume a uniform source brightness observed with a top-hat beam profile. A more physically reasonable approach may be to assume Gaussian profiles for both source and beam. Then the observed source size is given by the convolution of source and beam:

$$\Omega_s \otimes \Omega_b = \Omega_s + \Omega_b,$$

where Ω_b is the beam solid angle. Equations for submillimetre continuum optical depth and hydrogen gas mass can then be written (Gear 1988):

$$\tau(\nu) = 5.42 \times 10^{10} \frac{\theta_s^2 + \theta_b^2}{\theta_s^2 \theta_b^2} \frac{S(\nu)}{B(\nu,T_d)}, \tag{1.18}$$

where θ_s and θ_b are the FWHM (arcsec) of the source and beam and $S(\nu)$ is the flux density per beam from the source (Jy per beam), and

$$M(\mathrm{H}+\mathrm{H_2}) = 2.7 \times 10^{-19} \left[\frac{N(\mathrm{H}+\mathrm{H_2})}{\tau(\nu)}\right] \tau(\nu) \, (\theta_s D)^2 \, M_\odot, \tag{1.19}$$

with D in Mpc.

The unknown parameters are explicitly shown in equations (1.18) and (1.19). θ_s and T_d may be evaluated from mapping the source and fitting the spectrum, as described above. The remaining unknown factor is the optical depth to column density ratio, $N(\mathrm{H}+\mathrm{H_2})/\tau(\nu)$. As in the case of CO, this conversion factor has so far been determined only in the Milky Way. Various theoretical and observational studies have determined $N(\mathrm{H}+\mathrm{H_2})/\tau(\nu)$ in a variety of Galactic environments. Hildebrand (1983) adopts the value of the ratio given by Keene, Hildebrand & Whitcomb (1982), which in turn is based on the work of Whitcomb *et al.* (1981) on far-infrared grain properties. The 'Chicago assumptions' (Hildebrand 1983) give $N(\mathrm{H}+\mathrm{H_2})/\tau(\nu) = 1.2 \times 10^{25}$ atom cm^{-2} at 400 μm, with $\tau(\nu)$ varying as ν^2, translating to $N(\mathrm{H}+\mathrm{H_2})/\tau(\nu) = 1.2 \times 10^{25}\,(750/\nu)^2$ atom cm^{-2} (where ν is in GHz) at other wavelengths. Several studies have involved combining a theoretical grain model with an assumed interstellar radiation field (ISRF). Draine & Lee (1984), extending the successful silicate/graphite grain model of Mathis, Rumpl & Nordsieck (1977), combine dust with the ISRF as a function of galactocentric radius (Mathis, Mezger & Panagia 1983) to predict $N(\mathrm{H}+\mathrm{H_2})/\tau(\nu)$ in the diffuse ISM. Rowan-Robinson (1986), using a slightly different grain model with an opacity dependence at $\lambda > 30\,\mu$m of β=1 (as opposed to the more commonly adopted β=1.5–2) predicts conversion factors at submillimetre wavelengths nearly an order of magnitude lower than other studies. Fig. 1.2, adapted from Draine (1990) and Mezger (1990), compares the various observational and theoretical determinations of $N(\mathrm{H}+\mathrm{H_2})/\tau(\nu)$. Mezger (1990) gives a parametrized 'recommended range' of the reciprocal of the ratio, based on the available experimental and theoretical evidence, and depicted by the shaded region in Fig. 1.2 [note that this actually plots $\tau(\lambda)/N(\mathrm{H})$ against λ]:

$$\tau(\nu)/N(\mathrm{H}+\mathrm{H_2}) = \left(\frac{Z}{Z_\odot}\right)\, b \times \begin{cases} 7 \times 10^{-21}\,\lambda(\mu\mathrm{m})^{-2} & \lambda > 100\,\mu\mathrm{m}\ , \\ 7 \times 10^{-22}\,\lambda(\mu\mathrm{m})^{-1.5} & 40 \leq \lambda \leq 100\,\mu\mathrm{m}\ . \end{cases} \tag{1.20}$$

In equation (1.20), $Z/Z_\odot$ is the metallicity relative to the solar neighbourhood, while b is a parameter representing the different components of the ISM: b=1 (for the diffuse ISM) reproduces the models of Draine & Lee (1984); b=1.9 represents observational estimates in molecular gas (Hildebrand 1983; Pajot *et al.* 1989); b=3.4 refers to cold, dense dust (Rengarajan 1984). The Rowan-Robinson (1986) model lies somewhat above the shaded region, principally due to its adopted opacity law of $\tau(\nu) \propto \nu$ even at long

wavelengths. Mezger (1990) estimates that the conversion factor as represented in equation (1.20) is accurate to within a factor $\sim$2 in molecular clouds of moderate density. From a similar comparison of observational and theoretical work, Thronson (1988) estimates that $N(\mathrm{H}+\mathrm{H_2})/\tau(\nu)$ is constant to within a factor $\sim$3 in a variety of Galactic environments.

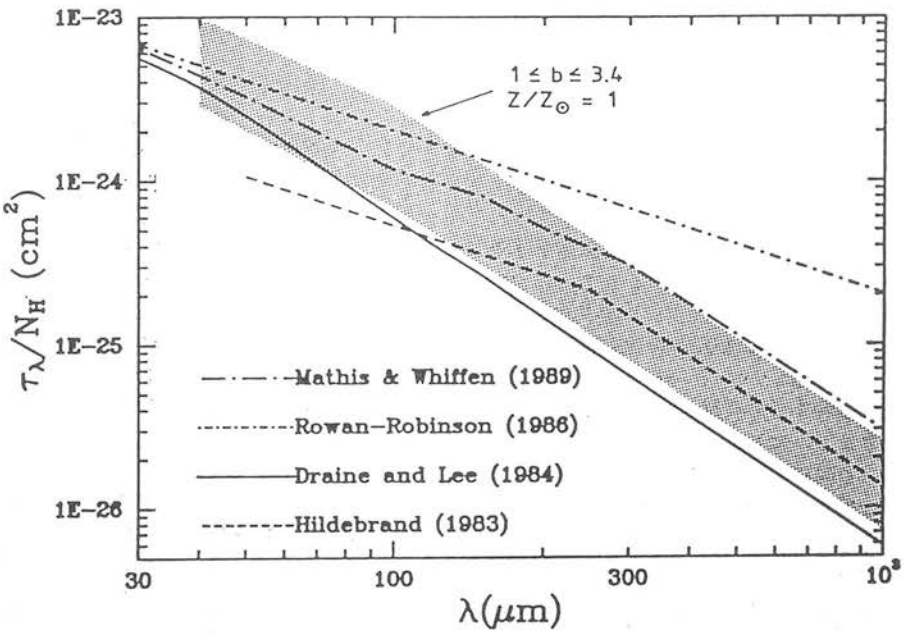

Figure 1.2: The dust conversion factor [plotted here as $\tau(\lambda)/N(\mathrm{H})$] as a function of wavelength for four models, with the parametrized range given by Mezger (equation 1.20) superimposed.

The submillimetre/millimetre continuum therefore provides an independent tracer of molecular hydrogen that is relatively free of the complex excitation and cloud chemistry effects that plague interpretation of CO data. The dust emission is optically thin, and so all the dust, and hence the H_2, is sampled. Whereas CO is very sensitive to high UV fields, as the molecule is easily dissociated, dust grains are not easily destroyed by UV and respond only via a very slow increase in temperature ($T_{\mathrm{dust}} \propto \chi^{1/4}$). The submillimetre flux has an approximately linear dependence on dust temperature, which is in principle relatively straightforward to determine from the infrared–millimetre spectrum.

The relative simplicity of the technique, however, does not make it free from error. Even for small beams, a galaxy is a composite object, and the continuum spectrum will be composed of emission from dust at a range of temperatures. The infrared-to-millimetre spectrum of the Milky Way has been extensively modelled (e.g. Cox & Mezger 1989) as arising from a number of different components. 'Cool' (20 K) dust in diffuse HI clouds is heated by the interstellar radiation field (ISRF). 'Warm' (30–50 K) dust in star-forming complexes (molecular cloud/HII regions) is heated by embedded sources, while 'hot' (>100 K) dust in HII regions, very close to the young stars, dominates in the mid-infrared (10–30 μm). 'Cold' dust ($\sim$10 K) is also present in quiescent molecular clouds and deep within the cores of more active clouds, heated by the near-infrared part of the ISRF or, for the most deeply embedded cores, by secondary far-infrared emission from the warmer outer layers of the cloud.

There is as yet little detailed modelling of the infrared-to-millimetre spectrum either of the Galactic Centre or of star-forming galaxies, although dust temperatures in these regions may be expected to be much higher than those in the disc of the Milky Way. High dust temperatures (>40 K) may be due to the greater spatial density of active star-forming regions with embedded sources, plus an elevated ISRF illuminating those clouds not directly associated with star formation. Hydrogen gas in the centres of galaxies is predominantly molecular rather than atomic (Young 1990).

The dust temperature derived from observations depends to an extent on the wavelengths at which the observations are made, and will be biased towards the temperature for which emission peaks at the wavelength of observation. So, for example, dust temperatures derived using only the 60 and 100 μm *IRAS* fluxes will tend to produce temperatures in the range 35–45 K, when in reality a range of temperature components may be present, including 'cool' dust not contributing to the *IRAS* fluxes at all. Long-wavelength (>300 μm) data are particularly valuable, as they are sensitive to the cooler dust that may easily be missed if only *IRAS* fluxes are used. Draine (1990) has pointed out that it is very easy to underestimate severely the dust mass in a galaxy by using only far-infrared fluxes and the dust temperatures derived from them. Submillimetre observations are invaluable for studying the contribution that cool dust/gas may make to the overall interstellar mass of a galaxy.

1.4 Motivation for the project

From the foregoing discussion, it is clear that, while the ability to trace accurately the mass and spatial morphology of H_2 is vital to our understanding of extragalactic star-forming processes, more observational and theoretical work is needed to resolve the difficulties surrounding the two principal mass tracers, CO lines and dust continuum.

The commissioning of the James Clerk Maxwell Telescope on Mauna Kea opened up new possibilities for sensitive millimetre- and submillimetre-wave continuum observations of galaxies at resolutions (7″–19″) comparable to those already achieved in molecular line studies. Mapping of infrared-bright galaxies at long wavelengths (where the dust emission is optically thin) affords the opportunity of a direct comparison with the CO morphology, both purporting to reliably trace the distribution of H_2. In addition, long-wavelength photometry fills an important gap in the far-infrared to millimetre spectra of extragalactic systems, allowing a determination of the dust, and hence H_2, mass that is independent of the assumptions that go into the CO technique, while at the same time investigating the extent to which *IRAS* fluxes may 'miss' emission from cooler components of dust.

It is clear, from the evidence presented in Section 1.2, that the ^{12}CO J=1–0 transition *alone* is not sufficient to trace reliably the molecular ISM in extragalactic star-forming environments where the clouds are under very different conditions of temperature, density and excitation than those in the Milky Way. Recent improvements in receiver technology, and the advent of large, sensitive millimetre-wave telescopes such as the Nobeyama 45-m and the IRAM 30-m offer the possibility of detection and mapping of other transitions and optically thinner isotopes of the molecule, such as ^{12}CO and ^{13}CO J=2–1 as well as ^{13}CO J=1–0. By comparing line strengths at the same spatial position and with similar beamsizes, the problems of different filling factors and source–beam coupling are avoided, and we may hope to investigate the variation of molecular gas excitation on spatial scales of a few hundred parsecs (∼15″).

The project described in this thesis was therefore set up with the aim of exploiting the new generation of millimetre telescopes to investigate the use of CO and dust as tracers of molecular hydrogen in star-forming galaxies.

1.4.1 Guide to the thesis

The remainder of the thesis is divided into six parts. In Chapters 2 and 3, submillimetre continuum mapping of the nearby, well-studied 'starburst' galaxy M82 is presented. A detailed comparison of the spatial morphology of the 450 μm emission with that of published CO maps at the same resolution is carried out and the implications for the interpretation of CO observations in galaxies discussed. Chapter 4 presents 800 μm mapping and 450–1100 μm photometry of three other nearby star-forming galaxies, M83, Maffei 2 and IC342. The morphologies of the 800 μm emission are compared with other tracers of star formation. The 450–1100 μm fluxes are combined with far-infrared photometry to fit dust temperatures and calculate dust optical depths and masses. In particular, the contribution of cool ($\sim$20 K) dust to the emission is considered. In Chapter 5, I present multitransition CO observations of one of these galaxies, the heavily obscured, infrared-bright spiral Maffei 2. The Nobeyama 45-m and IRAM 30-m telescopes were used to make a high-resolution (13″) ^{12}CO J=2–1 map, plus observations of the optically thinner ^{13}CO J=1–0 and J=2–1 lines. These are combined with existing ^{12}CO J=1–0 data to investigate the variation of line optical depth and excitation across the star-forming region. In addition, the very high linewidths of the CO spectra are studied. A simple model of a rotating galactic disc is constructed to investigate the contribution of the galaxy rotation curve to the observed linewidths, and the feasibility of supernova explosions providing sufficient energy input to sustain the implied velocity dispersions is discussed. Chapter 6 summarizes the main conclusions of the thesis, and outlines some directions in which future research might proceed. A preface to each chapter introduces the material contained therein, with details of publication, where relevant, and collaborators involved.

Copies of two published papers and details of published conference proceedings are included as an appendix. Several other appendices are also included. Appendix A outlines some of the techniques employed and problems encountered when making continuum observations in the technically difficult submillimetre/millimetre region, with particular emphasis on on the mapping of faint extragalactic sources. Appendix B concerns the contamination of dust continuum fluxes by molecular line emission. Appendix C outlines the derivation of equations used in the LTE analysis of molecular line data.

Appendix D derives a formula for the rotation curve of a spherically symmetric galaxy with massive core and low-density halo (as used in Chapter 5 to fit the rotation curve of Maffei 2), and Appendix E discusses the rotating-disc line-profile model in more detail than is included in Chapter 5. Appendix F contains the published papers.

M82, from Arp's *Atlas of Peculiar Galaxies* (1966).

Chapter 2

A 450 μm continuum map of M82 : comparison with the CO emission

As discussed in the Introduction, the two principal methods of tracing the molecular hydrogen content of galaxies – CO line and dust continuum observations – both rely on a conversion factor which has been derived in the Milky Way and is then applied to external galaxies. Millimetre-wave CO line observations exist for hundreds of galaxies, with many having been mapped at varying resolutions, but it is only relatively recently that submillimetre techniques have improved enough to make high-resolution dust continuum observations feasible for extragalactic objects. The JCMT was used to make a map at 450 μm of the dust continuum from the nearby star-forming galaxy M82, in order to compare it with the morphology as seen in CO. If both reliably trace the H_2, as supporters of the techniques claim, the maps should be spatially similar. These observations represent the first ever high-resolution submillimetre continuum mapping of an extragalactic system.

The work presented in this chapter was done in collaboration with Phil Puxley and Matt Mountain of the Royal Observatory, Edinburgh, Peter Brand of the University of Edinburgh and Naomasa Nakai of the Nobeyama Radio Observatory. It has been published in *Monthly Notices of the Royal Astronomical Society*, Vol. 243, p. 97 (1990), in a form very similar to that which appears here.

2.1 Introduction

An important step towards an understanding of the global processes of star formation in galaxies is the ability to determine accurately the mass of available material in molecular clouds. Unfortunately the major constituent, H_2, is difficult to detect directly, and so it is necessary to observe a tracer to calculate the molecular hydrogen column density $N(H_2)$. The J=1–0 rotational line of ^{12}CO is commonly employed. Under the assumption that the ^{12}CO emission is optically thick, as is nearly always the case in Galactic clouds (e.g. Lada 1985), and with excitation temperature $T_{ex} \simeq 10$ K, $N(H_2)$ follows from the ^{12}CO integrated intensity via $N(H_2)$ (cm^{-2}) = 4×10^{20} I_{CO} (K km s^{-1}) (Young & Scoville 1982). However, doubts have arisen over the constancy of this conversion factor, particularly in so-called 'starburst' galaxies where the presence of large numbers of hot young stars may invalidate the principal assumptions of optically thick ^{12}CO and $T_{ex} \simeq 10$ K (Section 1.2). An alternative method of H_2 mass determination is to observe the submillimetre continuum emission due to reradiation by dust grains, at characteristic temperatures $\sim$ 20–50 K, of the stellar UV, and convert to H_2 mass via the ratio $N(H_2)/\tau(\nu)$ where $\tau(\nu)$ is the continuum optical depth. The method has been discussed in detail by Hildebrand (1983) and Gear (1988). The submillimetre emission is usually optically thin, and so all the dust is sampled (Section 1.3).

To study the applicability of these two methods to extragalactic star-forming regions, submillimetre dust continuum mapping was performed of M82, a nearby galaxy already extensively observed in CO. M82 is a 'classic' starburst galaxy, the bulk of its energy output being in the infrared, with a far-infrared luminosity of 3×10^{10} $L_\odot$ (Telesco & Harper 1980). The multiwavelength observations are consistent with an intense episode of star formation in the central kiloparsec, which started some 5×10^7 yr ago (Rieke *et al.* 1980). Radio observations reveal numerous supernova remnants within 300 pc of the nucleus (Kronberg, Biermann & Schwab 1985). Hα filaments and X-ray emission extend several kiloparsecs perpendicular to the galactic plane (Lynds & Sandage 1963; Watson, Stanger & Griffiths 1984; Kronberg *et al.* 1985). CO and HI maps show a double-lobed structure, which is interpreted as a rotating molecular ring, 400 pc in diameter, enclosing the central starburst, with molecular and ionized gas being driven out of the galactic plane by the associated stellar winds and supernovae

(Weliachew, Fomalont & Greisen 1984; Lo *et al.* 1987; Nakai *et al.* 1987). In contrast to Galactic molecular clouds, ^{12}CO J=2–1/J=1–0 antenna temperature ratios of $\geq$2 have been interpreted as suggesting that the CO in the central regions of M82 is optically thin, perhaps in the form of small (few pc) hot (40 K), 6×10^3 $M_\odot$ clouds, quite unlike the Giant Molecular Clouds (40 pc, 10 K, 5×10^5 $M_\odot$) in the Milky Way (Knapp *et al.* 1980; Stark & Carlson 1984; Young & Scoville 1984; Nakai *et al.* 1987; Sofue 1988).

2.2 Observations

The central 40″ × 40″ of M82 was mapped at 450 μm in the dust continuum on the night of 1988 March 20, using the James Clerk Maxwell Telescope (JCMT) on Mauna Kea, Hawaii, and the common-user bolometer system UKT14 (filter width $\Delta\lambda \simeq 54\,\mu$m at 450 μm). The beamsize at 450 μm was 13″ (not diffraction limited, owing to the lower dish quality and pointing precision then available on the recently commissioned JCMT). A fully sampled 7 × 7 grid was mapped, spaced at 6.5″ and oriented along the major axis which lies at position angle PA = 65° (Nilson 1973). Using observations of the 450 μm peak at two different airmasses, the data were transformed out of the atmosphere with a zenith extinction coefficient $a(450\,\mu\text{m}) = 1.5$, taking account of the variation in airmass over the maps, which were then reduced and co-added using the continuum reduction software package NOD2 (Haslam 1974). The central pixel of the map was determined by peaking up on M82 at 800 μm. The 800 μm continuum peak is within 5″ of the 2.2 μm peak (Hughes, Gear & Robson 1990), at RA(1950) = $09^{\rm h}$ $51^{\rm m}$ $43.47^{\rm s}$, Dec.(1950) = 69° 55′ 00.3″ (Pipher *et al.* 1987). Pointing was checked by means of five-point scans before and after each map. It was found that the second map was shifted by $\simeq$ 7″ with respect to the first, along the minor axis, and this offset was corrected before the maps were added. The estimated positional uncertainty of the map is therefore 7″. 450 μm photometry of M82 from the night of 1988 February 6 (Hughes *et al.* 1990) was used to scale up the integrated flux from the map. In a 13″ beam centred at the peak, the 450 μm flux density is 15.5 ± 5 Jy.

2.3 Results

The 450 μm map is presented in Fig. 2.1(a). Fig. 2.1(b), to the same scale, shows the ^{12}CO J=1–0 interferometer map of Lo *et al.* (1987). It is immediately obvious that there is a morphological difference between the two maps. While in the CO map there are two distinct peaks, 25″ apart, situated asymmetrically either side of the dynamical (and 2 μm) nucleus, the 450 μm map has only one peak, to the south-west of the nucleus, with an extension to the north-east. Before considering physical reasons for the apparent absence of a second peak, it is necessary to check the telescope pointing – could the second peak have been missed entirely? This seems unlikely. Both 100 and 40 μm profiles along the major axis (Joy, Lester & Harvey 1987) show similar, single-peak morphology. The centre of the 450 μm map – the 800 μm peak – is within 5″ of the 2.2 μm nucleus. The positional accuracy of the map is $\simeq$ 7″ , and there was good agreement between the two maps in the position on the major axis of the 450 μm peak. From physical considerations – at 450 and 800 μm the emission is approaching the Rayleigh–Jeans tail for characteristic dust temperatures ($\simeq$ 20–45 K, see below) – it seems reasonable to assume that the emission at the two wavelengths comes from similar material. For these reasons, the peak of the map has been placed within $\simeq$ 7″ of the 2.2 μm peak – i.e. interior to the CO ring. It also seems unlikely that the structure results from two unresolved peaks. The resolution of the JCMT at 450 μm is comparable to that of the IRAM ^{12}CO J=2–1 map (13″ at 230 GHz – Loiseau *et al.* 1990), and better than that of the ^{12}CO J=1–0 Nobeyama map (16″ – Nakai *et al.* 1987), in which two maxima are clearly seen. If there are two continuum peaks, the 450 μm beam should have resolved them.

The position angle of the dust major axis is orientated at $\simeq$ 12° to the optical major axis, as has also been observed in the ^{12}CO J=1–0 maps of Olofsson & Rydbeck (1984) and Nakai *et al.* (1987). Integrating up the emission from the calibrated map gives a total flux density of $F(450\,\mu\mathrm{m}) = 49 \pm 21$ Jy over the 40″ × 40″ grid, where the quoted error is due to uncertainty in the 450 μm photometry and in the relative locations of the 450 μm photometric aperture and map peak. Neither synchrotron (*cf.* Klein, Wielebinski & Morsi 1988) nor bremsstrahlung [$S(450\,\mu\mathrm{m}) \sim 0.5$ Jy, Puxley *et al.* 1989] processes contribute significantly to the integrated emission at this wavelength.

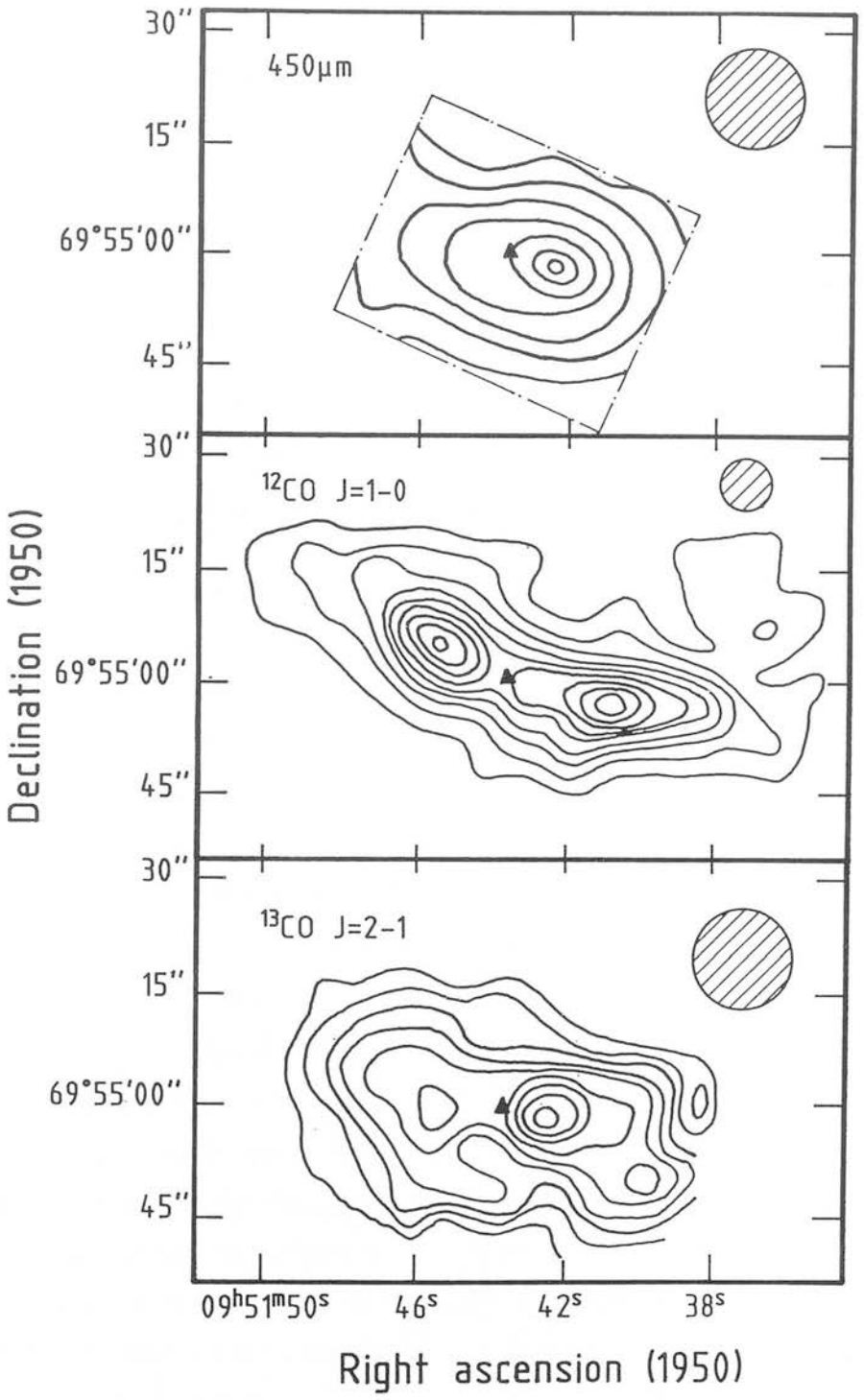

Figure 2.1: (a) The 450 μm continuum map of M82, contoured with a spacing of 1σ, from a 2σ base level of 3.7 Jy/beam. The continuum peak is located within 7″ of the 2.2 μm maximum at RA 09^h 51^m 43.47^s, Dec. 69° 55′ 00.3″ (Pipher *et al.* 1987, marked by a triangle). (b) The ^{12}CO J=1–0 interferometer map of M82, beamsize 7″, taken from Lo *et al.* (1987). (c) The 13″ ^{13}CO J=2–1 map of M82 from Loiseau *et al.* 1988. Note the large central peak which dominates over the two peaks of the 'ring'.

2.3.1 Molecular gas mass

The physics of emission from dust grains has been discussed in detail by Hildebrand (1983), and the advantages of using submillimetre observations to derive gas masses convincingly argued by Thronson (1988). Gear (1988) points out that, rather than assuming a uniform source brightness distribution and top-hat beam profile, as Hildebrand does, it is more realistic to assume Gaussian source and beam profiles, thus introducing a correction into Hildebrand's formulae (Section 1.3).

The dust continuum optical depth is given by

$$\tau(\nu) = 5.42 \times 10^{-16} \, [(\theta_s^2 + \theta_b^2)/\theta_s^2\theta_b^2] \, [S(\nu)/B(\nu, T_d)], \qquad (2.1)$$

where θ_s and θ_b are the FWHM (arcsec) of the source and beam profiles, respectively, $S(\nu)$ is the flux density into a beam centred on the peak of the source (Jy per beam), and $B(\nu,T_d)$ is the blackbody intensity at frequency ν and dust temperature T_d.

The determination of a reliable dust temperature depends on being able to fit the far-infrared spectrum of the source to a modified blackbody function of the form $\nu^\beta \; B(\nu, T_d)$ (assuming optically thin emission), where β characterizes the frequency dependence of the dust emissivity. The value of β is believed to increase from $\simeq 1$ at $50 \leq \lambda \leq 250\,\mu$m to $\beta \geq 2$ by $\lambda \sim 1000\,\mu$m (Hildebrand 1983), but its exact variation with frequency is not well known. Clearly the derived dust temperature depends on the value of β adopted. In general, β varying between 1 and 2 leads to an uncertainty of $\sim 30\%$ in the dust temperature (Thronson *et al.* 1989). In addition, it is not normally possible to fit the whole infrared spectrum to a single temperature – an excess of emission at the shorter wavelengths indicating hotter regions within the source (Gear 1988). It must be borne in mind that for a composite object such as a galaxy, any derived temperature will only be an average over the system (Thronson *et al.* 1987).

Telesco & Harper (1980) and Klein *et al.* (1988) both fit a $\nu^{1.5} \; B(\nu, T_d)$ function to the far-infrared spectrum of M82, for $\lambda \geq 30$–$40\,\mu$m, deducing a dust temperature of 45 K. Similarly, Hughes *et al.* (1990) obtain a best fit to the 40–1300 μm spectrum, including their new data at 800 and 1100 μm, of $\beta = 1.5$ and $T_d = 47$ K, while Thronson *et al.* (1987) adopt a temperature of 30 ± 10 K from a $\beta = 2$ fit to the far-infrared data. A $\beta = 1.5$ emissivity law will be used here, with a corresponding dust temperature of 47 K, from the work of Hughes *et al.*, although a fit to $\nu^{1.5} \; B(\nu, T_d)$ could be mimicked

by an emissivity law varying smoothly from $\beta = 1$ to 2 towards longer wavelengths (Gear *et al.* 1986). It should also be noted here that, although a single-temperature fit adequately explains the fluxes, the existence of a cool component of dust, emitting only at the longest wavelengths, is not completely ruled out by these data (see, e.g., Chapter 4).

The hydrogen column density can be calculated from

$$N(\mathrm{H} + \mathrm{H_2}) = 1.2 \times 10^{25}\ [750/\nu]^{\beta}\ \tau(\nu)\ \mathrm{atom\ cm^{-2}} \tag{2.2}$$

(Hildebrand 1983), where ν is in GHz. The total mass of gas in the source is then

$$M_{\mathrm{g}} = M(\mathrm{H} + \mathrm{H_2}) = 2.7 \times 10^{-19}\ N(\mathrm{H} + \mathrm{H_2})\ (\theta_{\mathrm{s}} D)^2\ M_{\odot}, \tag{2.3}$$

where D is the distance to the source in Mpc. Equation (2.3) includes a factor $\simeq 1.36$ to allow for helium and other heavy elements (Hildebrand 1983). In the case of M82, molecular hydrogen dominates over atomic hydrogen in the central 1 kpc (e.g. Lugten *et al.* 1986) and so M_{g} closely approximates the mass of molecular hydrogen in the inner regions of the galaxy.

The main sources of uncertainty in deriving the mass can now be clearly seen, namely, the assumed values of dust temperature and $N(\mathrm{H} + \mathrm{H_2})/\tau(\nu)$. I have adopted the value of $N(\mathrm{H} + \mathrm{H_2})/\tau(\nu)$ given in Hildebrand (1983), of 1.2×10^{25} atom cm^{-2} at 400 μm, which is derived from the work of Whitcomb *et al.* (1981) on the far-infrared properties of dust grains. The reliability of this number reflects the accuracy to which gas and dust parameters are known, which Thronson *et al.* (1987) estimate to be a factor of ~ 5 in the Galactic disc. Thronson (1988) plots a number of theoretically and experimentally derived values of the ratio and finds it to be constant, within a factor of $\simeq 3$, for a variety of Galactic objects, although it may scale inversely with metallicity (Thronson *et al.* 1989, see also the discussion in Section 1.3).

The dust optical depth, hydrogen column density and total gas mass can now be calculated. Fitting a two-dimensional Gaussian profile to the data gives a map FWHM (beam convolved with source) of $28'' \times 16''$. Then, using the 450 μm flux density of 15.5 ± 5 Jy in a $13''$ beam and taking $T_{\mathrm{d}} = 47$ K, equation (2.1) gives a value for the dust optical depth of 0.02 at 450 μm, consistent with the initial assumption that the submillimetre emission is optically thin. Adopting $\beta = 1.5$ gives a hydrogen column

density $N(\mathrm{H} + \mathrm{H_2}) = 2.6 \times 10^{23}$ atom cm^{-2} from equation (2.2). The distance to M82 is taken to be 3.25 Mpc (Tammann & Sandage 1968), leading finally to a total gas mass $M_g = (2.0 \pm 0.8) \times 10^8\ M_\odot$, where the quoted error reflects the uncertainties in the 450 μm flux density and fitted source size. Adoption of a ν^2 emissivity law and corresponding dust temperature of 30 K would increase the derived mass by a factor of 2.1 to $(4.2 \pm 1.8) \times 10^8\ M_\odot$. Of this total gas mass, atomic hydrogen contributes only about $0.1 \times 10^8\ M_\odot$ in the central 1 kpc (Weliachew *et al.* 1984).

This derived mass is consistent, within the accuracy of the technique, with previous estimates from submillimetre data. Thronson *et al.* (1989) calculate a mass of $3 \times 10^8\ M_\odot$ from a 1.3-mm flux of 0.9 Jy and an adopted dust temperature of 30 K. They propose that this mass is perhaps a factor of 3 too high, suggesting that the analysis of O'Connell & Mangano (1978) indicates a metallicity in M82 2–3 times that in the solar neighbourhood. However, other work has suggested values of heavy element abundances which are close to solar (Willner *et al.* 1977; Puxley *et al.* 1989). Jaffe, Becklin & Hildebrand (1984a) calculate a mass of $8 \times 10^7\ M_\odot$ from a large-beam 400 μm flux of 30 Jy and dust temperature of 45 K. Olofsson & Rydbeck (1984) and Lo *et al.* (1987) both obtain an $\mathrm{H_2}$ mass of $6 \times 10^7\ M_\odot$ from ^{12}CO J=1–0 data, assuming optically thin emission. Under the same assumption, Nakai *et al.* (1987) derive a mass of $1.1 \times 10^8\ M_\odot$ in the central 1.5′ from their ^{12}CO J=1–0 map. Assumption of optically thick CO and application of a 'constant conversion factor' leads to a mass an order of magnitude higher than in the optically thin case (Nakai *et al.* 1987).

2.4 Discussion

The difference in morphology between the CO and submillimetre maps is surprising if, as is commonly assumed, the CO and dust continuum are both reliable tracers of the molecular hydrogen. As molecular hydrogen forms on dust grains, it is reasonable to expect to find dust mixed with the $\mathrm{H_2}$. On the other hand, the association of $\mathrm{H_2}$ with CO is one of the cornerstones of the CO technique of mass determination. The 450 μm map is similar in its morphology to both the 100 and 800 μm data, and intermediate-resolution radio observations, while the double-lobed structure of CO is repeated in HI, HCN and $\mathrm{HCO^+}$ maps (Weliachew *et al.* 1984; Seaquist, Bell & Bignell 1985; Carlstrom

1988). Of particular interest is the marked spatial similarity between the morphology of the 450 μm emission and that of the ^{13}CO J=2–1 map shown in Fig 2.1c (from Loiseau *et al.* 1988). The fact that the long-wavelength dust continuum and the optically thin isotopic CO line both show a central peak, rather than a ring, is strong evidence for optical depth effects contributing to the differing ^{12}CO and 450 μm morphologies. This point is further discussed elsewhere in this section.

The peak of the 100 μm emission coincides with a region of particularly vigorous star formation $\sim 10''$ south-west of the nucleus, displaying recombination lines from HII regions, OH masers, and a bright, non-thermal radio source associated with the supernova remnant 41.9+58 (Weliachew *et al.* 1984; Kronberg, Biermann & Schwab 1981, 1985; Seaquist *et al.* 1985; Joy *et al.* 1987). A weak ^{12}CO 1–0 feature is seen in the interferometer map between the nucleus and the western lobe, and an extension of the western peak of HI, as well as peaks of the HCN and ^{13}CO J=2–1 emission are coincident with this area, leading to speculation on the presence of a 'giant molecular clump' in the vicinity of the star formation region (Weliachew *et al.* 1984; Lo *et al.* 1987; Carlstrom 1988; Loiseau *et al.* 1988).

A possible explanation of the differing morphologies, then, is that the two lobes are present in dust but are 'swamped' by submillimetre emission from the giant star-forming region. The blackbody flux observed from a population of N spherical dust grains, radius a, at distance D, is given by

$$F(\nu) = N\pi(a/D)^2 Q(\nu) B(\nu, T_{\rm d}) \tag{2.4}$$

(Hildebrand 1983), where $Q(\nu)$ is the emissivity of the grains at frequency ν. Thus flux density is proportional to the number of grains, which is equivalent to the amount of H_2 assuming a constant gas-to-dust ratio, and varies with temperature; for $\lambda \sim 450\,\mu$m, $B(\nu, T_{\rm d})$ can be approximated by $B(\nu, T_{\rm d}) \propto T_{\rm d}^{1.6}$, to within an accuracy of 10%, for $T_{\rm d}$ = 20–60 K (e.g. Jaffe *et al.* 1984b). An increase in temperature by approximately a factor of 1.5 from 47 K, or a two-fold increase in dust column density, would be needed to 'fill in' the central depression suggested by the ^{12}CO map of Lo *et al.* (1987). The data are not of sufficient signal-to-noise to attempt a temperature profile. However, the similarity of the map to the 100 μm slice of Joy *et al.* (1987), and comparison of their 100 and 40 μm profiles (Fig 2.2), suggests that there are no significant large-

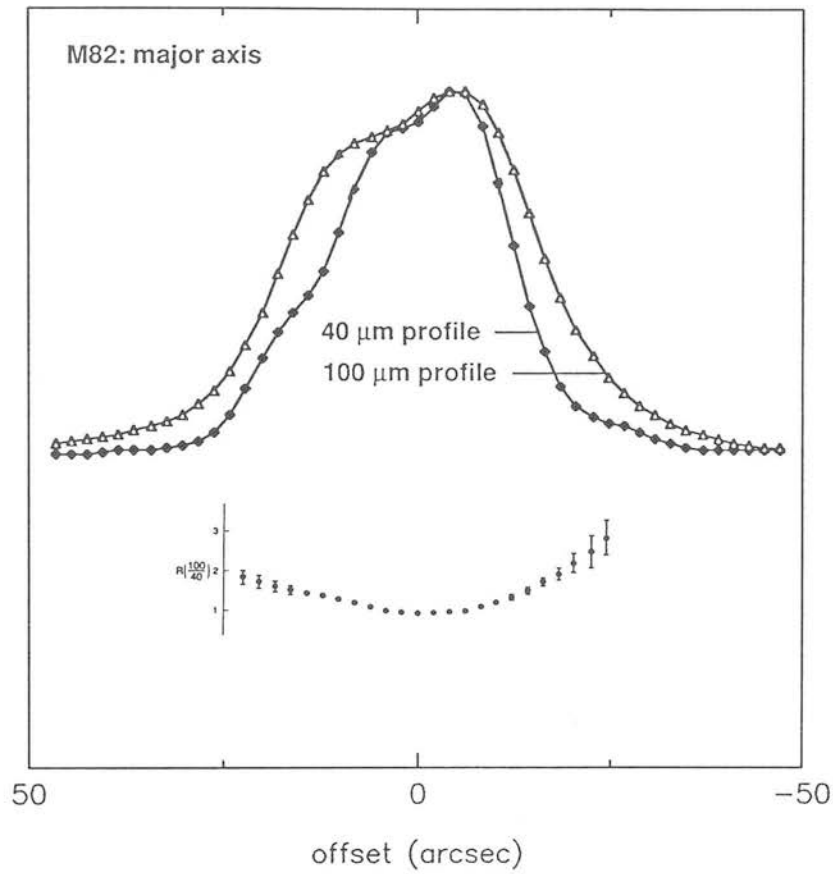

Figure 2.2: 40 and 100 μm scans along the major axis of M82 (Joy *et al.* 1987), and their ratio (from Telesco, Decher & Joy 1989).

scale temperature gradients over the central $\sim$20″ (300 pc) of the galaxy. Since the emission is optically thin, all the dust is sampled. It therefore seems likely that the submillimetre emission from M82 is tracing predominantly column density variations across the central regions of the galaxy.

If the submillimetre emission is assumed to be accurately following the column density of H_2 across M82, then it is apparent that some process must be enhancing the ^{12}CO emission in the lobes or depressing it in the interior regions. The CO emission from M82 is highly complex. Although the double-lobed structure apparent in ^{12}CO J=1–0 and 2–1 maps (Lo *et al.* 1987; Nakai *et al.* 1987; Loiseau *et al.* 1990) has been widely interpreted as representing a rotating molecular ring, the velocity structure of the CO is disturbed, and, it has been argued, not consistent with a simply rotating

disc or torus. The structural minor axis is not aligned with the axis of rotation, and the galactic plane appears warped (Lo *et al.* 1987).

The integrated intensity of CO emission, I_{CO}, is highly sensitive to changes in the physical and excitation conditions of the molecular clouds, such as gas number density, metallicity, optical depth and excitation temperature, and such variations must be taken into account when deriving H_2 masses by this method.

(i) *Gas number density.* For optically thick ^{12}CO emission, Maloney & Black (1988) find that $I_{CO} \propto n^{1/2}$, thus application of a 'constant' conversion factor to extragalactic molecular clouds will not give a reliable indication of the H_2 mass if those clouds differ from the ($n \simeq 200$ cm^{-3}) norm.

(ii) *Heavy-element abundance.* I_{CO} increases with increasing metallicity, although, as stated earlier, the heavy-element abundance in M82 may not differ significantly from solar neighbourhood values.

(iii) *Optical depth.* ^{12}CO J=1–0 emission is almost always optically thick in Galactic molecular clouds (e.g. Lada 1985). In the case of M82, however, large-beam observations give ^{12}CO J=2–1/J=1–0 antenna temperature ratios of $\simeq$ 2–3.5, suggesting that the ^{12}CO in the central regions is at least partially optically thin (Knapp *et al.* 1980; Sofue 1988). If the ^{12}CO emission were optically thin throughout the central region of M82, then it would be sampling all the gas; the ^{12}CO emission, like the dust, would be tracing molecular hydrogen column density, and the submillimetre and ^{12}CO maps would show similar morphology. Clearly this is not the case. The recently published ^{13}CO J=2–1 map [Fig. 2.1(c)] of Loiseau *et al.* (1988) shows a large central peak, coincident in position and velocity with the active south-western star-forming region, which dominates over the two peaks of the 'ring'. As ^{13}CO J=2–1 emission is nearly always optically thin, the ^{12}CO/^{13}CO J=2–1 antenna temperature ratio is a good tracer of changes in ^{12}CO optical depth. The ratio at the central peak of the ^{13}CO J=2–1 map is 6.8, compared to 9–25 over the rest of the map, implying that the ^{12}CO optical depth varies across the central regions of M82 (Loiseau *et al.* 1988). These data, together with the striking spatial similarity of the ^{13}CO and dust continuum maps discussed earlier, suggest that ^{12}CO optical depth variations are a likely cause of the differing ^{12}CO and submillimetre morphologies, although other effects may also contribute.

(iv) *Excitation temperature.* For optically thick CO emission, $I_{CO} \propto T_{ex}$ (Maloney

& Black 1988), while in the optically thin case, for $h\nu \ll kT_{\rm ex}$, $I_{\rm CO} \propto 1/T_{\rm ex}$ (Jaffe *et al.* 1984b). In addition, antenna temperature ratios in regions with an excitation temperature gradient can be very different to those resulting from a region at uniform temperature (Cantó, Rodríguez & Anglada 1987). Knowledge of the gas excitation temperature and optical depth is therefore vital for correct interpretation of CO data and line ratios. One factor which could have a marked effect on the gas temperature, and hence the CO emission, is the presence of intense UV radiation fields. Recent H53α measurements of the central region of M82 imply an ionization rate of 1.1×10^{54} Lyman continuum photons per second (Puxley *et al.* 1989). Assuming that these photons are produced by B0 stars with an effective temperature $\simeq$ 31 000 K, this translates to $\sim 5 \times 10^6$ B0 stars in the starburst region of M82 (Panagia 1973), with a resulting UV field $\geq 10^3$ times that in the solar neighbourhood (Maloney & Black 1988). In such intense UV fields, much of the CO emission may originate from the warm (100 K), dense (10^3 cm^{-3}) photodissociation regions at the boundaries between HII regions and molecular clouds, which have been extensively modelled by Tielens & Hollenbach (1985). In these regions, illuminated either from within by embedded stars or from outside by an intense galactic UV field, grain photoelectric ejection is the dominant heating mechanism, and the gas temperature can far exceed the dust temperature. The dust emission, on the other hand, is largely independent of the UV field strength (Thronson 1988). The existence of photodissociation regions in M82 is implied by the detection of the 158 μm [CII] line which arises in such interface zones, and has the same spatial distribution and velocity structure as the ^{12}CO J=1–0 line (Crawford *et al.* 1985). Maloney & Black (1988) suggest further that the anomalously high ^{12}CO J=2–1/J=1–0 antenna temperature ratios can be explained in terms of emission from photodissociation regions, with the optically thicker J=2–1 transition arising in the warmer outer layers of an externally illuminated cloud, so enhancing the observed ratio.

2.5 Conclusions

This chapter presented new high-resolution observations of M82 at 450 μm in the dust continuum. The map of the central 40″ shows distinct morphological differences to ^{12}CO maps of the same region. Whereas the CO maps show a double-peaked structure

believed to represent a 200-pc nuclear molecular ring, the 450 μm observations show one peak only. Consideration of observational uncertainties supports the assertion that the difference is real, and not a result of insufficient resolution or poor pointing. The 450 μm peak is located within 7″ of the 2.2 μm nucleus – interior to the CO 'ring'. The 450 μm emission is optically thin, and the integrated flux density over the map is 49 $\pm$ 21 Jy. Adoption of a dust temperature of 47 K results in a derived H_2 mass of 2.0 $\times$ 10^8 $M_\odot$, which increases by a factor of 2.1 if a lower dust temperature (30 K) is used. This is similar to previous estimates from submillimetre and CO observations, although assumption of optically thick ^{12}CO and corresponding 'constant conversion factor' leads to a somewhat higher derived mass.

The submillimetre continuum and ^{12}CO line cannot both be considered to be reliable tracers of molecular hydrogen. It is possible that a double-peaked dust structure is being 'swamped' by enhanced emission from a large star formation region south-west of the nucleus. However, the similarity of the 450 μm map to the 100 μm slice and the correspondence of the 100 and 40 μm profiles imply that there are no large dust temperature gradients across the central region of M82; hence the dust emission is likely to trace column density variations only. It therefore seems probable that some effect is enhancing the CO emission in the lobes or depressing it in the inner regions. The CO emission in M82 is very complex and the integrated intensity is sensitive to changes in gas number density, metallicity, optical depth and excitation temperature. It is likely that a combination of optical depth variations and excitation temperature gradients are a major cause of the differing morphologies. Observations of the ^{13}CO J=2–1 transition, a reliable tracer of the ^{12}CO optical depth, indicate significant variations of $\tau(^{12}\mathrm{CO})$ across the galaxy. The intense UV flux in the central starburst region of M82 ($\geq$ 10^3 $\times$ solar neighbourhood) and the detection of [CII] 158 μm emission both suggest that much of the CO may originate in warm, dense photodissociation regions at the interfaces between HII regions and molecular clouds, where the gas temperature can greatly exceed the dust temperature.

These conclusions suggest that CO data must be treated with caution when applied to the extreme environments of vigorous extragalactic star formation regions, and that the effects on the CO emission of such parameters as optical depth and excitation temperature must be thoroughly investigated if CO lines are to be reliably used to

trace the molecular gas content of extragalactic systems. In Chapter 5 of this thesis, multitransition CO observations of another nearby star-forming galaxy, Maffei 2, are analysed in an attempt to overcome these difficulties.

Chapter 3

Diffraction-limited 450 μm observations of M82

The discovery, described in the previous chapter, that maps of the star-forming galaxy M82 made in CO line and dust continuum are spatially dissimilar, has potentially serious implications for the use of ^{12}CO and dust as molecular mass tracers. However, it must be borne in mind that the observations, performed in March 1988, were some of the first made with the recently commissioned JCMT, and suffered from pointing errors of $\sim 7''$ and non-diffraction-limited resolution. Over the following two years, the telescope surface and pointing improved greatly, and in December 1990, M82 was observed again at 450 μm, this time at diffraction-limited, $7''$ resolution.

The work presented in this chapter was done in collaboration with Phil Puxley and Matt Mountain of the Royal Observatory, Edinburgh, Peter Brand of the University of Edinburgh and Naomasa Nakai of the Nobeyama Radio Observatory. It has been published in *Monthly Notices of the Royal Astronomical Society*, Vol. 252, 6P (1991), in a form very similar to that presented here.

3.1 Introduction

The advent of sensitive millimetre-wave telescopes has encouraged the study of molecular gas in galaxies using the relatively easily detected ^{12}CO J=1–0 transition as a tracer of molecular hydrogen. However, it is becoming increasingly doubtful whether ^{12}CO is a reliable probe of either the total mass or spatial distribution of H_2 in regions of vigorous star formation, where numerous massive young stars greatly influence conditions in the clouds (e.g. Maloney & Black 1988). An alternative tracer is submillimetre continuum emission from 20–50 K dust mixed with the molecular gas, and heated by the UV from young stars. It has been argued by several authors that the continuum emission is a more reliable tracer of H_2 than the CO line, having both low optical depth and relative insensitivity to such parameters as temperature and UV field strength (e.g. Thronson 1988).

Chapter 2 presented 450 μm continuum mapping of the nearby starburst galaxy M82 with the James Clerk Maxwell Telescope, for a direct comparison with the CO emission. The 450 μm map, made with a 13″ beam, shows a strikingly different morphology to ^{12}CO maps of the same region and at the same spatial resolution. While ^{12}CO J=1–0 and J=2–1 observations reveal a double-peaked structure, interpreted as a rotating, 400 pc diameter ring enclosing the nuclear starburst (Lo *et al.* 1987; Nakai *et al.* 1987; Loiseau *et al.* 1990), the 450 μm map has only one peak, inside the CO ring. Such a morphological difference is inconsistent with both the CO and the dust reliably tracing H_2. There is no strong evidence, from far-infrared data (Joy, Lester & Harvey 1987), of dust temperature variations sufficient to explain the discrepancy. The 450 μm map closely resembles a ^{13}CO J=2–1 map of the central region which, unlike the ^{12}CO , is centrally peaked (Loiseau *et al.* 1988). Furthermore, detection of [CII] 158 μm and H53α emission from M82 implies the existence of a highly disturbed nuclear region with the molecular clouds bathed in the radiation of $\sim 10^6$ hot young stars and the CO intensity perhaps governed more by the UV field than by the molecular mass (Crawford *et al.* 1985; Puxley *et al.* 1989). It was concluded in Chapter 2 that the 450 μm observations were tracing a concentration of molecular gas not seen in ^{12}CO, and that line optical depth and excitation effects may be a significant cause of the differing morphologies. The 450 μm data added to the growing evidence that ^{12}CO is *not* a reliable tracer of

H_2 in regions of vigorous star formation.

However, the observations presented in Chapter 2 were limited by the then lower quality dish surface and pointing precision of the recently commissioned JCMT, which did not permit mapping at diffraction-limited resolution and introduced fairly large ($\sim$ 7″) pointing uncertainties. Since the original observations, in March 1988, the dish surface and pointing have improved to such an extent that diffraction-limited (7″) observations are now feasible. The value of such data is clear – the opportunity to verify the previous results with high pointing accuracy and a resolution sufficient for a direct comparison with CO interferometer data that show the double-peaked structure very clearly (Lo *et al.* 1987).

3.2 Observations

The observations were made on the night of 1989 December 18–19, using the James Clerk Maxwell Telescope on Mauna Kea, Hawaii. M82 was observed at 450 μm in the continuum with the common-user ^{3}He-cooled bolometer UKT14 (Duncan *et al.* 1990), and the aperture set to 27 mm, resulting in a diffraction-limited beamsize of 7″.

A scan was made along the major axis of M82, oriented at a position angle of 76° (east from north) and centred at RA(1950) = $09^h\ 51^m\ 43.53^s$, Dec.(1950) = 69° 55′ 00.7″. The scan direction is consistent with the apparent CO and dust major axes, which are offset from the optical major axis of M82 (Nakai *et al.* 1987). The data are fully sampled at 3″ spacing with an integration time $\sim$ 2 min per point, leading to signal-to-noise ratios ranging from $\sim 4\sigma$ at the edge to $\sim 27\sigma$ at the centre of the scan. The beam was chopped 150″ away in azimuth to get good sky cancellation.

When working at the diffraction limit of the telescope, accurate pointing becomes very important (see Appendix A). Pointing and focus checks were performed on the bright, evolved stars IRC10216 and CRL618, and on Mars. Over the whole night, the rms pointing error was $\sim$1.6″ in azimuth and $\sim$3.6″ in elevation. However, five-point scans carried out immediately before and after the M82 observation showed that the pointing was accurate to $\leq$2″ over this period. These five-points were carried out using IRC10216, which at RA(1950) = $09^h\ 45^m\ 14.8^s$, Dec(1950) = +13° 30′ 41″ is the closest bright submillimetre pointing source to M82.

Frequent calibration observations are essential at submillimetre wavelengths, because of the possibility of rapid ($\sim$ 1 hr) variations in atmospheric opacity. Observations were made of CRL618 and OMC-1, both reasonably bright and well calibrated at 450 μm, and Mars. 450 μm fluxes were adopted (in a 19″ beam) for CRL618 and OMC-1 of 11±1.3 and 770±120 Jy respectively (G. Sandell, JCMT user note). For Mars, a brightness temperature of 215.1 K (Griffin *et al.* 1986) and 450 μm flux of 788.3 Jy were used. From the calibration results, the M82 data were transformed out of the atmosphere with a 450 μm extinction of 0.7±0.05 (virtually constant throughout the night) and UKT14 sensitivity at 450 μm of 41±3 Jy/mV. The accuracy of calibration is affected by the dependence of the 450 μm filter effective frequency on both source spectral index and atmospheric water vapour content. A major source of uncertainty when making diffraction-limited observations at 450 μm is the fact that, despite the high surface accuracy of the JCMT, the beam shape is poorly known (and probably not Gaussian), and the error beam non-negligible. The beam–source coupling will therefore differ for a point source (CRL618), disc (Mars) or extended object (M82). The total uncertainty in the 450 μm flux could therefore be as high as 30% . Poor weather meant that a beam map of Mars could not be made during the observing run. However, the derived fluxes agree very well with previous photometry (Hughes, Gear & Robson 1990). Using data from Wild (1990), the contribution to the 450 μm continuum flux of the ^{12}CO J=6–5 line at 691 GHz was estimated (see Appendix B) to be $\leq$0.3 Jy/beam and therefore negligible.

3.3 Results

In Fig. 3.1 the 450 μm data are presented, together with slices from the ^{12}CO J=1–0 interferometer observations of Lo *et al.* (1987) and the ^{13}CO J=2–1 IRAM data of Loiseau *et al.* (1988) taken along the same scan direction, for comparison. The 450 μm flux density at each observed position is given in Table 3.1.

It can be seen from Fig. 3.1 that the 450 μm scan has two peaks $\sim$18″ apart. The position of the larger south-western peak is coincident, within the pointing errors, with the peak of the original 450 μm map (Chapter 2) and that of the ^{13}CO J=2–1 data (Loiseau *et al.* 1988). The north-eastern peak is approximately coincident with the

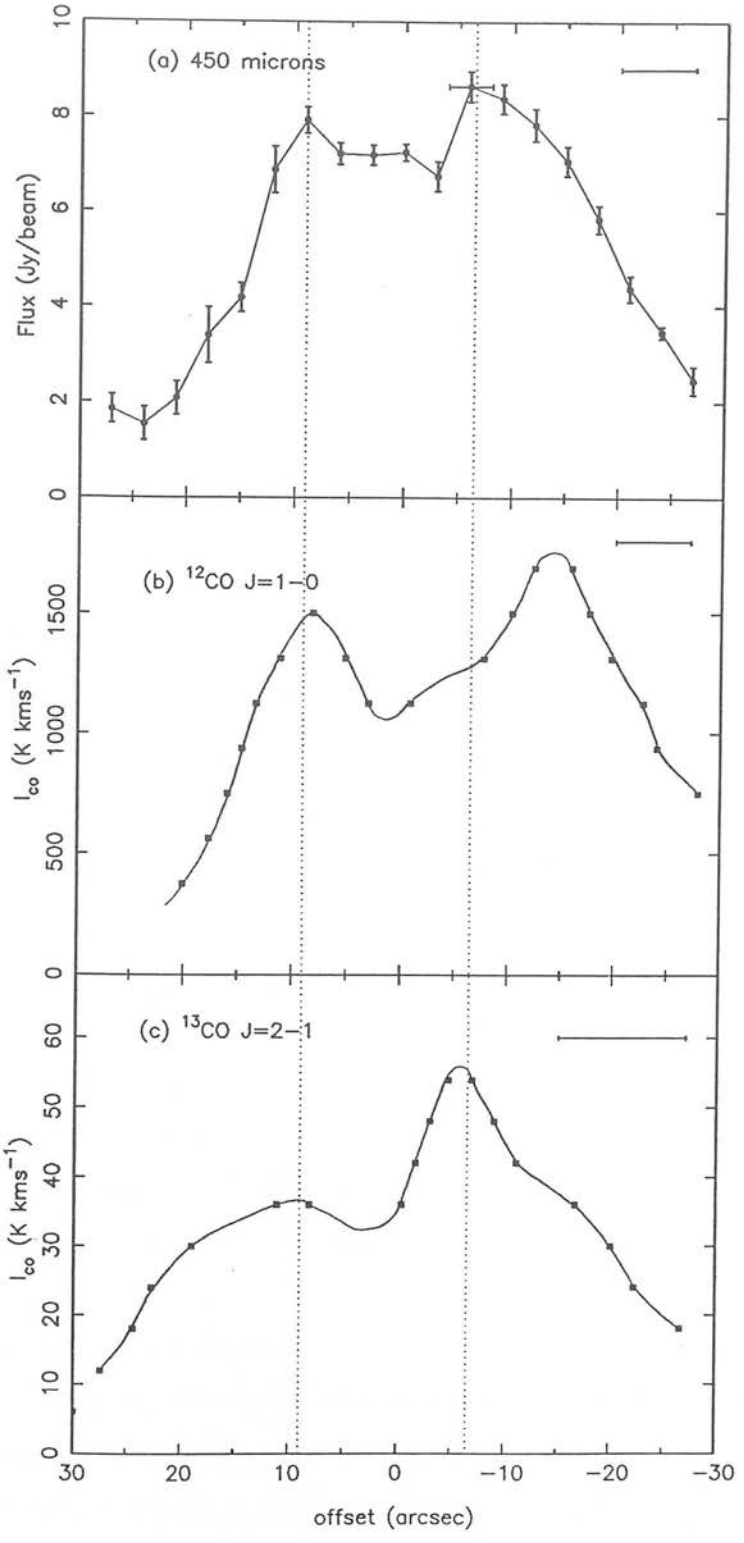

Figure 3.1: Scans along the major axis of M82, in ^{12}CO J=1–0, ^{13}CO J=2–1, and 450 μm dust continuum. The CO scans were produced by interpolating between the contour levels (indicated by filled squares) of the published maps. The beamwidth is represented by a horizontal line. (a) Continuum observations at 450 μm with 7″ resolution (this work). The vertical error bars represent observational noise – there is an additional overall calibration error of $\leq$30%. The horizontal error bar on the data point at offset –3″ represents the pointing uncertainty of $\leq$2″ . Note that this is much smaller than the offset between the south-western CO and dust peaks. (b) ^{12}CO J=1–0 interferometer observations from Lo *et al.* (1987), with 7″ resolution. (c) ^{13}CO J=2–1 observations, from Loiseau *et al.* (1988), at 12″ resolution.

Position[a] (arcsec)	Flux Density (Jy/beam)	Error[b] (Jy/beam)
−27.0	2.46	0.29
−24.0	3.46	0.12
−21.0	4.38	0.27
−18.0	5.84	0.29
−15.0	7.06	0.31
−12.0	7.83	0.34
−9.0	8.38	0.31
−6.0	8.64	0.32
−3.0	6.74	0.31
0.0	7.24	0.18
3.0	7.18	0.21
6.0	7.21	0.23
9.0	7.92	0.28
12.0	6.87	0.49
15.0	4.18	0.31
18.0	3.39	0.58
21.0	2.08	0.35
24.0	1.54	0.35
27.0	1.85	0.30

(a) With respect to the central position [RA(1950) = $09^h\ 51^m\ 43.53^s$, Dec.(1950) = 69° 55′ 00.7″], along a line inclined at position angle 76° east of north. (b) Statistical errors only. There is an overall calibration error of ≤30%.

Table 3.1: Flux density at 450 μm along the major axis of M82 (7″ beam).

north-eastern maximum of the ^{12}CO (Lo *et al.* 1987), and a secondary peak in the ^{13}CO map. Note however that there is *no* feature in the 450 μm slice to correspond with the main south-western ^{12}CO peak of Lo *et al.* The ^{12}CO maximum is offset by ∼6″ from the continuum data – an offset too large to be explained by the pointing errors of ≤2″.

To compare the new continuum data with the previous 450 μm map, the scan was smoothed with a Gaussian filter to a resolution of 13″. Lack of knowledge of minor axis fluxes will not introduce large errors in the case of M82, as the submillimetre emission is nearly unresolved along the minor axis (extent ∼9″, Chapter 2). The results of this smoothing are presented in Fig. 3.2. It can be seen that, at 13″ resolution, the two peaks blend into one, ∼8″ south-west of the nucleus, with a plateau extending to the north-east, similar to the original map. The peak is rather less sharply defined than in the original 13″ map, although this is perhaps in part due to the non-Gaussian beam shape of the high-resolution data and the errors introduced by smoothing the

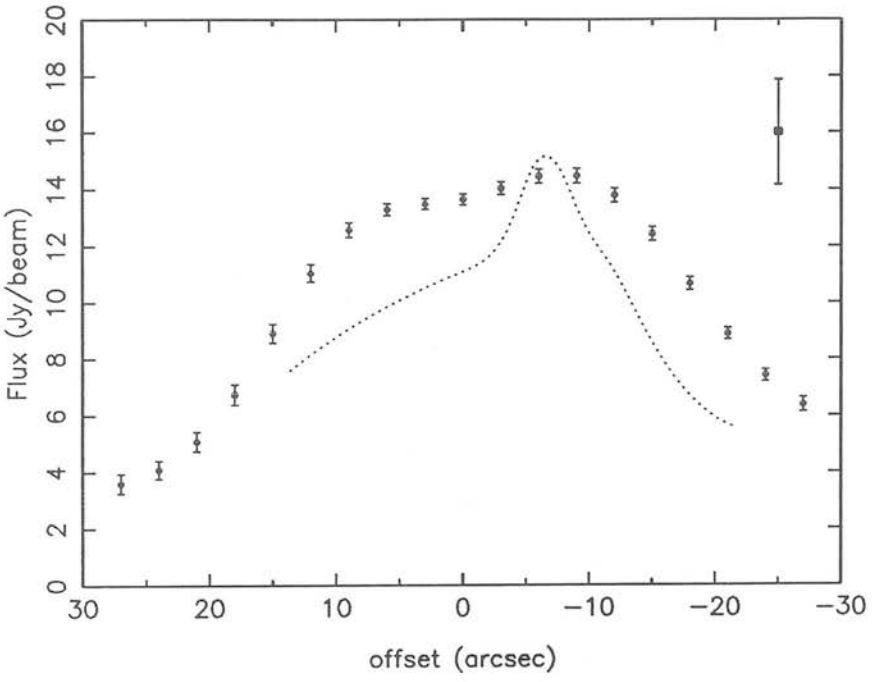

Figure 3.2: The 450 μm continuum fluxes smoothed into a 13″ Gaussian beam, for comparison with a slice through the map of Chapter 2, which is represented by a dotted line. Scan direction and central position are as for Fig. 3.1. The errors on the smoothed data points are statistical. The large vertical error bar shows the typical uncertainty in the fluxes of the original map.

one-dimensional slice. However, the flux into a 13″ beam at the peak is calculated to be 14.5±0.7 Jy, and the integrated flux from the slice is 42 Jy, in very good agreement with the original 450 μm photometry and 13″ map flux [Hughes *et al.* (1990), Chapter 2]. This gives confidence in the accuracy of the calibration and demonstrates that the new data are essentially consistent with the previous results at lower resolution.

3.4 Discussion

Since the original map was analysed, a number of new observations have appeared in the literature which throw more light on the nature of the interstellar medium in M82. Improving receiver technology has enabled the detection, and in some cases, mapping,

of rare isotopes and higher frequency transitions of CO, as well as observations of other molecular species such as CS, HCN and HCO^+ (Nguyen-Q-Rieu, Nakai & Jackson 1989; Mauersberger & Henkel 1989; Harris *et al.* 1989; Baan *et al.* 1990; Wild 1990; Tilanus *et al.* 1991; Turner, Martin & Ho 1991). The advantage of observing other transitions, isotopes and species is that they probe regimes of temperature and density to which the low-J lines of ^{12}CO are not sensitive, and allow for more sophisticated modelling of the excitation of the molecular gas. High-resolution continuum mapping at wavelengths from 10 μm to 3.3 mm has also been reported (Telesco, Decher & Joy 1989; Dietz *et al.* 1989; Krügel *et al.* 1990; Telesco *et al.* 1991; Carlstrom & Kronberg 1991). In Chapter 2 the differing CO and dust morphologies were attributed to optical depth or excitation effects, although an enhanced dust temperature in the star-forming region south-west of the nucleus could not be completely ruled out. This conclusion can now be re-examined in the light of the new data.

3.4.1 Interpretation of molecular line data.

^{12}CO 2–1/1–0 antenna temperature ratios of $\geq$2 in M82 have been interpreted as arising from warm, optically thin gas, quite unlike Galactic molecular clouds (Knapp *et al.* 1980; Olofsson & Rydbeck 1984; Loiseau *et al.* 1990). However, M82 seems to be unique among galaxies in having a large 2–1/1–0 ratio (e.g. Verter & Rickard 1989), and the $^{12}CO/^{13}CO$ J=2–1 ratio appears more consistent with optically thick ^{12}CO (Loiseau *et al.* 1988, 1990). Maps of the 1–0, 2–1 and 3–2 transitions of ^{12}CO all show the double-peaked 'ring' structure (Lo *et al.* 1987; Nakai *et al.* 1987; Loiseau *et al.* 1990; Tilanus *et al.* 1991), while observations of the much optically thinner ^{13}CO and $C^{18}O$ isotopes display a large central maximum, consistent with the 450 μm morphology (Loiseau *et al.* 1988; Wild 1990).

An idea of the optical depth of the emission comes from comparing the ^{12}CO and ^{13}CO J=2–1 lines (Loiseau *et al.* 1988, 1990). By assuming the same excitation temperature for both isotopes (LTE) and adopting a $[^{12}CO]/[^{13}CO]$ abundance ratio R, the ^{12}CO and ^{13}CO optical depths can be calculated from the antenna temperature ratio via

$$\frac{T(^{12}CO)}{T(^{13}CO)} = \frac{[1 - e^{-\tau(12)}]}{[1 - e^{-\tau(13)}]}, \qquad (3.1)$$

where $\tau(12) = R\,\tau(13)$.

From their J=2–1 observations, and by adopting R=60 (Wannier 1980), Loiseau *et al.* (1988) derive ^{12}CO optical depths of 2–10. The highest optical depths are found in between the ^{12}CO lobes, where the ^{13}CO peaks. There is some evidence that the [^{12}CO]/[^{13}CO] abundance ratio R varies from its solar neighbourhood value throughout the Milky Way, and may be as low as 24–30 at the Galactic Centre (e.g. Langer & Penzias 1990). In this case, the ^{12}CO optical depths resulting from equation (3.1) are quite low ($\sim$1) at some positions in M82, but still reach values of >4 at the ^{13}CO peak. If external heating of the clouds is significant (Young & Scoville 1984; Maloney & Black 1988), then the apparent ^{12}CO/^{13}CO ratio may be artificially high, reflecting the fact that the optically thicker ^{12}CO line will arise in the warmer outer layers of a cloud. The true ratio may thus be lower than observed, and the ^{12}CO optical depth even higher. Thus, as was concluded in Chapter 2, the 450 μm observations and the rare CO isotopes may simply be tracing molecular gas not seen in ^{12}CO because of high optical depth.

The above analysis is very simple and relies on the validity of the assumption of LTE. However, attempts at more detailed multitransition analysis have met with only limited success because of the complexity of the interstellar medium in M82. Wild (1990) applies a one-component, non-LTE radiative transfer model to observations of ^{12}CO, ^{13}CO and C^{18}O and finds his data to be consistent with a high ^{12}CO optical depth, but Tilanus *et al.* (1991) cannot explain their observed line ratios by any simple one-component model.

The detection of the J=6–5 and 7–6 transitions of ^{12}CO, as well as CS, HCN, HCO$^+$, CH_3CCH, CH_3CN and even the rare isotopes C^{34}S and H^{13}CN, all suggest large amounts of warm (>40 K), dense (n >10^4 cm^{-3}), clumpy gas in the interstellar medium of M82 (Mauersberger & Henkel 1989; Nguyen-Q-Rieu *et al.* 1989; Harris *et al.* 1989; Baan *et al.* 1990; Mauersberger *et al.* 1990; Wild 1990). Wolfire, Tielens & Hollenbach (1990) model the central kiloparsec of M82 in terms of an ensemble of photodissociation regions (PDRs), consisting of $\sim 3 \times 10^5$ small ($\sim$1 pc), dense clouds irradiated by a UV field $\sim 10^4$ times that in the solar neighbourhood. A picture emerges of a highly disturbed interstellar medium in which the molecular clouds have been swept up by stellar winds, supernovae and HII regions into small, dense, warm

clumps or filaments, embedded in low-density ionized gas and bathed in UV from $\sim 10^6$ hot young O and B stars.

Interpretation of CO data is highly dependent on the physical, excitation and chemical state of the interstellar medium (e.g. Maloney & Black 1988). It is therefore unsurprising that simple one-component models appear not to work in a region as complex and disturbed as the centre of M82. The validity of the commonly adopted method of using a Galactic conversion factor to obtain $N(H_2)$ from observations of ^{12}CO J=1–0 depends on the assumption that extragalactic molecular clouds have similar physical conditions to those in the disc of the Milky Way (i.e. $n \sim 200$ cm^{-3}, $T \sim 10$ K, $\tau \gg 1$). In the nuclei of actively star-forming galaxies this is very unlikely to be true. Maloney & Black (1988) predict that it is possible to overestimate $N(H_2)$ by factors of up to 5 in starburst nuclei.

Wild (1990) uses optically thin $C^{18}O$ data to deduce $N(H_2)$ and hence calculate the conversion factor $N(H_2)/I_{CO}$ along the major axis of M82. He finds that not only is the conversion factor ~ 3 times lower than the accepted Milky Way value of 4×10^{20} cm^{-2} (K km s^{-1})$^{-1}$ (Young & Scoville 1982), but that it varies by a factor of ~ 2 along the major axis. It is possible that $C^{18}O$ is subject, to a lesser extent, to the same excitation and abundance effects as ^{12}CO . The high-resolution 450 μm data may be used for an independent calculation of $N(H_2)/I_{CO}$ in M82.

The column density of H_2 can be derived in a straightforward way from the submillimetre flux using the method outlined by Hildebrand (1983) and modified by Gear (1988) for Gaussian source and beam profiles (see Section 1.3).

The dust continuum optical depth is given by

$$\tau(\nu) = 5.42 \times 10^{-16} \, [(\theta_s^2 + \theta_b^2)/\theta_s^2\theta_b^2] \, [S(\nu)/B(\nu, T_d)], \tag{3.2}$$

where θ_s and θ_b are the FWHM (arcsec) of the source and beam profiles, respectively, $S(\nu)$ is the flux density from the source (Jy per beam), and $B(\nu, T_d)$ is the blackbody intensity at frequency ν and dust temperature T_d.

The hydrogen column density is then

$$N(H_2) = 6.0 \times 10^{24} \, [750/\nu(\mathrm{GHz})]^{\beta} \, \tau(\nu) \ \mathrm{cm}^{-2}, \tag{3.3}$$

where β gives the frequency dependence of the dust emissivity, and Hildebrand's (1983) value of $N(H+H_2)/\tau(\nu)$ has been adopted, assuming that the neutral hydrogen in the

central region of M82 is predominantly molecular (Weliachew, Fomalont & Greisen 1984). A dust temperature of 47 K and β=1.5 as derived from the 40–1300 μm spectrum (Hughes *et al.* 1990) is assumed. A discussion of the possible sources of error of this method was given in Chapters 1 and 2 and is outlined briefly in the next section. For the purposes of the calculation the major axis scan was decomposed (by least-squares fitting) into two Gaussians of FWHM 22.5″ and 11.9″ (beam convolved with source) at major axis offsets of –8.5″ and 9.4″ respectively. Values of I_{CO} were taken from the 7″-resolution interferometer map of Lo *et al.* (1987). The results are plotted in Fig 3.3, together with those of Wild (1990) for comparison. From the 450 μm data I find, as does Wild, that the derived $N(H_2)/I_{CO}$ ratio is up to three times lower in M82 than the accepted Milky Way value, consistent with the prediction by Maloney & Black (1988) that $N(H_2)$ may be overestimated in the centres of star-forming galaxies if the Galactic conversion factor is applied. A variation of the ratio across M82 (up to a factor of 2) is also observed, although the detailed structure differs from that inferred by Wild (1990), which may in part be due to the effects of excitation or abundance on the $C^{18}O$ data, or of dust temperature on the 450 μm emission.

3.4.2 Dust continuum emission from galaxies.

In Fig. 3.4, the 450 μm scan is compared to maps at 1.3 and 3.3 mm, as well as a scan of the 10 μm continuum taken along the same line as the submillimetre data (Krügel *et al.* 1990; Telesco *et al.* 1991; Carlstrom & Kronberg 1991). The distributions at all four wavelengths are broadly similar, with the emission confined to the 'starburst' region interior to the CO ring.

The infrared-to-millimetre spectrum of the disc of the Galaxy has been extensively modelled (e.g. Cox & Mezger 1989; see Chapter 1) as thermal dust emission from several temperature components: 'cool' (20 K) dust in diffuse HI clouds, heated by the interstellar radiation field (ISRF), 'warm' (30–50 K) dust in star-forming HII region/molecular cloud complexes, heated by embedded sources, and 'hot' (>100 K) dust in HII regions, very close to the exciting stars, and emitting at 10–30 μm. At wavelengths beyond the far-infrared, other processes such as bremsstrahlung start to contribute, and may dominate by ~3 mm (e.g. Carlstrom & Kronberg 1991).

There is as yet little detailed modelling of the long-wavelength spectrum either of

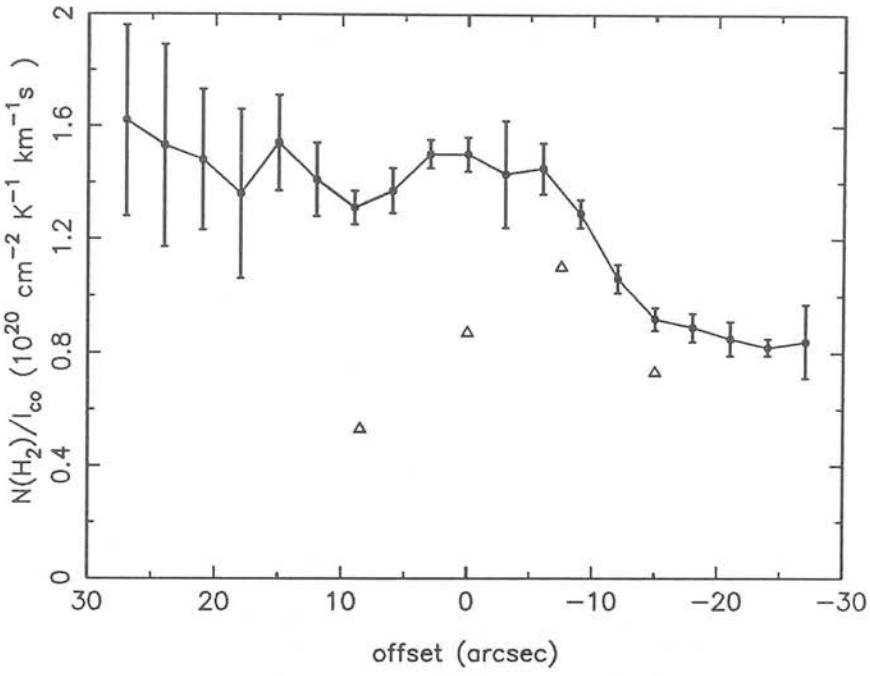

Figure 3.3: The CO-to-H_2 conversion factor, $N(H_2)/I_{CO}$, along the major axis of M82. The filled circles represent the conversion factor calculated from the 450 μm observations as described in the text. The open triangles show values calculated by Wild (1990), using $C^{18}O$ observations. Note that both data sets give values of $N(H_2)/I_{CO}$ below the accepted Galactic value of $\simeq 4 \times 10^{20}$ cm^{-2} (K km s^{-1})$^{-1}$.

the Galactic Centre or of the nuclei of starburst galaxies. Dust temperatures in these regions can be expected to be much higher than in the disc of a quiescent spiral. The mid-infrared to millimetre spectrum of M82 can be fitted by two modified blackbodies at 47 and 155 K (Hughes *et al.* 1990), dominating the submillimetre and mid-infrared fluxes respectively. The interstellar medium of M82 is highly clumped and disturbed, with small, dense, dusty clouds coexisting with ionized gas, so within any large beam (e.g. $7'' = 110$ pc on M82) there will be emission from a number of dust and gas components. Thus it is not surprising that the 10 μm to 3.3 mm observations have broadly similar distributions, especially if the dust emission is optically thin throughout this wavelength range. The warm 47 K emission, which dominates at 450 μm, is probably a

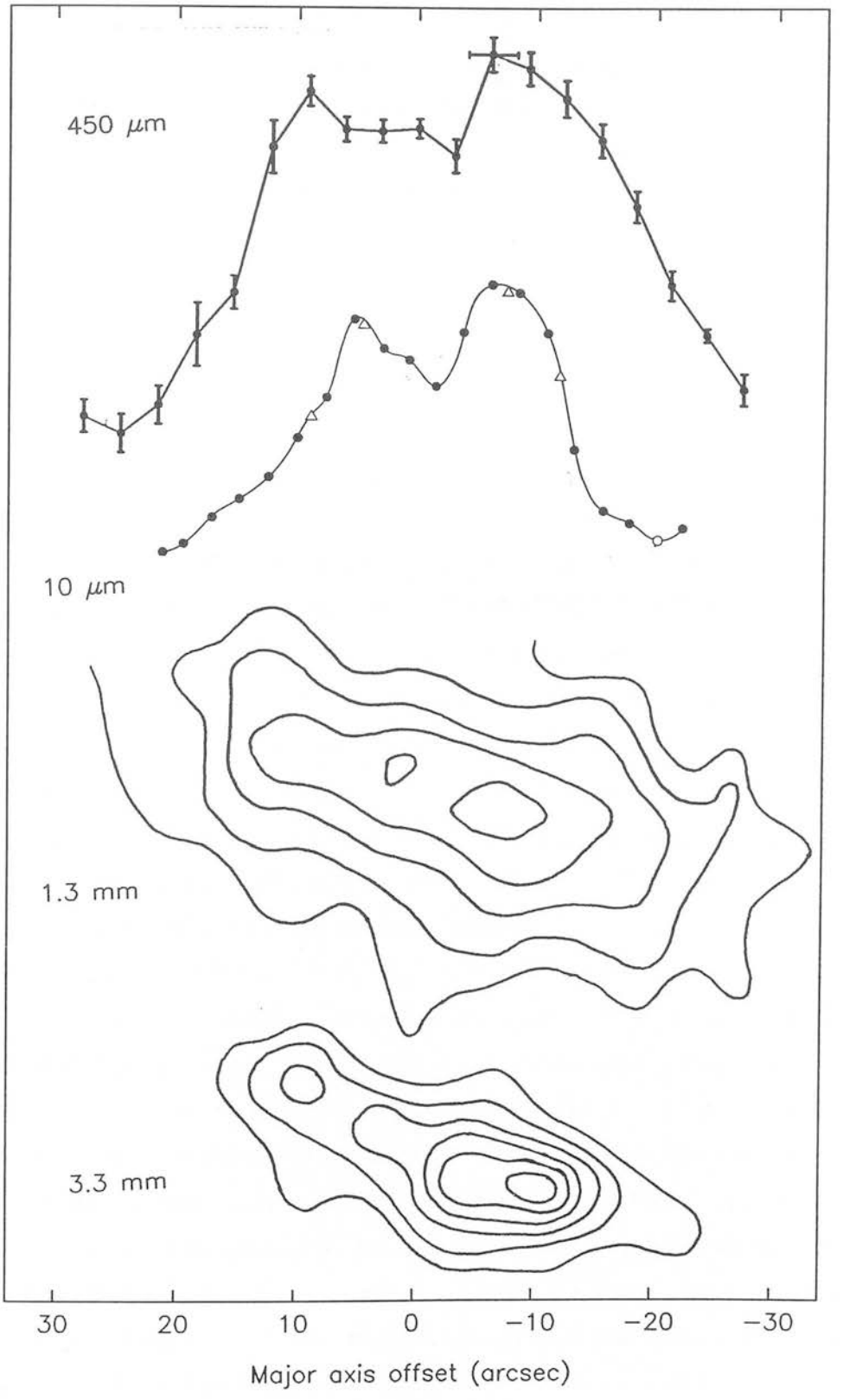

Figure 3.4: The 450 μm scan compared to maps at 1.3 and 3.3 mm, and a scan at 10 μm. See text for discussion.

combination of dust heated by embedded sources in star-forming complexes, and diffuse cirrus emission heated by an ISRF far higher than that in the disc of the Milky Way. The temperature of the cirrus-emitting dust is determined by the UV field strength – e.g. for the grain model of Rowan-Robinson (1990), when χ=1 (where χ is the UV field relative to that in the solar neighbourhood), T ~16 K as observed in the disc of the Milky Way, whereas for χ ~1000, T >45 K as is inferred for M82 and other starburst galaxies.

The submillimetre/millimetre continuum provides an independent tracer of molecular hydrogen that is free of the complex excitation and cloud chemistry effects that plague the interpretation of CO data. The dust emission is optically thin, so all the dust, and hence the H_2, is sampled. CO emission is very sensitive to high UV fields, as the molecule is easily dissociated. It is believed that much of the ^{12}CO J=1–0 emission in galaxies such as M82 may arise from the warm (>50 K) CII/C/CO transition zones in photodissociation regions, at the boundaries between HII regions and molecular clouds (e.g. Crawford *et al.* 1985). In these circumstances, the CO may be tracing UV field strength rather than H_2 column density. In contrast, dust grains are not easily destroyed by high UV fields and respond only via a very slow increase in temperature. The submillimetre flux, and hence derived $N(H_2)$, has an approximately linear dependence on dust temperature [$S(\nu) \propto T_d^{1.6}$ at 450 μm – Chapter 2]. The dust temperature itself is relatively straightforward to determine from the infrared–millimetre data by fitting a modified blackbody function [$\nu^\beta\ B(\nu, T_d)$] to the spectrum.

The relative simplicity of the technique does not make it free from error, however. Even for small beams, a galaxy is very much a composite object, and the infrared–millimetre spectrum will be composed of emission from dust at a range of different temperatures. The derived dust optical depth, and hence $N(H_2)$, is dependent on the dust temperature adopted. Long-wavelength (λ >300 μm) observations are particularly valuable, as they are more sensitive to the cool ($\leq$30 K) dust that is easily missed if only far-infrared fluxes are used, and reduce the inevitable errors that follow from trying to fit several temperature components to a small number of data points. Apart from the pitfalls of spectrum fitting, the largest source of error lies with the conversion factor $N(H_2)/\tau(\nu)$. As in the case of CO, the conversion factor in use has been derived from observations within the Milky Way, and is then assumed also to be valid in other

galaxies. Although it may be as accurate as ±50–100% in the Milky Way (Mezger 1990), its possible variation in extragalactic environments is not well understood. However, the value of the conversion factor is not critically dependent on the details of gas excitation, as is the case for CO, but on grain parameters. These might perhaps not be expected to vary drastically both between and within most galaxies, given the relative insensitivity, compared to CO, of both H_2 and grains to such factors as increased UV field. It therefore seems likely that the knowledge of $N(H_2)/\tau(\nu)$ is no less accurate than that of $N(H_2)/I_{CO}$, and is probably better, although further theoretical modelling such has already been carried out for the Milky Way (e.g. Cox & Mezger 1989) is clearly needed.

3.5 Conclusions

The nearby star-forming galaxy M82 has been observed at 450 μm in the dust continuum, with diffraction-limited, 7″ resolution. Because of the small minor axis extent of the galaxy at 450 μm (∼9″), the one-dimensional slice along the major axis loses very little flux, and may therefore be considered representative of the flux distribution from the entire nuclear region. The data are consistent, both in flux and morphology, with earlier observations (Chapter 2) at lower resolution.

The scan has a main peak ∼8″ south-west of the nucleus of the galaxy, with a secondary peak to the north-east. This morphology differs from that of ^{12}CO J=1–0 at the same high resolution – specifically, there is *no* feature in the map to correspond to the south-western lobe of ^{12}CO, while the main peak of the 450 μm scan is barely visible in CO. In contrast, the optically thin tracers of ^{13}CO and C^{18}O, as well as the 1.3 mm continuum, bear a strong resemblance to the 450 μm scan, all four peaking within the CO lobes.

Although ^{12}CO 2–1/1–0 ratios of >2 appear to indicate optically thin gas in M82, simple LTE analysis of the ^{12}CO and ^{13}CO J=2–1 lines suggests that the ^{12}CO is quite optically thick at the centre of the galaxy, even for the low ^{12}CO/^{13}CO abundance ratios of ∼25 that may apply to the centres of galaxies. Thus the continuum observations could simply be tracing molecular gas not seen in the ^{12}CO line because of high optical depth. However, recent attempts at sophisticated non-LTE modelling by several

authors have led to contradictory conclusions, and a wealth of multitransition observations of isotopes of CO, CS and other molecules all point to an interstellar medium so complex and disturbed that it seems likely that CO, with its sensitivity to gas excitation and cloud chemistry, is an unreliable tracer of the bulk of the molecular material in this galaxy. Indeed, the 450 μm data imply that the CO-to-H_2 conversion factor, $N(H_2)/I_{CO}$, varies along the major axis and is up to three times lower than the Milky Way value, supporting the growing body of evidence that application of a 'constant conversion factor' can lead to overestimates of $N(H_2)$ in many actively star-forming galaxies.

The submillimetre dust continuum, on the other hand, would seem to provide a more direct, straightforward method of tracing molecular hydrogen column density, free from the complex dependence on UV field and excitation, and the necessity for sophisticated radiative transfer modelling, that plague interpretation of molecular line data. Although not without pitfalls, chiefly the accuracy of the conversion factor $N(H_2)/\tau(\nu)$, and the multicomponent nature of the dust continuum spectrum, the simplicity of the method, coupled with the low optical depth of submillimetre emission, means that observation of the dust continuum is an important tool in the investigation of the interstellar media of external galaxies. Further theoretical modelling of dust emission from galactic nuclei, such has already been performed for the disc of the Milky Way, would be very welcome.

Chapter 4

Dust continuum observations of nearby star-forming galaxies

The results presented in the previous two chapters, of 450 μm mapping of M82, indicate the potential of this method as an independent tracer of the molecular interstellar medium in star-forming galaxies. A logical next step is to carry out submillimetre continuum mapping of other nearby infrared-bright galaxies for which CO observations already exist or are planned. 450 μm mapping is unfeasible for most extragalactic sources, even under good sky conditions, so it was decided to observe at 800 μm. This gives probably the best combination of resolution, atmospheric transparency, expected source strength and minimal contamination by non-dust processes, of all the commonly used submillimetre/millimetre atmospheric windows (see Appendix A). The selected targets were the nearby starburst systems IC342, Maffei 2 and M83. IC342 has already been observed extensively in CO, M83 has been mapped in the ^{12}CO J=1–0 line, and high-resolution ^{12}CO and ^{13}CO 1–0 and 2–1 observations of Maffei 2 are presented in Chapter 5 of this thesis. As well as mapping at 800 μm, photometry was carried out at 450–1100 μm, to combine with existing far-infrared/millimetre data and help constrain the long-wavelength spectrum.

The observations presented in this chapter were carried out over an 18-month period from December 1988 to May 1990, and form part of an on-going project of JCMT continuum observations involving Phil Puxley and Matt Mountain of the Royal Observatory Edinburgh, Peter Brand of the University of Edinburgh and Naomasa Nakai of the Nobeyama Radio Observatory, Japan. Due to the scheduling of the IC342 run, on the same night as the M82 run described in Chapter 3, the IC342 observations were performed by Tim Hawarden of the Joint Astronomy Centre in Hilo.

4.1 Introduction

The long-wavelength dust continuum is potentially a useful check on the reliability of ^{12}CO as a tracer of the molecular interstellar medium of star-forming galaxies, providing a method of estimating molecular hydrogen masses that is independent of the assumptions about cloud excitation that are involved with application of the CO technique.

This chapter presents submillimetre dust continuum mapping and photometry of three nearby spiral galaxies, Maffei 2, IC342 and M83. All three exhibit strong far-infrared continuum and molecular line emission, along with other signatures of active star formation in their central $\sim$1 kpc regions. Table 4.1 summarizes the adopted physical parameters of the target galaxies.

Table 4.1: Adopted galaxy parameters for dust continuum observations.

	Maffei 2	IC342	M83
Central position RA, Dec. (1950)	$02^h\ 38^m\ 8.5^s$ $+59°\ 23'\ 24''$ (1)	$03^h\ 41^m\ 57.2^s$ $+67°\ 56'\ 27''$ (2)	$13^h\ 34^m\ 11.53^s$ $-29°\ 36'\ 42.18''$ (3)
Position angle of major axis (E from N)	30° (4)	0° (5)	45° (6)
Distance (Mpc)	5 (4,7)	4.5 (8)	3.7 (9)
IRAS fluxes	$S(60) = 92.9$ Jy $S(100) = 224.8$ Jy	$S(60) = 85.2$ $S(100) = 125.9$	$S(60) = 103.3$ $S(100) = 212.1$
Inclination (0° = face-on)	65° (4)	25° (10)	24° (11)
Hubble type	Sbc (4,7)	Scd (12)	SBc (13)

References: (1) Weliachew *et al.* 1988. (2) Becklin *et al.* 1980 (Near-infrared peak). (3) Rumstay & Kaufmann 1983. (4) Allen & Raimond 1972. (5) Lo *et al.* 1984. (6) Danver 1942. (7) Spinrad *et al.* 1973. (8) Baker *et al.* 1977; Sandage & Tammann 1975. (9) de Vaucouleurs 1979. (10) Rogstad *et al.* 1973. (11) Talbot *et al.* 1979. (12) Tully 1988. (13) Sandage & Tammann 1981.

Maffei 2 is an almost edge-on, Sbc spiral, lying at low Galactic latitude and heavily

obscured at optical wavelengths. Studies have therefore been largely confined to the near-infrared and beyond. The possibility that Maffei 2 is physically associated with the giant elliptical galaxy Maffei 1, only 43′ away on the plane of the sky (although their respective distances from us are uncertain) has not been discounted (e.g. Bottinelli *et al.* 1971; Love 1972). Strong non-thermal radio emission and near-infrared recombination lines suggest active, massive star formation in the central kiloparsec (Seaquist, Pfund & Bignell 1976; Ho *et al.* 1989; Ho, Beck & Turner 1990a). Intense molecular line emission from Maffei 2, one of the first extragalactic objects in which the ^{12}CO J=1–0 line was detected (Rickard, Turner & Palmer 1977a), preceded its appearance as one of the brightest non-merging extragalactic sources in the *IRAS* survey [$S(100\,\mu\mathrm{m}) \simeq$ 200 Jy], and established its classification as a 'starburst' galaxy, with a far-infrared spectrum similar to that of M82. The CO emission is concentrated in the central $\sim$1 kpc of the galaxy. High-resolution interferometer data resolve a long, narrow bar-like morphology, and two peaks $\sim$10″ apart either side of the nucleus, interpreted as an expanding molecular ring, possibly created by the starburst, triggered by inflow of gas along the bar (Ishiguro *et al.* 1989). As in the case of M82, ratios of CO transitions have been taken to imply that the molecular gas is both warmer and optically thinner than in Galactic molecular clouds, although observations of rare isotopes demonstrate that the situation is not clear-cut (Chapter 5). Line emission from other molecular species such as CS and N_2H^+ (Mauersberger *et al.* 1989; Mauersberger & Henkel 1991) provides further evidence of warm, dense gas in the nuclear star-forming region. Detection of the 158 μm [CII] line (Stacey *et al.* 1991), from photodissociation regions, implies intense UV fields which may influence the excitation and chemistry of the molecular clouds in this galaxy.

IC342 is an almost face-on Scd galaxy, lying close to the Galactic plane only a few degrees away from Maffei 2 in the sky. It is bright at all wavelengths from near-infrared to radio, and displays all the hallmarks of active nuclear star formation, including strong thermal and non-thermal radio continuum, molecular line emission, warm dust continuum, and far-infrared lines from ionized carbon in photodissociation regions (Becklin *et al.* 1980; Turner & Ho 1983; Rickard & Harvey 1984; Crawford *et al.* 1985; Hummel & Gräve 1990). IC342 is a particularly intense source of molecular line emission, and, along with M82 and NGC 253, is the extragalactic source in which many molecular

species were first detected. The ^{12}CO emission is elongated north–south into a bar-like structure (Sofue *et al.* 1987; Eckart *et al.* 1990). At very high resolution, the bar is resolved into two narrow parallel ridges, which combine at the nucleus to form a ~100 pc diameter ring associated with highly non-circular velocities (Ishizuki *et al.* 1990). CO line ratios suggest that the gas is warm ($\geq$30 K) and that excitation conditions vary with position in the nuclear region (Eckart *et al.* 1990). IC342 remains the only extragalactic source in which inversion transitions of ammonia have been studied in detail, their detection implying the presence of very warm (>50 K) gas (Ho *et al.* 1990b). A wealth of other molecular species and isotopes have been detected and in some cases mapped in IC342, including ^{12}CO and ^{13}CO (J=1–0, 2–1 and 3–2), ^{12}CO J=6–5, CN, HNC, CS, HNCO, N_2H^+, $H^{13}CO$, HCN and HCO^+ (Henkel, Mauersberger & Schilke 1988; Mauersberger & Henkel 1989; Wall & Jaffe 1990; Steppe *et al.* 1990; Nguyen-Q-Rieu *et al.* 1990; Wild 1990; Mauersberger & Henkel 1991; Harris *et al.* 1991).

M83 is an almost face-on, striking 'grand design' SBc galaxy lying at a distance of ~4 Mpc. Like Maffei 2 and IC342, it is an intense source of thermal and non-thermal radio continuum, molecular lines, mid- and far-infrared dust continuum, near-infrared recombination lines and far-infrared [CII] lines from the actively star-forming region (Telesco & Harper 1980; Cowan & Branch 1985; Crawford *et al.* 1985; Ondrechen 1985; Sukumar, Klein & Gräve 1987; Telesco *et al.* 1987; Turner, Ho & Beck 1987). M83 was one of the first extragalactic sources to be observed in CO (Rickard *et al.* 1977b). The ^{12}CO J=1–0 emission is strongly concentrated in the central ~45″ and elongated along the optical bar. Wide CO profiles and non-circular distortions of the velocity field are characteristic of the nuclear region (Handa *et al.* 1989). Because M83 is so far south (Dec. = –29°) and therefore unattainable, or at very low maximum elevation, from most large millimetre-wave telescopes, observations of other CO transitions, or of additional molecular species, are very sparse, although the nuclear region has been mapped in ^{12}CO J=2–1 with the JCMT (Handa *et al.*, in preparation), and the J=2–1 transition of CS has also been detected, demonstrating that dense gas is present (Mauersberger *et al.* 1989).

4.2 Observations

All the observations were performed with the 15-m James Clerk Maxwell Telescope (JCMT) on Mauna Kea, Hawaii, with the ^{3}He-cooled bolometer UKT14 (Duncan *et al.* 1990). Further details of the observing and calibration procedures involved with continuum observations on the JCMT are given in Appendix A.

4.2.1 Maffei 2

The Maffei 2 observations were made during PATT time on 3–4 December 1988. The central $\sim$40″ of Maffei 2 was mapped at 800 μm and additional photometry of the map centre was performed at 800 and 1100 μm . The UKT14 aperture was fully open (65 mm), resulting in diffraction-limited (18.5″) resolution at 1100 μm and a beamsize of 15.8″ for the 800 μm data. The mapping and photometry was centred at RA(1950) = $02^h\ 38^m\ 8.5^s$, Dec.(1950) = +59° 23′ 24″. We chopped 150″ away in azimuth to get good sky cancellation. At the map centre, signal-to-noise ratios of 19 and 8 at 800 and 1100 μm were achieved in on-source integration times of $\sim$5 min.

Pointing and focus checks were performed frequently using Mars, the evolved star (and point source) CRL618 and the powerful radio source 3C84. The rms pointing errors ranged from 1″–3″ (azimuth) and 2″–4″ (elevation) with average values 1.6″ and 2.8″ respectively. The sky was more unstable on the second night, with the pointing drifting quickly.

Calibration and extinction correction was performed using Mars and CRL618. The published sensitivities of UKT14 at 800 and 1100 μm (G. Sandell, JCMT User Note, June 1988) were assumed (see Appendix A), and are presented in Table 4.2 along with the adopted fluxes of the calibrator sources. The atmospheric opacity varied from 0.1 to 0.3 at 1100 μm and from 0.5 to 0.9 at 800 μm, and the data were transformed out of the atmosphere using appropriate values of extinction.

Data reduction was performed using the JCMT continuum reduction package NOD2 (Haslam 1974). As the telescope was not yet fully commissioned in December 1988, it was decided to make the 800 μm maps by raster scanning in azimuth and elevation, since this is the natural mode of operation of the JCMT, and the coordinate system for which the reduction software is set up. This mapping procedure turned out to

Table 4.2: Calibration details for Maffei 2: 3–4 December 1988.

	800 μm	1100 μm
Beamsize [a]	15.8″	18.5″
Flux density of Mars (Jy) [b]	2129.47	1187.81
Flux density of CRL618 (Jy) [c]	3.59±0.22	2.26±0.09
Sensitivity (Jy/mV) [d]	8.5	11.8

(*a*) 65-mm aperture. (*b*) Assuming a brightness temperature of 209 K and angular semidiameter of 6.4″ in December 1988. (*c*) G. Sandell, JCMT Internal Memo. (*d*) G. Sandell, JCMT User Note.

be somewhat ill-advised, for reasons that are discussed below, and led to problems in the production of a reliably contoured 800 μm map. There are definite advantages in mapping by raster scanning, rather than point-by-point photometry, if the source is bright, such as M82. The relative calibration and pointing between pixels will be more reliable for a raster-scanned grid. However, for sources that are quite weak at submillimetre wavelengths, there are technical difficulties. Raster-scanned maps are limited to $\sim$1 hr in duration by the necessity for frequent calibration and pointing measurements, allowing only a short (<1 min) integration time per map point and resulting in low signal-to-noise ratios ($\sim 6\sigma$) even at the map peak. The usual practice is therefore to make several maps of $\sim$1 hr each, separated by pointing and calibration measurements, and to co-add these maps to improve the signal-to-noise ratio. This is straightforward when all the maps are in RA–Dec. and there is a direct pixel-to-pixel correspondence. However, the orientation angle of an Az–El grid with respect to RA–Dec. changes throughout the night. In addition, for long ($\sim$1 hr) maps, the sky is rotating under the map as it is made, and a regular grid in Az–El becomes distorted when transformed back to the RA–Dec. frame. The problem then is how to co-add reliably maps which are on completely different, and non-regular, grids. The JCMT continuum reduction software contains a routine which will convert an Az–El map to

RA–Dec. and interpolate it on to a regular grid. The interpolation algorithm has a tendency to produce spuriously large or small fluxes at the edges of the map, and for small grids one has to be careful that these 'edge effects' do not encroach too far into the data. While mapping in Az–El and subsequent interpolation onto an RA–Dec. grid is probably reliable for large maps of bright Galactic objects, for faint extragalactic sources requiring co-addition of several maps the reduction difficulties may outweigh the advantages of relative calibration and pointing accuracy.

Four maps of Maffei 2 were made during the two-night observing run. The grid spacing in each case was 6″ – thus with a 15.8″ beam the maps are somewhat oversampled. The map dimensions were chosen depending on the hour angle, to optimize the coverage of Maffei 2 assuming a dust morphology similar to that seen in CO (major axis position angle 30°). The integration time for each map point was $\sim$ 1 min (on-plus off-source). Two of the maps were made at low elevation ($30° - 40°$) and detections made at only a few of the map points. These maps were therefore not included in the analysis. The other two maps achieved signal-to-noise ratios ranging from ~ 6–7σ at the centre to $<1\sigma$ at the edges. The two maps consist of regular Az–El grids of 5×9 and 7×7 pixels respectively.

The individual maps were transformed from Az–El to RA–Dec. coordinates using the NOD2 routine CONVERT. Contour maps of the 800 μm emission are presented in Fig. 4.1, where the 'edge effects' caused by the interpolation can be clearly seen. It is also apparent that there is a pointing shift of about 1 pixel in each direction, between the maps. This is consistent with a small pointing drift observed during the second map – the first map is therefore regarded as being correctly positioned.

The central $\sim$30″ $\times$ 36″ of the contour maps were least-squares fitted by a two-dimensional Gaussian function at a position angle of 30°. The two maps were consistent in both flux level and source size, indicating that the calibration is accurate and the interpolation is giving reliable results. The peak flux densities of the individual maps were completely consistent with the high signal-to-noise 800 μm photometry. The two maps were therefore combined, weighted by their respective average noise levels. Table 4.3 gives the individual pixel fluxes of the averaged maps.

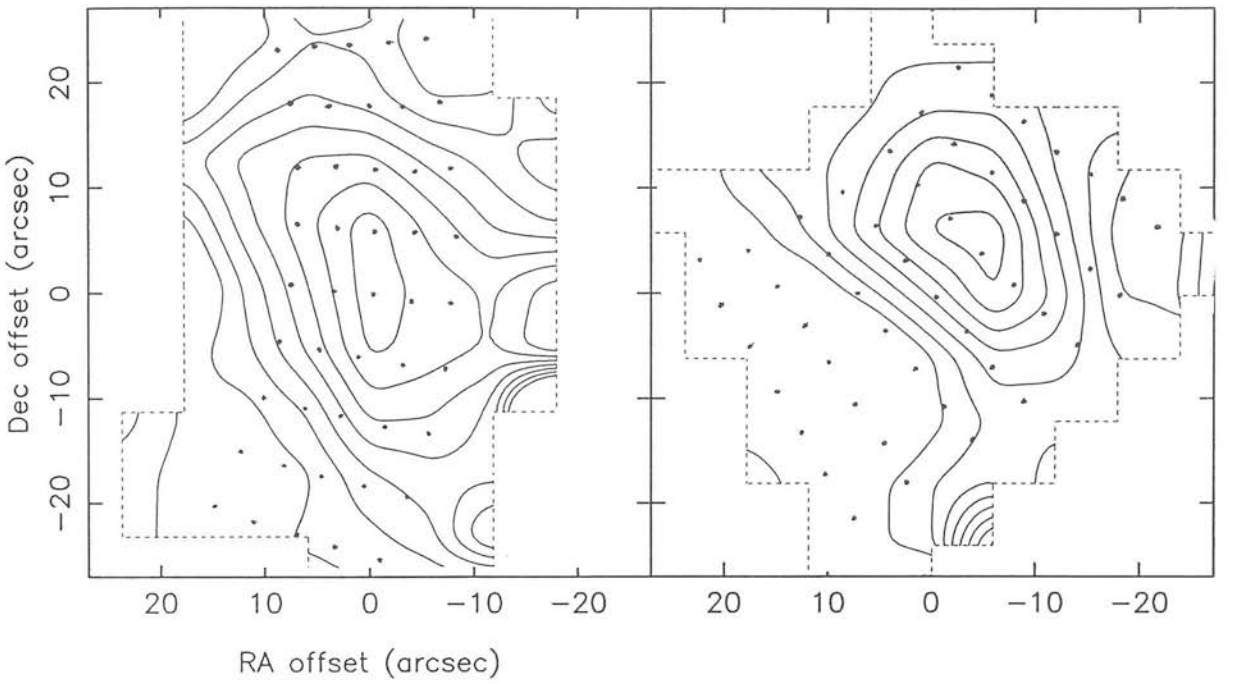

Figure 4.1: Two individual maps of Maffei 2 which were co-added to produce the final map presented in Fig. 4.8. The 'edge effects' resulting from the transformation between Az/El and RA/Dec. coordinates can be clearly seen, as can a ∼1 pixel offset between the two maps. Superimposed on the maps are the observed grids of pixels (in RA, Dec.), which can be seen to have been quite distorted by the rotation of the sky while the maps were being made.

4.2.2 IC342

The IC342 observations were carried out during PATT time on 18–21 December 1989, and consisted of mapping and photometry at 800 μm and photometry of the map centre at 450 μm. The aperture of UKT14 was set to 47 mm, resulting in diffraction-limited (13.5″) resolution at 800 μm and a beamsize of $\simeq$13″ for the 450 μm data. Because of the anticipated weakness of the submillimetre emission from IC342, it was decided not to attempt raster scanning to make the 800 μm map, but instead to map via point-by-point photometry, allowing much longer integration times for each pixel. Relative calibration between pixels then becomes very important, as adjacent portions of the map may be observed at quite different times, and the opacity of the atmosphere at submillimetre wavelengths is rarely constant over the course of a night. The central 30″ × 40″ of IC342 was mapped at 800 μm. The fully sampled map consists of a grid of 28

Table 4.3: Summary of the Maffei 2 data.

RA, Dec. Offset (arcsec)[1]		800 μm flux density (Jy)[2]	RA, Dec. Offset (arcsec)[1]		800 μm flux density (Jy)[2]
18.0	−18.0	0.001	0.0	0.0	0.614
12.0	−18.0	−0.032	−6.0	0.0	0.448
6.0	−18.0	0.063	−12.0	0.0	0.314
0.0	−18.0	0.211	18.0	6.0	0.099
−6.0	−18.0	0.252	12.0	6.0	0.301
−12.0	−18.0	0.258	6.0	6.0	0.483
18.0	−12.0	−0.010	0.0	6.0	0.551
12.0	−12.0	−0.027	−6.0	6.0	0.370
6.0	−12.0	0.131	−12.0	6.0	0.229
0.0	−12.0	0.381	18.0	12.0	0.197
−6.0	−12.0	0.362	12.0	12.0	0.308
−12.0	−12.0	0.249	6.0	12.0	0.375
18.0	−6.0	0.014	0.0	12.0	0.381
12.0	−6.0	0.134	−6.0	12.0	0.264
6.0	−6.0	0.333	−12.0	12.0	0.203
0.0	−6.0	0.578	18.0	18.0	−0.018
−6.0	−6.0	0.472	12.0	18.0	0.188
−12.0	−6.0	0.330	6.0	18.0	0.236
18.0	0.0	−0.002	0.0	18.0	0.201
12.0	0.0	0.251	−6.0	18.0	0.074
6.0	0.0	0.461	−12.0	18.0	0.087

(1) Offset from map centre at RA $02^h\ 38^m\ 8.5^s$, Dec. $+59°\ 23'\ 24''$. (2) Average of two maps weighted by respective average noise levels. Error on average fluxes ~0.08 Jy (from the average noise levels of the original maps. There is an additional global calibration error of ~10%).

points, oriented in RA, Dec. with a grid spacing of 6.5″ . The grid points were chosen to correspond with the morphology of the CO emission, which appears extended north–south (Sofue *et al.* 1987). The map was centred at RA=$03^h\ 41^m\ 57.2^s$, Dec.(1950)= $+67°\ 56'\ 27''$, the near-infrared peak. Each observation typically consisted of ~3 min on-source integration and was repeated up to four times to improve signal-to-noise. We chopped 120″ away in azimuth. Signal-to-noise ratios of $\sim 20\sigma$ at the map centre were achieved, decreasing to $\sim 2\sigma$ at the outer positions. At 450 μm, an on-source integration time of 5 min resulted in a $\sim 6\sigma$ detection at the central position. The data were checked to remove any spikes in individual on–off samples, which can markedly decrease the signal-to-noise while leaving the mean signal relatively unaffected (Appendix A).

Pointing and focus checks were performed frequently using Jupiter and 3C84. The pointing was extremely stable, rms pointing errors ranging from 1.2″–2.1″ (azimuth) and 1.4″–3.0″ (elevation) over the four nights of the run, with average values 1.6″ and 2.2″ respectively, much less than the beam spacing of the map.

Calibration and extinction corrections were performed using Jupiter, the compact HII regions W3(OH) and W75(N), and 3C84. From observation of Jupiter at two different airmasses it was possible to estimate a value for the sensitivity of UKT14 at 800 μm of 9.8 Jy/mV, a value differing by only $\sim$10% from the published value which dates from June 1988 (G. Sandell, JCMT User Note). This value was then applied to the other calibration data to derive atmospheric opacity variations throughout the night. Accurate fluxes were not available for 3C84, which therefore had itself to be calibrated before it could be used as an additional monitor of the extinction at 800 μm. Adopted values of 800 and 450 μm flux densities for Jupiter, W3(OH) and W75(N), together with the derived flux density for 3C84 and the adopted sensitivities of UKT14 at these wavelengths are presented in Table 4.4. The sky opacity varied from 0.3–1.0 at 800 μm, and appropriate values were used to transform each map point out of the atmosphere. At 450 μm the extinction was found to be 1.1$\pm$0.3.

We reobserved the centre of the map frequently at 800 μm to check the consistency of the calibration. The mean of the 14 central pixel observations was 0.43$\pm$0.06 Jy (where the error is the standard deviation of the values). This was adopted as the central 800 μm flux of IC342. Thus the relative calibration between the separately observed groups of pixels is consistent to 13% . The fluxes for the other 27 positions were scaled up to be consistent with a central flux density of 0.43 Jy. The derived fluxes at each position are presented in Table 4.5.

4.2.3 M83

M83 was observed during the nights of 1–4 May 1990. Mapping was carried out at 800 μm, with photometry of the map centre at 1100 and 450 μm. All observations were performed with the detector aperture fully open (65 mm), resulting in diffraction-limited (18.5″) resolution at 1100 μm, and beamsizes of 15.8″ and 17.5″ at 800 and 450 μm, respectively. The central 38″ $\times$ 30″ of M83 was mapped at 800 μm, in the form of a regular grid of 42 points, oriented parallel and perpendicular to the axis of

Table 4.4: Calibration details for IC342: December 18–21 1989.

	800 μm[a]	450 μm[a]
Flux density of Jupiter [b]	3315.30 Jy	8441.51 Jy
Flux density of W3(OH) [c]	23.4±1.2 Jy	–
Flux density of W75(N) [c]	26.1±2.4 Jy	–
Derived flux density of 3C84 [d]	2.1±0.2 Jy	–
Sensitivity of UKT14 (Jy/mV)	9.8 [e]	25.6 [f]

(*a*) 47-mm aperture, 13″ beam. (*b*) From brightness temperatures of 162.5 K at 800 μm and 148.5 K at 450 μm and angular semidiameter of 22.9″ in December 1989. (*c*) G. Sandell, JCMT internal memo. (*d*) Errors in the derived flux of 3C84 come from the scatter in the values calculated throughout the run. (*e*) Derived from observations of Jupiter. (*f*) Derived from 450 μm observations made during the second half of the night (see Chapter 3).

the bar (PA=45° – Danver 1942) and spaced at 7.5″ , thus fully sampled. The map was centred at RA(1950)=13^h 34^m 11.53^s, Dec.(1950)=–29° 36′ 42.18″ . We chopped 150″ away in azimuth for good sky subtraction. As in the case of IC342, the mapping was done point by point, rather than raster scanned, to get high signal-to-noise ratios. On-source integration times of $\leq$5 min per point (32 on–off samples) resulted in signal-to-noise ratios ranging from $\sim 20\sigma$ at the centre to $\sim 1\sigma$ at the edges of the map. At the other wavelengths, signal-to-noise ratios of 10σ and 3.4σ (5 min on-source integration) at 1100 and 450 μm, respectively, were achieved. The data were checked to remove any spikes in individual samples.

The map points were observed in groups of about five, preceded and followed by pointing and calibration measurements. Each group of map points included a reobservation of the central position, to check the consistency of the calibration. Pointing and focus checks were performed on Jupiter, the bright, evolved star IRC10216 and the quasar 3C279. The rms pointing errors varied from 2.3″–2.7″ (azimuth), and 1.6″–2.7″

Table 4.5: Summary of the IC342 observations.

Map Offset (arcsec)[1]		800 μm flux density (Jy)[2,3]	Statistical error (Jy)[3]	Total error (Jy)[4]
0.0	0.0	0.433	0.009	0.044
0.0	6.5	0.403	0.019	0.045
−6.5	6.5	0.365	0.013	0.039
−6.5	0.0	0.398	0.017	0.044
−6.5	−6.5	0.196	0.009	0.022
0.0	−6.5	0.401	0.020	0.046
6.5	−6.5	0.261	0.017	0.032
6.5	0.0	0.383	0.015	0.042
6.5	6.5	0.253	0.015	0.030
6.5	13.0	0.174	0.013	0.022
0.0	13.0	0.137	0.012	0.018
−6.5	13.0	0.065	0.013	0.018
−13.0	6.5	0.073	0.026	0.027
−13.0	0.0	0.165	0.022	0.030
−13.0	−6.5	0.167	0.026	0.032
−13.0	−13.0	0.057	0.022	0.023
−6.5	−13.0	0.259	0.022	0.035
0.0	−13.0	0.121	0.017	0.030
6.5	−13.0	0.145	0.020	0.026
13.0	−6.5	0.026	0.021	0.021
13.0	0.0	0.096	0.017	0.026
13.0	6.5	0.179	0.019	0.029
13.0	13.0	0.089	0.019	0.026
6.5	19.5	0.121	0.018	0.022
0.0	19.5	0.039	0.017	0.017
−19.5	0.0	0.027	0.018	0.018
−19.5	−6.5	0.067	0.027	0.028
−6.5	−19.5	0.094	0.023	0.025
0.0	−19.5	0.059	0.027	0.028

(1) Offsets in RA, Dec., with respect to the map centre at RA(1950) = $03^h\ 41^m\ 57.2^s$, Dec.(1950)= $+67°\ 56'\ 27''$. (2) Flux in a 13.5″ beam. (3) The flux density and error come from the weighted mean and error of all the individual observations of a particular offset, where the errors are the statistical uncertainty of the integration (see Appendix A). (4) Combination in quadrature of the observational uncertainties and calibration errors of ∼10–20% . There is an additional global uncertainty of ∼13% due to the scatter in the derived values of flux density at the central position.

(elevation).

Primary calibration was performed using Jupiter and IRC10216. These set quite early in the shift, so the quasar 3C279, as the only other bright submillimetre source available, was used as an extinction monitor for the remainder of the night. The sky opacity varied on too short a time-scale (<1 hr) to derive accurate extinctions from observations of calibrators at two different airmasses and thence calculate a value for the sensitivity of UKT14 (Jy/mV) from photometry of Jupiter (see Appendix A). It was therefore necessary to assume that the published sensitivities were still valid and use Jupiter and IRC10216 to calibrate 3C279, which was then used to derive extinction values and calibrate M83 for the remainder of the night. The adopted values of 1100, 800 and 450 μm flux density for Jupiter and IRC10216, sensitivities for UKT14, and the derived fluxes for 3C279 at these wavelengths, are summarized in Table 4.6. The sky extinction was found to vary from a ~0.15–1.0 at 800 μm, and the map data were transformed out of the atmosphere using a value of a interpolated from the nearest calibration observations. The 1100 and 450 μm photometry was extinction corrected using sky opacities of ~0.2 and 3 respectively. The central position was observed a total of 14 times at 800 μm. The mean of these central fluxes was 0.46±0.05 Jy (the error being the standard deviation of the 14 values), and this was adopted as the central 800 μm flux of M83. Thus the relative calibration between the separately observed groups of map points is consistent to ~11%. The fluxes for the other 41 positions were scaled to be consistent with a central flux density of 0.46 Jy, and are presented in Table 4.7.

4.2.4 Integrated submillimetre flux density

The 800 μm mapping can be used, together with the peak fluxes presented in Table 4.8, to calculate the integrated 800 μm emission in the central ~30″–40″ of the three galaxies. If it is then assumed that the source size is the same at 800, 1100 and 450 μm, the 800 μm integrated flux density can be used with the photometry at 1100 and 450 μm to estimate the integrated fluxes at these wavelengths. If there is in reality a temperature gradient with $T_{\rm dust}$ decreasing away from the nucleus (probably a reasonable assumption for a galaxy with nuclear star formation), then this approach will result in a slight overestimate of the 450 μm integrated flux (since the apparent source size will

Table 4.6: Calibration details for M83: May 1–4 1990.

	1100 μm	800 μm	450 μm
Beamsize [a]	18.5″	15.8″	17.7″
Flux density of Jupiter [b]	3002.88 Jy	4314.9 Jy	14621.5 Jy
Flux density of IRC10216 [c]	2.5±0.3 Jy	5.3±0.7 Jy	14.1±2.1 Jy
Derived flux density of 3C279 [d]	5.7±0.4 Jy	4.2±0.3 Jy	3.3±0.5 Jy
Sensitivity of UKT14 (Jy/mV)	11.8	8.5	15.5

(*a*) 65-mm aperture. (*b*) From brightness temperatures of 162.5 K at 800 μm, 170 K at 1100 μm, 148.5 K at 450 μm and angular semidiameter of 16.7″ in May 1990. (*c*) G. Sandell, JCMT internal memo (mean of all observations of IRC10216). (*d*) Errors in the derived flux of 3C279 come from the scatter in the values calculated throughout the run.

be smaller at 450 μm) and vice versa at 1100 μm.

Two different methods can be used to estimate the integrated emission from the 800 μm map. If it is assumed that both the source and beam are Gaussian in shape, then the total flux density can be calculated from the peak flux density and the source and beam solid angles Ω_s and Ω_b via

$$S_{\rm total} = S_{\rm peak} \left(\frac{\Omega_s + \Omega_b}{\Omega_b} \right). \tag{4.1}$$

However, the source profiles are not always well fitted by Gaussians, neither are they clearly resolved along all axes (see Section 4.3).

An alternative method involves correcting for the oversampling of the flux in the map, and assumes that the beam is Gaussian while putting no constraints on the source morphology (Moore 1989). The oversampling factor is obtained as follows: consider a Gaussian beam of FWHM θ_b mapping a point source of flux density P, at a spatial sampling interval $x, y{=}\theta_b/K$. Then the total observed flux density from the map will

Table 4.7: Summary of the M83 observations.

Grid Offset (arcsec)[1]		RA, Dec. Offset (arcsec)[2]		800 μm flux density (Jy)[3]	Statistical error (Jy)[4]	Total error (Jy)[5]
15.0	22.5	−5.3	26.5	0.053	0.019	0.020
7.5	22.5	−10.6	21.2	0.025	0.021	0.021
0.0	22.5	−15.9	15.9	0.032	0.032	0.032
22.5	15.0	5.3	26.5	0.094	0.018	0.022
15.0	15.0	0.0	21.2	0.069	0.017	0.020
7.5	15.0	−5.3	15.9	0.089	0.010	0.018
0.0	15.0	−10.6	10.6	0.265	0.028	0.046
−7.5	15.0	−15.9	5.3	0.064	0.022	0.024
−15.0	15.0	−21.2	0.0	0.034	0.016	0.017
22.5	7.5	10.6	21.2	0.085	0.023	0.026
15.0	7.5	5.3	15.9	0.135	0.059	0.063
7.5	7.5	0.0	10.6	0.277	0.060	0.077
0.0	7.5	−5.3	5.3	0.440	0.020	0.061
−7.5	7.5	−10.6	0.0	0.233	0.016	0.035
−15.0	7.5	−15.9	−5.3	0.119	0.015	0.021
−22.5	7.5	−21.2	−10.6	0.045	0.016	0.018
22.5	0.0	15.9	15.9	0.092	0.044	0.046
15.0	0.0	10.6	10.6	0.317	0.054	0.068
7.5	0.0	5.3	5.3	0.276	0.025	0.044
0.0	0.0	0.0	0.0	0.457	0.010	0.055
−7.5	0.0	−5.3	−5.3	0.421	0.023	0.061
−15.0	0.0	−10.6	−10.6	0.179	0.021	0.031
−22.5	0.0	−15.9	−15.9	0.127	0.015	0.021
−30.0	0.0	−21.2	−21.2	0.079	0.030	0.032
22.5	−7.5	21.2	10.6	0.043	0.021	0.022
15.0	−7.5	15.9	5.3	0.073	0.015	0.018
7.5	−7.5	10.6	0.0	0.178	0.017	0.027
0.0	−7.5	5.3	−5.3	0.396	0.019	0.053
−7.5	−7.5	0.0	−10.6	0.287	0.024	0.046
−15.0	−7.5	−5.3	−15.9	0.215	0.026	0.040
−22.5	−7.5	−10.6	−21.2	0.138	0.029	0.037
15.0	−15.0	21.2	0.0	0.035	0.009	0.010
7.5	−15.0	15.9	−5.3	0.114	0.012	0.018
0.0	−15.0	10.6	−10.6	0.164	0.022	0.030
−7.5	−15.0	5.3	−15.9	0.194	0.024	0.036
−15.0	−15.0	0.0	−21.2	0.154	0.012	0.025
−22.5	−15.0	−5.3	−26.5	0.138	0.020	0.029
7.5	−22.5	21.2	−10.6	0.019	0.013	0.013
0.0	−22.5	15.9	−15.9	0.051	0.022	0.023
−7.5	−22.5	10.6	−21.2	0.048	0.023	0.024
−15.0	−22.5	5.3	−26.5	0.110	0.017	0.022
−22.5	−22.5	0.0	−31.8	0.084	0.031	0.033

(1) Offsets on a grid oriented along the CO bar (PA=45°), with respect to the map centre at RA 13^h 34^m 11.53^s, Dec. −29° 36′ 42.18″. (2) Offsets in RA, Dec., with respect to the map centre. (3) Flux in a 15.8″ beam. (4) Observational uncertainties. (5) Combination in quadrature of the observational uncertainties and calibration errors of ∼12–18% . There is an additional global error of ∼11% due to the scatter in the derived values of the flux density at the central position.

Table 4.8: Results of 450–1100 μm photometry.

Galaxy	1100 μm [a]	800 μm	450 μm
Maffei 2	0.18±0.02 Jy	0.61±0.07 Jy [b]	–
IC342	–	0.43±0.06 Jy [c]	3.5±1.4 Jy [d]
M83	0.14±0.02 Jy	0.46±0.05 Jy [b]	5.2±2.9 Jy [e]

(*a*) 18.5″ beam (65-mm aperture) diffraction limited. (*b*) 15.8″ beam (65-mm aperture). (*c*) 13.5″ beam. (*d*) 13″ beam (47-mm aperture). (*e*) 17.7″ beam (65-mm aperture).

be

$$F_{\rm total} = \sum_m \sum_n P \exp\left\{-4\ln 2 \left[\left(\frac{nx}{\theta_{\rm b}}\right)^2 + \left(\frac{my}{\theta_{\rm b}}\right)^2\right]\right\} = A\ P.$$

The true flux is then obtained by dividing the total measured flux by the oversampling factor A. For example, for K=2 (fully sampled), A=4.51 (Moore 1989). The integrated flux in the 800 μm maps is then obtained by simply adding up all the pixels in the map and dividing by the appropriate oversampling factor. The two methods agree very well, except in the case of Maffei 2 where the integrated flux as calculated from the former method is about 40% higher than that derived from the oversampling algorithm. The noise level in the Maffei 2 map is quite high, which may partially explain the discrepancy, and errors in the Az–El/RA–Dec. transformation may also contribute.

To obtain the integrated flux at the other wavelengths, it is assumed that the ratio (peak flux density)/(total flux density) is independent of wavelength. For IC342, the 450 and 800 μm fluxes were observed with the same beamsize (13″). In the case of M83 and Maffei 2, the 800 μm photometry and mapping were performed with a 15.8″ beam while the observations at 450 and 1100 μm have $\simeq$18″ resolution. The 800 μm peak fluxes were therefore smoothed into an 18″ beam [by convolving with a Gaussian weighting of FWHM $(18^2–15.8^2)^{1/2}$ $\sim$9″] before taking the ratio of (peak flux)/(total flux).

The derived integrated fluxes at 450, 800 and 1100 μm are presented in Table 4.9. In Tables 4.10, 4.11 and 4.12, published continuum fluxes at wavelengths from the

Table 4.9: Integrated 450–1100 μm fluxes (Jy).

Wavelength	Maffei 2	IC342	M83
450 μm [a]	–	3.5±1.4 [b]	5.2±2.9 [c]
800 μm [a]	0.61±0.07 [d]	0.43±0.04 [e]	0.46±0.05 [d]
1100 μm [a,f]	0.18±0.02	–	0.14±0.02
800 μm [g]	0.72±0.08	–	0.56±0.06
800 μm (integrated)	1.5±0.2	1.07±0.12	1.2±0.3
1100 μm (integrated)	0.38±0.08	–	0.29±0.09
450 μm (integrated)	–	8.7±3.7	10.9±6.8

(*a*) Observed peak flux density (Jy). (*b*) In a 13″ beam. (*c*) In a 17.7″ beam. (*d*) In a 15.8″ beam. (*e*) In a 13.5″ beam. (*f*) In an 18.5″ beam. (*g*) In an 18″ beam.

mid-infrared to centimetre radio are summarized for the three galaxies.

4.2.5 Contamination of thermal fluxes

Before combining the long-wavelength data with far-infrared measurements to fit a dust temperature, it is necessary to consider the possible contamination of the pure submillimetre thermal dust fluxes by emission from other processes.

Radio continuum emission

Radio continuum emission from galaxies is composed of two components, both with a power-law spectrum of the form $S(\nu) \propto \nu^{-\alpha}$. Non-thermal synchrotron emission from supernova remnants usually has $\alpha \sim 0.5$–0.8 and drops off quite fast into the millimetre region. Thermal free–free emission, on the other hand, can have a spectral index as low as $\alpha = 0.1$, and can make a significant contribution at millimetre wavelengths. For

Table 4.10: Published infrared to radio fluxes for IC342.

Wavelength	Flux density (Jy)	Remarks	Reference
10 μm	1.62±0.3	18″ beam	1
12 μm	3.8	*IRAS* flux	2
20 μm	6.17±1.4	18″ beam	1
25 μm	18.76	*IRAS* flux	2
40 μm	41±4	50″ beam	3
50 μm	71±7	50″ beam	3
50 μm	75±15	60″ beam	1
60 μm	85.15	*IRAS* flux	2
100 μm	125.97	*IRAS* flux	2
100 μm	140±30	60″ beam	1
100 μm	101±3	50″ beam	3
160 μm	75±8	50″ beam	3
200 μm	<300 (3σ)	60″ beam	1
1 mm	<8 (3σ)	55″ beam	4
1.3 mm	0.25±0.15	33″ beam	5
2.8 cm	0.066±0.004	nuclear region	6
6 cm	0.08±0.01	central source	1
6 cm	0.094±0.01	central source	6
6.3 cm	0.096±0.06	nuclear region	7
11 cm	0.10±0.01	central source	1
21.2 cm	0.18±0.018	central source	6
49 cm	0.275±0.03	central source	7
91.7 cm	0.332±0.03	central source	6

References: (1) Becklin *et al.* 1980; (2) *IRAS* Point Source Catalogue; (3) Rickard & Harvey 1984; (4) Elias *et al.* 1978; (5) Thronson *et al.* 1987; (6) Hummel & Gräve 1990; (7) Gräve & Beck 1988.

example, Carlstrom & Kronberg (1991) estimate that the 3.3-mm flux from the centre of the starburst galaxy M82 is almost entirely free–free. Published radio fluxes for the central regions of Maffei 2, M83 and IC342 are included in Tables 4.10–4.12. Several authors have attempted to separate the thermal and non-thermal components of the radio emission and determine spectral indices.

Turner & Ho (1983) observed IC342 at 2 and 6 cm. They adopted a free–free spectral index of α=0.1 and a non-thermal spectral index of 0.6, concluding that, by 2 cm, all of the emission is thermal. Extrapolating their 2-cm flux of 38 mJy (nuclear region) with α=0.1 gives a free–free contribution to the integrated 800 μm flux density of just 0.03 Jy.

Table 4.11: Published infrared to radio fluxes for Maffei 2.

Wavelength	Flux density (Jy)	Remarks	Reference
10 μm	1.06	central $\sim$15″	1
12 μm	3.63	*IRAS* flux	2
25 μm	9.27	*IRAS* flux	2
40 μm	29.3±3.5	50″ beam	3
50 μm	58±44	50″ beam	3
60 μm	92.96	*IRAS* flux	2
100 μm	224.83	*IRAS* flux	2
100 μm	85.3±5.8	50″ beam	3
100 μm	70	30″ beam	4
160 μm	97.7±8.7	50″ beam	3
3.7 cm	0.067±0.01	central source	5
6 cm	0.07	central source	1
11.1 cm	0.120±0.007	central source	5
21 cm	0.21±0.01	central source	6

References: (1) Ho *et al.* 1989. (2) *IRAS* Point Source Catalogue; (3) Rickard & Harvey 1984; (4) Sellgren *et al.* 1978; (5) Seaquist *et al.* 1976; (6) Allen & Raimond 1972;

Sukumar *et al.* (1987) observed M83 at 91.7, 20.5 and 6.1 cm, deriving α (non-thermal)=0.8 and a thermal fraction of 21% at 6.1 cm. A 6.1-cm flux density of 141.7 mJy and adopted α (thermal)=0.1 gives 1100 μm flux densities of 0.005 Jy (synchrotron) and 0.02 Jy (free–free), less at 800 μm. Even if the free–free spectrum were completely flat, the contamination at 1100 μm would be only 0.03 Jy – less than the error of the 1100 μm photometry.

Ho *et al.* (1989) observed Maffei 2 at 2 and 6 cm, and derived thermal and non-thermal fluxes of 20 and 70 mJy respectively, leading to contributions of $\leq$0.01 Jy at 1100 μm.

It is clear from the above that contamination from either thermal or non-thermal radio continuum processes is negligible at millimetre and submillimetre wavelengths, at least for $\lambda \leq$1100 μm, in these sources.

Molecular line emission

The situation as regards contamination by molecular line emission needs careful consideration. It is usually assumed by Galactic observers that the contribution to the

Table 4.12: Published infrared to radio fluxes for M83.

Wavelength	Flux density (Jy)	Remarks	Reference
10 μm	2.6±0.3	20″ beam	1
10.8 μm	3.3±0.2	central ~20″	2
12 μm	4.72	*IRAS* flux	3
25 μm	19.61	*IRAS* flux	3
33 μm	28±9	50″ × 28″ beam	4
60 μm	103.25	*IRAS* flux	3
83 μm	131±26	30″ beam	4
100 μm	212.05	*IRAS* flux	3
100 μm	110	central source	5
540 μm	14±6	83″ beam	6
6.1 cm	0.142±0.002	central 55″ × 35″	7
20.5 cm	0.210±0.010	central source	7
91.7 cm	0.471±0.009	central source	7

References: (1) Rieke 1976; (2) Telesco *et al.* 1987; (3) *IRAS* Point Source Catalogue; (4) Telesco & Harper 1980; (5) Smith *et al.* 1990; (6) Hildebrand *et al.* 1977; (7) Sukumar *et al.* 1987.

continuum flux density from molecular line emission is negligible, as Galactic molecular lines are very narrow [although some recent observations have suggested that a significant fraction of the millimetre-wave continuum from warm, dense star-forming regions such as Orion may arise from a 'forest' of molecular lines (Sutton *et al.* 1984)]. With extragalactic observations, the situation is reversed – most molecular isotopes and species are far too weak to contribute much flux, but those that are detected, such as the ^{12}CO low-J transitions, have such wide line profiles ($\leq$200 km s^{-1} FWHM) that their contribution to the continuum fluxes should be carefully investigated.

The only transitions that shall be considered here are those of ^{12}CO. The J=6–5 line lies near the centre of the 450 μm filter. So far, this transition has been detected in only one extragalactic source, M82 (Wild 1990). In this object, the contribution from the molecular line to the 450 μm flux is negligible (Chapter 3). The ^{12}CO J=2–1 transition lies at the very edge of the 1100 μm filter, and the ^{12}CO J=3–2 line occurs at about the 50% transmission level of the 800 μm filter (Duncan *et al.* 1990). It is therefore important to estimate the contributions that these lines will make to the 800 and 1100 μm fluxes.

The contribution to the continuum flux density from a spectral line of peak main-

beam brightness temperature $T_{\rm mb}$ is (Appendix B):

$$S(\nu)_{\rm cont} = \frac{2k\Omega_{\rm b}}{B} \left(\frac{\nu}{c}\right)^3 \int T_{\rm mb}\, dv, \tag{4.2}$$

where ν is the frequency of observation, $\Omega_{\rm b}$ the beam solid angle, B the bandwidth (in Hz) of the UKT14 filter, and the integral is performed over velocity.

^{12}CO J=2–1 emission has been mapped in Maffei 2 (Chapter 5), while the J=3–2 line has been observed in IC342 (Steppe *et al.* 1990; Wall & Jaffe 1990). To estimate the contribution of the J=2–1 line to the 1100 μm emission, the 13″ IRAM observations from Chapter 5 of this thesis can be used, although these will overestimate the contribution in an 18″ beam, due to the effects of beam dilution on the line strength. For the J=3–2 line in IC342, the observations of Wall & Jaffe (1990) can be used, since their observations were made with the JCMT.

The integrated intensity of the ^{12}CO J=2–1 line at the peak of the Maffei 2 map is ~270 K km s^{-1}. The bandwidth of UKT14 at 1100 μm is ~77 GHz. From equation (4.2), therefore, the estimated contribution to the 1100 μm flux density in a 13″ beam (3×10^{-9} sr) is $\leq$0.01 Jy, less than the error on the 1100 μm photometry. There are no published ^{12}CO J=2–1 observations of M83, so it shall be assumed that the relative contribution in this galaxy is similarly small.

Wall & Jaffe (1990) detected ^{12}CO J=3–2 emission from IC342 with the JCMT, in a 13″ beam. The integrated intensity varies from 139 K km s^{-1} at the map centre (which coincides with the continuum map origin) to ~40 K km s^{-1} at positions 20″ away. The filter width of UKT14 at 800 μm is ~100 GHz, resulting in an 800 μm flux density contamination of ~0.02 Jy at the map centre, falling to 0.007 Jy at the edges. Again, these fluxes are smaller than the errors on the 800 μm photometry (amounting to ~5% of the flux density at the map centre). In addition, neither the 2–1 nor the 3–2 lines occur at the peak of the UKT14 filter response functions, but towards the edges. There are no published J=3–2 observations of Maffei 2, but it shall be assumed, as for IC342, that the contamination level is very small.

4.3 Morphology of the dust emission

Because the dust continuum emission is optically thin, it is a useful tracer of the distribution of the molecular gas, as well as its mass, free from the effects of high optical depth which can restrict the usefulness of ^{12}CO. At the time of writing, very little extragalactic mapping has been carried out using the optically thinner ^{13}CO isotope, but in at least one case where data do exist, that of the starburst galaxy M82, the morphology of the ^{13}CO emission has differed markedly from that of the ^{12}CO, resembling far more the far-infrared/submillimetre structure, and indicating optical depth variation across the galaxy (Chapters 2 and 3; Loiseau *et al.* 1988, 1990).

In the following section, the morphology of the 800 μm emission in these three galaxies is discussed in relation to other tracers of the interstellar medium and star formation, particularly CO.

4.3.1 IC342

The 800 μm emission (Fig. 4.2) is concentrated in the central mapped $\sim$40″ region. There is some evidence, at the $\sim 6\sigma$ level, that emission continues beyond the confines of the map, at a position angle slightly east of north. A spur extends $\sim$10″ south-west of the map centre. On inspection of the individual pixels, however, the feature is seen to be due to a high flux density at (ΔRA, ΔDec.) = (−13,−6.5). Because of the way in which the map was made (point-by-point over four nights) this pixel was observed on a different night to its neighbours. Although the pixel-to-pixel calibration is believed to be good to 13%, it is perhaps risky to attach too much weight to the reality of this 'spur'.

To estimate the spatial extent of the emission, single Gaussian functions were fitted to the fluxes along slices in RA and Dec. through the map centre. These scans, together with the best-fitting Gaussians and the beam profile superimposed for comparison, are plotted in Fig. 4.3. The emission is clearly extended in RA, marginally so in Dec., with fitted FWHM (beam convolved with source) of 21.1″±0.8″ in RA (reduced χ^2=1.7) and 19.0″±0.8″ in Dec. (reduced χ^2=1.6), although the source profile appears flattened at the peak compared to a true Gaussian. Deconvolving a 13.5″ Gaussian beam gives a source size of 16.2″ (RA) and 13.4″ (Dec.). The peak of the emission is within 1″ of

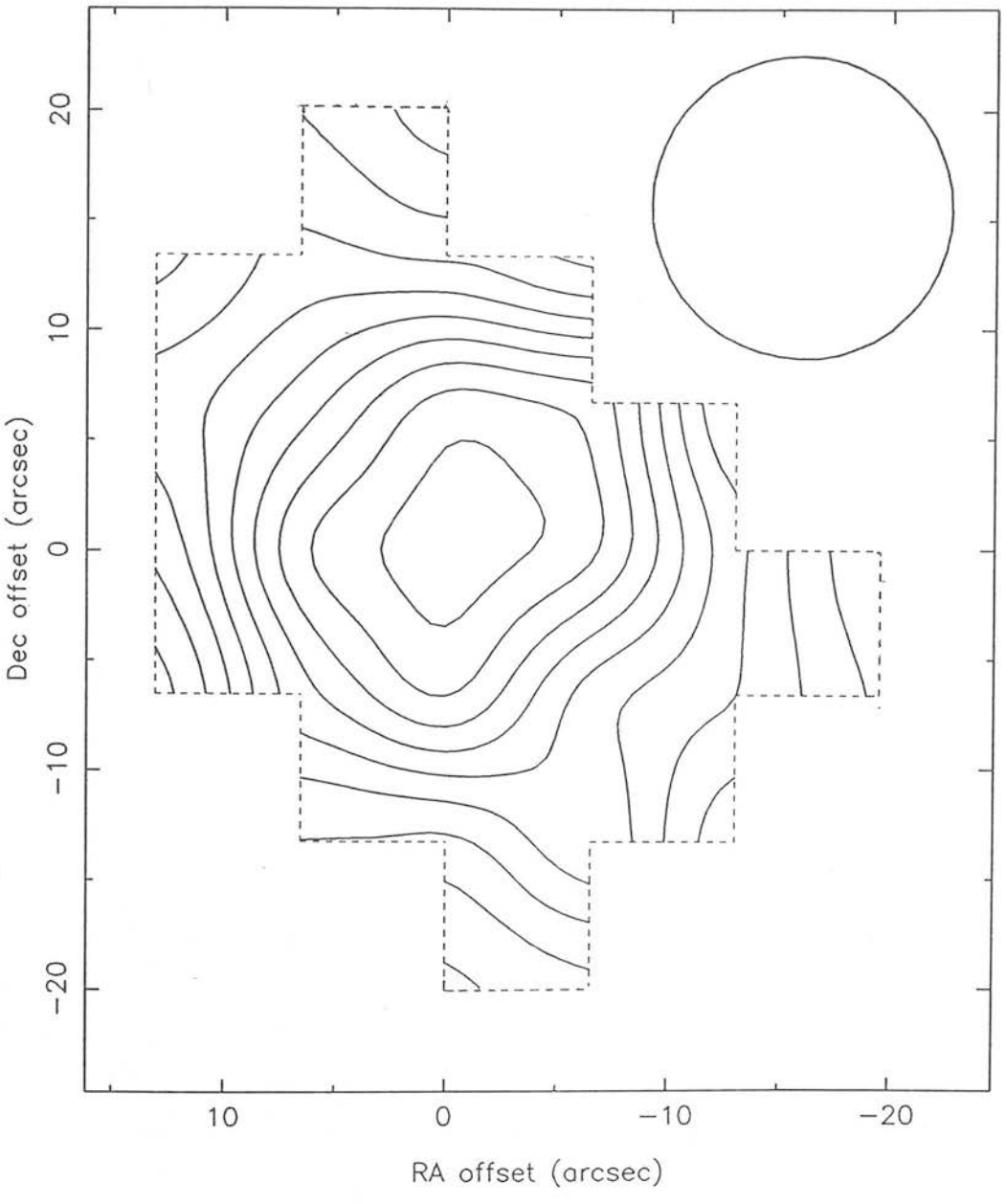

Figure 4.2: An 800 μm continuum map of the central $\sim 30'' \times 40''$ of IC342, with 13.5″ resolution. The contours are spaced at 1σ intervals from a 1σ base level of 0.04 Jy/beam (1σ = average observational+calibration error over map). Offsets are in RA, Dec. (arcsec) from the map centre at RA(1950) = $03^{h}\ 41^{m}\ 57.2^{s}$, Dec.(1950) = $+67°\ 56'\ 27''$. The dashed line shows the extent of the mapped area, while the beamsize is represented by a circle.

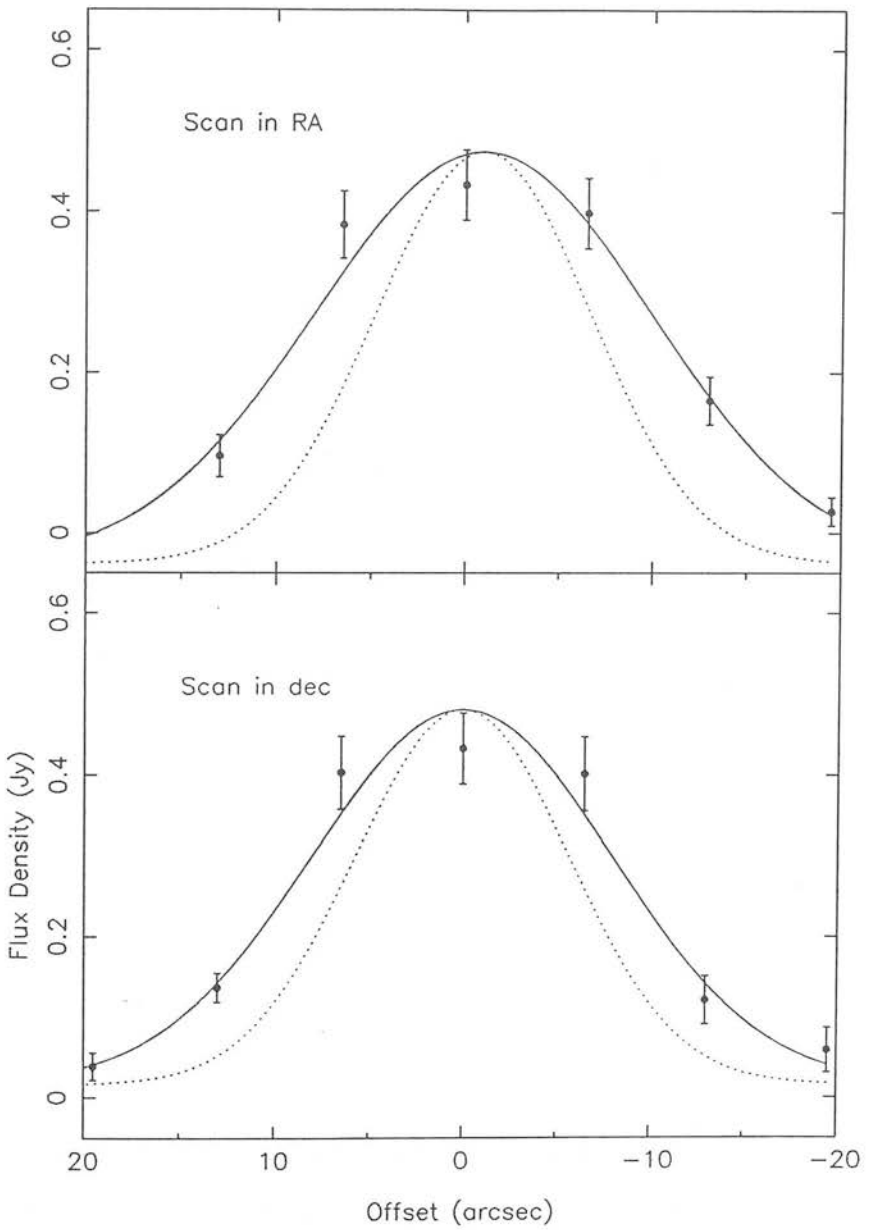

Figure 4.3: Scans in RA and Dec. taken from the IC342 800 μm map in Fig. 4.2. The map pixels are represented by filled circles, with error bars including both the observational and calibration uncertainties. The 13.5″ beam profile, assumed Gaussian, is shown by a dotted line. Also shown are the best-fitting single Gaussian functions through the data points, with FWHM (beam convolved with source) of 21.1″ and 19.0″ in RA and Dec., respectively.

the map centre, the near-infrared peak (Becklin *et al.* 1980).

In Fig. 4.4, the 800 μm map is compared to the morphology of ^{12}CO J=1–0 (Ishizuki *et al.* 1990), ^{12}CO and ^{13}CO J=2–1 (Eckart *et al.* 1990) and 21-cm radio continuum (Condon *et al.* 1982). The 800 μm emission is generally spatially coincident with these other tracers of star formation in the central $\sim$40″ . The suggestion in the 800 μm map of low-level emission extended to the east of north is consistent with the position angle of the ^{13}CO emission. The source sizes of CO and dust are similar in RA [Eckart *et al.* (1990) quote $\leq$13″ perpendicular to the bar, whereas the corresponding dimension in dust is $\sim$16″$\pm$1″]. However, while no strong extension is seen *along* the bar (apart from the suggestion of low-level emission), the CO is clearly extended north–south (size $\sim$30″, Eckart *et al.* 1990). The flux of optically thin dust emission is given by (Section 1.3) $F(\nu) \propto N(\mathrm{H_2})B(\nu, T_\mathrm{d}) \propto N(\mathrm{H_2})T_\mathrm{d}$ at 800 μm, which is almost on the Rayleigh–Jeans tail for dust temperatures T_d >20 K. One possible explanation is that a drop in the average dust temperature away from the nucleus has caused a reduction in continuum flux. Indeed, non-LTE modelling of the ^{12}CO and ^{13}CO line ratios by Eckart *et al.* (1990) implies that the gas temperature drops from $\geq$30 K at the centre to $\sim$13 K at distances greater than 20″ north and south of the nucleus. As further evidence of a temperature decrease away from the nucleus, the ^{12}CO J=3–2 emission, which probably traces warmer gas than the J=1–0, is slightly more confined than the 1–0 with an extent of $\sim$22″ in the north–south direction (Steppe *et al.* 1990). The ^{12}CO 2–1 and ammonia transitions are also somewhat more concentrated than the ^{12}CO 1–0 (Eckart *et al.* 1990; Ho *et al.* 1990). The modelling of Eckart *et al.* implies that the density of the molecular gas traced by CO stays fairly constant at a few $\times$ 10^3 molecules cm^{-3}. However, this does not rule out the presence of denser gas to which the CO will not be sensitive but the dust, being optically thin, will. The presence of dense gas in the central $\sim$30″ of the galaxy is supported by the detection and mapping of CS J=2–1 emission there (Mauersberger & Henkel 1989).

4.3.2 M83

Like IC342, the 800 μm emission from M83 is concentrated in the central $\sim$50″ region covered by the map (Fig. 4.5). An apparent feature extending $\sim$15″ north-east along the bar is caused by a high flux density in a single pixel, and, as in the case of IC342,

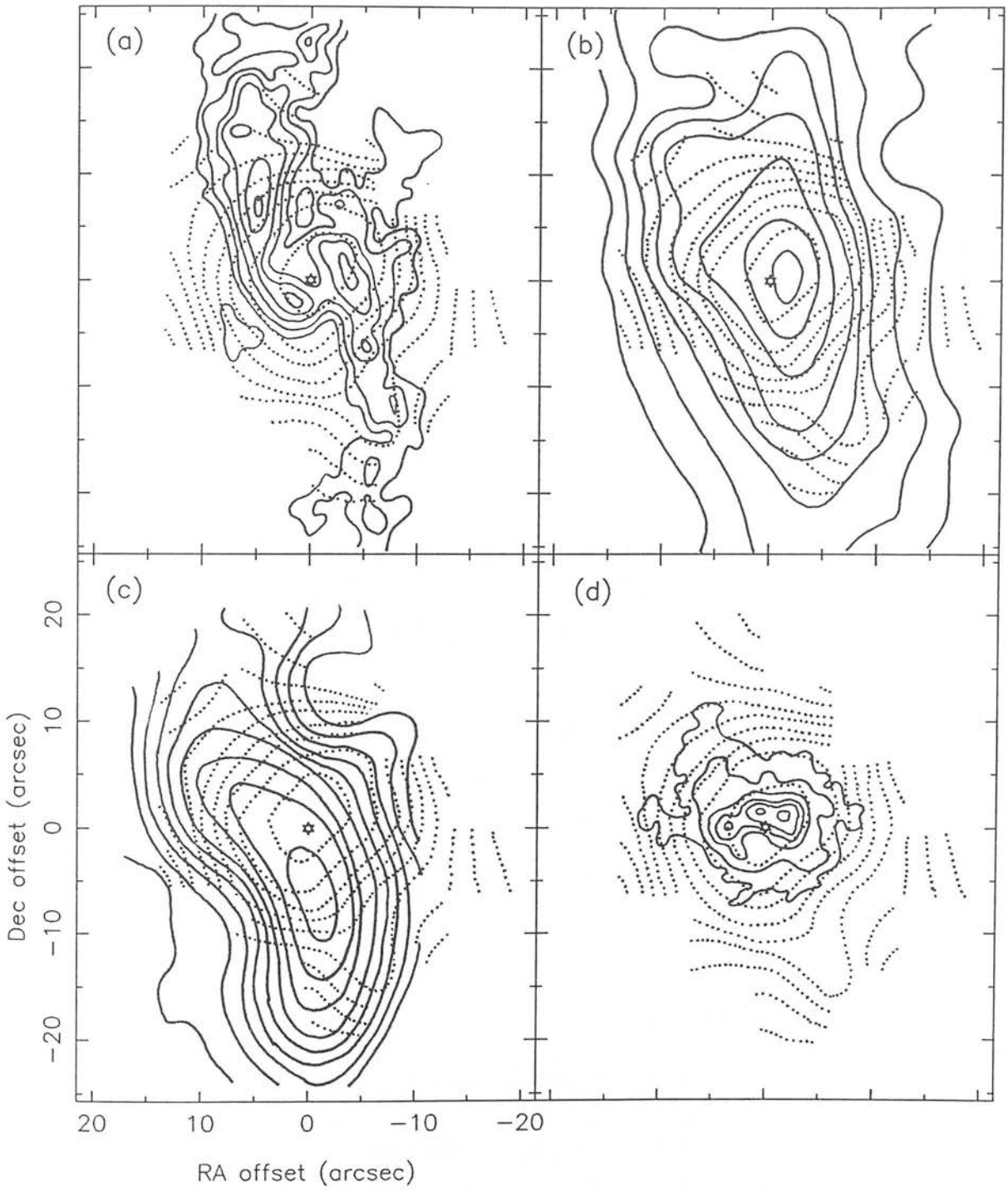

Figure 4.4: The 800 μm contour map of IC342 compared with the morphology as seen in other star-formation tracers: (a) ^{12}CO J=1–0 (Ishizuki *et al.* 1990); (b) ^{12}CO J=2–1 and (c) ^{13}CO J=2–1 (Eckart *et al.* 1990); (d) 21-cm radio continuum (Condon *et al.* 1982). In each case, the 800 μm map is represented by dotted contours. Offsets are in RA, Dec. with respect to the 800 μm map centre, marked by a star.

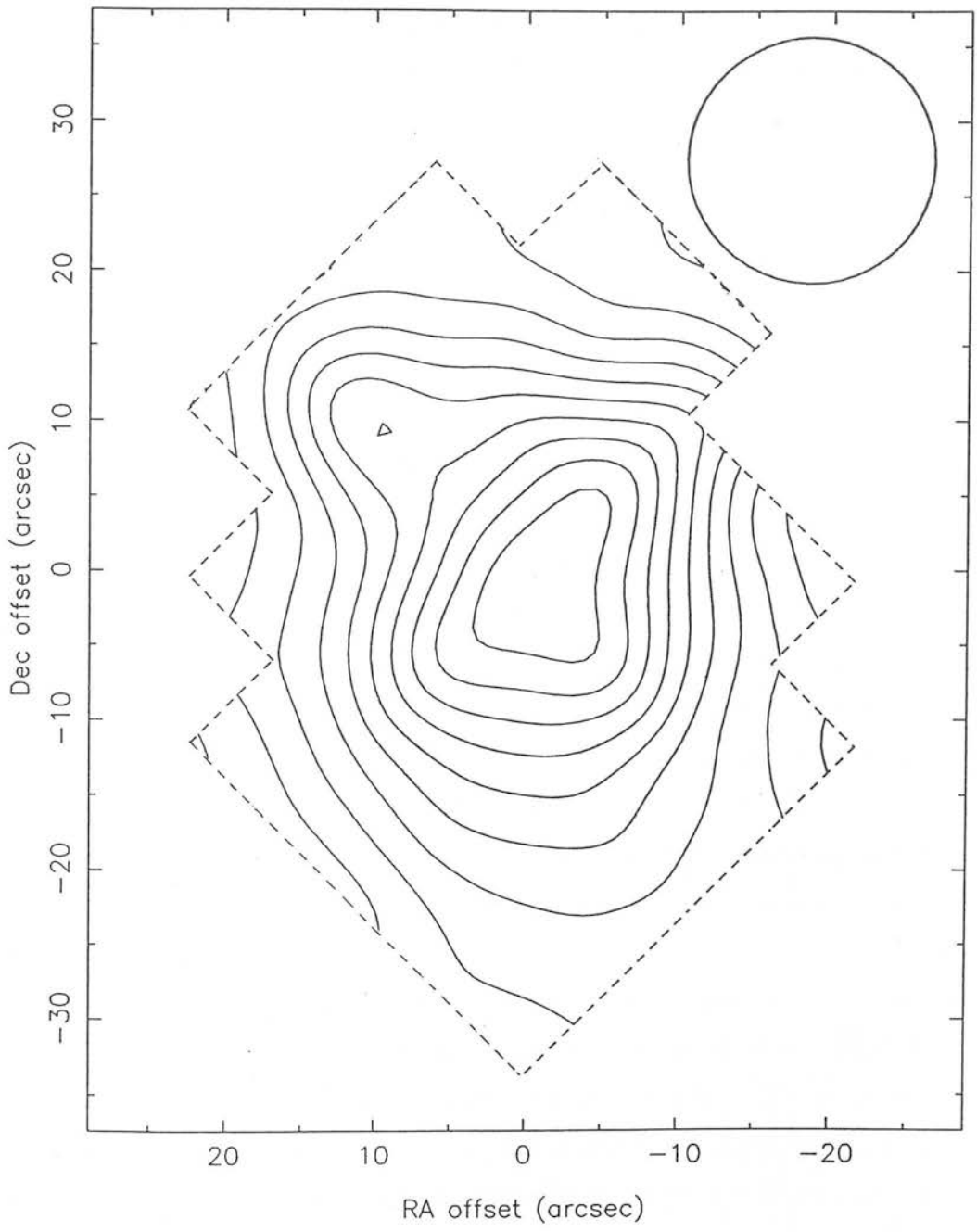

Figure 4.5: An 800 μm continuum map of the central ~38″ × 30″ of M83, with 15.8″ resolution. The contours are spaced at 1σ intervals from a 1σ base level of 0.04 Jy/beam (1σ = average observational+calibration error over map). Offsets are in arcsec, along the major and minor axes of the bar (PA=45°), with respect to the map centre at RA(1950) = $13^h\ 34^m\ 11.53^s$, Dec.(1950) = −29° 36′ 42.18″. The dashed line shows the extent of the mapped area, while the beamsize is represented by a circle.

too much reliance should not be placed on it. It is interesting to note, however, that in a ^{12}CO J=1–0 Nobeyama map of M83 at the same 16″ resolution, published in conference proceedings (Sofue *et al.* 1987) there is indeed a secondary peak of emission ∼15″ from the map centre, although it is not as obvious in the final published version of the map (Handa *et al.* 1990).

Gaussian functions were fitted to slices along the major and minor axes of the bar (PA=45°). The fluxes used in the fit are plotted in Fig. 4.6, along with the best-fitting Gaussians and the beam profile. It is interesting that the emission appears slightly more extended perpendicular to the bar, rather than parallel to it as might be expected. In the perpendicular direction, the fitted FWHM (beam–source convolved) is 28.4″±1.2″ (reduced χ^2=1.9), while along the bar, FWHM = 21.6″±1.9″ (reduced χ^2=1.0). Deconvolving the 15.8″ beam then gives source sizes $\theta_{\rm major}$=14.7″, $\theta_{\rm minor}$=23.6″. The peak of the emission is within an arcsecond of the centre of the map.

Smith, Lester & Harvey (1990) have made observations of M83 at 100 μm with the Kuiper Airborne Observatory, and obtain a source size for the far-infrared emission of 18″–19″ (deconvolved). Considering the asymmetry of the 800 μm map, the differing resolutions of the two sets of observations and the fact that Smith *et al.* used slightly different scan directions, this source size is completely consistent with that derived at 800 μm. As in the 800 μm map, Smith *et al.* note a slight asymmetry in their data consistent with the secondary feature seen in the preliminary Nobeyama CO map of Sofue *et al.* (1987).

In Fig. 4.7 the 800 μm map is compared to the morphology at ^{12}CO J=1–0 (Handa *et al.* 1989), 10 μm (Telesco *et al.* 1987), Hα (de Vaucouleurs *et al.* 1983), and 6-cm radio continuum (Cowan & Branch 1985). The dust emission is spatially consistent with all these star formation tracers. As in the case of IC342, the 800 μm emission does not display the same extent along the major axis as does the CO. However, Sofue *et al.* (1987) and Handa *et al.* (1989) note that the CO emission is strongly concentrated in the central ∼20″, with some 40% of the total emission falling within the boundaries of the 800 μm map. The central concentration was partially resolved by their 16″ beam. If there is dust emission associated with the more extended low-level structure apparent in the CO map, it is too faint to be detected in a short UKT14 integration. There are very little molecular line data apart from the ^{12}CO J=1–0 map of M83, due to

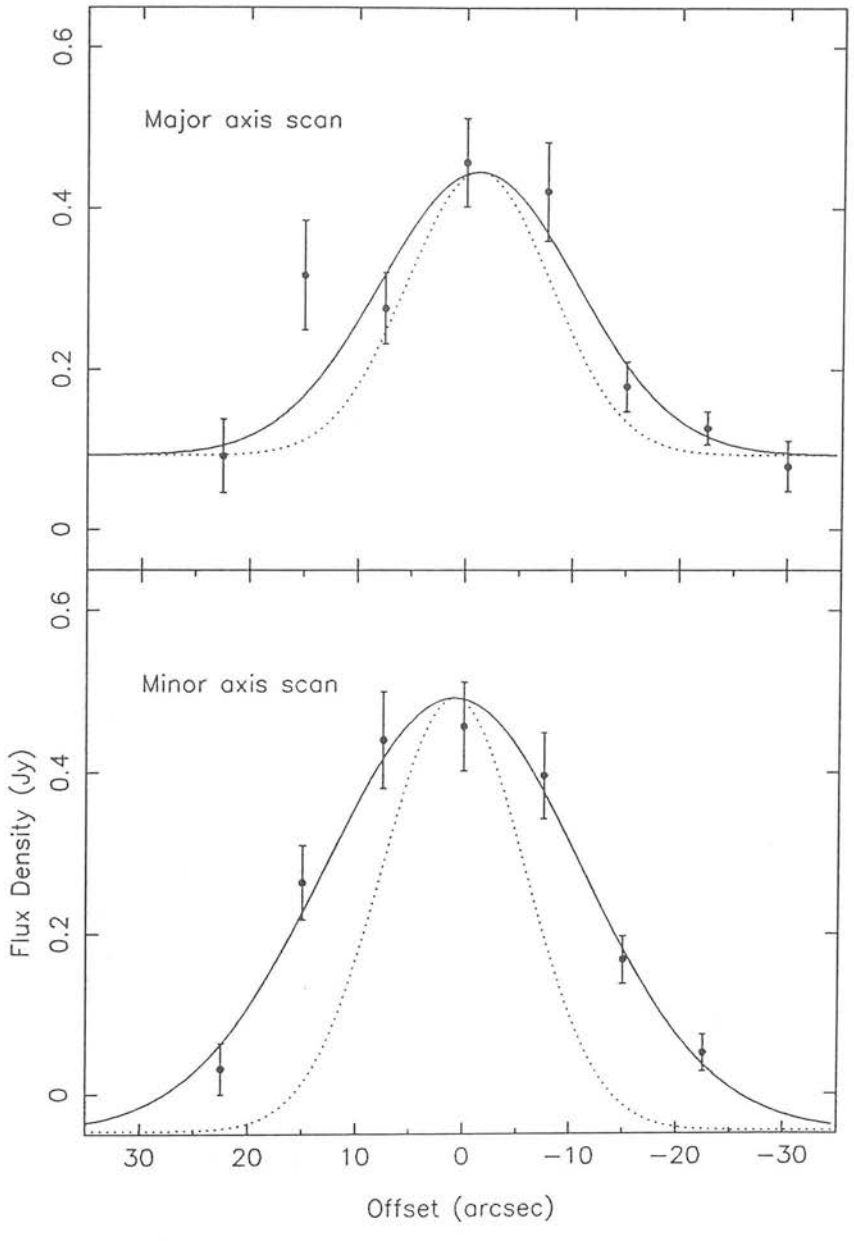

Figure 4.6: Scans along the major and minor axes of the M83 bar, taken from the 800 μm map in Fig. 4.5. The map pixels are represented by filled circles, with error bars including both the observational and calibration uncertainties. The 15.8″ beam profile, assumed Gaussian, is shown by a dotted line. Also shown are the best-fitting single Gaussian functions through the data points, with FWHM (beam convolved with source) of 21.6″ along the major axis and 28.4″ along the minor axis.

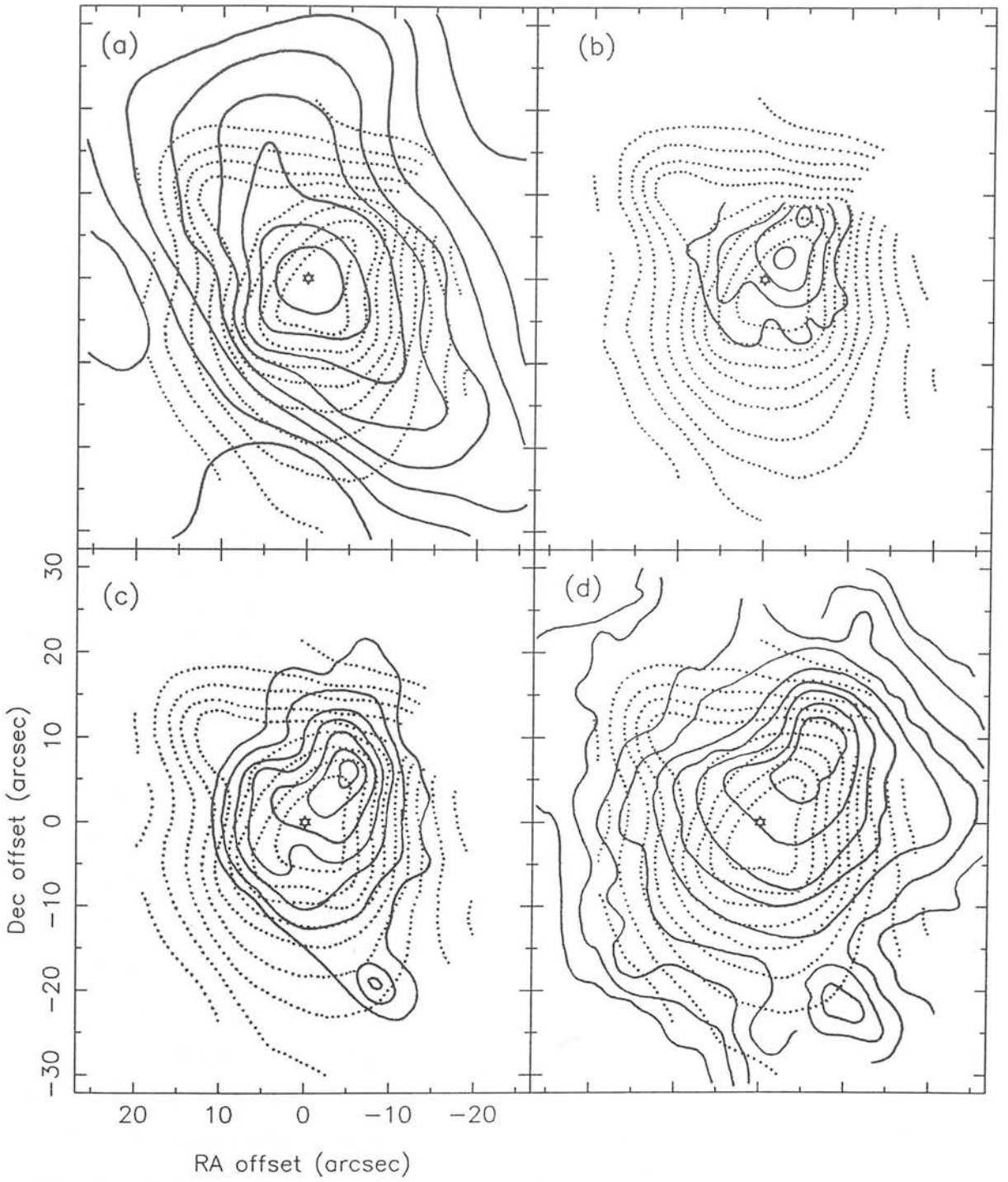

Figure 4.7: The 800 μm contour map of M83 compared with the morphology as seen in other star-formation tracers: (a) ^{12}CO J=1–0 (Handa *et al.* 1990); (b) 10 μm continuum (Telesco *et al.* 1987); (c) 6-cm radio continuum (Cowan & Branch 1985); (d) Hα line (de Vaucouleurs *et al.* 1983). In each case, the 800 μm map is represented by dotted contours. Offsets are in RA, Dec. with respect to the 800 μm map centre, marked by a star.

its very low declination and resulting inaccessibility to many of the large millimetre-wave telescopes, such as IRAM, so there has been no published attempt to evaluate the variation of excitation conditions across the nucleus although it is likely that such gradients will exist.

4.3.3 Maffei 2

The 800 μm emission from Maffei 2 (Fig. 4.8) is clearly extended along the major axis of the galaxy, at position angle $\sim$30°. The signal-to-noise ratio of the observations is quite low ($\sim 7.5\sigma$ at the peak) due to the relatively short integration time per point compared to the maps of IC342 and M83. The morphology of the final map, as well as the two maps of which the final map was composed, can be fitted by a two-dimensional Gaussian function at a position angle of 30°. The peak of the emission is within an arcsecond of the map centre, and the FWHM (beam convolved with source) is 36.5″±2.3″ along the major axis and 21.3″±1.1″ along the minor axis. The fitted parameters of the individual maps are consistent with each other and with the final map. Deconvolving a 15.8″ Gaussian beam from the fitted profiles leads to a final source size of 32.9″ × 14.3″.

In Fig. 4.9 the 800 μm map is compared to the morphology of ^{12}CO J=1–0 emission (Ishiguro *et al.* 1990), radio continuum (Seaquist *et al.* 1976), 10 μm continuum (Ho *et al.* 1989) and the Hα line (P. McCarthy, unpublished). Comparison with the ^{12}CO J=2–1 emission presented in Chapter 5 shows that the overall morphologies of the 800 μm map and the 13″-resolution ^{12}CO 2–1 map are in good agreement, and the source sizes as derived from the J=2–1 line and the 800 μm continuum are similar. Low-resolution ^{12}CO J=1–0 observations also give a major axis extent of about 33″ (Weliachew, Casoli & Combes 1988).

The CO interferometer map shows a narrow structure, interpreted as a molecular bar, with two peaks separated by $\sim$10″ – this was not resolved by the JCMT beam. As in the case of M83, the 10 μm emission is spatially more concentrated than the 800 μm, being confined to the central 8″ of Maffei 2 (Ho *et al.* 1989), but the overall shape is similar. The 3.7-cm radio continuum, which is predominantly non-thermal, is resolved into several discrete components at the nucleus of the galaxy – possibly powerful supernova remnants. The 10 μm emission arises largely from a much warmer

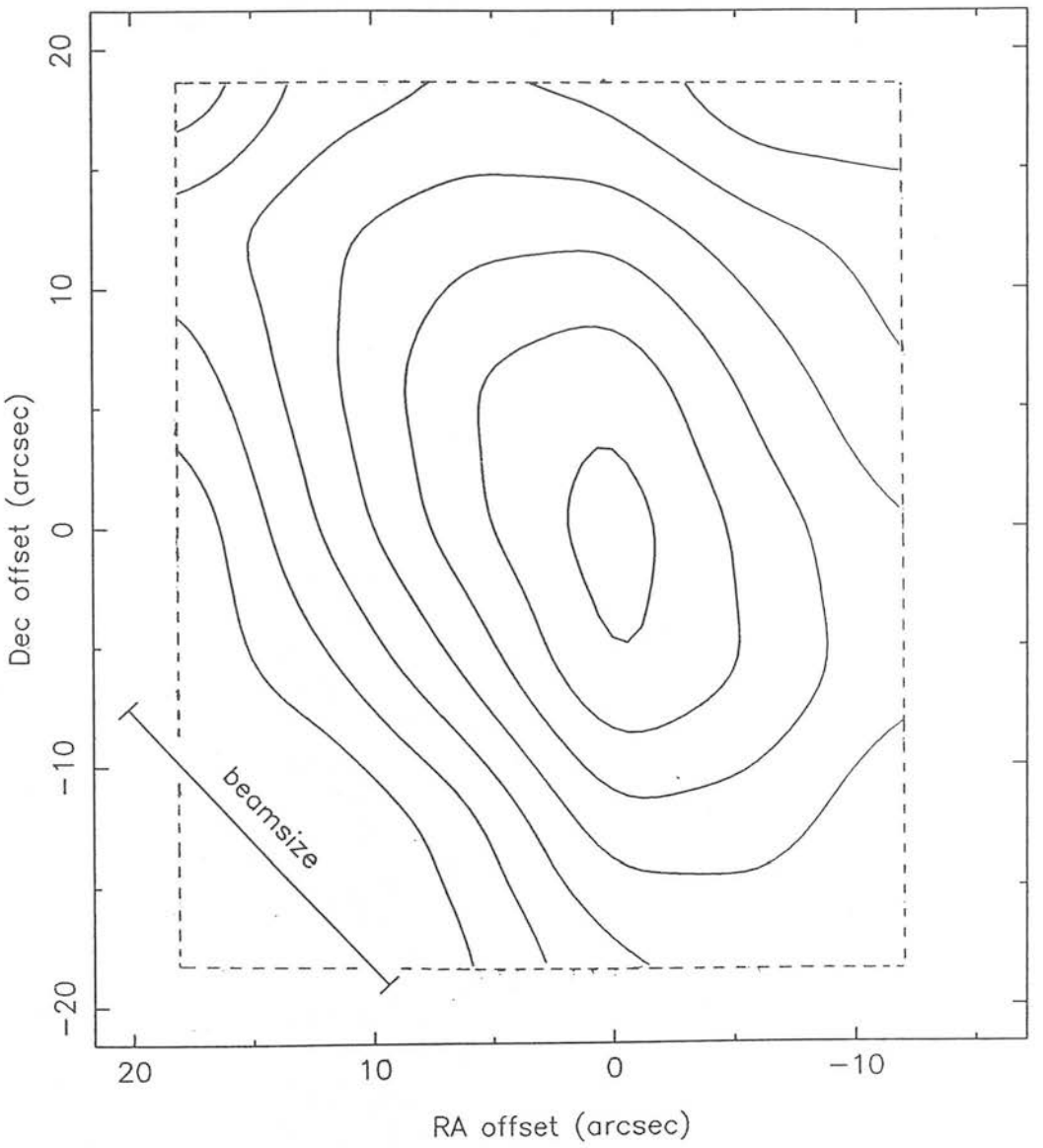

Figure 4.8: An 800 μm continuum map of the central $\sim 30'' \times 36''$ of Maffei 2, with 15.8″ resolution. The contours are spaced at 1σ intervals from a 1σ base level of 0.08 Jy/beam (1σ = average observational+calibration error over map). Offsets are in RA, Dec. (arcsec) from the map centre at RA(1950) = $02^{h}\ 38^{m}\ 08.5^{s}$, Dec.(1950) = $+59^{\circ}\ 23'\ 24''$. The dashed line shows the extent of the mapped area, while the beamwidth is represented by a solid line.

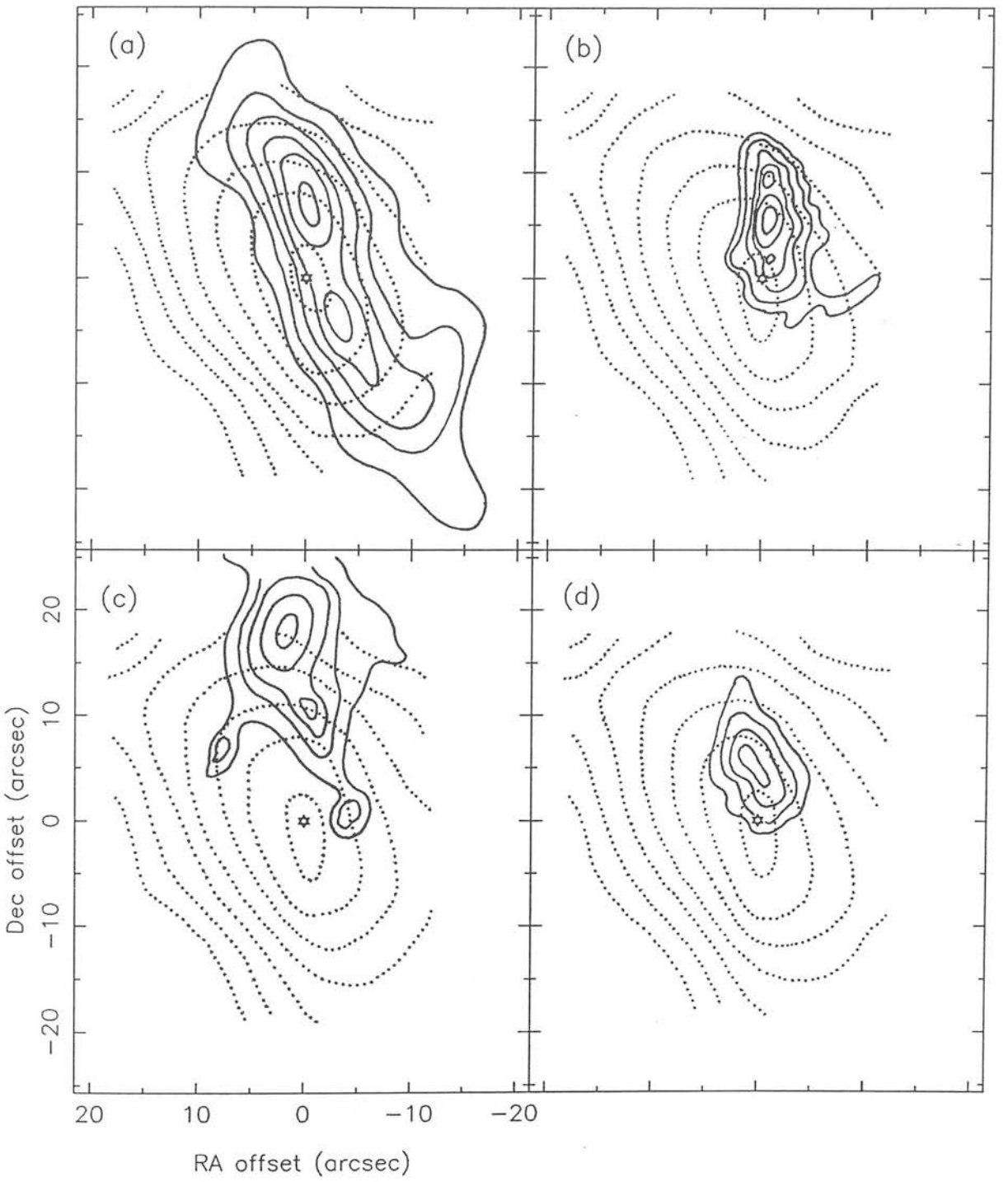

Figure 4.9: The 800 μm contour map of Maffei 2 compared with the morphology as seen in other star-formation tracers: (a) ^{12}CO J=1–0 (Ishiguro *et al.* 1989); (b) 3.7-cm radio continuum (Seaquist *et al.* 1976); (c) Hα line (McCarthy, unpublished); (d) 10 μm continuum (Ho *et al.* 1989). In each case, the 800 μm map is represented by dotted contours. Offsets are in RA, Dec. with respect to the 800 μm map centre, marked by a star.

(>100 K) component of the ISM than does the submillimetre flux. Its spatial similarity to the non-thermal radio continuum leads Ho *et al.* to suggest that the 10 μm flux arises mainly from small grains associated with massive stars and with the supernovae that are producing the radio emission. This explains the much closer spatial correlation between the 10 μm and radio flux than between the 10 and 800 μm continuum emission.

4.4 Dust temperature and molecular hydrogen mass

One of the chief motivations behind performing these observations is to obtain an estimate for the molecular gas mass present in the nuclear regions of these galaxies, by a method that is independent of the assumptions that govern the use of ^{12}CO as a mass tracer. In this way, we might hope to gain some insight into the reliability of the two methods when applied to regions of active star formation.

The molecular hydrogen mass is obtained from the observed submillimetre flux density by the method outlined in Section 1.3 (Hildebrand 1983; Gear 1988). The submillimetre continuum optical depth is found via

$$\tau(\nu) = 5.42 \times 10^{10} \frac{\theta_s^2 + \theta_b^2}{\theta_s^2 \theta_b^2} \frac{S(\nu)}{B(\nu, T_d)}, \tag{4.3}$$

[where θ_s and θ_b are the source and beam FWHM (arcsec), $S(\nu)$ the flux density per beam and $B(\nu, T_d)$ the Planck function for dust temperature T_d and frequency ν]. The hydrogen column density is

$$N(\mathrm{H} + \mathrm{H_2}) = 1.2 \times 10^{25} \left(\frac{750}{\nu}\right)^{\beta} \tau(\nu) \text{ atom cm}^{-2}, \tag{4.4}$$

leading to a gas mass

$$M(\mathrm{H} + \mathrm{H_2}) = 2.7 \times 10^{-19} N(\mathrm{H} + \mathrm{H_2}) (\theta_s D)^2 \ M_\odot, \tag{4.5}$$

with D the distance to the source in Mpc. This gives the total mass of hydrogen (atomic + molecular). In the centres of spiral galaxies the fraction of atomic hydrogen compared to molecular is generally very small (e.g. Young 1990). The uncertainties of this method [primarily the value of $N(\mathrm{H+H_2})/\tau(\nu)$] were discussed in Section 1.3. Assuming that the value of the conversion factor given by Hildebrand (1983) applies to the extragalactic interstellar medium, the remaining unknowns are the dust temperature

T_d and emissivity spectral index β. The value of β can be constrained, from observation and theory, to lie between 1 and 2, although its exact variation with wavelength is very uncertain (e.g. see the review by Helou 1989). The dust temperature is determined from a fit to the long-wavelength data. The JCMT photometry, at 450–1100 μm, is alone insufficient to determine T_d, since it lies approximately on the Rayleigh–Jeans tail of the dust emission, the slope of which is insensitive to temperature [$F(\nu) \propto \nu^{2+\beta}$]. The flux from a 30-K blackbody will peak at around 100 μm, therefore far-infrared data are needed to constrain a fit to T_d. At mid-infrared wavelengths (<30 μm), however, a significant fraction of the flux may arise from a hot (>100 K) component of dust in HII regions, and also from very small grains heated transiently by absorption of single photons (Leger & Puget 1984). Photometry at wavelengths shortward of about 30 μm should therefore not be used.

4.4.1 The far-infrared to radio spectrum

In Tables 4.10 to 4.12 are presented published flux densities for the central regions of the three target galaxies at wavelengths ranging from ~10 μm to ~90 cm. Most published far-infrared and submillimetre photometry has been done with quite large (30″–50″) beams. However, if the dust emission is confined to the region covered by the 800 μm JCMT maps, then it is reasonable to use these large-beam fluxes together with the integrated 800 μm intensities to fit source parameters. In the case of M83, for which 100 μm high-resolution spatial information exists (Smith *et al.* 1990), the far-infrared source size is consistent with that derived from the 800 μm map (Section 4.3). This does not, however, rule out the presence of more extended low-level emission, evidence of which lies in the fact that the *IRAS* 100 μm fluxes (beamsize ~3′–4′, Neugebauer *et al.* 1984) are up to a factor of 2 larger than those from 30″–50″ resolution photometry.

Fig. 4.10(a)–(c) shows the far-infrared to radio continuum spectra of the three galaxies, plotted from the data in Tables 4.10 to 4.12. The emission peaks at ~100 μm, consistent with blackbody emission from dust at ~30–40 K. The (thermal+non thermal) radio continuum emission drops off very quickly towards millimetre wavelengths, implying that its contribution to the dust emission is negligible (Section 4.2).

There are virtually no previous observations in the important millimetre and submillimetre wavelength range of the spectrum. The submillimetre observations presented

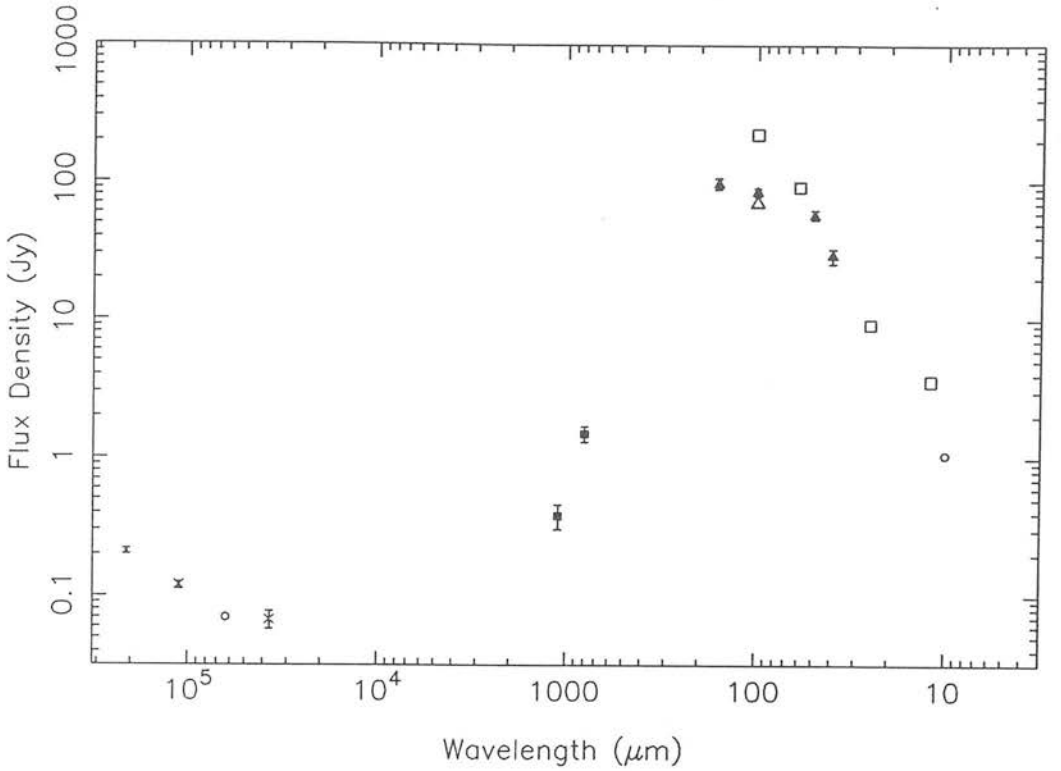

Figure 4.10: (a) The far-infrared to radio continuum spectrum of the central ~30″–40″ of Maffei 2. The data are taken from the literature as follows: open squares – *IRAS* Point Source Catalogue; filled triangles – Rickard & Harvey (1984); crosses – Seaquist *et al.* (1976); dots – Allen & Raimond (1972); open triangle – Sellgren *et al.* (1978); open circles – Ho *et al.* (1989); filled squares – this work.

here are therefore invaluable for determining the shape of the spectrum longward of 200 μm. In particular, the long-wavelength data can be used to check the suggestion (e.g. Devereux & Young 1990) that much of the dust mass of a galaxy may reside in relatively cool dust not traced by the *IRAS* fluxes, and consequently that using the *IRAS* data may result in underestimates of the total dust (and hence, gas) mass in the nuclear region.

4.4.2 Dust temperature and derived gas masses

To determine the temperature of the emitting dust, the spectrum should be fitted with a modified blackbody function of the form $\nu^\beta\, B(\nu, T_\mathrm{d})$ (Section 1.3). Only photometry longward of $\simeq$30 μm should be fitted, to avoid contamination by hot dust at mid-infrared wavelengths. For dust at a single temperature T_d, the flux density at frequency

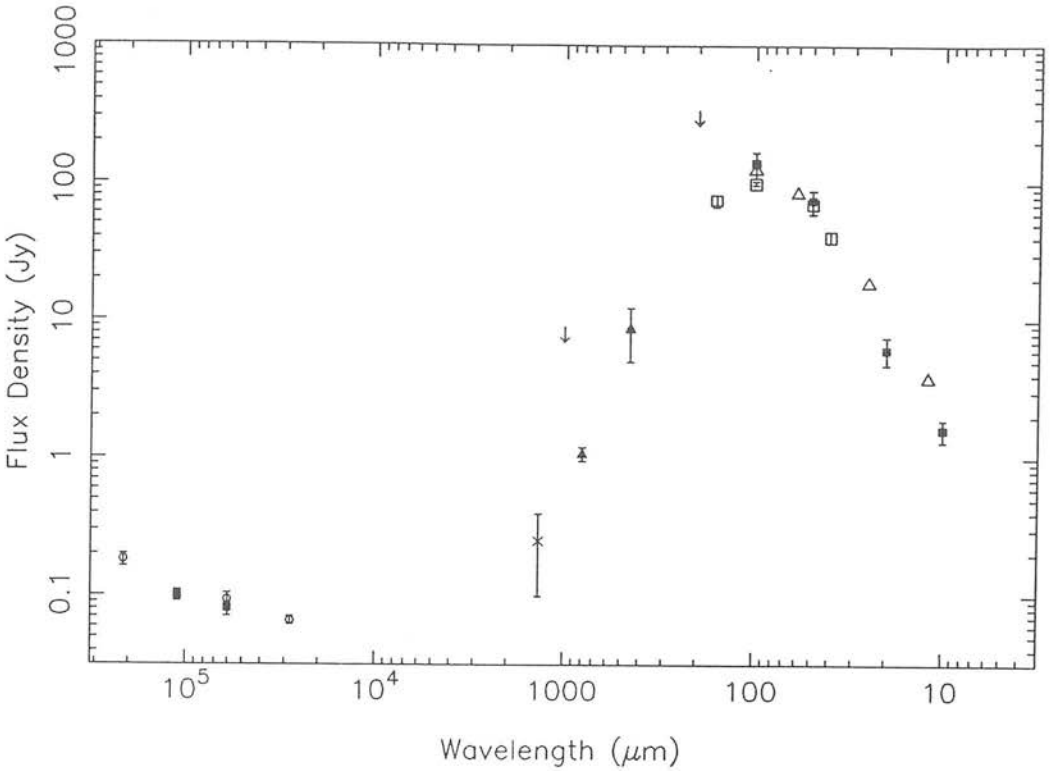

Figure 4.10: (b) The far-infrared to radio continuum spectrum of the central ~30″–40″ of IC342. Open triangles – *IRAS* Point Source Catalogue; open squares – Rickard & Harvey (1984); cross – Thronson *et al.* (1987); filled squares – Becklin *et al.* (1980); open circles – Hummel & Gräve (1990); filled triangles – this work.

ν is given by

$$S(\nu) = \frac{2h\nu^3}{c^2}\,\Omega_{\rm s}\,\left(e^{h\nu/kT_{\rm d}}-1\right)^{-1}\,\tau_0\,\left(\frac{\nu}{\nu_0}\right)^{\beta},$$

with β lying between 1 and 2 (e.g. Hildebrand 1983). As a first attempt at interpreting the submillimetre spectra of Maffei 2, M83 and IC342, the data were least-squares fitted to a single-temperature modified blackbody function of the form given above, with τ_0 the optical depth at ν_0=375 GHz (800 μm). The free parameters of the fit were $T_{\rm d}$ and $(\Omega_{\rm s}\tau_{800})$, with three possible values of β = 1.0, 1.5 and 2.0, spanning the range predicted by theoretical and observational work.

The best fits to the data for the three values of β are plotted in Fig. 4.11, and the parameters of the fits are summarized in Table 4.13. From Fig. 4.11 it is clear that only β=1.0 with corresponding dust temperature ~45 K comes close to fitting the data for any of the galaxies. Values of β >1.0 fail to predict the 450–1100 μm fluxes by factors

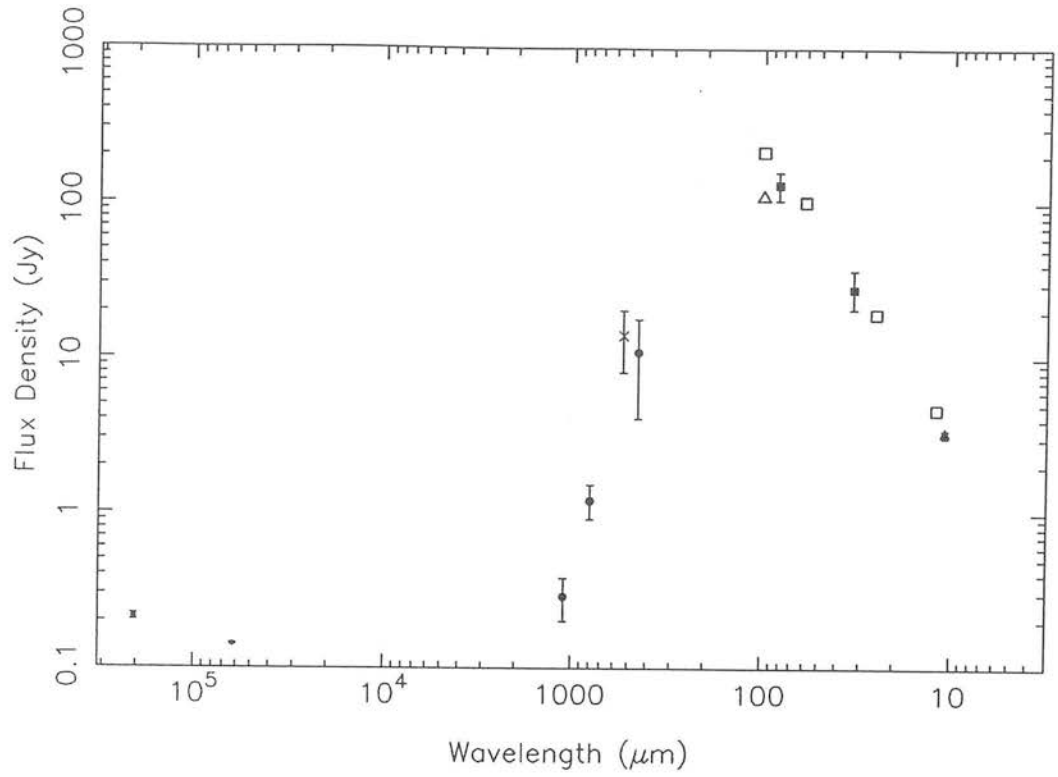

Figure 4.10: (c) The far-infrared to radio continuum spectrum of the central ~30″–40″ of M83. Open squares – *IRAS* Point Source Catalogue; filled triangle – Telesco *et al.* (1987); filled squares – Telesco & Harper (1980); open triangle – Smith *et al.* (1990); cross – Hildebrand *et al.* (1977); dots – Sukumar *et al.* (1987); filled circles – this work.

of ~2–6.

There is observational and theoretical evidence that β is not constant throughout the whole far-infrared to millimetre region, but that it steepens from ~1 at far-infrared wavelengths to ~2 by 1000 μm , although the exact form of the variation is uncertain (e.g. Hildebrand 1983). A single-temperature fit with varying β was therefore also attempted, using β=1 for $\lambda \leq$250 μm and β=2 for $\lambda >$250 μm, as suggested by Hildebrand (1983). The results of this fitting are presented in Fig. 4.12 and Table 4.13. Although the short-wavelength points are well fitted, once again the spectrum falls short of predicting the submillimetre fluxes by factors ~2–4. The agreement with the long-wavelength data would be better if the change of β from 1 to 2 occurred at a longer wavelength, say $\sim$ 600 μm . Only in the case of M83 does the single-temperature model give a reasonable fit, with $T_{\rm d} \simeq$ 36 K.

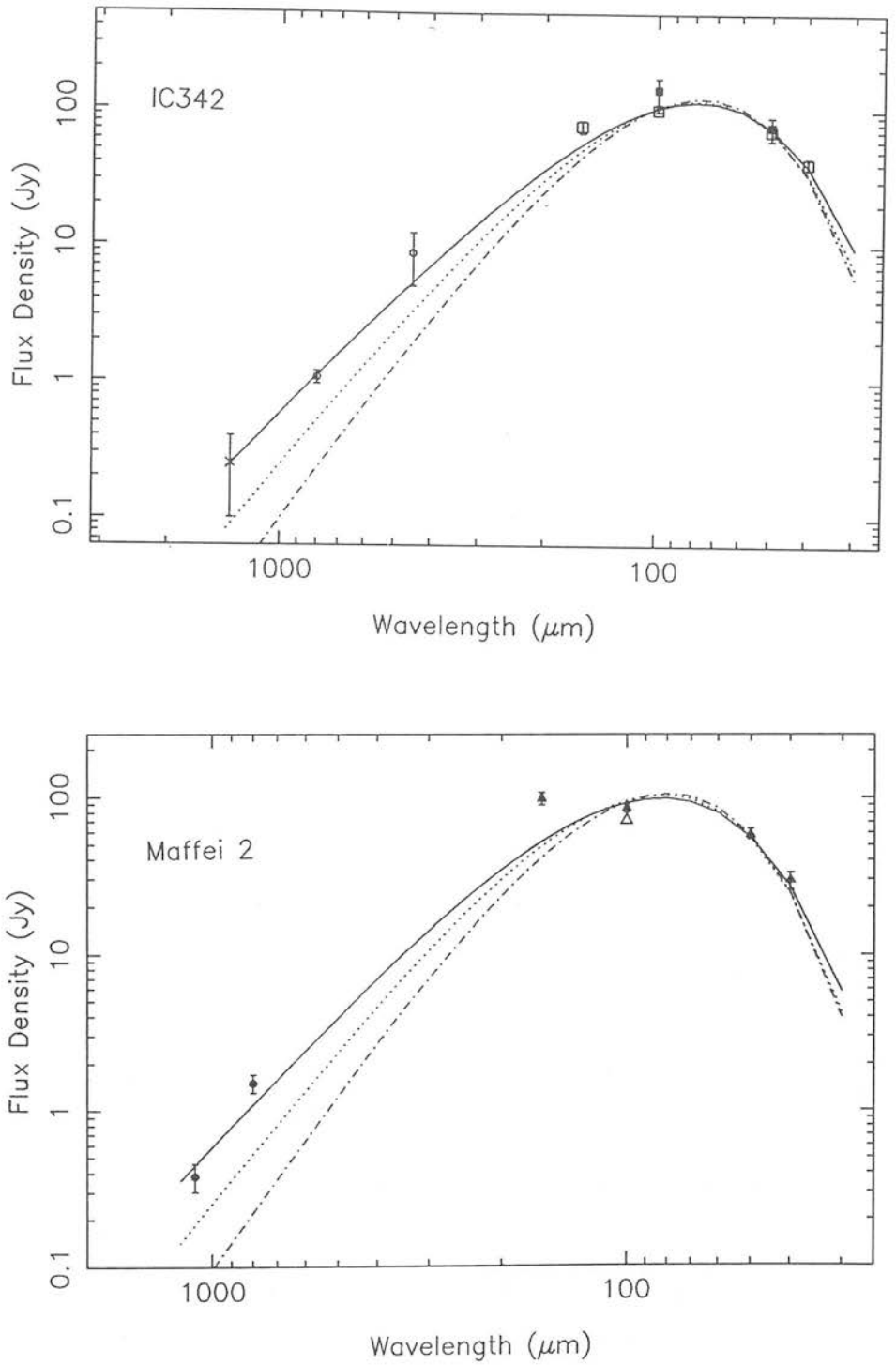

Figure 4.11: Single-temperature, modified blackbody fits to the 40–1100 μm spectra of IC342, Maffei 2 and M83. The data points are as in Fig. 4.10, however, the *IRAS* data have not been included in the fit. Three emissivity laws are represented; β=1.0 (solid line), β=1.5 (dotted line) and β=2.0 (dot–dashed line). The best-fitting dust temperatures for each galaxy and emissivity law are summarized in Table 4.13.

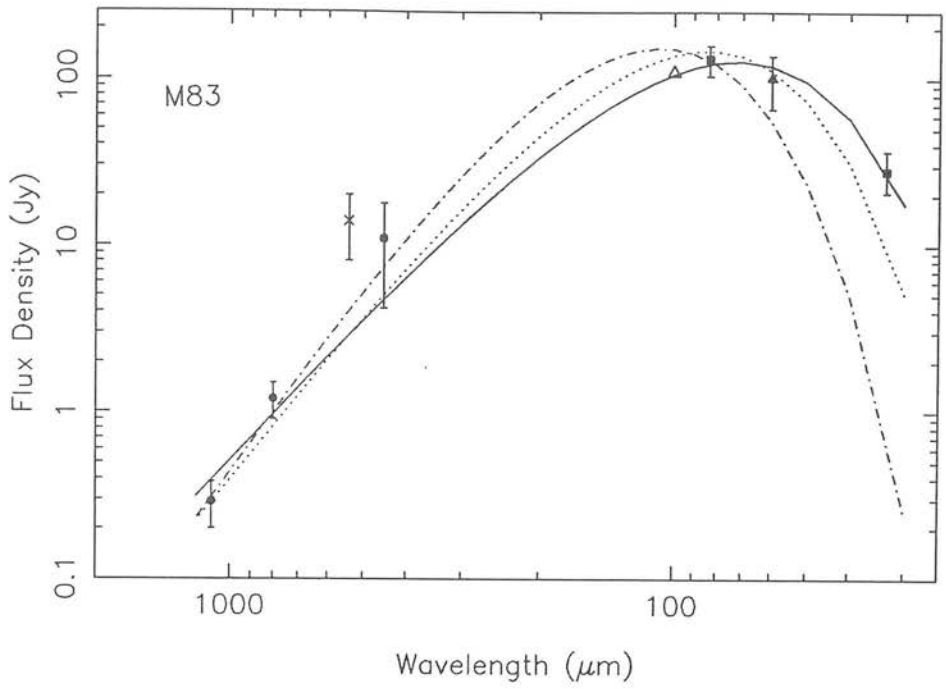

Figure 4.11: – continued

The above results lead naturally on to the fundamental question, quite apart from the possible variation of β with wavelength, of whether one is justified in fitting a single temperature at all. A 13″ beam, at the distance of IC342, for example, covers an area of $\sim 6 \times 10^4$ pc^2, and will include dust from all phases of the gaseous ISM at a correspondingly wide range of temperatures. Modelling of the disc of the Milky Way (Cox & Mezger 1989) implies temperature components ranging from >100 K in HII regions and ~30–40 K in active star-forming complexes, through 20 K in the diffuse atomic gas, heated by the interstellar radiation field (ISRF) of disc stars, to very cold (<15 K) dust in quiescent molecular clouds.

The nuclear region of a star-forming galaxy is likely to be quite different to that of the disc of a normal spiral such as the Milky Way, and it is possible that much of the gas will be at temperatures ≥30 K, heated either by embedded sources in star-forming regions, or by an intense ISRF two or three orders of magnitude higher than that in the disc of the Milky Way. Few published submillimetre observations of galaxies exist, and it is only comparatively recently that enough data points have been obtained, for a few galaxies, to even attempt spectral fits to more than one temperature. Even so,

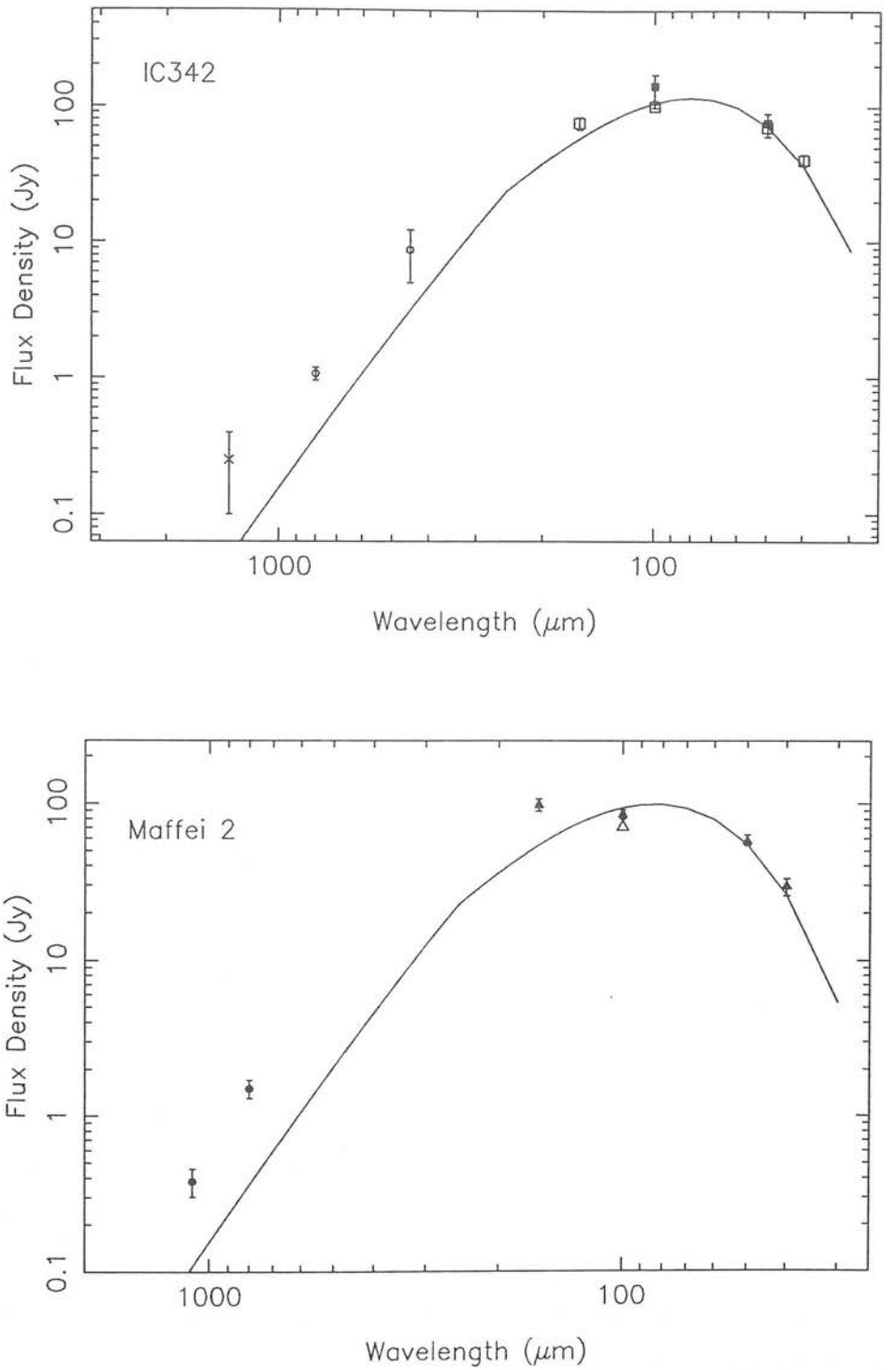

Figure 4.12: Single-temperature, modified blackbody fits to the spectra of IC342, Maffei 2 and M83, adopting a Hildebrand emissivity law (β=1.0 for $\lambda \leq$250 μm, β=2.0 for $\lambda >$250 μm).

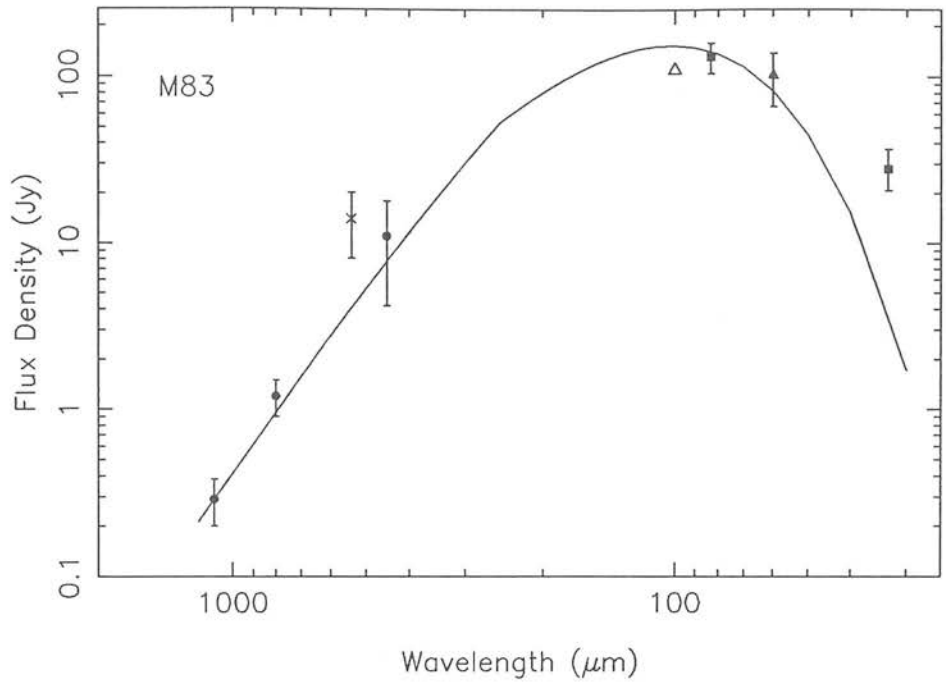

Figure 4.12: – continued

contradictory results are already emerging as to whether or not a multitemperature fit is needed or whether the data can be adequately explained by a single-temperature dust component (Chini *et al.* 1986; Eales, Wynn-Williams & Duncan 1989).

From the long-wavelength data presented here it is clear that the only way in which a single-temperature component can adequately fit the observations (with the possible exception of M83) is with an opacity–frequency dependence described by β=1 almost all the way to 1000 μm, and $T_{\rm d} \geq$40 K. Given the current uncertainty over the value of β, and the scarcity of extragalactic dust models, this scenario cannot be ruled out, although the assumption of isothermal dust in such a composite object must be a risky one.

For $\beta >$1, or for an emissivity law which steepens from 1 to 2 at short submillimetre wavelengths, a single-temperature model is not sufficient and an additional component of cool dust is needed to explain the 450–1100 μm fluxes. This example illustrates the value of very long-wavelength data, for the far-infrared fluxes alone are quite adequately fitted by a single component of warm ($\sim$40 K) dust.

As a next step, therefore, the data were fitted with a two-component dust temperature distribution. A fraction $f_{\rm w}$ of the dust was assumed to be warm, with temperature $T_{\rm w}$, the remaining dust being at a temperature $T_{\rm c}$. The 30–1300 μm data were fitted

Table 4.13: Results of single-temperature spectrum fitting.

Model	Parameter	IC342	M83	Maffei 2
	$T_{\rm d}$ (K)	47.2	51.4	44.6
β=1.0	$(\Omega_{\rm s}\tau_{800\,\mu{\rm m}})$ (sr)	6.6×10^{-12}	5.2×10^{-12}	7.0×10^{-12}
	Reduced χ^2	1.6	1.1	8.3
	$T_{\rm d}$ (K)	41.6	38.8	39.7
β=1.5	$(\Omega_{\rm s}\tau_{800\,\mu{\rm m}})$ (sr)	3.6×10^{-12}	6.2×10^{-12}	3.9×10^{-12}
	Reduced χ^2	6.3	1.8	15.2
	$T_{\rm d}$ (K)	38.0	27.2	36.8
β=2.0	$(\Omega_{\rm s}\tau_{800\,\mu{\rm m}})$ (sr)	1.8×10^{-12}	1.2×10^{-11}	1.8×10^{-12}
	Reduced χ^2	12.2	2.6	21.9
	$T_{\rm d}$ (K)	46.3	36.3	44.1
	$(\Omega_{\rm s}\tau_{250\,\mu{\rm m}})$ (sr)	2.3×10^{-11}	8.1×10^{-11}	2.4×10^{-11}
β=1.0–2.0	Reduced χ^2	7.7	2.1	16.3

to a function of the form

$$\begin{aligned} S(\nu) &= S_{\rm warm} + S_{\rm cool} \\ &= \frac{2h\nu^3}{c^2}\,(\Omega_{\rm s}\tau_0)\,\left(\frac{\nu}{\nu_0}\right)^{\beta}\,\left[f_{\rm w}\,\left(e^{h\nu/kT_{\rm w}}-1\right)^{-1} + (1-f_{\rm w})\,\left(e^{h\nu/kT_{\rm c}}-1\right)^{-1}\right], \end{aligned}$$

with the free parameters being $T_{\rm w}$, $T_{\rm c}$, $f_{\rm w}$ and $(\Omega_{\rm s}\tau_0)$, where this time τ_0 is the optical depth at 250 μm, and β follows the Hildebrand (1983) form of β=1 for $\lambda \leq$250 μm and β=2 at longer wavelengths.

The resultant two-temperature fits are plotted with the data in Fig. 4.13, while the fit parameters are summarized in Table 4.14. It appears that the data can be very well fitted by a two-component dust temperature distribution, with dust at ~40–50 K dominating at far-infrared wavelengths, and ~20 K dust making up the deficit in the submillimetre region. Both of these temperatures are consistent with dust components that appear in the Cox & Mezger (1989) models of the galactic disc, with 40–50 K dust residing in star-formation/molecular-cloud complexes, and cooler dust in the diffuse ISM, or embedded in quiescent molecular clouds. What is surprising is the amount of

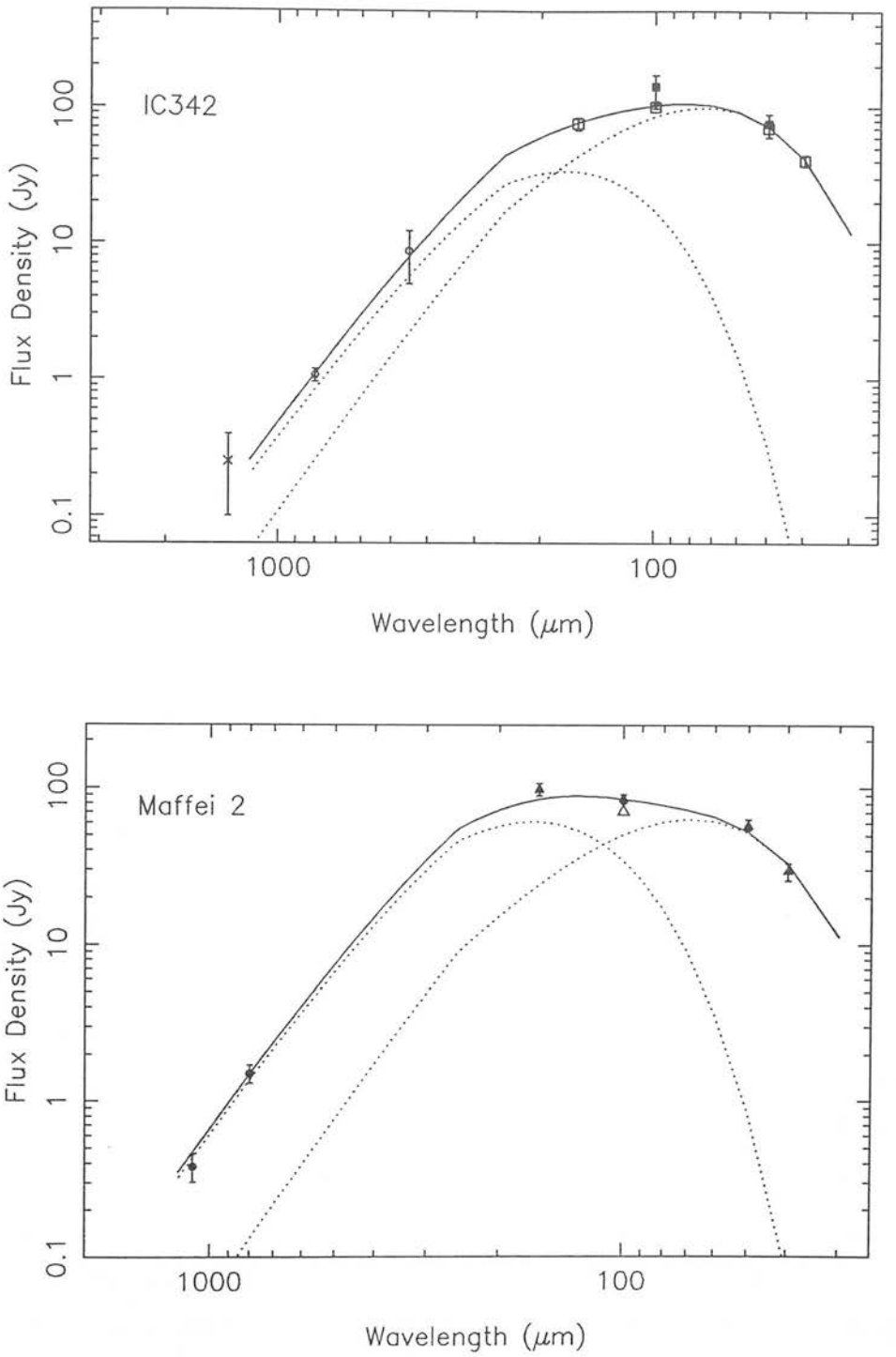

Figure 4.13: Two-temperature modified blackbody fits to the long-wavelength data for IC342, Maffei 2 and M83. An emissivity law with β increasing from 1 to 2 between 100–1000 μm (Hildebrand 1983) is assumed. The solid line shows the sum of the contributions from a warm ($\sim$50 K) and a cool (20–26 K) dust component, represented in the plots by dotted lines. The best-fitting dust temperatures for each galaxy are summarized in Table 4.14. Emission from the cool dust component dominates the emission longward of 100 μm for the two-temperature model.

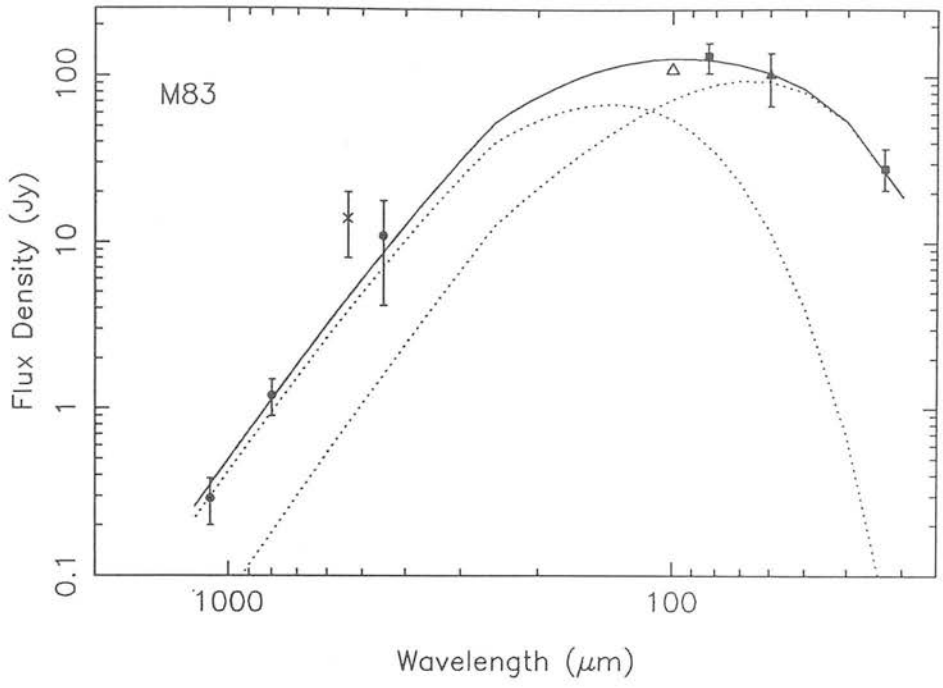

Figure 4.13: – continued

cool dust necessary to explain the long-wavelength data – the fraction of warm dust, f_w, is only ~7–8% for M83 and IC342, and drops as low as ~3% for Maffei 2.

It is possible that the fits presented here are not unique – i.e. that there are other combinations of free parameters that minimize χ^2, besides those to which the fitting program converged. To check this, the reduced χ^2 was evaluated as a function of the temperatures of the warm and cool dust components, which were allowed to vary between 10 and 70 K. The resulting contour plots of χ^2 are shown in Fig. 4.14. It can be seen that χ^2 reaches a minimum in only one region of the temperature plane, implying that the fits are unique. (The apparent second minimum in each contour plot is a mirror image of the first, due to the fact that the fitting program does not 'know' which component of the dust is supposed to be cool and which warm, and therefore also finds a minimum at T_c ~45 K, T_w ~20 K.)

In Table 4.15 are presented the molecular hydrogen column densities and total gas masses calculated from the flux densities at 800 μm and the fitted dust temperatures, using equations (4.3–4.5). [It is assumed that $N(H+H_2) \simeq N(H_2)$, i.e. that the fraction of hydrogen in atomic form is very small in the central kiloparsec of these galaxies.] The assumption of a two-component temperature distribution is a simplification and there will actually be a range of dust temperatures. The fraction of cool dust derived from the

Table 4.14: Results of double-temperature spectrum fitting.

Galaxy	Warm dust temperature (K)	Cool dust temperature (K)	Warm dust fraction (%)	Reduced χ^2
IC342	50.0	21.4	9.1	0.5
M83	55.3	26.8	7.1	0.8
Maffei 2 (1)	53.9 (48.1)	22.3 (17.2)	3.0 (4.9)	3.2 (1.9)

(1) The numbers in brackets represent the fit if the 160 μm point is excluded.

fit may therefore be an upper limit, with there being in reality a contribution from dust at intermediate temperatures. Using the far-infrared data only, and assuming a single temperature and ~45-K dust, will give a lower limit to the total gas mass, ignoring as it does the possibility of any cool dust contributing to the emission. Table 4.16 summarizes published molecular hydrogen column densities and masses derived from CO observations of Maffei 2, IC342 and M83.

Discussion

The results presented in this section demonstrate that, if the Hildebrand emissivity law is adopted, with β steepening from 1 to 2 at long wavelengths, then the dust emitting at submillimetre and millimetre wavelengths is quite distinct from that comprising the *IRAS* fluxes, and is cool (~20–25 K as opposed to ~40–50 K for the *IRAS*-emitting dust). The amount of cool dust implied by the fits is unexpectedly large for the nuclear region of an infrared-bright, star-forming galaxy and, if correct, has a significant effect on the derived molecular hydrogen masses, as can be seen from Table 4.15. If only the far-infrared data are used (i.e. the 'warm' part of the two-component fit) then peak

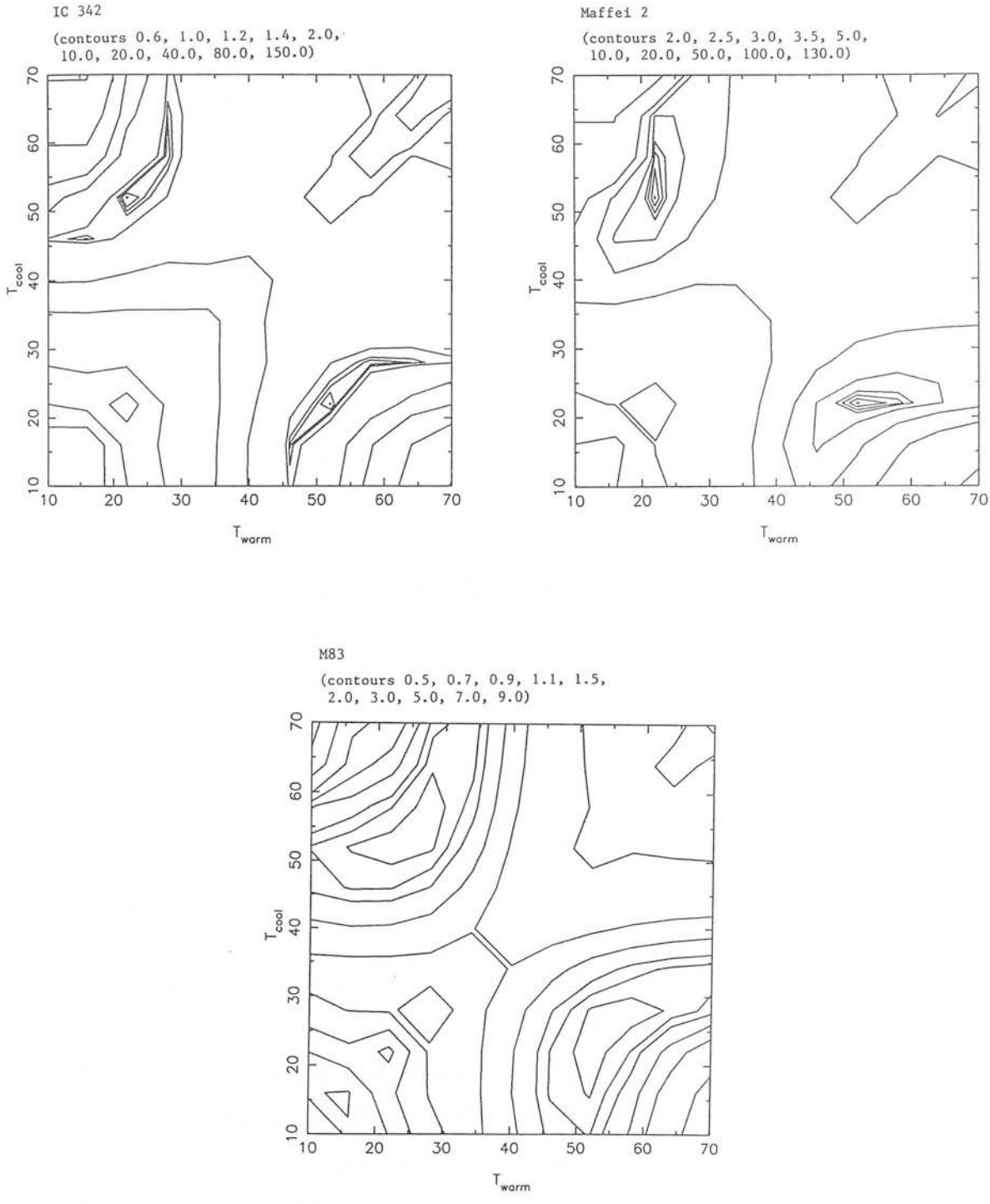

Figure 4.14: Plots of the χ^2 surfaces for the two-component dust temperature fits described in the text. The reduced χ^2 is contoured as a function of the two dust temperatures, $T_{\rm w}$ and $T_{\rm c}$. The double-minimum structure of the contour plots is due to the fact that the fitting program doesn't 'know' which component of the dust is to be warm and which cool.

column densities of $\sim$2–7 $\times$ 10^{21} mol cm^{-2} are derived, with molecular hydrogen masses of $\leq$2 $\times$ 10^{7} $M_{\odot}$. In contrast, the cool material contributes column densities of 4–7 $\times$ 10^{22} cm^{-2} and corresponding gas masses of 1–4 $\times$ 10^{8} $M_{\odot}$, an order of magnitude higher. The value of having long-wavelength points can be seen here – even fitting a single-temperature spectrum, if the submillimetre points are included, significantly reduces the discrepancy incurred by using *IRAS* fluxes only. In the cases studied here, the one-temperature, β=1 fits give column densities of 1–2 $\times$ 10^{22} cm^{-2} and gas masses of 0.3–1 $\times$ 10^{8} $M_{\odot}$, a factor of $\sim$3 improvement over *IRAS*, although still $\sim$3 times less than derived from the two-component fit results.

These column densities and masses may be compared with those derived from CO observations (Table 4.16). Using ^{12}CO and the 'constant conversion factor' gives column densities of $\sim$4–7 $\times$ 10^{22} cm^{-2}, while non-LTE modelling, or using ^{13}CO data and assuming LTE, result in slightly lower values of $\sim$1–4 $\times$ 10^{22} cm^{-2}. The gas masses obtained from these column densities are all in the region of $\sim$2 $\times$ 10^{8} $M_{\odot}$ (Handa *et al.* 1990; Eckart *et al.* 1990; Chapter 5). Direct comparison between CO- and dust-derived H_2 masses is difficult because the emission regions represented are not exactly the same, the submillimetre source sizes appearing smaller. However, it can be seen that including the cool dust component brings the derived gas masses much closer to those obtained from CO data. In the case of Maffei 2, the continuum-derived mass appears even to exceed that calculated from CO and approaches the total *dynamical* mass deduced from the CO rotation curve (Chapter 5). It is possible that, in the case of Maffei 2, the low signal-to-noise ratio of the map, coupled with the interpolation from an Az–El to an RA–Dec. grid, has resulted in a derived source size that is too large. Certainly, Maffei 2 is the only one of the three galaxies in which the CO- and dust-emitting regions appear of comparable size, while the integrated 800 μm flux derived from the fitted source size is 40% higher than that derived using the 'oversampling' algorithm (Moore 1989 – see Section 4.2).

As stated earlier, there are as yet very little extragalactic submillimetre continuum data in the literature, and it is only very recently that enough data have existed, for a few galaxies, to even attempt a fit to more than one dust temperature. The results have been contradictory. Chini *et al.* (1986) state that a fit to two temperatures (53 and 16 K) is needed to explain their long-wavelength data for *IRAS* galaxies. However,

as they fit two dust temperatures to only three data points (at 100, 350 and 1300 μm), their findings cannot be regarded as conclusive. Eales *et al.* (1989), reobserving some of Chini *et al.*'s galaxies, find significant discrepancies between their observed long-wavelength fluxes and extrapolations of the Chini *et al.* fits. Eales *et al.* found that their data were fit satisfactorily by a single dust component at 27–48 K, while the errors on their points were too high to distinguish between different emissivity laws. They stress, however, that their data *do not* rule out a component of cool dust, hidden by the errors on their long-wavelength photometry. Hughes *et al.* (1990), too, manage to fit the spectrum of M82 with a $\nu^{1.5}$ emissivity law and dust temperature of 47 K, with no shortfall in flux at submillimetre wavelengths.

Most of the published dust continuum studies assume a single-temperature dust distribution and correspondingly high dust temperatures ($\sim$ 30–50 K), deriving gas masses of a few $\times$ 10^{7-8} $M_{\odot}$. The two-temperature fits presented here, on the other hand, require that at least 90% of the dust is cool, with temperatures of 20–25 K. Is such a scenario plausible in the centres of galaxies for which observational evidence at all wavelengths points towards massive star formation and warm gas? ^{12}CO line ratios in Maffei 2 and IC342 are consistent with a warm ($T > 30$ K) interstellar medium, while detection of the 158 μm [CII] transition from all three galaxies suggests that a large fraction of the neutral ISM may be associated with warm, dense UV-illuminated photodissociation regions (Crawford *et al.* 1985; Eckart *et al.* 1990; Stacey *et al.* 1991; Chapter 5).

The dust emission is very optically thin, so all the dust, and hence the gas with which it is mixed, is sampled. The ^{12}CO on the other hand appears, from isotopic line ratios, to be quite optically thick, at least in Maffei 2 and IC342 (Eckart *et al.* 1990; Chapter 5). As will be discussed in Chapter 5, the molecular gas in a region of prolific star formation is likely to have been swept up, by the combined effects of stellar winds and supernovae, into small clouds and filaments, which may be heated mainly from the outside. In such circumstances, then, a possible scenario is that the outer UV-illuminated layers of the clouds are warm, 30–50 K, while the interiors, shielded from the effects of star formation, are cooler, 20–25 K. The dust emission, being optically thin, samples the whole cloud and splits into two temperature components, a small fraction arising from the hot outer layers and the bulk from the cooler cloud interior.

Table 4.15: Gas masses derived from the continuum data.

	IC342	M83	Maffei 2
Peak 800 μm flux density (Jy)	0.43±0.06	0.46±0.05	0.61±0.07
Beamsize (arcsec)	13.5	15.8	15.8
Source size (arcsec)	16.2 × 13.4	23.6 × 14.7	32.9 × 14.3
Distance (Mpc)	4.5	3.7	5.0
Single-temperature fit			
Dust temperature (K)	47.2	51.4	44.7
Emissivity index β	1.0	1.0	1.0
Peak $N(H_2)$ (mol cm^{-2})	1.7×10^{22}	1.1×10^{22}	1.6×10^{22}
$M(H_2)$ ($M_\odot$)	4.0×10^7	2.9×10^7	1.0×10^8
Two-temperature fit			
T_w (K)	50.0	55.3	53.9
T_c (K)	21.4	26.8	22.3
Warm dust fraction (%)	9.1	7.1	3.0
Emissivity index β	2.0	2.0	2.0
Peak $N(H_2)_w$ (mol cm^{-2})	7.2×10^{21}	3.2×10^{21}	2.2×10^{21}
Peak $N(H_2)_c$ (mol cm^{-2})	7.5×10^{22}	4.3×10^{22}	7.0×10^{22}
$(M(H_2))_w$ ($M_\odot$)	1.7×10^7	8.3×10^6	1.4×10^7
$(M(H_2))_c$ ($M_\odot$)	1.8×10^8	1.1×10^8	4.4×10^8
Fraction of 800 μm flux from warm dust (%)	23.2	15.9	8.7
Fraction of 800 μm flux from cool dust (%)	76.8	84.1	91.3

This proposition is supported by the fact that, in the starburst galaxy M82, the ^{13}CO J=2–1 morphology closely resembles that at 450 μm, while neither the continuum nor the isotopic line emission is consistent with the double-peaked structure seen in ^{12}CO (Chapter 2). It would be interesting to compare the morphologies seen at far-infrared wavelengths and in ^{12}CO, with similar resolution – currently far-infrared observations rely on the Kuiper Airborne Observatory which has a beamsize considerably larger than those of the latest generation of millimetre-wave telescopes. Such a picture is also consistent with the observed CO ratios. The ^{12}CO, being optically thick, will arise from the warm outer layers of the cloud. As is observed in Maffei 2 and IC342, the ^{12}CO J=2–1/J=1–0 antenna temperature ratio may be enhanced above the 'optically thick' maximum ratio of 1, because the optically thicker 2–1 line would be emitted from the region that is closest to the cloud surface, and hence warmest (Maloney & Black 1988; Eckart *et al.* 1990; Chapter 5). The optically thinner ^{13}CO, on the other hand, would arise from the cooler cloud interior, and this would be reflected in ^{13}CO 2–1/1–0 ratios not much greater than 1, as is again observed (Eckart *et al.* 1990; Chapter 5). In such a situation, the H_2 mass derived from ^{12}CO observations would be that of the warm outer layers, but may be overestimated, because of the effect of elevated gas temperature on the CO-to-H_2 conversion factor (e.g. Maloney & Black 1988; Chapter 1). It might be expected also that the H_2 column densities and masses derived from ^{13}CO and from cool dust emission would be comparable. In fact the cool-dust-derived column densities in Maffei 2 and IC342 exceed those derived from ^{13}CO by factors of up to 5, although this may be in part due to error in our knowledge of the relevant conversion factors $N(\mathrm{H+H_2})/\tau(\nu)$ and $N(\mathrm{H_2})/N(^{13}\mathrm{CO})$ (see Chapter 1).

An alternative picture may be one in which the cool and warm components of dust and CO emission arise from entirely different components of the ISM, with the warm dust/gas associated with star-formation/HII-region complexes, and the cool submillimetre fluxes originating from quiescent neutral gas (atomic + molecular) heated by the general interstellar radiation field. The neutral interstellar medium in galaxy nuclei is believed to be predominantly molecular, rather than atomic as is the case in the Galactic disc (e.g. Weliachew, Fomalont & Greisen 1984). In this scenario, then, the far-infrared fluxes might be said to trace current/recent star formation, while the submillimetre data trace potential/future star formation in the guise of quiescent molecular

Table 4.16: Gas masses derived from published CO data.

	IC342	M83	Maffei 2
Peak $N(H_2)$ (cm^{-2})	4–5 $\times$ 10^{22} (5)	$\sim$7 $\times$ 10^{22} (9)	$\sim$4.4 $\times$ 10^{22} (1) 1.1 $\times$ 10^{22} (2) 2 $\times$ 10^{22} (3)
Total gas mass ($M_\odot$)	2 $\times$ 10^8 (6) 1.5 $\times$ 10^8 (7)	2 $\times$ 10^8 (8)	1–4 $\times$ 10^8 (4)
Reference	Eckart *et al.* 1990	Handa *et al.* 1990	Chapter 5

(1) In a 13″ beam, from ^{12}CO J=2–1 data and applying the standard ^{12}CO conversion factor. Uncertainty of a factor $\sim$2. (2) Calculated from ^{13}CO J=2–1 data and an excitation temperature of 20 K, assuming LTE. (3) As for (2), but with an excitation temperature of 40 K. (4) From total ^{12}CO J=2–1 emission and the standard conversion factor. (5) From non-LTE clumpy cloud modelling of CO emission (20″ beam) (6) In central 2.5 kpc^2, from ^{12}CO J=1–0 emission using standard conversion factor. (7) In central 1.5 kpc^2, from ^{13}CO J=1–0 emission. (8) In a 16″ beam, from ^{12}CO J=1–0 emission and standard conversion factor. (9) In central 30″, from ^{12}CO J=1–0 emission and standard conversion factor.

fuel. Such a model has been applied to the continuum spectrum of the Milky Way disc (Cox & Mezger 1989). In the central kiloparsec of a star-forming galaxy, however, the radiation field may be up to 2–3 orders of magnitude more intense than in the disc of the Milky Way, and even dust associated with quiescent gas might be expected to reach equilibrium temperatures of $\sim$40 K (e.g. Rowan-Robinson 1990). There is as yet no published detailed modelling of dust emission from the centres of galaxies, of the sort that has been carried out for the Milky Way disc. Such modelling would be very welcome as the sensitivity and resolution available with millimetre-wave telescopes increase.

Of course, it should be stressed that the results and discussion here are somewhat artificial in the sense that they pertain to solutions for particular, *assumed* forms of the emissivity spectral index, β. The value of β assumed can have a dramatic effect on the derived dust temperatures and gas masses. The value of β and its dependence on wavelength are poorly constrained by both observation and theory, beyond the fact that β lies between 1 and 2 and probably steepens to 2 at some wavelength longward of about 100 μm. Observational derivations of β, from both Galactic and extragalactic

studies of a wide range of objects, are evenly scattered between 1 and 2 (Helou 1989). In addition to lack of knowledge of β, there are a number of other factors which will affect the accuracy of a spectral fit. Calibration errors in the photometry, errors introduced by the varying beamsizes used at different wavelengths, and contamination of the dust fluxes by other processes (although these are not expected to be significant at long wavelengths, the contribution to fluxes shortward of 100 μm of emission from very small or transiently heated grains is not easy to evaluate) all contribute to the uncertainty. In addition, as can be seen from Fig. 4.14, reasonable fits (reduced $\chi^2 \sim 1$) can be obtained, in the cases of M83 and IC342 at least, for temperatures in the range T_w = 45–60 K, T_c = 15–30 K, and warm dust fractions from 2–18% , all of which conspires to increase the uncertainty in the derived masses.

Although the Hildebrand emissivity law and multitemperature dust distribution are physically plausible, the scenario of β=1 all the way to 1000 μm and a single dust temperature cannot be conclusively ruled out. The dust temperatures resulting from such a fit (30–50 K) are plausible for the high-UV environment of a starburst. In the case of the active starburst M82, also, the 40–1100 μm spectrum is satisfactorily modelled by a single dust component at 47 K and emissivity law of β=1.5, with no flux shortfall at submillimetre wavelengths (Hughes *et al.* 1990). Whichever picture is correct, the importance of submillimetre observations to constrain the shape of the spectrum longward of the *IRAS* fluxes cannot be over-emphasized, and is clearly demonstrated by the data presented here.

4.5 Summary and conclusions

This chapter presented 800 μm mapping and 450, 800 and 1100 μm photometry of three nearby, infrared-bright galaxies, IC342, Maffei 2 and M83. All three show multiwavelength evidence of vigorous star formation in their nuclear regions, and have previously been mapped in transitions of CO.

The galaxies turned out to be strong emitters of submillimetre radiation, with peak flux densities of 0.4–0.6 Jy at 800 μm. The level of contamination of these fluxes by free–free/non-thermal radio continuum, or by emission from the low-J lines of CO, was considered and found to be negligible.

The submillimetre continuum is potentially useful as an independent tracer of the morphology and mass of molecular hydrogen. All three galaxies are spatially extended in at least one direction with respect to the 800 μm beam, the peak of the emission being coincident with the galactic nucleus (as defined by the near-infrared or radio peak). There is generally good spatial agreement between the dust emission and other star-formation/ISM tracers although a detailed comparison is not possible at the resolutions employed. In the case of M83, a hint of a second peak $\sim$15″ north-east along the bar, while due to elevated flux in a single pixel and perhaps not real, is consistent with asymmetries seen in a 100 μm continuum scan and in the preliminary version of a ^{12}CO J=1–0 map. The submillimetre source sizes of M83 and IC342 ($\leq$20″) are smaller than seen in CO ($\sim$30″) and this may be due to a fall-off in temperature or cloud density away from the nucleus. Only Maffei 2 shows a continuum source size comparable to that seen in CO, but here the low signal-to-noise ratio, coupled with the transformation from Az/El to RA/Dec. coordinates, may have introduced errors. The maps show no marked morphological discrepancies with the CO emission such as were seen in M82 (Chapters 2 and 3).

The observed 450–800 μm fluxes were combined with published far-infrared to radio data to constrain the slope of the long-wavelength spectrum. The spectrum peaks at $\sim$100 μm, consistent with dust at $\sim$30–40 K. There are virtually no previous data in the important millimetre/submillimetre region. The spectra were first fitted with single-temperature, modified blackbody functions with emissivity spectral indices β=1, 1.5 or 2. Only β=1, with corresponding dust temperature $\sim$ 45 K, came close to fitting the whole spectrum, β >1 models failing to fit the long-wavelength points by factors of >2. A single-temperature fit with a Hildebrand emissivity law (β increasing from 1 to 2 at 250 μm) also failed to fit the JCMT data. Multiple dust temperature components are likely to be present in a composite object such as a galaxy. The data were therefore fitted with a two-component model of 'warm' ($\sim$35–55 K) and 'cool' (20–25 K) dust. It was found that a large fraction of cool dust ($\sim$90%) is needed to produce the submillimetre fluxes, a result which is surprising for three galaxies whose interstellar media are presumed dominated by star formation.

The high derived fraction of cool dust implies that the dust emitting at submillimetre wavelengths is quite distinct from that comprising the *IRAS* fluxes, and has a

significant effect on the gas masses derived from the continuum data. Gas masses of 1–4 $\times$ 10^8 $M_\odot$ emerge from the cool component, an order of magnitude higher than those derived using *IRAS* fluxes and warm dust only, and closer to masses obtained from CO data. Detailed comparison of the CO- and dust-derived gas masses is difficult because of such factors as the different source sizes, and uncertainties in the various conversion factors arising from physical, excitation and chemical properties of the ISM. If we adopt the multitemperature picture as correct, then the value of using long-wavelength JCMT data is demonstrated by the fact that even a single-temperature fit results in gas masses that are much closer to those derived by other methods than if far-infrared data only are used.

A possible explanation for the high derived fraction of cool dust is that the submillimetre emission arises from the cool interiors of externally heated clouds that are also traced by optically thin isotopic CO observations. The warm outer cloud layers produce the *IRAS* fluxes and the optically thick ^{12}CO emission. This scenario is consistent with observed ^{12}CO and ^{13}CO line ratios. Alternatively, the submillimetre- and *IRAS*-emitting dust may reside in completely different components of the ISM, with the warm dust in star-forming regions and the cool dust in the quiescent ISM, although in a region of prolific star formation even the general interstellar radiation field may be able to heat dust to $\sim$40 K.

Although submillimetre continuum data clearly have an advantage over CO observations in terms of optical thinness and dependence of dust-to-gas conversion factors on cloud properties, this should not obscure the fact that dust continuum observations still have considerable uncertainty attached to them. The emissivity spectral index, β, is poorly constrained by both theory and observation, and there is disagreement in the literature over whether a multitemperature fit is needed at all. As demonstrated here, uncertainty in the form of the spectral fit has a marked effect on the derived temperatures and masses. While the long-wavelength spectrum of the Milky Way has been extensively modelled in terms of emission from different components of the ISM, no such modelling exists in the literature for the nuclei of external galaxies, with which observations may be compared. Such modelling is clearly needed.

Quite apart from theoretical considerations, the reliability of dust continuum data is affected by observational errors, both in terms of the differing beamsizes used at

various wavelengths, and concerning the particular difficulties involved with submillimetre mapping. The observer is forced to choose between raster-scanned, noisy maps, or point-by-point photometry which increases the signal-to-noise ratio at the expense of relative calibration between pixels. These problems should be alleviated with the commissioning of SCUBA (Sub-Millimetre Continuum Bolometer Array) on the JCMT in a few years' time. SCUBA will consist of an array of 37 or 91 detectors (at 855 and 450 μm respectively) and will result in improvements in mapping times of up to a factor of 10^3 (Cunningham & Gear 1990). We have almost reached the limit of infrared-bright, nearby galaxies that can be mapped in a reasonable amount of time (a few nights) with the current receiver UKT14, so instrumentation such as SCUBA will be essential if one wants to do more than single-point photometry or small strip maps of galaxies with *IRAS* 100 μm fluxes less than about 100 Jy.

Other major hurdles at submillimetre wavelengths include the rapidly variable atmospheric transmission, and the scarcity of reliable calibrator sources not only for the principal 450, 800 and 1100 μm filters, but also for the less frequently used 600 μm, 850 μm and 2-mm bandpasses where little or no calibration data exist. Hopefully the ongoing secondary calibrator programme will eventually remedy this, allowing accurate photometry and mapping at the full range of wavelengths for which UKT14 is equipped. The introduction of skydips to monitor atmospheric attenuation will reduce the amount of time the observer has to spend measuring calibrators and extinction monitors (currently at least 50% of the allocated time for the careful observer). Ideally, in the future, submillimetre astronomers will be able to combine high-resolution multiwavelength spatial information with grain models, to investigate the variation of emission properties across a galaxy and the interstellar components producing the long-wavelength flux. In so doing, the great advantage dust continuum has over CO, that of low optical depth, can be fully exploited.

Chapter 5

The molecular interstellar medium of Maffei 2

The results presented in the previous chapters, as well as the work reviewed in the Introduction, seem to indicate that, while the millimetre-wave CO lines are in principle a valuable tracer of molecular hydrogen, their interpretation is complex, and use of a single, probably optically thick transition (e.g. ^{12}CO J=1–0) is likely to lead to errors. To start to investigate the existence and effect of optical depth and excitation temperature variations, it is necessary to observe different isotopes and transitions.

In this chapter, two of the new generation of large millimetre-wave telescopes are used to make a high-resolution CO-line study of the nearby star-forming spiral, Maffei 2. ^{12}CO and ^{13}CO J=1–0 and 2–1 data are used to investigate the variation of excitation conditions across the galaxy and the effect of these on the derivation of H_2 column densities. The large linewidths observed are considered in the context of the energy source necessary to sustain them, which is generally believed to be frequent supernova explosions arising from the high rate of massive star formation expected in this galaxy.

The work presented in this chapter was carried out in collaboration with Naomasa Nakai of the Nobeyama Radio Observatory, Phil Puxley and Matt Mountain of the Royal Observatory Edinburgh and Peter Brand of the University of Edinburgh. Due to nearly simultaneous scheduling of two of the runs, some of the observations were carried out by Phil Puxley, and Toby Moore of the Herzberg Institute in Ottawa.

5.1 Introduction

The J=1–0 transition of the CO molecule is a valuable tracer of molecular hydrogen in the cool, optically thick, quiescent giant molecular clouds (GMCs) of the Milky Way. In active star-forming regions, or in the nuclei of 'starburst' galaxies, the situation is considerably more complex. The energy input from massive young stars in the form of UV heating, stellar winds, mass outflow and supernovae is likely to result in a cloud population that is smaller, denser, warmer and faster moving than GMCs in the disc of a 'normal' spiral galaxy. Under such circumstances, the ability of CO to measure reliably the distribution and mass of molecular hydrogen cannot be taken for granted.

Cornerstones of the CO technique are the assumptions of optically thick CO and cool, moderately dense ($T_{\rm ex}$ = 10 K, n = 200 cm^{-3}) gas. With observations of only a single CO transition (^{12}CO J=1–0), it is not possible to investigate the validity of these assumptions in external galaxies. When first the ^{12}CO J=2–1 line, and later rarer isotopes such as ^{13}CO, began to be detected in extragalactic objects (e.g. Rickard *et al.* 1977a,b; Encrenaz *et al.* 1979), the first signs of a more complex picture began to emerge. In the nearby, vigorously star-forming galaxy M82, for example, ^{12}CO 2–1/1–0 antenna temperature ratios of 2–4 were observed (Knapp *et al.* 1980; Sutton, Masson & Phillips 1983), and interpreted as implying the existence of small ($\sim$ few pc), hot (40 K), optically thin clouds in the nucleus of the galaxy. Large-beam observations of ^{12}CO and ^{13}CO in several spirals suggested that the ^{12}CO/^{13}CO ratio varied from position to position within a galaxy and within galaxies, indicating large-scale variations in the properties of the clouds (Rickard & Blitz 1985). ^{12}CO/^{13}CO integrated intensity ratios of $\sim$9–16 are observed, much larger than the typical values of $\sim$5 observed in the Galactic disc (Encrenaz *et al.* 1979; Solomon & Sanders 1979; Rickard & Blitz 1985).

Most of these observations were performed with large (arcminute) beams, averaging over kiloparsec scales and introducing the possibility of beam dilution effects when the beamsize exceeded the extent of the CO-emitting region (Sargent *et al.* 1985). Indeed, higher resolution observations of ^{12}CO and ^{13}CO J=2–1 in M82 seem to suggest optical depth variations on scales of 7″ (=110 pc), with the gas becoming quite optically thick to ^{12}CO at the centre (Loiseau *et al.* 1988, 1990; Chapters 2 and 3). Young & Scoville (1984) and Maloney & Black (1988) suggest external heating of optically thick clouds

as a possible cause of the high 2–1/1–0 ratios.

With the new generation of large millimetre-wave telescopes (JCMT, Nobeyama, IRAM), high-resolution (10″–20″) mapping of CO transitions and isotopes has become possible for some of the nearer, infrared-bright, gas-rich galaxies, providing the opportunity of investigating optical depth and excitation variations on scales of a few hundred parsecs. The high velocity resolution available with such observations also permits study of the kinematics of the central regions of galaxies which are typically heavily obscured at visible or even near-infrared wavelengths.

Maffei 2 is a nearby, heavily extinguished spiral galaxy lying so low in the Galactic plane (b=−0.5°) that it was discovered in the infrared (Maffei 1968). After a flurry of activity, mostly at radio wavelengths, to uncover its basic nature (e.g. Allen & Raimond 1972; Spinrad *et al.* 1973; Wright & Seielstad 1973), it excited little more interest until the late 1970s when the discovery of strong, non-thermal radio continuum and 2.6-mm CO emission established it as a candidate for some sort of nuclear activity and so worthy of further attention (Seaquist, Pfund & Bignell 1976; Rickard *et al.* 1977a). Since then, the emergence of Maffei 2 as one of the brightest extragalactic *IRAS* sources [$S(100\,\mu\mathrm{m})$=224 Jy], with a far-infrared spectrum similar to M82, along with detections of near-infrared recombination-line emission, mid-infrared continuum from hot dust and the far-infrared fine-structure line of ionized carbon from photodissociation regions, has placed it firmly in the category of vigorously star-forming galaxies (Ho *et al.* 1989; Ho, Beck & Turner 1990a; Stacey *et al.* 1991). The adopted physical parameters of Maffei 2 are summarized in Table 5.1.

After the initial observation in 1977 of ^{12}CO – one of the first extragalactic objects in which the line was detected – limited large-beam mapping of ^{12}CO J=1–0 and 2–1 was carried out and the ^{13}CO J=1–0 line was detected (Rickard & Blitz 1985; Sargent *et al.* 1985; Weliachew, Casoli & Combes 1988). The CO is concentrated in the central kiloparsec of the galaxy, and interferometer observations reveal a long, narrow, bar-like structure and evidence for an expanding ring, similar to that postulated to exist in M82, possibly created by a nuclear starburst (Nakai *et al.* 1987; Ishiguro *et al.* 1989). Line ratios of ^{12}CO 2–1/1–0 and ^{12}CO/^{13}CO 1–0 suggest that the gas in Maffei 2 is partially optically thin, although this may be a beam dilution effect (Sargent *et al.* 1985). The ^{12}CO/^{13}CO ratios vary on scales of 10″–20″, implying large-scale excitation gradients

Table 5.1: Adopted physical parameters of Maffei 2.

Hubble Type[1,2]	Sbc
Central position of map[3]	RA(1950) $02^h\ 38^m\ 08.5^s$ Dec.(1950) $+59°\ 23'\ 30''$
V_{LSR}	0 km s^{-1}
Major axis position angle (E from N)[1,3]	30°
Inclination[1,3] (90° = edge-on)	65°
Distance[1,2]	5 Mpc
IRAS fluxes[4]	S(60 μm) = 92.9 Jy S(100 μm) = 224.8 Jy

(1) Allen & Raimond 1972; (2) Spinrad *et al.* 1973; (3) Seaquist *et al.* 1976; (4) *IRAS* Point Source Catalogue.

(Weliachew *et al.* 1988). This conclusion is supported by evidence from far-infrared photometry that the dust temperature decreases away from the nucleus, and that the observed contrast between nuclear and disc emission may largely be a temperature effect (Rickard & Harvey 1983). The recent detections of CS and N_2H^+ emission are further evidence of warm, dense nuclear gas (Mauersberger *et al.* 1989; Mauersberger & Henkel 1991).

High-resolution high signal-to-noise ratio mapping of additional isotopes and transitions are important to check and extend upon the original limited, large-beam data, to study optical depth and excitation temperature variations on scales of hundreds of parsecs across the central region, relate these to other star-formation diagnostics and tracers and hence investigate the reliability of CO as a tracer of the molecular ISM in Maffei 2. The velocity resolution available (~10–20 km s^{-1} for linewidths of several hundred km s^{-1}) provides an extinction-free probe of the internal kinematics of this heavily obscured star-forming galaxy.

5.2 Observations and results

5.2.1 The ^{12}CO J=2–1 observations

The ^{12}CO J=2–1 map was made with the IRAM 30-m telescope at Pico Veleta, Spain, on 18–20 April 1989. There was a lot of cloud during parts of the run, which affected receiver system temperature and pointing accuracy. The beamsize of the 30-m at 230 GHz is 13″, corresponding to a linear scale of 315 pc at the adopted distance to Maffei 2 of 5 Mpc.

The 1.3-mm SIS receiver equipped with a 512 × 1 MHz filterbank was used, giving a velocity coverage of ~670 km s^{-1}, and velocity resolution of 1.3 km s^{-1} at 230 GHz. The receiver was tuned to an LSR velocity of 0 km s^{-1}, as the systemic velocity of Maffei 2, though poorly determined, is known to be near zero (e.g. Spinrad *et al.* 1973). The system temperature of the receiver varied from 560–790 K (single sideband), depending on the time of day, weather conditions and source elevation.

Observation was by position switching between Maffei 2 and a reference position offset by ΔRA = +30″, ΔDec. = −720″ (Rickard *et al.* 1977a) from the centre of the galaxy. This large offset was necessary, due to the low Galactic latitude of Maffei 2, to achieve an emission-free reference position.

A fully-sampled 9 by 12 grid (108 spectra) was observed in ^{12}CO J=2–1, oriented in RA, Dec., and centred on RA(1950) = 02^{h} 38^{m} 08.5^{s}, Dec.(1950) = +59° 23′ 30″ [the radio continuum peak – Seaquist *et al.* (1976)]. The pixel spacing was 7″ , giving a total spatial coverage of ~ 1′ × 1′ . The map was made by raster scanning in RA, with a total of ~2 min on-source integration per map point. Calibration by the chopper-wheel method was carried out about every 30 min. This yielded antenna temperatures on the T_a^* scale – that is, corrected for atmospheric and ohmic losses, but not for beam efficiencies. The accuracy of calibration is estimated to be ~15–20% (e.g. Mauersberger *et al.* 1988). Pointing was checked every 1.5–2 hr by continuum observations of W3(OH). The pointing accuracy was at times adversely affected by the weather, and was noticeably worse in elevation, the rms error being about 2″ (azimuth) and 6″ (elevation).

Data reduction was performed with the IRAM CLASS software (Guilloteau & Lucas 1988). Individual scans were summed, and baselines subtracted. In all but a few

cases, it was sufficient to fit a linear baseline, an occasional high-frequency ripple being removed using a Fast Fourier Transform algorithm. A few scans with particularly bad baselines were discarded. The spectra were binned to a velocity resolution of 13 km s^{-1}, leading to rms noise levels (T_a^*) of ~0.03 K. Further analysis was performed in Edinburgh using the Starlink SPECX package (Padman 1991).

5.2.2 The ^{13}CO J=2–1 data

The ^{13}CO J=2–1 observations were made with the IRAM 30-m on 12–14 September 1989. The instruments and observational procedure were the same as for the ^{12}CO observations – the 1.3-mm SIS receiver was used with the 512 × 1 MHz filterbank tuned to 220 GHz and a central LSR velocity of 0 km s^{-1}. The system temperature varied between 570–1000 K. Pointing was checked every hour on W3(OH), and the rms error over the run was estimated to be only 2.2″ (azimuth) and 4.2″ (elevation). Each observation consisted of five subscans (30 s on, 30 s off) and was typically repeated 5–15 times at each galaxy position, calibrating after every scan (i.e. every 5 min).

Nineteen positions were observed in ^{13}CO J=2–1, ranging from ΔRA = −14″ to +21″ and ΔDec. = −21″ to +21″. The beamsize at 220 GHz was 13″. During data reduction, a few spikes and channel dropouts were removed, and baselines were subtracted. Scans with very bad baselines, or that were taken when the pointing was poor, were thrown out and the remainder averaged, resulting in an on-source integration time of between 10 and 20 min per point. The spectra were binned to 13 km s^{-1} resolution, yielding an rms noise (T_a^*) of 0.01 K.

5.2.3 The ^{13}CO J=1–0 data

The ^{13}CO J=1–0 observations were made with the 45-m telescope of the Nobeyama Radio Observatory, Japan, during two observing runs on 28–30 April 1989 and 11–16 May 1990. The 1989 run was partially affected by high winds and the 1990 run by low cloud, but about 56 hours in total of usable observing time was achieved.

The beamsize of the 45-m at the frequency of ^{13}CO J=1–0 (110 GHz) is 17″, corresponding to ~410 pc at the distance of Maffei 2. We used an 85–115 GHz Schottky receiver, which gave system temperatures of ~700 K in 1989, and 800–900 K in 1990.

The backend was two arrays of 2048-channel acousto–optical spectrometers (AOS) with bandwidths of 250 MHz (680 km s^{-1} at 110 GHz). The velocity resolution of the AOS was 0.33 km s^{-1}.

Observation was by position switching, with one off position observed for every three on positions, for more efficient use of allocated time. The adopted central position, reference position and LSR velocity were all as for the J=2–1 observations. A typical observation consisted of 30 × 2-min cycles – a total of 15 min on source per point. Each map point was observed between four and eight times.

Pointing was checked every 1–1.5 hr using 40-GHz observations of the nearby SiO maser source SPer (RA = $02^h\ 19^m\ 15.15^s$, Dec. = 58° 21′ 34.5″). The pointing accuracy in 1989 was affected by strong wind. The rms pointing error was found to be 7.5″ (azimuth), 4.3″ (elevation) in 1989 and 3.5″ (azimuth), 3.4″ (elevation) in 1990. During much of the 1990 observations, the drift of the telescope in azimuth was found to be quite systematic and linear with time, and this fact was used on occasion to apply a small (few arcsec) correction during an observation. Averaging many scans together somewhat reduces the impact of poor pointing, although the resulting effective beamsize is probably slightly greater than 17″ .

Calibration by the chopper-wheel method was carried out several times during the course of a 1-hr observing sequence, yielding temperatures on the T_a^* scale and estimated as accurate to ≃15% (N. Nakai, private communication).

During the 1989 run, 14 positions were observed in ^{13}CO J=1–0, at a grid spacing of 7.5″, corresponding to existing ^{12}CO 1–0 data (Nakai *et al.*, in preparation). The spectra were taken on a rotated RA–Dec. grid, oriented at 30° east of north – the position angle of the major axis of Maffei 2 (Table 5.1) – and extending to ±30″ along the major axis and ±15″ along the minor axis. During the 1990 run, these positions were reobserved, plus four additional ones. The three central positions, (0,0), (–7.5,0) and (7.5,0) were previously observed at high signal-to-noise ratio by N. Nakai – making 21 profiles in all.

Data reduction was performed using the LINEPROC software package at Nobeyama. Each 30-s scan was inspected, those with bad baselines being discarded before the scans from each observation were averaged and linear baselines subtracted. Data taken just before a bad pointing check were also thrown out. The data from 1989 and 1990 were

compared. In most cases the line profiles and peak antenna temperatures agreed well – in the cases where they didn't, this was usually traced to poor pointing during the 1989 run and the affected scans were discarded. Including this source of uncertainty, antenna temperatures are estimated to be correct to ~15–20%. The spectra were binned over 60 channels (~20 km s^{-1}) leading to an average rms noise level (T_a^*) of 0.008 K.

Table 5.2: Observational details.

Transition	Frequency (GHz)	Telescope	Beamsize	Telescope efficiencies
^{12}CO J=2–1	230.537990	IRAM 30-m	13″	$F_{\rm eff}$=0.917[1] $B_{\rm eff}$=0.45
^{13}CO J=2–1	220.398682	IRAM 30-m	13″	$F_{\rm eff}$=0.881[1,3] $B_{\rm eff}$=0.45
^{13}CO J=1–0	110.201370	NRO 45-m	17″	$\eta_{\rm mb}$=0.45[2]

(1) $T_{\rm mb} = F_{\rm eff}\ T_a^*/B_{\rm eff}$ (for details of the IRAM calibration procedure, see Downes 1989). (2) $T_{\rm mb} = T_a^*/\eta_{\rm mb}$. (3) $F_{\rm eff}$ for the ^{13}CO J=2–1 observations was determined by a skydip during the run.

The telescope parameters relevant to the observations are presented in Table 5.2. Fig 5.1 compares the grid sizes and offsets observed with the IRAM and Nobeyama telescopes.

5.2.4 Results

Figs 5.2, 5.3 and 5.4 present the ^{13}CO J=1–0, ^{12}CO J=2–1 and ^{13}CO J=2–1 profiles at the observed positions in Maffei 2. The spectra are displayed on a scale of main-beam brightness temperature, $T_{\rm mb}$, which, for source dimensions of the order of the beamsize, represents the radiation temperature of the source convolved with the antenna pattern. For comparison, in Figs 5.5 and 5.6 are displayed the ^{12}CO J=1–0 and 2–1 spectra observed at the same grid positions as the ^{13}CO 1–0 and 2–1 data (the ^{13}CO J=1–0 profiles are from Nakai *et al.* in preparation). In Tables 5.3, 5.4 and 5.5 are summarized the derived parameters of the profiles at positions where the emission was well detected, namely, peak antenna temperature $T_{\rm mb}$, integrated intensity $I_{\rm CO}$, LSR velocity of the

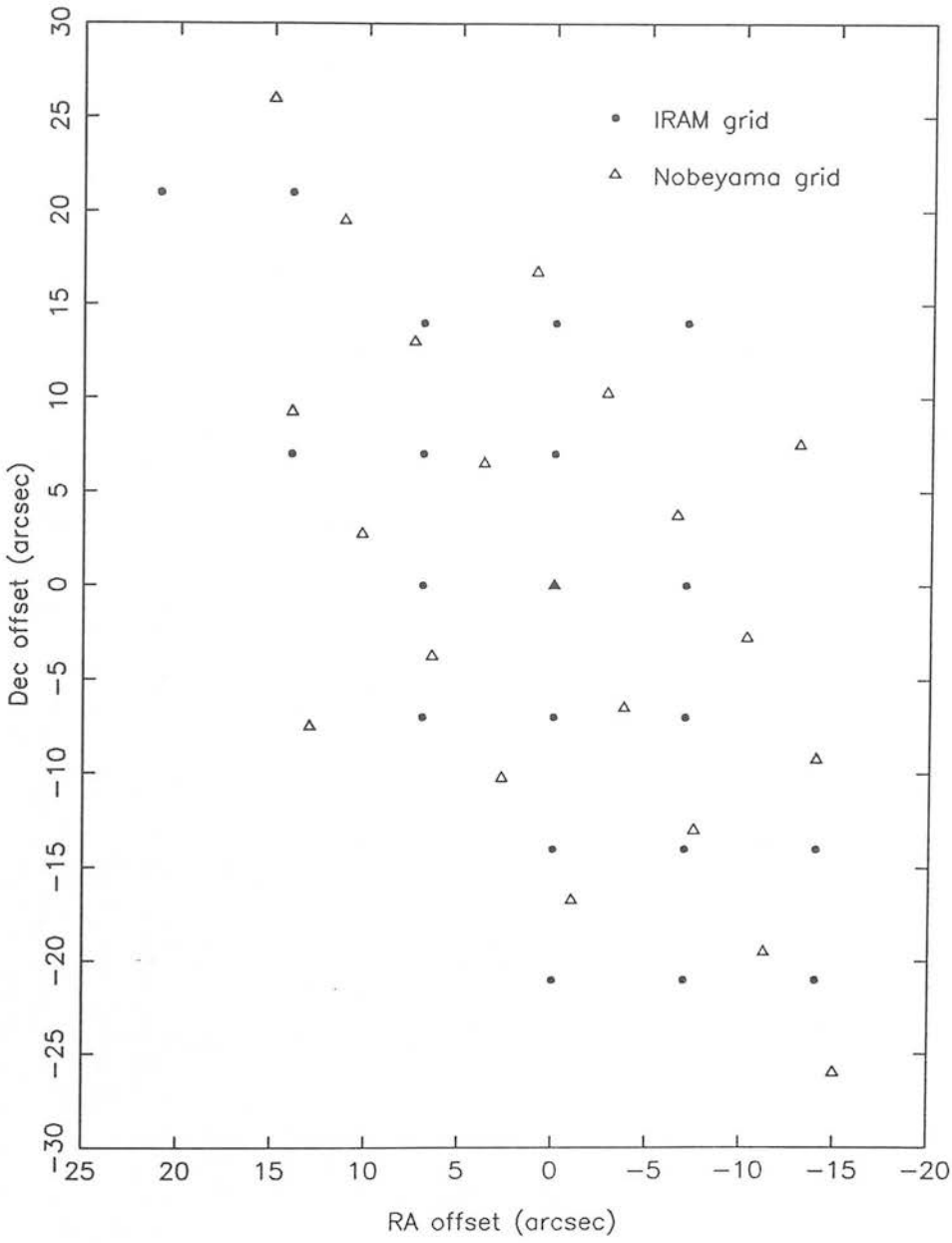

Figure 5.1: Offsets observed in ^{13}CO J=2–1 (filled circles) and ^{13}CO J=1–0 (open triangles) on the same grid, for comparison. The ^{12}CO J=2–1 observations were made on a regular grid extending to ±28″ in RA and +42″, −35″ in Dec.

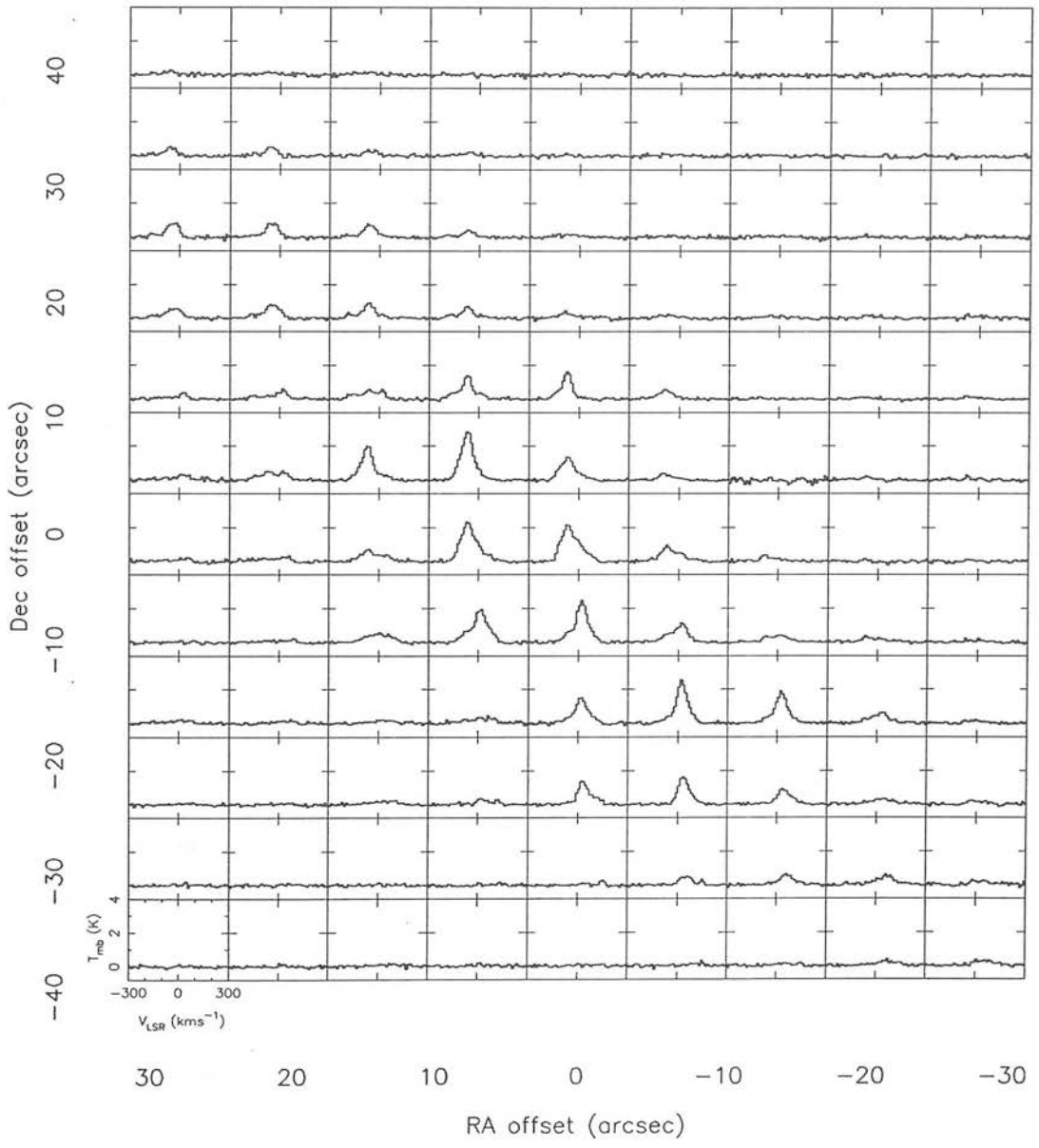

Figure 5.2: The observed ^{12}CO J=2–1 profiles from the central ∼60″ × 80″ of Maffei 2 (108 spectra). The profiles are presented in units of main-beam brightness temperature ($T_{\rm mb}$), binned over 13 km s^{-1}. Offsets are in RA and Dec. (arcsec) from the map centre at 1950 coordinates 02$^{\rm h}$ 38$^{\rm m}$ 8.5$^{\rm s}$, +59° 23′ 30″.

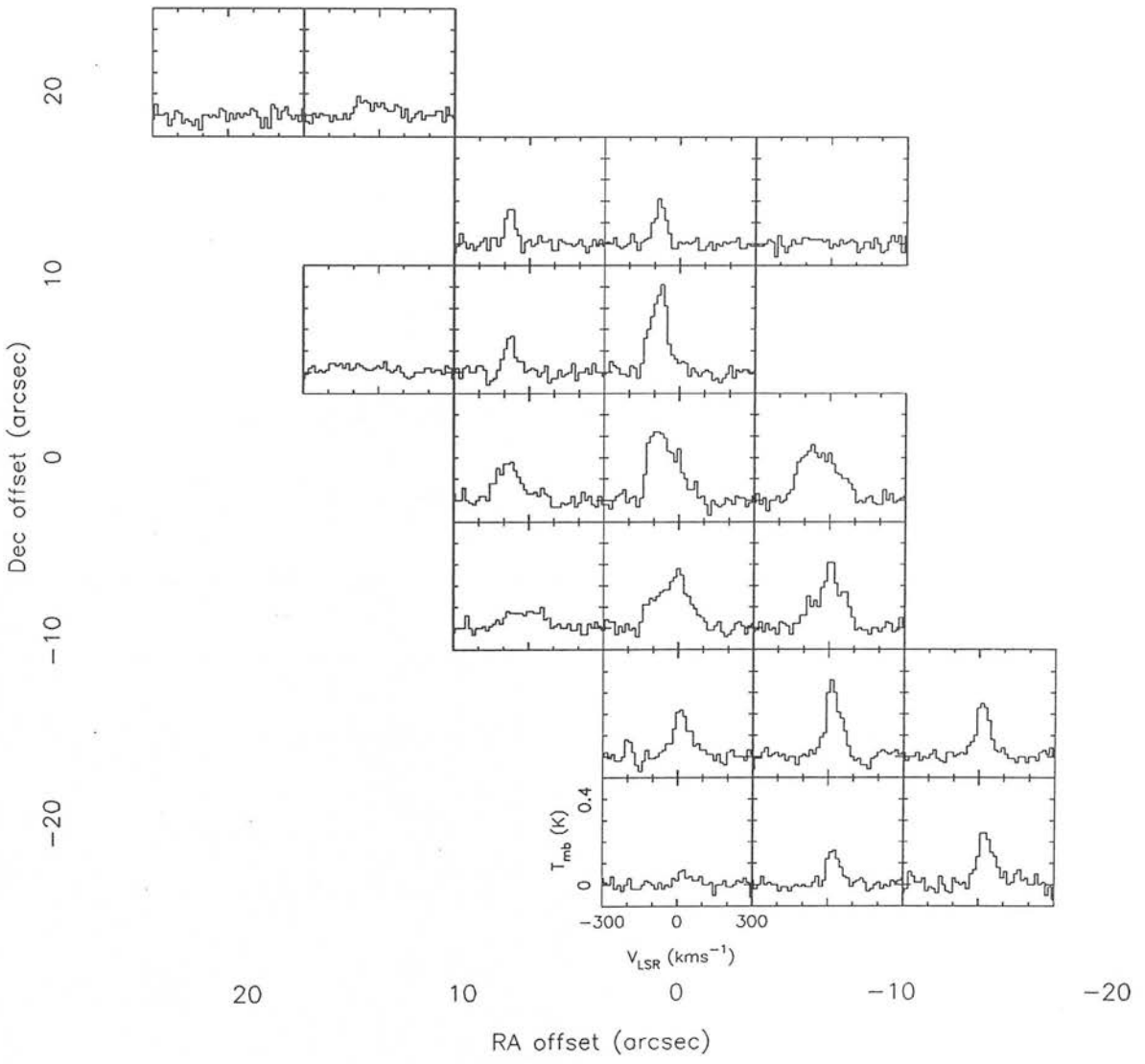

Figure 5.3: Observed ^{13}CO J=2–1 profiles from the central ∼40″ of Maffei 2, in units of main-beam brightness temperature ($T_{\rm mb}$). Offsets are in RA and Dec. (arcsec) from the map centre. The spectra are binned over 13 km s^{-1} to improve signal-to-noise ratio.

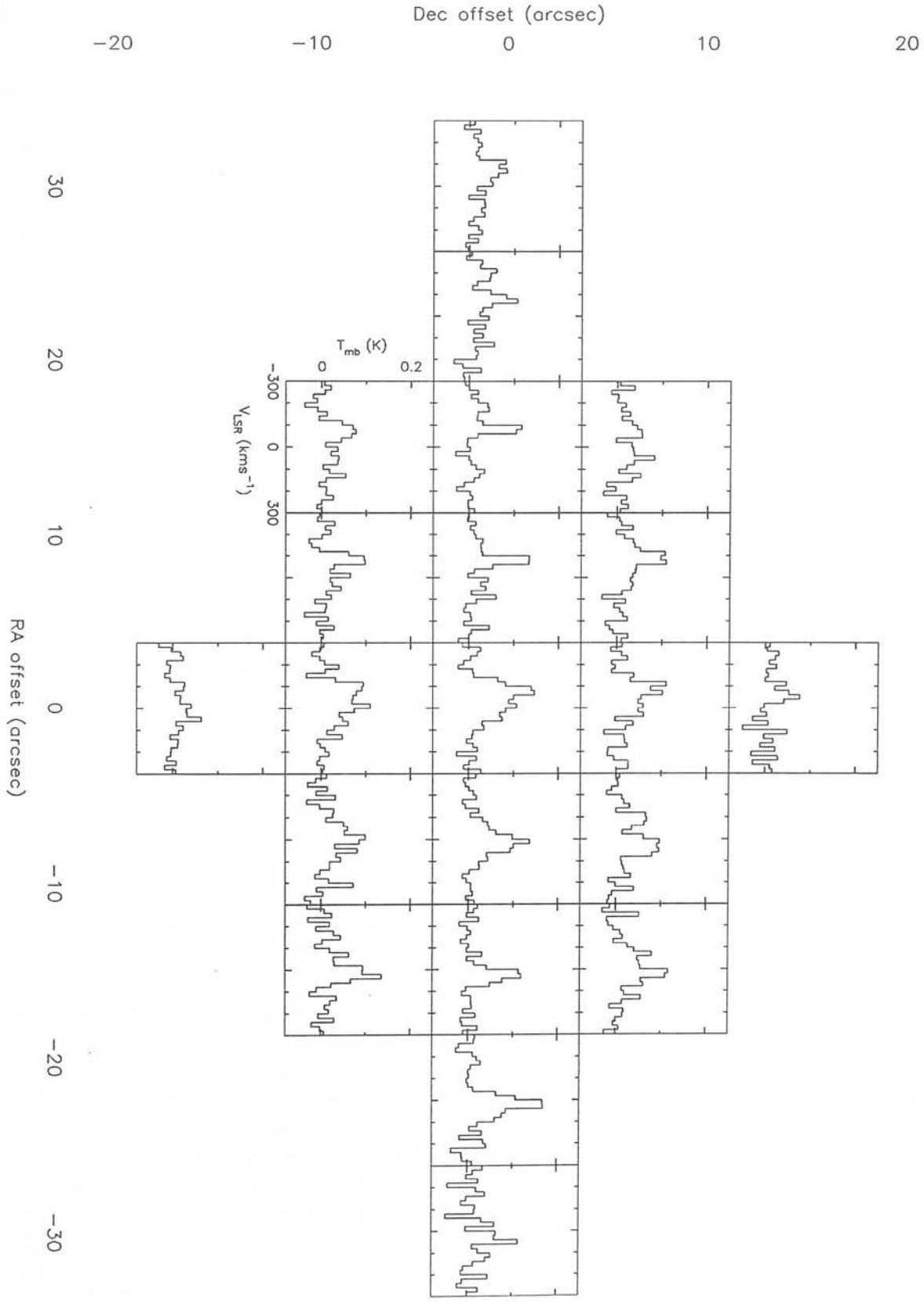

Figure 5.4: Observed ^{13}CO J=1–0 profiles from Maffei 2, in units of main-beam brightness temperature ($T_{\rm mb}$). The offsets are in arcseconds along the major and minor axes of the galaxy (PA=30°). The data have been binned over 20 km s^{-1}.

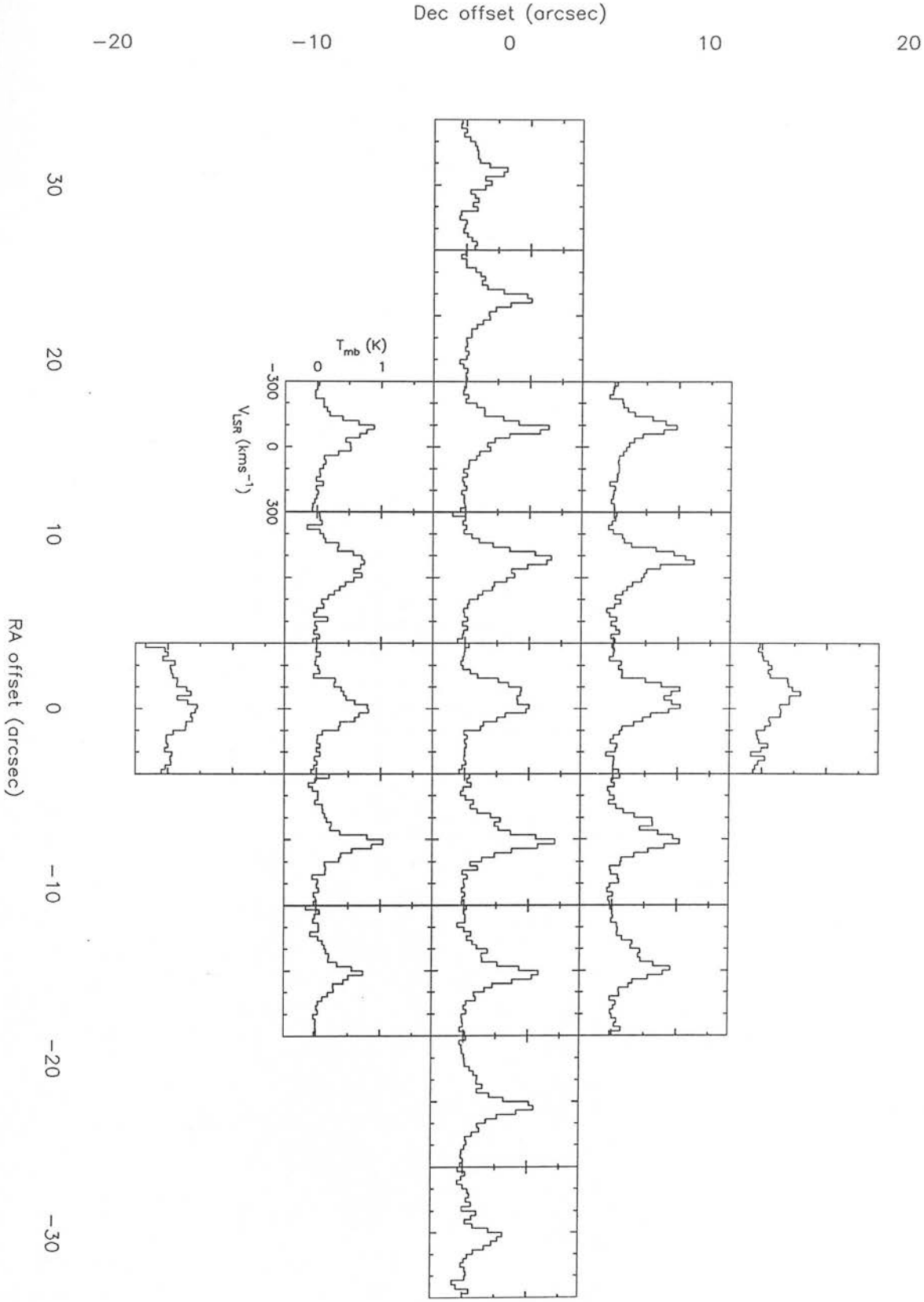

Figure 5.5: ^{12}CO J=1–0 profiles from the centre of Maffei 2, at offsets also observed in the ^{13}CO J=1–0 transition. The ^{12}CO data are from Nakai *et al.* (in preparation).

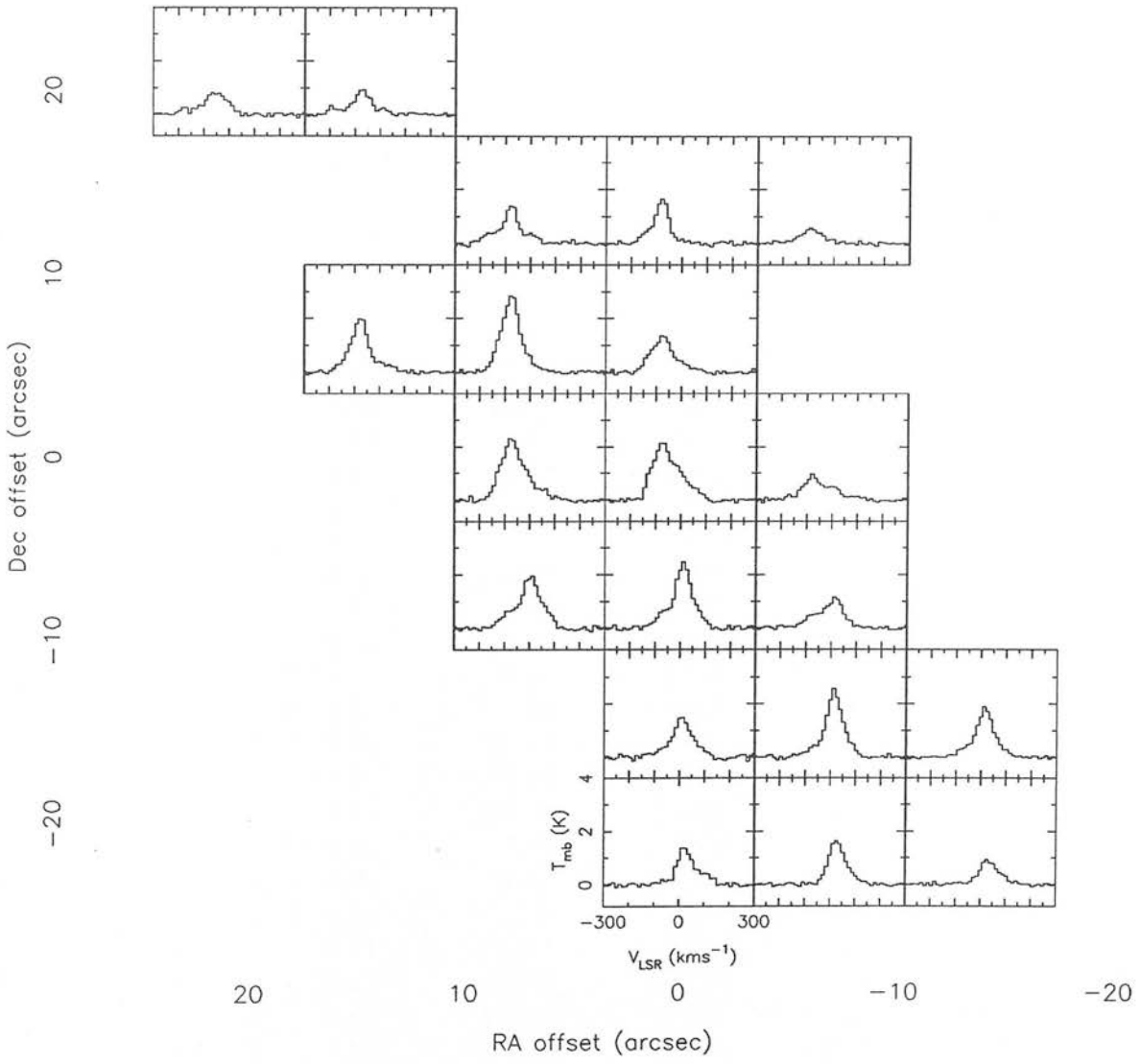

Figure 5.6: ^{12}CO J=2–1 profiles from the central ∼20″ of Maffei 2, at offsets also observed in the ^{13}CO J=2–1 transition (Fig. 5.3).

Table 5.3: Summary of the ^{12}CO J=2–1 observations.

Offset (arcsec)[1]		Peak T_{mb} (K)[2]	I_{CO} (K km s^{-1})[2,3]	v_{peak} (km s^{-1})[4]	Δv_{fwhm} (km s^{-1})[5]	rms noise (K)[6]
+28	+42	0.27	19.79	−63.6	72.7	0.07
+28	+35	0.53	40.58	−68.9	76.3	0.06
+21	+35	0.51	43.55	−70.7	84.9	0.05
+14	+35	0.36	30.72	−63.0	85.9	0.06
+ 7	+35	0.22	16.73	−65.3	75.8	0.05
+28	+28	0.85	81.80	−31.8	95.7	0.07
+21	+28	0.82	83.97	−56.5	102.6	0.06
+14	+28	0.81	76.09	−77.1	94.0	0.06
+ 7	+28	0.44	42.11	−75.3	94.7	0.05
+28	+21	0.57	72.69	−30.6	127.3	0.05
+21	+21	0.80	98.74	−63.5	123.3	0.05
+14	+21	0.95	99.63	−71.1	104.4	0.05
+ 7	+21	0.70	74.09	−83.4	105.9	0.06
0	+21	0.46	44.29	−93.5	96.2	0.06
− 7	+21	0.24	22.48	−74.8	93.9	0.05
−21	+21	0.23	21.09	−55.5	90.8	0.05
−28	+21	0.30	25.87	−81.1	86.6	0.05
+28	+14	0.39	31.21	+17.7	79.8	0.05
+21	+14	0.62	64.69	+14.4	105.1	0.05
+14	+14	0.59	88.35	−67.5	148.9	0.05
+ 7	+14	1.39	138.72	−74.8	99.9	0.05
0	+14	1.64	129.36	−78.8	78.8	0.05
− 7	+14	0.58	58.94	−90.9	100.9	0.05
−28	+14	0.23	17.95	−85.4	78.9	0.03
+28	+ 7	0.35	44.37	+ 2.6	127.7	0.08
+21	+ 7	0.55	91.69	+12.8	167.5	0.05
+14	+ 7	2.00	197.49	−73.5	98.7	0.05
+ 7	+ 7	2.89	281.54	−73.6	97.5	0.05
0	+ 7	1.39	151.10	−73.8	108.2	0.05
− 7	+ 7	0.44	36.69	−101.7	83.9	0.05
−21	+ 7	0.25	21.58	−77.5	85.3	0.05
−28	+ 7	0.30	18.95	−75.7	62.9	0.05
+21	0	0.35	46.82	+48.8	134.8	0.06
+14	0	0.72	96.90	−70.5	135.2	0.06
+ 7	0	2.35	270.95	−73.9	115.1	0.05
0	0	2.19	266.49	−72.5	121.8	0.05
− 7	0	0.97	115.91	−77.8	119.9	0.05
−14	0	0.36	32.91	−87.1	92.1	0.05
+14	− 7	0.58	94.55	− 0.7	162.5	0.05
+ 7	− 7	1.99	225.19	+ 8.3	112.9	0.05
0	− 7	2.47	239.64	+12.9	97.2	0.06
− 7	− 7	1.17	133.15	+15.7	114.1	0.05
−14	− 7	0.39	64.77	+ 4.7	163.6	0.05
−21	− 7	0.37	42.98	−78.0	117.1	0.05

Table 5.3: – continued

Offset (arcsec)[1]		Peak T_{mb} (K)[2]	I_{CO} (K km s^{-1})[2,3]	v_{peak} (km s^{-1})[4]	Δv_{FWHM} (km s^{-1})[5]	rms noise (K)[6]
+28	−14	0.27	39.05	+ 7.9	147.3	0.05
+21	−14	0.25	22.42	+65.8	89.1	0.05
+14	−14	0.22	33.07	+13.0	149.0	0.05
+ 7	−14	0.45	64.79	+54.1	144.3	0.07
0	−14	1.52	153.55	+ 6.6	101.3	0.06
− 7	−14	2.58	224.29	+13.6	86.9	0.05
−14	−14	1.91	175.95	+15.3	92.1	0.05
−21	−14	0.61	75.13	+23.8	122.4	0.05
−28	−14	0.21	14.55	−12.8	69.5	0.05
+14	−21	0.26	46.82	+29.2	181.4	0.05
+ 7	−21	0.35	39.69	+11.2	113.0	0.05
0	−21	1.44	129.99	+18.8	89.9	0.05
− 7	−21	1.64	143.84	+24.9	87.9	0.05
−14	−21	0.93	92.68	+25.3	99.3	0.05
−21	−21	0.31	47.63	+43.8	153.8	0.05
−28	−21	0.23	19.81	−31.2	84.9	0.05
− 7	−28	0.51	54.59	+55.8	107.7	0.05
−14	−28	0.64	65.24	+49.0	101.8	0.05
−21	−28	0.60	71.16	+50.3	117.7	0.05
−28	−28	0.30	37.82	−23.6	127.2	0.07
−21	−35	0.38	33.46	+61.8	88.2	0.06
−28	−35	0.34	41.27	+48.5	121.1	0.06

(1) Offsets in RA, Dec., with respect to the map centre: RA (1950) = $02^h\ 38^m\ 08.5^s$, Dec(1950) = $+59°\ 23'\ 30''$. (2) Calibration uncertainty of ±15–20% (e.g. Mauersberger *et al.* 1988). (3) Calculated from $I_{CO} = \int T_{mb}\, dv$. (4) Error of ±5 km s^{-1}. (5) Calculated from $\Delta v_{fwhm} = I_{CO}/T_{mb}$ which is almost exact for a Gaussian line profile. (6) Binned over 13 km s^{-1}. For positions at which ^{12}CO J=2–1 was not detected, the average rms noise was 0.06 K.

line peak, and FWHM of the line. Contour maps of integrated intensity and peak antenna temperature for the ^{12}CO J=2–1 transition are shown in Figs 5.7 and 5.8. In Fig. 5.9 the ^{12}CO J=2–1 map is compared with contour maps of ^{12}CO 1–0 single-dish and interferometer emission, 2, 10, 800 μm and radio continuum, and Hα line emission (Seaquist *et al.* 1976; Ho *et al.* 1989; Ishiguro *et al.* 1989; Nakai *et al.*, in preparation; P. McCarthy, unpublished; M. Mountain, unpublished; Chapter 4).

Table 5.4: Summary of the ^{13}CO J=2–1 observations.

Offset (arcsec)[1]		Peak T_{mb} (K)[2,3]	I_{CO} (K km s^{-1})[3,4]	v_{peak} (km s^{-1})[5]	Δv_{fwhm} (km s^{-1})[6]	rms noise (K)[7]
+21	+21	nd	nd	nd	nd	0.03
+14	+21	0.09	7.61	−79.9	86.4	0.03
+ 7	+14	0.18	8.29	−75.2	46.1	0.02
0	+14	0.22	10.79	−79.4	49.5	0.02
− 7	+14	nd	nd	nd	nd	0.02
+14	+ 7	nd	nd	nd	nd	0.02
+ 7	+ 7	0.19	8.17	−74.3	43.9	0.02
0	+ 7	0.42	32.24	−71.7	77.1	0.03
+ 7	0	0.19	20.82	−72.3	110.7	0.02
0	0	0.33	42.24	−86.4	129.6	0.02
− 7	0	0.26	42.45	−70.2	164.6	0.03
+ 7	− 7	0.10	14.88	−11.3	143.0	0.02
0	− 7	0.29	38.59	− 0.0	135.4	0.02
− 7	− 7	0.33	34.05	+ 5.9	103.8	0.02
0	−14	0.22	19.01	+ 8.7	86.8	0.03
− 7	−14	0.36	23.83	+13.0	65.8	0.02
−14	−14	0.25	18.03	+12.7	72.4	0.02
0	−21	0.07	4.12	+22.0	57.9	0.03
− 7	−21	0.16	10.68	+21.6	66.4	0.02
−14	−21	0.24	20.13	+20.6	82.8	0.03

(1) Offsets in RA, Dec. with respect to the map centre: RA (1950) = 02^h 38^m 08.5^s, Dec.(1950) = +59° 23′ 30″. (2) nd = no detection. (3) Calibration uncertainty of ±15–20% (e.g. Mauersberger *et al.* 1988). (4) Calculated from $I_{CO} = \int T_{mb} dv$. (5) Error of ±5 km s^{-1}. (6) Calculated from $\Delta v_{fwhm} = I_{CO}/T_{mb}$ which is almost exact for a Gaussian line profile. (7) Binned over 13 km s^{-1}.

5.3 Morphology of the molecular gas

The ^{12}CO J=2–1 integrated intensity map (Fig 5.7) shows that the molecular emission in Maffei 2 is strongly concentrated in the central ∼30″ by 40″ and elongated, with major axis position angle ∼34°. Underlying the central concentration is lower level (disc?) emission extended along the major axis. The ^{12}CO J=2–1 emission is spatially consistent, within the pointing errors, with morphology seen in the single-dish ^{12}CO J=1–0 map (Nakai *et al.*, in preparation) and also the 800 μm dust continuum map (Chapter 4). The nuclear structure is resolved by the IRAM beam along both the major and minor axes – the long, narrow molecular bar seen by Ishiguro *et al.* (1989) in their interferometer map (Fig 5.9) is not apparent in the 2–1 data.

Table 5.5: Summary of the ^{13}CO J=1–0 observations.

Offset (arcsec)[1]		Peak T_{mb} (K)[2]	I_{CO} (K km s^{-1})[2,3]	v_{peak} (km s^{-1})[4]	Δv_{fwhm} (km s^{-1})[5]	rms noise (K)[6]
0.0	0.0	0.16	20.39	−68.7	124.3	0.02
+7.5	0.0	0.17	11.14	−68.7	66.3	0.01
+15.0	0.0	0.13	8.31	−68.7	62.0	0.01
+22.5	0.0	0.13	12.67	−68.7	95.9	0.02
+30.0	0.0	0.12	12.62	−68.7	104.3	0.02
− 7.5	0.0	0.15	14.87	+20.9	100.5	0.01
−15.0	0.0	0.14	8.48	+30.9	58.8	0.01
−22.5	0.0	0.19	15.75	+40.9	84.2	0.02
−30.0	0.0	0.14	8.92	+50.8	62.8	0.03
+ 7.5	+ 7.5	0.13	14.52	−78.7	110.8	0.02
0.0	+ 7.5	0.12	12.80	−108.6	109.4	0.02
− 7.5	+ 7.5	0.14	14.79	+20.9	108.8	0.02
+ 7.5	− 7.5	0.11	8.55	−68.7	78.4	0.02
0.0	− 7.5	0.12	17.09	− 8.9	144.8	0.02
− 7.5	− 7.5	0.11	12.09	− 8.9	110.9	0.03
0.0	+15.0	0.12	4.18	−38.9	35.1	0.02
0.0	−15.0	0.08	5.31	+60.8	70.8	0.01
+15.0	+ 7.5	0.10	10.36	+60.8	102.6	0.02
−15.0	+ 7.5	0.15	14.66	+30.9	100.4	0.02
+15.0	− 7.5	0.11	9.87	−58.8	91.4	0.01
−15.0	− 7.5	0.16	11.18	+30.9	71.2	0.02

(1) Offset along major and minor axes of Maffei 2 (PA=30°) with respect to map centre: RA (1950) = 02^h 38^m 08.5^s, Dec(1950) = +59° 23′ 30″. (2) Calibration error ±15–20% (N. Nakai, private communication). (3) Calculated from $I_{CO} = \int T_{mb}\, dv$. (4) Error of ±10 km s^{-1}. (5) Calculated from $\Delta v_{fwhm} = I_{CO}/T_{mb}$, which is almost exact for a Gaussian line profile. (6) Binned over 20 km s^{-1}.

In Fig. 5.10 are shown representative slices along the major and minor axes of the integrated intensity map. The major axis slice shows one peak, north-east of the nucleus, with a plateau to the south-west. To estimate the extent of the emission, the major axis FWHM was calculated, where the 'maximum' is here defined as halfway between the 'peak' and the 'plateau'. The major axis extent is found to be ∼38″ which, after deconvolving the 13″ beam gives an approximate source size of ∼36″ by 13″ – or a major-to-minor axis ratio of 2.8. The inclination of Maffei 2 is about 65° – a thin disc viewed at this inclination would have an axial ratio of 2.4. Thus the ^{12}CO J=2–1 integrated intensity map is consistent with a highly inclined, thin disc of FWHM ∼36″

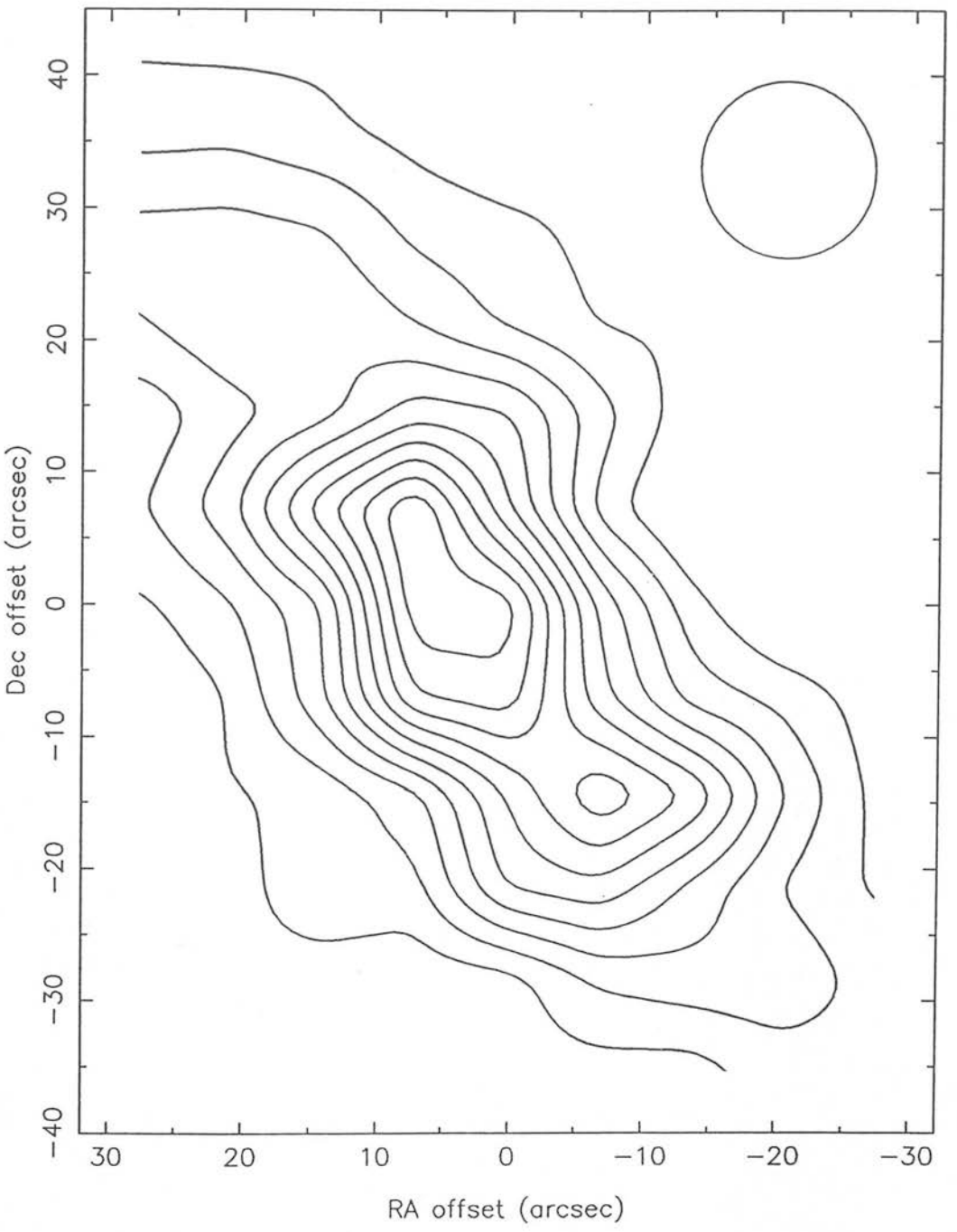

Figure 5.7: The integrated intensity ($\int T_{\rm mb}\ {\rm d}v$) of ^{12}CO J=2–1 emission from the central arcminute of Maffei 2. The contour levels are 25 K km s^{-1} from a base level of 25 K km s^{-1}. The 13″ FWHM beam is represented by an open circle. Offsets are in arcsec (RA, Dec.) from the map centre at RA(1950)=02$^{\rm h}$ 38$^{\rm m}$ 08.5$^{\rm s}$, Dec.(1950)=+59° 23′ 30″.

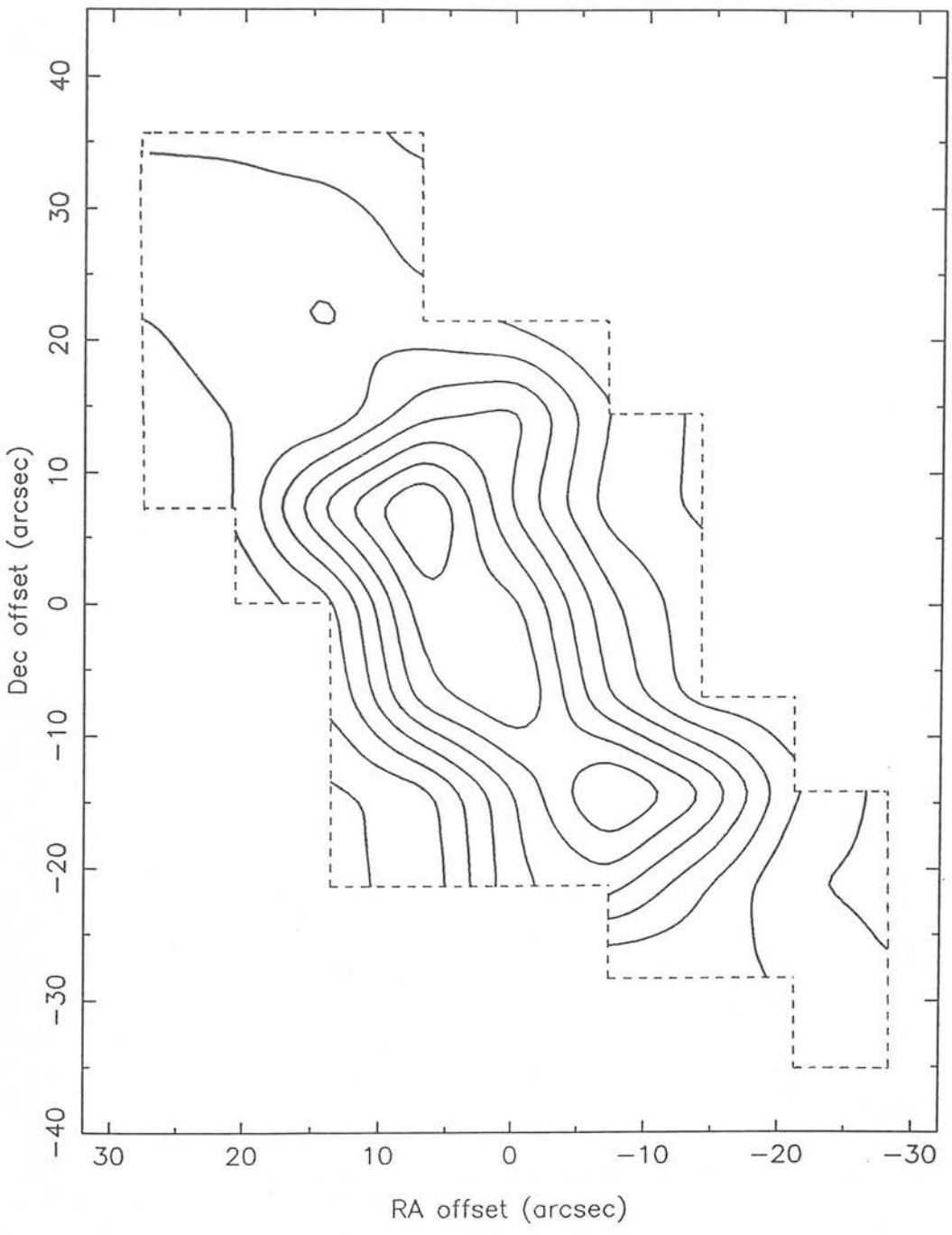

Figure 5.8: Peak main-beam brightness temperature for the ^{12}CO J=2–1 transition. The lowest contour is 0.3 K, and the contour interval is 0.3 K. The offsets are in RA, Dec. from the map centre as in Fig.5.7.

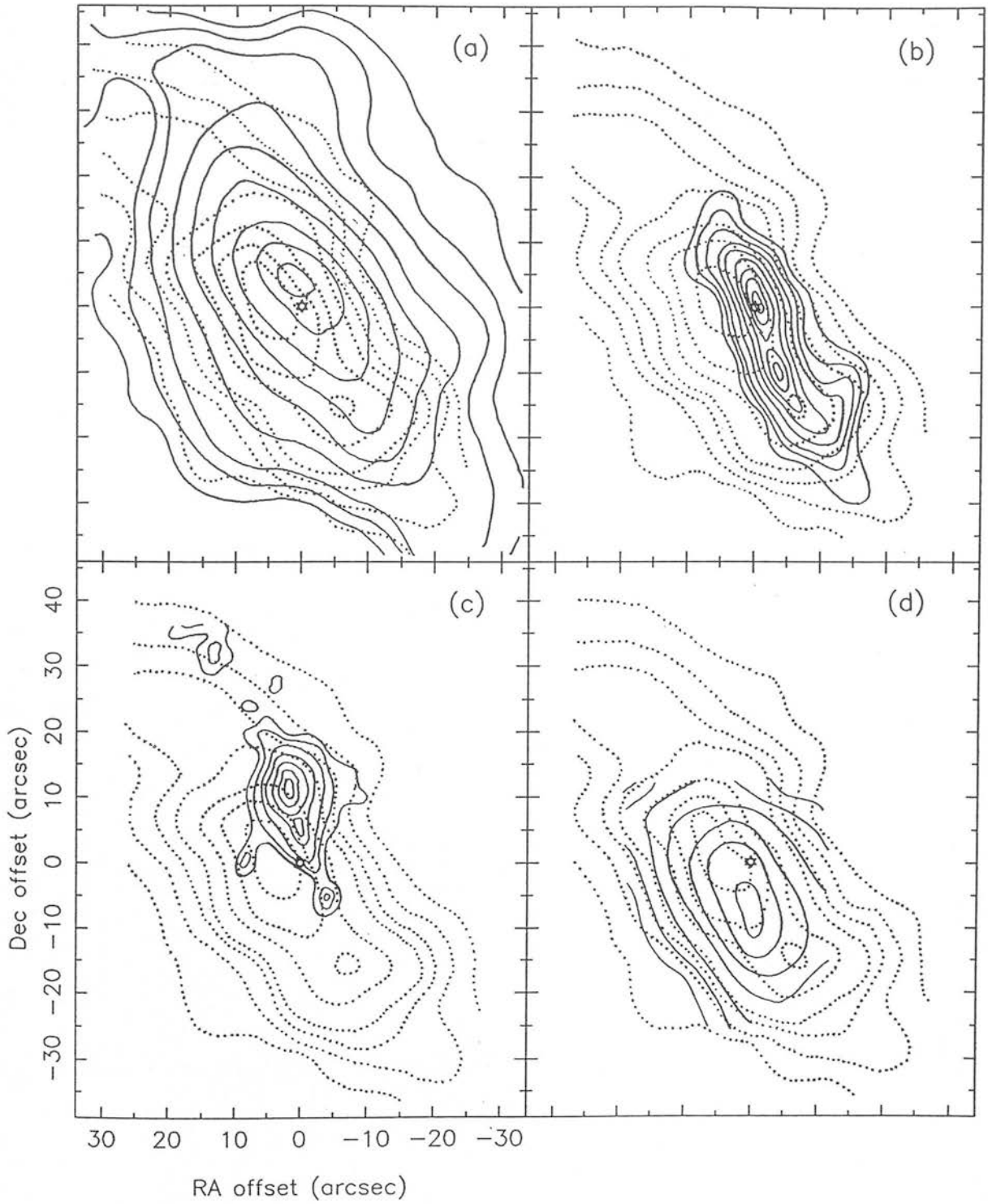

Figure 5.9: The ^{12}CO J=2–1 structure of Maffei 2 compared to: (a) ^{12}CO J=1–0 single-dish data (Nakai *et al.* in preparation); (b) ^{12}CO J=1–0 interferometer data (Ishiguro *et al.* 1989); (c) Hα line (P. McCarthy, unpublished); (d) 800 μm dust continuum (Chapter 4); (e) 2 μm continuum (M. Mountain, unpublished); (f) 3.7-cm radio continuum (Seaquist *et al.* 1976); (g) 10 μm continuum (Ho *et al.* 1990), and (h) ^{13}CO J=1–0 interferometer data (Hurt *et al.* 1991).

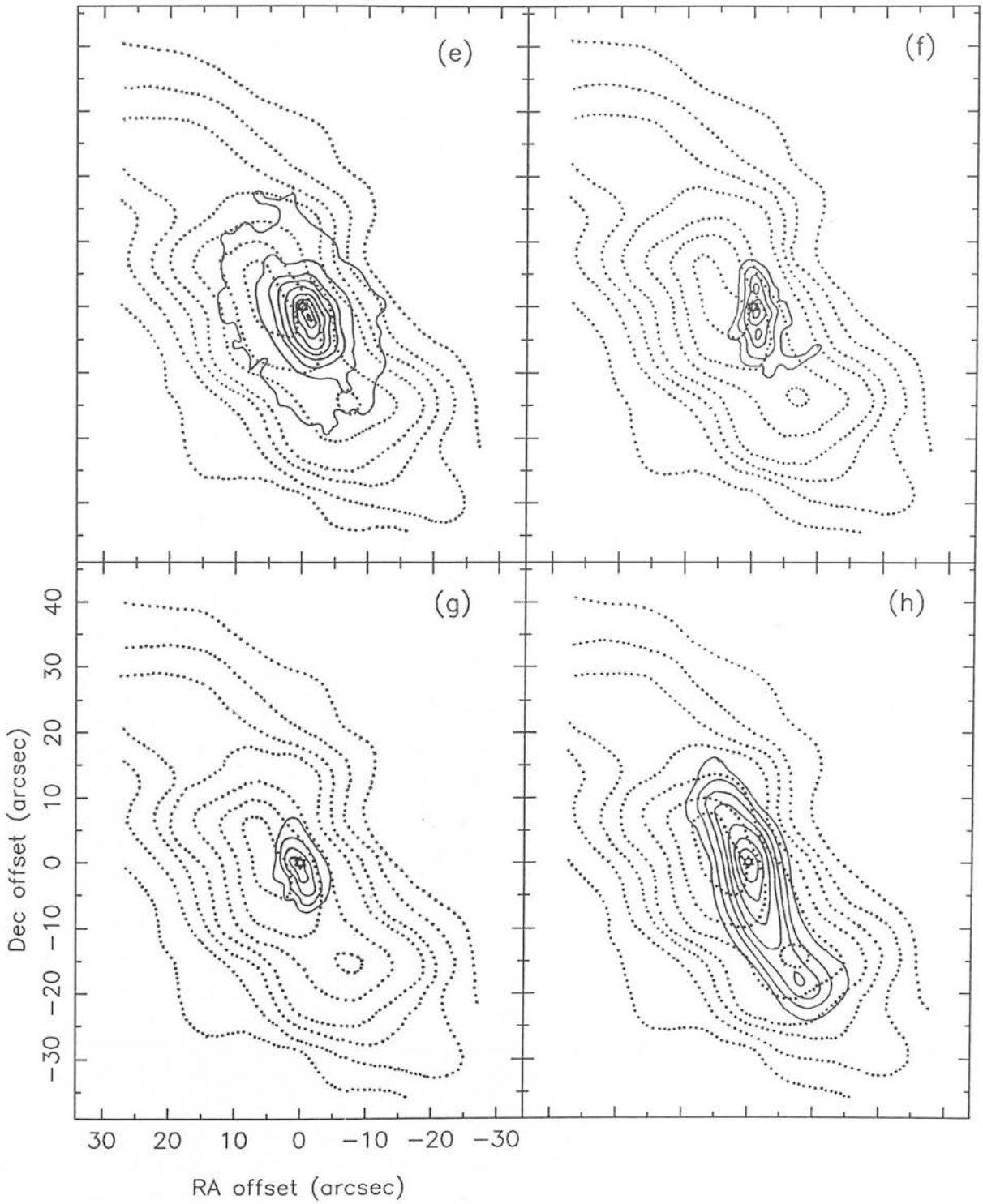

Figure 5.9 – continued

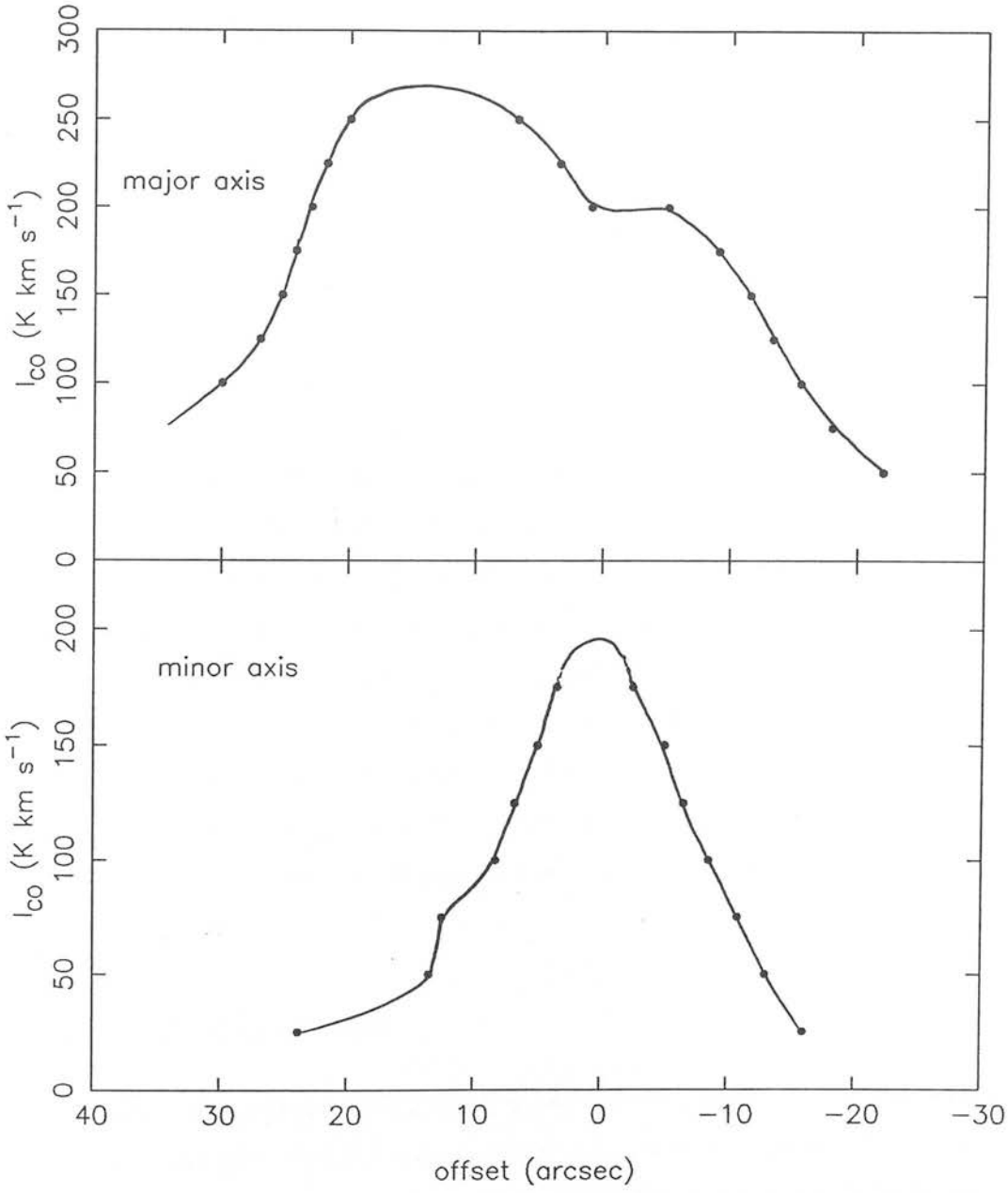

Figure 5.10: ^{12}CO J=2–1 integrated intensity slices along the major and minor axes of Maffei 2, taken from the contour map in Fig. 5.7, along a line at PA 30° through a point 10″ south-west of the map centre.

– or a radius of 440 pc at the assumed distance to Maffei 2 of 5 Mpc. This 'nuclear disc' is superimposed on weaker, more extended emission, possibly from the main galactic disc. This type of 'nuclear disc plus galactic disc' morphology has been observed in other infrared-bright spirals, e.g. NGC 891 (Sofue *et al.* 1987), and may reflect the increased star-forming activity near the nuclei of such galaxies.

The 'peak + plateau' morphology of the emission along the major axis does not appear in the 17″-resolution ^{12}CO J=1–0 map (Fig 5.9a). One possible interpretation is that there are two peaks, merged by the beam. It would be tempting to identify a double-peaked structure with a ring viewed nearly edge-on, such as has been postulated in the case of M82 (Nakai *et al.* 1987) – indeed, such a ring is suggested in Maffei 2 by the interferometer observations of Ishiguro *et al.* (1989). However, the peaks observed by Ishiguro *et al.* are offset from those implied in the 2–1 map by ∼5″, and are much closer together. An alternative picture is that we are seeing a concentration of molecular emission superimposed on the nuclear disc, as a result of increased gas excitation or column density to the north-east of the map centre. This interpretation will be discussed later in the context of the CO line ratios and deduced excitation conditions of the gas. It is interesting that the 'peak + plateau' morphology is also seen in a recent ^{13}CO J=1–0 interferometer map (Hurt & Turner 1991). Hα line emission also, tracing gas in HII regions surrounding young stars, is concentrated to the north and east, although the Hα morphology may be affected by patchy extinction in front of or within this heavily obscured galaxy.

5.4 Gas kinematics

Observations of millimetre-wave line profiles that are well resolved in velocity are invaluable for investigating the kinematics of galaxies, free from the effects of dust extinction. This is particularly true for Maffei 2 which, being low down in the Galactic plane, is inaccessible to optical spectroscopy.

The CO line profiles from an extragalactic system such as Maffei 2 are composed of emission from many clouds within the beam. For example, the 13″ IRAM beam covers a region >300 pc across at the distance of Maffei 2, whereas the largest Galactic GMC complexes have sizes ≤80 pc (Sanders, Scoville & Solomon 1985). The emission

contributing to a particular profile can be thought of as originating from a population of clouds rotating as a whole around the galaxy with a velocity determined by their gravitational potential, but possessing also a velocity dispersion – both individual internal velocity dispersion of a particular cloud or cloud complex, and cloud–cloud dispersion within the population. These dispersions are affected by the injection and redistribution of kinetic energy within the region. Energy is injected via stellar winds, supernovae and HII regions, and redistributed through cloud–cloud collisions and interactions, triggered star formation and various emission mechanisms. There may also be large-scale expansion or outflow of gas.

The detailed shape of the profiles is a result of differing physical and excitation conditions of the gas. Double or multiple peaks may result when several kinematically distinct emission regions are present within a beam, resulting in large-scale variation in the motions of clouds.

In the following sections, it is assumed that, along the major axis at least, the velocity of the line peak is representative of the galactic rotational velocity at the centre of the beam, and the linewidth is due both to the velocity dispersion of the clouds, and to the effect of observing a steeply rising rotation curve with a large beam. Any expansion or contraction in the plane of the galaxy will not show up in the major-axis velocities, as such motions will have no radial component.

Tables 5.3 to 5.5 give the peak velocity and FWHM of the ^{12}CO J=2–1, ^{13}CO J=2–1 and ^{13}CO J=1–0 lines at each of the observed positions. The velocity structure of the ^{12}CO J=2–1 profiles becomes quite complex in the extreme north-east and south-west of the mapped region, with double-peaked profiles indicating the presence of several velocity components within the beam. Possibly this is connected with the start of spiral arms seen in radio continuum emission (Seaquist *et al.* 1976) or with the start of a nuclear bar-like morphology (e.g. Ishiguro *et al.* 1989).

5.4.1 The velocity field of the gas

Fig. 5.11 shows a sequence of channel maps for the ^{12}CO J=2–1 emission, integrated over 30 km s^{-1} wide velocity ranges, from –210 to 150 km s^{-1}. The rotation of the galaxy shows up clearly, with the peak integrated intensity shifting from the north-east to the south-west as the velocity goes from negative to positive. Fig. 5.12 shows the

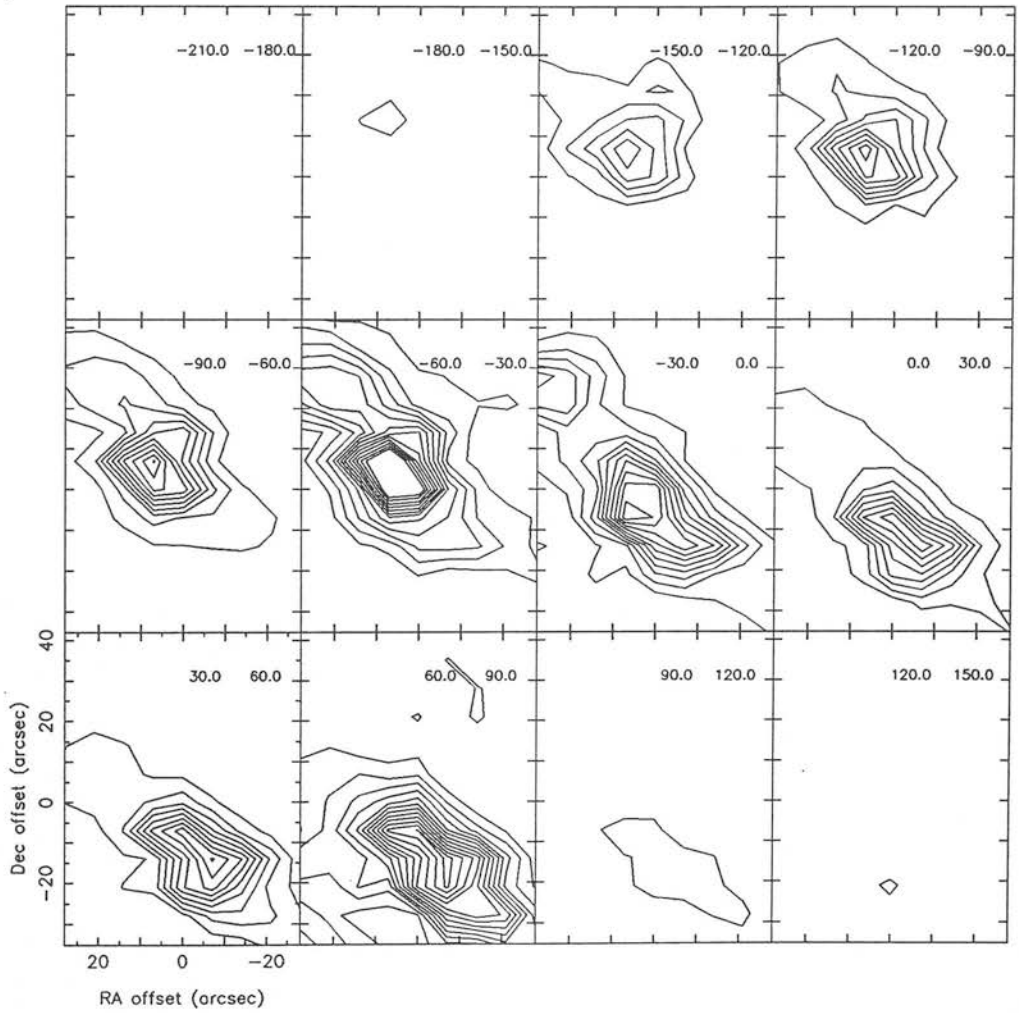

Figure 5.11: ^{12}CO J=2–1 channel maps, showing integrated intensity over 30 km s^{-1} intervals, from –210 to 150 km s^{-1}. The rotation of the galaxy is clearly seen.

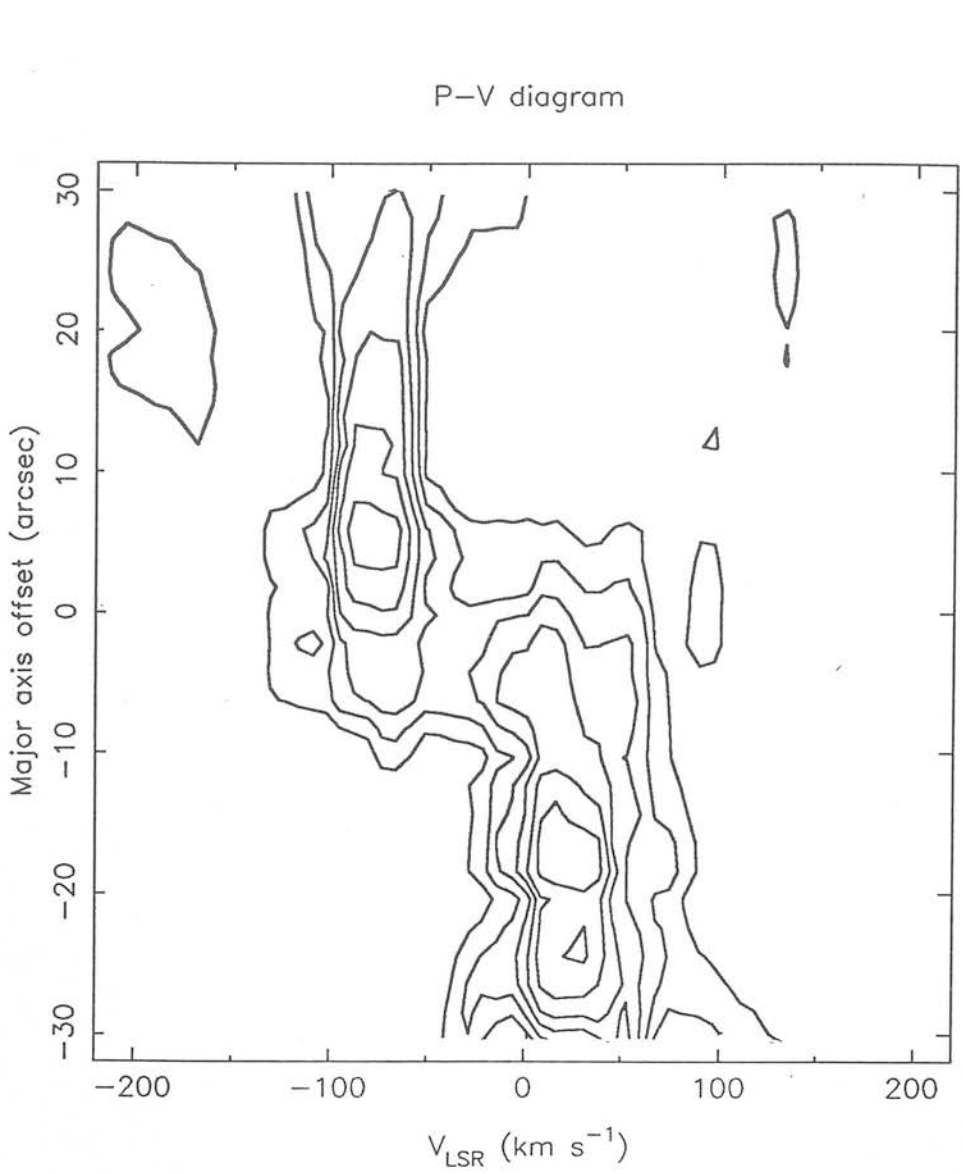

Figure 5.12: Position–velocity diagram for the ^{13}CO J=1–0 profiles observed along the major axis of Maffei 2.

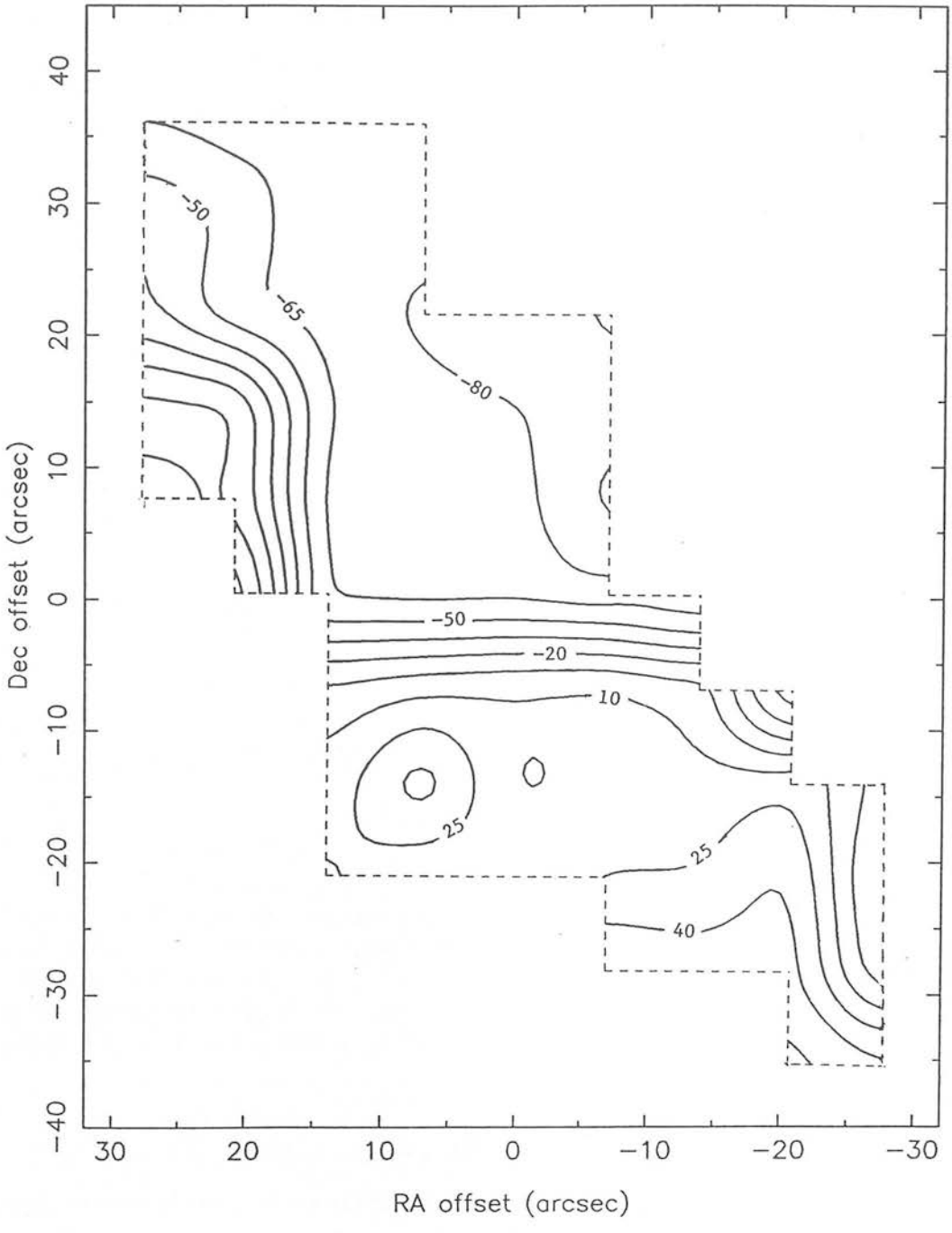

Figure 5.13: The velocity field of the central region of Maffei 2, calculated from the peak velocities of the ^{12}CO J=2–1 profiles. Note the steep velocity gradient in the central $\sim$10″, and the tilt of the isovelocity contours away from the minor axis in this region.

position–velocity diagram (P–V) constructed from the ^{13}CO J=1–0 profiles along the major axis, while Fig. 5.13 shows the velocity field of the molecular gas, derived from the peak velocities of the ^{12}CO J=2–1 profiles. In Fig. 5.14 the galaxy rotation curve is derived from the velocity field (corrected for galactic inclination) and compared to the peak velocities, along the major axis, of the ^{13}CO J=1–0 data (taken from the P–V diagram), and that of the central ^{13}CO J=2–1 profile. The agreement is very good, considering the sensitivity of the profiles to pointing errors, especially near the centre, and the weakness of the ^{13}CO emission, necessitating binning over large velocity ranges.

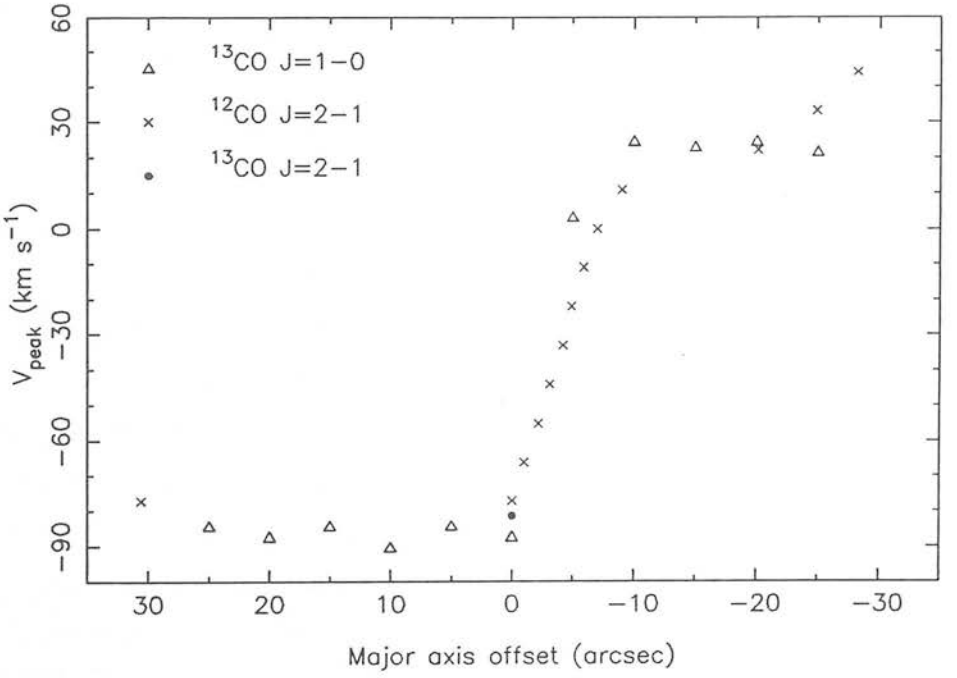

Figure 5.14: Peak velocity as a function of radius, calculated from the ^{13}CO J=1–0, ^{12}CO J=2–1 and ^{13}CO J=2–1 data. The ^{13}CO J=1–0 points (open triangles) come from the position–velocity diagram (Fig. 5.12), the ^{12}CO J=2–1 data (crosses) from the contours of the velocity field (Fig. 5.13), and the ^{13}CO J=2–1 point (filled circle) from the peak velocity of the observed profile at (0,0).

The velocity field, rotation curve and P–V diagram are typical of spiral galaxies – rigid rotation at the centre and differential rotation in the outer regions, characterized by a very steep velocity gradient in the central ~20″ (450 pc) as the velocity flips over from positive to negative, and almost constant velocity elsewhere. In the extreme north-east and south-west of the mapped region, the velocity field is distorted, probably by the complex double-peaked profiles emitted from these regions (see Fig. 5.2).

The velocity information along the major axis can be used to make an estimate

of the systemic velocity and dynamical centre of Maffei 2. If it is assumed that the velocity is approximately constant outside the rigidly rotating central region, then the mean of the velocities either side of the nucleus may be used to estimate a systemic velocity of $\sim$–29 km s^{-1}. This is within the range of previous estimates (e.g. Bottinelli *et al.* 1971; Shostak & Weliachew 1971; Spinrad *et al.* 1973; Wright & Seielstad 1973; Rickard *et al.* 1977a). The position of the dynamical centre may then be estimated from the ^{12}CO J=2–1 velocity field as lying $\sim$3″ south-west of the map centre, and spatially coincident with the peak of the stellar mass distribution as traced by the 2 μm continuum (Fig. 5.9).

The isovelocity contours in the central $\sim$20″ of Maffei 2 are not parallel to the minor axis, but instead are inclined by an angle of $\sim$ 30°, indicating a small minor axis velocity gradient. This effect has been noticed in the near-nuclear velocity fields of other nearby gas-rich spirals (e.g. Handa *et al.* 1990). One possible explanation is that the assumed major axis is not the true major axis of the galaxy, perhaps because of heavy, patchy extinction, although this seems unlikely in Maffei 2, as the CO major axis, presumably unaffected by extinction, is oriented at $\simeq$34°, whereas the apparent kinematical major axis has a position angle of $\sim$0°. An alternative explanation is that the misalignment of the physical and kinematical axes is due to large-scale expansion or contraction in the plane of the galaxy. In the case of Maffei 2, as argued by Ishiguro *et al.* (1989), if the south-western spiral arm-like structure seen in infrared and radio continuum (Spinrad *et al.* 1973; Seaquist *et al.* 1976) *is* a trailing spiral arm, then the inclination of Maffei 2 must be such that we are viewing the 'underside' of the disc, for the appearance of the arms to be consistent with the direction of rotation as determined from the peak velocities of CO. In such a configuration, the observed tilting of the isovelocity contours would be due to expansion, rather than contraction. Ishiguro *et al.* explain this naturally as an expanding molecular ring, created by a burst of star formation at the nucleus, a model which had previously been suggested for M82 also (Nakai *et al.* 1987). The individual J=1–0 profiles, however, show no conclusive evidence of a minor-axis velocity gradient. The gradient appears only in the contour plot of peak velocity, and therefore it is possible that the effect may be partly one of resolution – that of observing a highly inclined (and therefore narrow) structure with a moderately large beam. However, the ^{13}CO J=1–0 data are also quite noisy and have

been binned over a large velocity range (20 km s^{-1}), so, while the data do not show conclusive evidence of expansion, neither can it be ruled out.

5.5 Linewidths

One of the most striking characteristics of the observed CO profiles is their width – the FWHM of the ^{12}CO J=2–1 line is $\geq$70 km s^{-1} over the whole of the mapped region, exceeding 160 km s^{-1} at some near-central positions. Even the ^{13}CO profiles, which are presumably unaffected by any optical depth effects, typically exceed 60 km s^{-1} FWHM, reaching $\sim$150 km s^{-1} at the centre of the galaxy (see Figs 5.2–5.4). Such remarkable linewidths are typical of highly inclined galaxies, e.g. M82 (Nakai *et al.* 1987), and even in face-on spirals such as M83 and IC342 the linewidths are typically $\sim$100 km s^{-1} FWHM (Handa *et al.* 1990; Eckart *et al.* 1990).

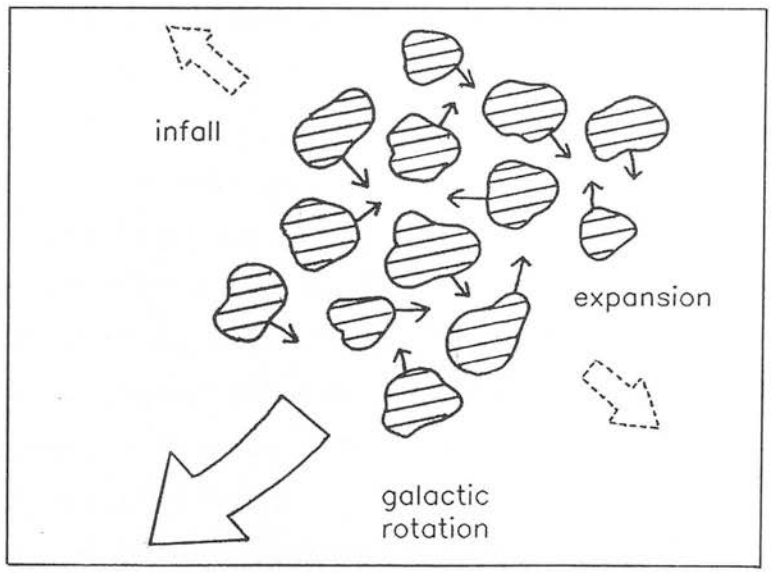

Figure 5.15: Schematic diagram of a molecular cloud ensemble observed with a large beam, demonstrating the components of the line velocity structure – galactic rotation, infall, expansion and cloud velocity dispersion (both inter- and intra-cloud).

As discussed in Section 5.4, the width of CO line profiles is determined by several mechanisms (Fig 5.15): (i) the rotation curve of the galaxy – the presence of a rotational velocity gradient will result in a 'spreading out' of the line as different clouds within the beam possess different rotational velocities; (ii) the internal and cloud–cloud dispersion

of the clouds within the beam, and (iii) any large-scale motion such as expansion or infall.

In the disc of the Milky Way, molecular gas is organized into clumpy giant molecular cloud complexes, with masses 10^{4-6} $M_{\odot}$, diameters of 40–100 pc and mean number densities $n(H_2)\sim200$ cm^{-3} (Sanders *et al.* 1985) (although higher densities exist on smaller scales). Within the complexes, individual clumps have supersonic internal velocity dispersions of 1–3 km s^{-1} FWHM, while cloud–cloud velocity dispersions inside a complex of $\sim$ 15 km s^{-1} and random motions of complexes with Δv $\sim$10 km s^{-1} are observed (Stark 1984; Falgarone & Puget 1988; Wilson & Walmsley 1989). The supersonic internal cloud velocity dispersions can be supported over long time-scales by the energy input of outflows from young stellar objects embedded in the clouds (Lada 1988). Within GMC complexes, energy is injected from supernovae and expanding HII regions, and an equilibrium established, with energy lost via inelastic cloud–cloud collisions (e.g. McKee & Ostriker 1977; Falgarone & Puget 1988). At the largest scales, gravitational scattering of complexes off each other in a differentially rotating disc can produce velocity dispersions $\sim$15 km s^{-1} (Jog & Ostriker 1988).

Conditions in the star-forming nuclear regions of a galaxy such as Maffei 2 will little resemble the relatively quiescent disc of a 'normal' spiral like the Milky Way. Vigorous massive star formation with accompanying mass outflow, stellar winds, HII regions and supernovae will result in a substantial injection of energy into the molecular gas as well as disruption and fragmentation of clouds. Molecular clouds in star-forming regions are therefore likely to be smaller, denser, warmer and faster moving than GMCs in the disc of the Milky Way (see also Section 5.6). It is perhaps unsurprising that large linewidths are a characteristic feature of extragalactic CO profiles (e.g. M82 – Nakai *et al.* 1987; M83 – Handa *et al.* 1990). Despite this, it is a matter of some debate as to whether even the energy injection from a vigorous starburst is enough to explain the enormous linewidths ($\leq$160 km s^{-1} FWHM) observed, when compared to typical Milky Way velocity dispersions of $\sim$10 km s^{-1} (e.g. Ostriker 1990).

It would be instructive, therefore, to know how much of the CO linewidth observed in Maffei 2 is due to the galaxy's rotation curve, and how much must be explained by other processes. This would place restrictions on the magnitude, and therefore nature, of the energy sources involved.

5.5.1 Modelling extragalactic linewidths

A very simple model of a rotating disc galaxy has been constructed which will enable, for a given rotation curve, the prediction of linewidths to be expected purely from the broadening effects of rotation. The galaxy is modelled as a thin rotating disc inclined to the line of sight, with the equation of the galaxy rotation curve specified. The disc is 'observed' with a Gaussian beam, which is divided into a grid of pixels. The rotational velocity of each pixel within the beam is then converted into velocity in the line of sight, and a histogram 'line profile' constructed. Details of the model are given in Appendix D.

This is a greatly simplified approach, assuming that each 'pixel' has the same brightness, and that there is no pixel–pixel shadowing or 'radiative interaction' between pixels – i.e. that the radiation from a pixel escapes from the galaxy before another pixel is encountered.

To obtain an equation for the observed rotation curve of Maffei 2 it is necessary to fit the velocity data to some model. The model needs to be physically plausible if it is expected to fit the data, but will be greatly simplified and by no means unique. The aim here is not to carry out a definitive investigation of the gravitational structure of the galaxy, but to obtain an equation that can be used to model the observed linewidths.

In Fig 5.16 is presented the variation of peak CO velocity with radius along the major axis of Maffei 2. At each position, the peak velocity is derived from the ^{12}CO J=2–1 velocity field and the ^{13}CO J=1–0 position–velocity diagram. The velocity of the central ^{13}CO J=2–1 profile is also included. The errors are due to the scatter in values at each position, plus the uncertainty in the knowledge of the peak velocities due to the binning together of channels.

The velocities are inclination-corrected, and have been transformed into the 'rest frame' of Maffei 2 – that is, positions and velocities measured with respect to the dynamical centre and systemic velocity of the galaxy, as determined in Section 5.4.1. The rotation curve is modelled by a massive, compact, constant-density (and therefore rigidly rotating) spherical core, and a much less dense, differentially rotating spherical halo. Because of the size of the beam, we have no detailed spatial information on the shape of the rotation curve as it flips over from positive to negative inside R $\sim$10″,

therefore the simplest form, rigid rotation, is assumed.

For a massive spherically symmetric compact core and low-density halo, the dependence of velocity on radius outside the core can be shown to be (Appendix E):

$$v(R)^2 = \frac{4\pi}{3} G r_c^3 (\rho_c - A r_c^{-\alpha}) \frac{1}{R} + \frac{4\pi}{3} A G R^{2-\alpha}, \tag{5.1}$$

where R = galactocentric radius with respect to the dynamical centre, r_c = radius of the compact core, ρ_c = mass density of the compact core, $\rho(R) = \rho_o (R/r_o)^{-\alpha}$ = mass density of halo as a function of R, and $A = 3\rho_o r_o^{\alpha}/(3-\alpha)$.

The scatter in the data is too large to constrain a fit to all the unknowns. As the primary purpose of fitting the rotation curve is to produce an equation that fits the data, is physically plausible and can be input to the linewidths model, r_c, ρ_c and α are fixed, and A fitted. The simplest possible density model, that of constant density (α=0), is used. In this case, A=ρ_0=density of halo. Next, r_c is taken to be the radius of the molecular ring detected by Ishiguro *et al.* (1989), since it is known that such rings often form at the turnover radius of the rotation curve (e.g. Lesch *et al.* 1990).

The radius and rotation velocity of the ring are 200 pc and 65 km s^{-1} respectively (Ishiguro *et al.* 1989). At a distance of 5 Mpc, 200 pc corresponds to 8.3″. The core dynamical mass is then given by

$$M_c = \frac{v_c^2 r_c}{G} = 1.9 \times 10^8 M_\odot, \tag{5.2}$$

and the core density by

$$\rho_c = \frac{3 M_c}{4\pi r_c^3} = 5.67 M_\odot \text{ pc}^{-3}. \tag{5.3}$$

Assuming that the rotation curve of Maffei 2 is symmetrical with respect to the dynamical centre, the method of least squares (minimizing χ^2) can then be applied to deduce the value of A that best fits the data.

The observational data and fitted results are summarized in Table 5.6. Only the seven points that were clearly outside the region of rigid rotation were used in the fit. The fitted curve is shown superimposed on the data in Fig 5.16. The best fit (reduced $\chi^2 = 1.1$) was obtained for a value of A = 0.21 $M_\odot$ pc^{-3} – the density of the halo is much lower than the density of the core.

The fitted rotation curve is then given by :

Table 5.6: Fitted rotation curve.

R (arcsec)[1]	R (parsec)[2]	V_{obs} (km s^{-1})[3,4]	V_{fit} (km s^{-1})[4]
12	291	50.5±6.1	55.9
13	315	55.0±11.1	54.5
17	412	54.0±5.2	51.4
18	436	52.0±7.6	51.1
22	533	56.5±9.3	51.4
23	558	53.5±9.3	51.7
28	679	52.0±7.6	54.8

(1) Offsets with respect to dynamical centre (3″ south-west of the map centre). (2) Assuming the distance to Maffei 2 is 5 Mpc. (3) From CO peak velocities. (4) Velocities are rotational velocities in the plane of the galaxy. The observed LSR velocity in the line of sight is given by $V \sin i$, where i is the inclination angle of Maffei 2 (65°).

$$R < 200 \text{ pc} \quad (8.3'') \qquad v = \ 0.33\ R, \tag{5.4}$$

$$R > 200 \text{ pc} \qquad v = \ (8.1 \times 10^5/R + 0.0039\ R^2)^{1/2}, \tag{5.5}$$

where v = velocity in km s^{-1}.

The fitted rotation curve can be used to calculate the dynamical mass of the galaxy, since for a spherically symmetric distribution of matter:

$$M_{dyn}(R) = v_{rot}(R)^2\ R/G, \tag{5.6}$$

hence, for R <200 pc, from equation (5.4):

$$M_{dyn}(R) = 23.8\ R^3\ M_\odot, \tag{5.7}$$

while for R >200 pc:

$$M_{dyn}(R) = (1.8 \times 10^8) + 0.9\ R^3\ M_\odot, \tag{5.8}$$

(equation 5.5), where R is in parsecs. The calculated dynamical mass as a function of radius is shown in Fig 5.17. The total dynamical mass of the observed region (R <600 pc) is $3.7 \times 10^8\ M_\odot$.

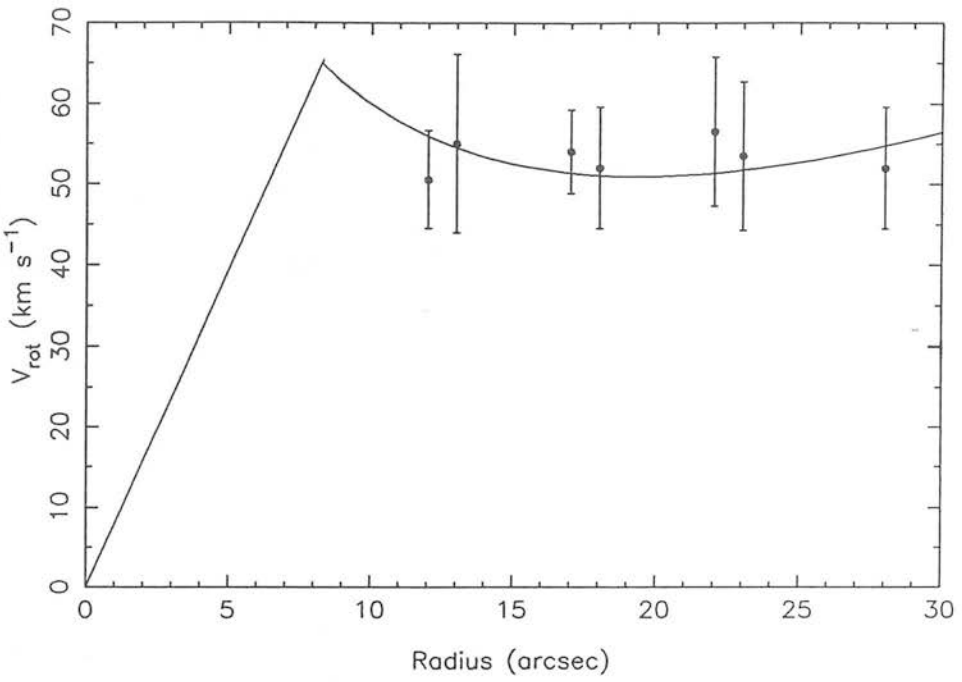

Figure 5.16: Rotational velocity (corrected for galaxy inclination) as a function of galactocentric radius, taken from ^{12}CO J=2–1, ^{13}CO J=1–0 and ^{13}CO J=2–1 peak profile velocities. The error bars reflect the scatter in the velocities derived using different transitions, and also the uncertainty introduced by binning over velocity channels to improve the signal-to-noise ratio. Superimposed on the data is a best-fitting rotation curve consisting of a massive, rigidly rotating core of radius 200 pc, and a uniform, low-density, differentially rotating halo.

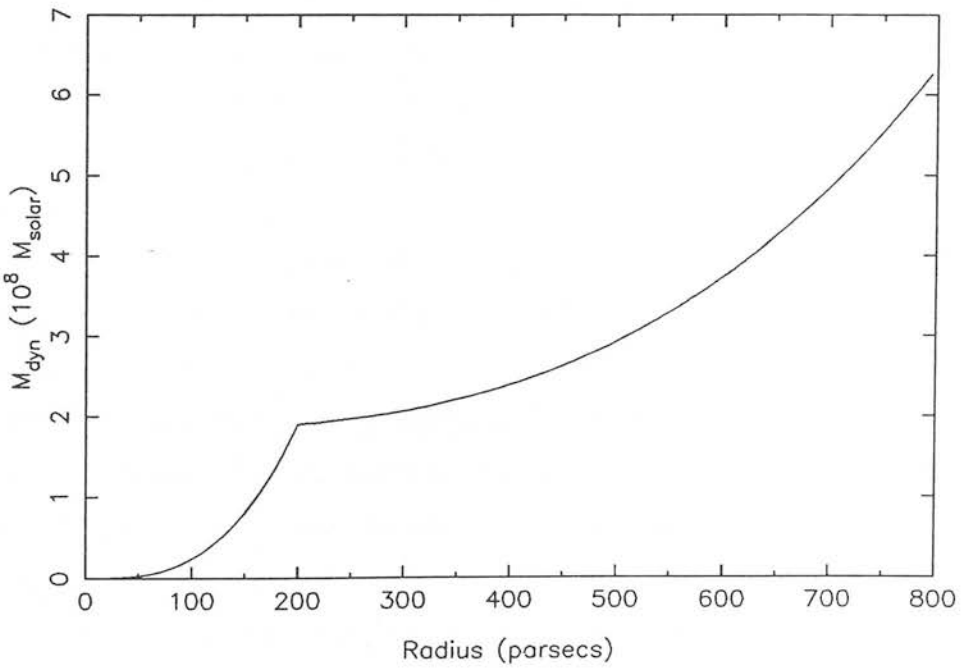

Figure 5.17: The dynamical mass of Maffei 2 as a function of galactocentric radius, calculated from the core + halo model of Section 5.5.1.

Model results

The model was applied to the ^{13}CO J=1–0 and 2–1 profiles which should not be greatly affected by optical depth effects. The line profiles resulting from 'observing' a thin rotating disc with the rotation curve of Maffei 2 are presented in Figs 5.18 and 5.19, for grids and beamsizes corresponding to both the IRAM and Nobeyama observations. The model profiles reproduce well the overall shapes of the line profiles, including their asymmetry. In Tables 5.7 and 5.8 the FWHM of the model profiles are compared to the observed linewidths. These model FWHM give the linewidths to be expected *purely* from the convolution of the beam and the rotation curve. It is clear that these are significantly less than the observed linewidths. For example, at (0,0), the ^{13}CO J=2–1 line is 130 km s^{-1} wide , yet the model predicts a linewidth of only 33 km s^{-1}. At each position, the quantity $\Delta v_{\rm disp} = (\Delta v^2_{\rm obs} - \Delta v^2_{\rm model})^{1/2}$ is calculated – this represents the 'excess' linewidth that cannot be explained by rotation and must therefore represent the velocity dispersion of the clouds. The excess linewidths range from ~30–40 km s^{-1} up to ~150 km s^{-1} at some near-nuclear positions. Such velocity dispersions are far in excess of typical values (~ 10 km s^{-1}) deduced for the Milky Way, but are in line with values inferred for other infrared-bright galaxies such as M83 (Handa *et al.* 1990).

To check that the derived velocity dispersions can reproduce the observed linewidths, the model was run a second time. Each pixel in the beam was regarded as a molecular 'cloud' or 'cloud complex' and, as well as a specified rotational velocity around the galactic centre, had assigned to it an 'internal velocity dispersion'. Each pixel was then considered to possess a Gaussian distribution of velocities about its galactic rotation velocity, and contributed flux in a range of velocity bins.

The one-dimensional velocity dispersions derived during the first run of the model were thus fed back into the program. The resulting line profiles are displayed in Figs 5.20 and 5.21 and it can be seen, without attempting any accurate fit of the linewidths, that they are quite consistent with the widths actually observed at each position. Thus the model seems to be producing meaningful results.

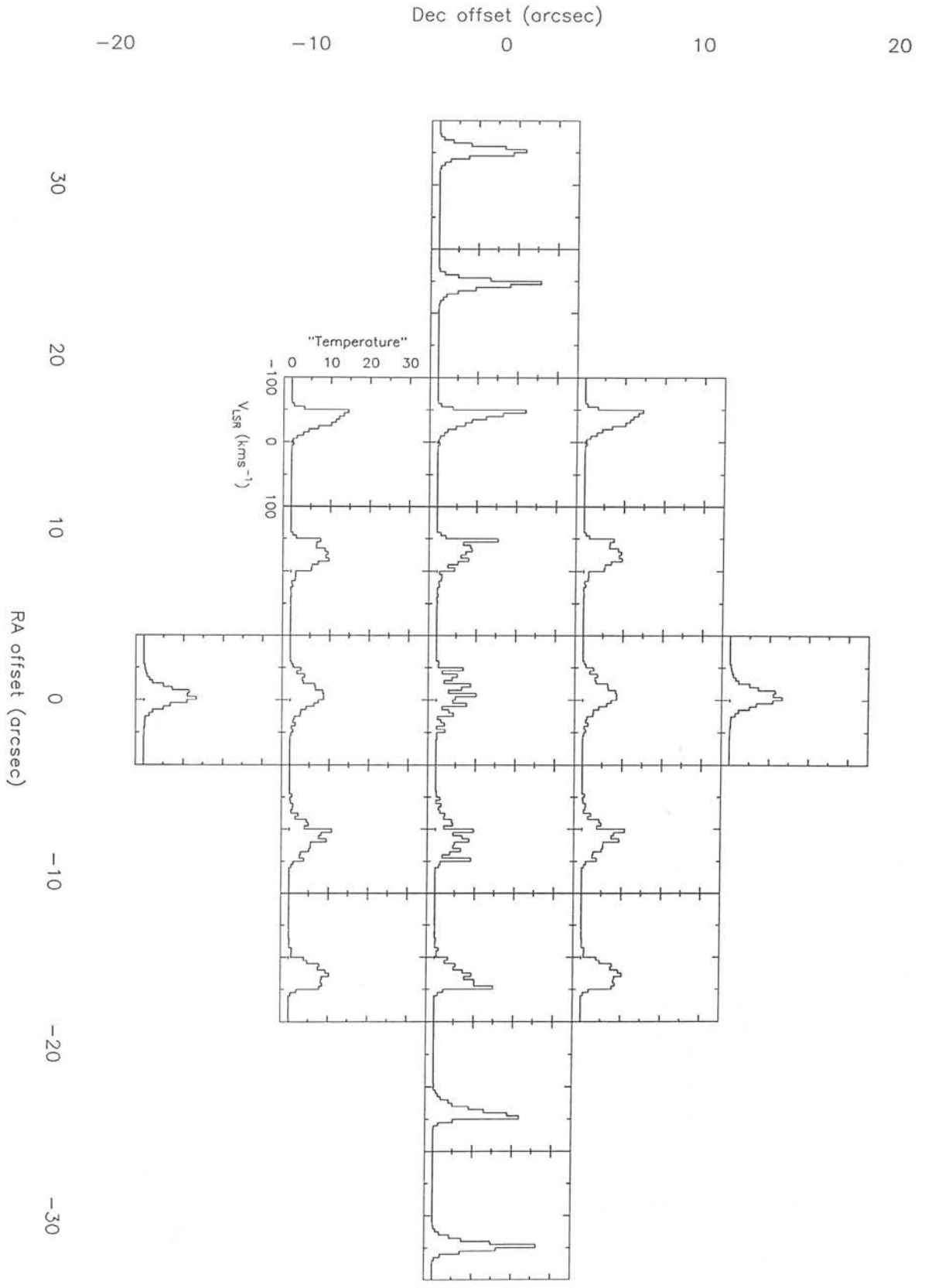

Figure 5.18: CO profiles, on the Nobeyama grid, computed from the model described in Section 5.5, with the rotation curve of Maffei 2, and zero cloud velocity dispersion.

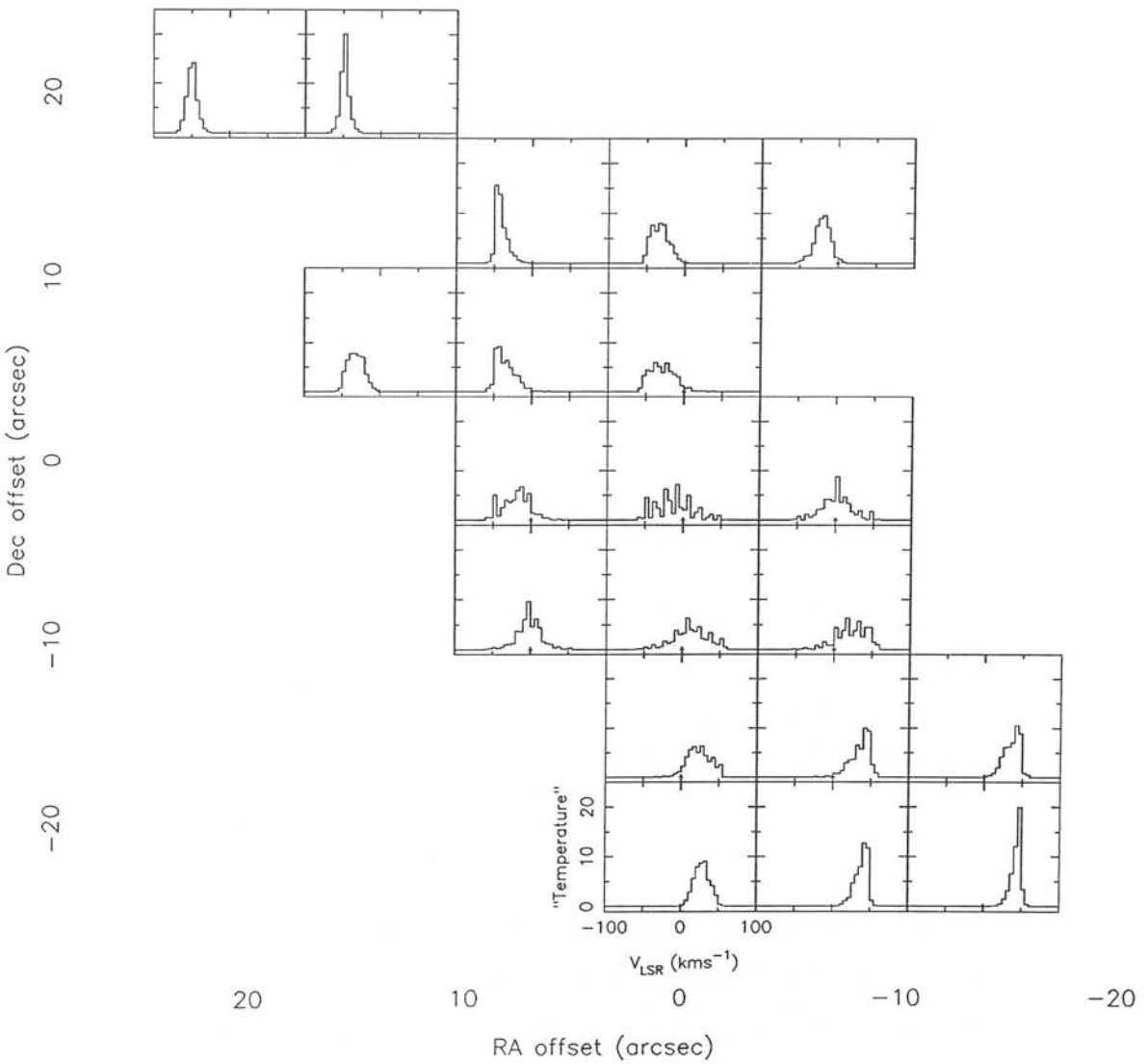

Figure 5.19: CO profiles, on the IRAM grid, computed from the model described in Section 5.5, with the rotation curve of Maffei 2, and zero cloud velocity dispersion.

Table 5.7: Results of linewidth model for ^{13}CO J=1–0 profiles.

Offset (arcsec)[1]		$\Delta v_{\rm obs}$ (km s^{-1})[2]	$\Delta v_{\rm model}$ (km s^{-1})[3]	$\Delta v_{\rm disp}$ (km s^{-1})[4]
0.0	0.0	124.3	41	118
+7.5	0.0	66.3	27	61
+15.0	0.0	62.0	19	59
+22.5	0.0	95.9	16	95
+30.0	0.0	104.3	19	103
− 7.5	0.0	100.5	43	91
−15.0	0.0	58.8	27	52
−22.5	0.0	84.2	19	82
−30.0	0.0	62.8	15	61
+ 7.5	+ 7.5	110.8	43	102
0.0	+ 7.5	109.4	48	99
− 7.5	+ 7.5	108.8	38	102
+ 7.5	− 7.5	78.4	43	66
0.0	− 7.5	144.8	48	137
− 7.5	− 7.5	110.9	38	104
0.0	+15.0	35.1	31	17
0.0	−15.0	70.8	31	64
+15.0	+ 7.5	102.6	28	99
−15.0	+ 7.5	100.4	40	92
+15.0	− 7.5	91.4	28	87
−15.0	− 7.5	71.2	40	59

(1) Offsets with respect to the map centre: RA (1950) = $02^{\rm h}\ 38^{\rm m}\ 08.5^{\rm s}$, Dec(1950) = $+59°\ 23'\ 30''$. (2) Observed FWHM of line. (3) FWHM resulting from the model. (4) Component of the observed line FWHM unaccounted for by the model: $\Delta v^2_{\rm disp} = \Delta v^2_{\rm obs} - \Delta v^2_{\rm model}$.

Discussion

The large cloud–cloud velocity dispersions necessary to produce the linewidths observed in Maffei 2 are typical of galaxies with enhanced star formation. Lines of 200 km s^{-1} width are seen in the starburst region of the edge-on system M82, while in the face-on spirals M83 and IC342, where the line-of-sight velocity due to galactic rotation is very small, the CO profiles are still ∼100 km s^{-1} wide (Handa *et al.* 1990; Eckart *et al.* 1990). Handa *et al.* model the position–velocity field of M83 and conclude that a cloud velocity dispersion of 100 km s^{-1} is necessary to produce the observed nuclear linewidths. Random cloud motions of ∼70–130 km s^{-1} have also been deduced for the spirals NGC 6946 and IC342 (Young & Scoville 1982). Such large velocities are in

Table 5.8: Results of linewidth model for ^{13}CO J=2–1 profiles.

Offset (arcsec)[1]		$\Delta v_{\rm obs}$ (km s^{-1})[2]	$\Delta v_{\rm model}$ (km s^{-1})[3]	$\Delta v_{\rm disp}$ (km s^{-1})[4]
+14	+21	86.4	12	86
+ 7	+14	46.1	15	44
0	+14	49.5	30	40
+ 7	+ 7	43.9	26	35
0	+ 7	77.1	40	66
+ 7	0	110.7	35	105
0	0	129.6	33	125
- 7	0	164.6	27	162
+ 7	- 7	143.0	25	141
0	- 7	135.4	38	130
- 7	- 7	103.8	38	97
0	-14	86.8	38	78
- 7	-14	65.8	24	61
-14	-14	72.4	23	67
0	-21	57.9	27	51
- 7	-21	66.4	19	64
-14	-21	82.8	12	82

(1) Offsets with respect to the map centre: RA (1950) = 02$^{\rm h}$ 38$^{\rm m}$ 08.5$^{\rm s}$, Dec(1950) = +59° 23′ 30″. (2) Observed FWHM of line. (3) FWHM resulting from the model. (4) Component of the observed line FWHM unaccounted for by the model: $\Delta v^2_{\rm disp} = \Delta v^2_{\rm obs} - \Delta v^2_{\rm model}$.

marked contrast to the disc of the Milky Way, in which cloud–cloud dispersions of ~10 km s^{-1} are typical (Stark 1984).

Any mechanism invoked to explain the large velocity dispersions observed in star-forming galaxies must be able to account for velocities of ~100 km s^{-1} involving ~ 10^8 $M_\odot$ of gas, implying kinetic energies of ~10^{55} erg. Several authors have suggested that energy input from a high rate of supernova explosions may be able to fuel the large cloud–cloud velocity dispersions or the expanding molecular rings inferred in several starburst galaxies. For example, the molecular rings suggested by observations of both Maffei 2 and M82, as well as the high linewidths at the centre of M83, have been modelled as arising naturally from a supernova rate of 0.04–0.3 supernovae per year, with a conversion efficiency of supernova energy to gas kinetic energy of 1–3% (Nakai *et al.* 1987; Ishiguro *et al.* 1989; Handa *et al.* 1990). In this scenario, ~0.4–9 $\times 10^{55}$ erg of kinetic energy is dumped into the clouds, and, it is argued, sustains the high velocities observed. However, these simple models are likely to provide only an upper limit to

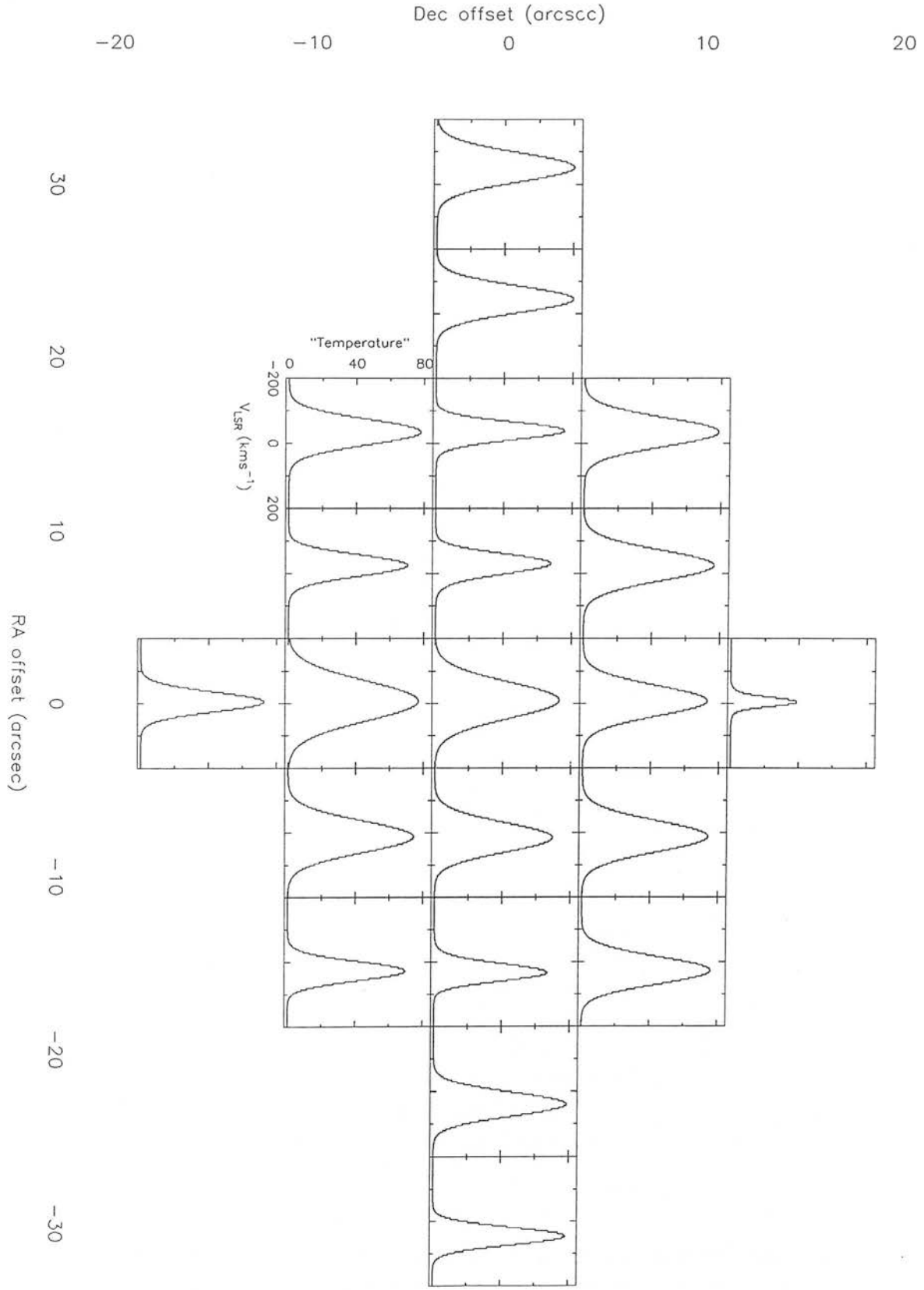

Figure 5.20: CO profiles, on the Nobeyama grid, computed from the model described in Section 5.5, with a cloud–cloud Gaussian velocity dispersion predicted by the model as necessary to explain the observed linewidths.

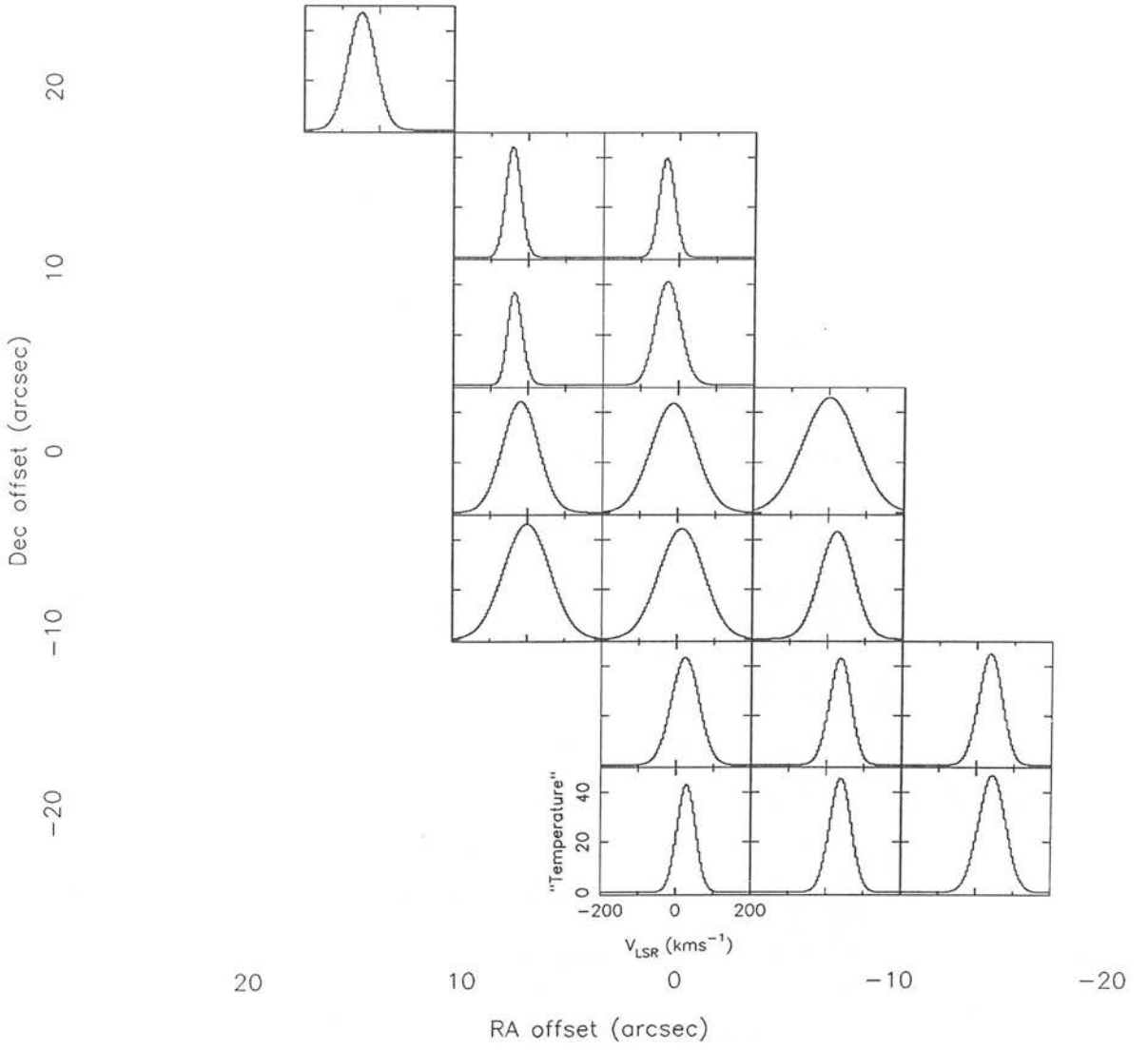

Figure 5.21: CO profiles, on the IRAM grid, computed from the model described in Section 5.5, with a cloud–cloud Gaussian velocity dispersion predicted by the model as necessary to explain the observed linewidths.

the velocity dispersion sustainable via supernova explosions. They assume that, once kinetic energy is acquired by a cloud, it will not lose that energy, and will stay at the velocity to which it has been accelerated by the supernova – in effect, that each supernova accelerates a certain mass of gas to 100 km s^{-1}, say, and that it then stays at that velocity while the remainder of the gas is accelerated by successive supernovae to join it. In reality, clouds will lose their kinetic energy over time, via inelastic collisions with each other, and this will affect the equilibrium velocity dispersion achieved.

The most rigorous work to date on the effect of supernova explosions in a cloudy interstellar medium is that of McKee & Ostriker (1977). Although they specifically exclude molecular clouds from their models, considering only HI clouds embedded in a low-density intercloud medium, the principle of their calculations may still be usefully applied to the clumpy molecular ISM of an extragalactic starburst.

McKee & Ostriker calculate the fraction of the energy of a supernova that is converted to cloud kinetic energy, via collisions between the expanding supernova shell and the clouds. For their specific model, of small (~2 pc) neutral clouds embedded in a tenuous intercloud medium, this is about 5×10^{49} erg per supernova, or about 5% of the total energy of the supernova. This fraction depends on the assumed properties of the ISM as well as those of the supernovae, but is consistent with other work (e.g. Chevalier 1974), and can therefore probably be regarded as a reliable approximation to the fraction of supernova energy converted to kinetic energy of molecular clouds.

The kinetic energy that clouds gain from collisions with expanding supernova shells is gradually lost in inelastic collisions between clouds, being converted to other forms such as cloud heating, radiation, etc. The energy lost in a completely inelastic collision between two clouds, masses m_1 and m_2, with relative velocity $\Delta\mathbf{v} = \mathbf{v}_1 - \mathbf{v}_2$, is

$$\Delta E = -\frac{1}{2}\,|\Delta\mathbf{v}|^2\,\frac{m_1 m_2}{m_1 + m_2}.$$

Averaging over a Gaussian distribution of cloud velocities, with dispersion σ, and a cloud collision cross-section equal to $\pi(r_1 + r_2)^2/2$, (r being the radius of a cloud), the average rate of energy loss per unit volume is

$$\frac{d\dot{E}}{dV} = -2.72\,N_{\rm cl}^2\,\sigma^3\left\langle \frac{m_1\,m_2}{m_1 + m_2}\,(r_1 + r_2)^2 \right\rangle \tag{5.9}$$

(McKee & Ostriker 1977), where $N_{\rm cl}$ is the number density of clouds, and the average is performed over the assumed cloud size and mass distribution. For the cloud population assumed by McKee & Ostriker, applying the Galactic disc supernova rate (10^{-13} supernovae pc^{-3} yr^{-1}), balancing the energy input from supernovae with the energy loss from inelastic collisions results in a cloud velocity dispersion for the neutral ISM of 7.9 km s^{-1}, close to the observed value in the Milky Way.

The above arguments can be applied for a very simplified estimate of the supernova rate that would be necessary to produce the linewidths observed in the starburst region of Maffei 2. In the Milky Way, molecular clouds are clumpy on all scales, from giant molecular clouds of 100-pc diameter down to the smallest cores $\leq$1 pc across (e.g. Bally 1989). A rigorous treatment would take account of the cloud size and density distribution, as McKee & Ostriker have done for neutral clouds. For this estimate it is assumed that the molecular gas consists of an ensemble of clouds of diameter a, with supernovae distributed evenly among them. From filling-factor arguments (Section 5.6.2) it can be estimated that a <15–35 pc. If the gas density $n(\rm H_2)\sim2\times10^3$ cm^{-3} (Section 5.6.3), then the mass of a cloud of diameter 20 pc will be $\sim3.8\times10^5\,M_\odot$. From ^{13}CO J=1–0 observations (Section 5.6.2), the molecular hydrogen column density observed in a 17″ beam is $\sim1.0\times10^{22}$ cm^{-2}, implying a molecular hydrogen mass within the beam of $2\times10^7\,M_\odot$ (for a distance to Maffei 2 of 5 Mpc). For a disc inclination of 65°, this gas mass is contained within a volume of 2.5×10^7 pc^3. The $2\times10^7\,M_\odot$ of gas is modelled as consisting of $\sim$60×20 pc diameter clouds, with a cloud number density $N_{\rm cl}\sim 2.4\times10^{-6}$ pc^{-3}.

Substituting $r_1 = r_2 = 10$ pc, $m_1 = m_2$=$3.8\times10^5\,M_\odot$ and $N_{\rm cl} = 2.4\times10^{-6}$ pc^{-3} into equation (5.9) then gives

$$\left(\frac{d\dot{E}}{dV}\right)_{\rm out} = 2.4\times10^{34}\,\sigma^3 \text{ erg pc}^{-3}\text{ yr}^{-1}$$

(with σ in km s^{-1}).

The energy supplied in supernova explosions, assuming a conversion rate to kinetic energy of 5% , or 5.2×10^{49} erg per supernova, is

$$\left(\frac{d\dot{E}}{dV}\right)_{\rm in} = 5.2\times10^{49}\,S \text{ erg pc}^{-3}\text{ yr}^{-1},$$

where S is the supernova rate in pc^{-3} yr^{-1}.

Equating the above two equations then gives the supernova rate required to produce a given three-dimensional velocity dispersion σ:

$$S = 4.6 \times 10^{-16} \sigma^3 \text{ pc}^{-3} \text{ yr}^{-1}.$$

At the centre of Maffei 2, the excess line FWHM (i.e. that not explained by the rotation curve) is $\sim$100 km s^{-1} (one-dimensional, line-of-sight velocity). The energy input from supernovae will be required to sustain cloud motions in three dimensions, therefore the appropriate value of σ ($=\sqrt{3}$ FWHM/2.4) is $\simeq$70 km s^{-1}. The minimum supernova rate needed to produce this velocity dispersion is then

$$S = 1.6 \times 10^{-10} \text{ pc}^{-3} \text{ yr}^{-1},$$

or roughly 1600 times the Milky Way value. If the fraction of supernova energy converted to cloud kinetic energy is less than 5%, the required supernovae rate will be even higher. To sustain σ=70 km s^{-1} with an energy conversion efficiency of 2% would require a supernova rate 4000 times the solar neighbourhood value. At some near-nuclear positions in Maffei 2 FWHM of $\sim$140 km s^{-1} need to be sustained, implying supernova rates up to 10^4 times the Milky Way value. Are such high supernova rates plausible?

The supernova rate in Maffei 2

To attempt to estimate the supernova rate in Maffei 2, I compare it to another nearby, vigorously star-forming galaxy, M82. Various observational and theoretical studies have led to estimated supernova rates for M82 of 0.1–0.3 yr^{-1} in the starburst region (Kronberg & Wilkinson 1975; Rieke *et al.* 1980). The supernova rate will depend on the starburst activity, particularly since the initial mass function of starbursts may be biased towards massive stars which end their lives as supernovae (Scalo 1990). The 158 μm line of ionized carbon, which arises in the photodissociated interfaces between HII regions and molecular clouds, has been proposed as a diagnostic of starburst activity in galaxies (Stacey *et al.* 1991). The observed [CII] 158 μm luminosities (in a 55″ beam) from M82 and Maffei 2 are 4.9×10^7 and 1.3×10^7 $L_\odot$, respectively, while the luminosity of M82 integrated over the inner 120″ diameter region is 6.4×10^7 $L_\odot$ (Stacey *et al.* 1990). Assuming a distance to Maffei 2 of 5 Mpc, and to M82 of 3.3 Mpc, 55″ corresponds to diameters on the galaxies of 1.3 kpc and 880 pc, respectively,

while the inner 120″ of M82 represents a region 1.9 kpc across. Therefore the [CII] luminosities from Maffei 2 and M82, in similar size regions, are in the approximate ratio 1:4–5. For comparison with a Galactic source, the total [CII] luminosity in the Orion giant molecular cloud and HII region is $\sim$ 560 $L_{\odot}$ (Russell *et al.* 1980; Stacey *et al.* 1991). Maffei 2 could therefore be considered as consisting of $\sim$ 2.3 $\times 10^4$ 'Orions' (although Stacey *et al.* caution that extragalactic [CII] emission cannot be viewed simply as a superposition of Orions). One can also compare the *IRAS* fluxes of Maffei 2 and M82. Although differences in far-infrared luminosity cannot be interpreted simply as variations in either the heating of the dust, nor the total dust column, but will in reality be a combination of the two (see Chapters 1–4), wavelengths shortward of 60 μm are more sensitive to warm dust in star formation regions rather than in the general molecular interstellar medium (e.g. Cox & Mezger 1989). The *IRAS* flux densities at 25 and 60 μm, respectively, are 9.3 and 92.9 Jy for Maffei 2, and 274, 1168 Jy for M82. Including a distance correction factor of $(3.3/5)^2$, the M82:Maffei 2 ratio is $\sim$13:1 at 25 μm and $\sim$6:1 at 60 μm. The total *IRAS* far-infrared luminosities (42.5–122.5 μm) are in the ratio 1.6 $\times 10^{10}$:4.3 $\times 10^9$ = 4:1. From the above arguments, I estimate that the intensity of the starburst activity, and hence the approximate supernova rate in Maffei 2, is between 4 and 10 times less than in M82. Whether this is due to a lower star formation efficiency, less gas, or some other factor, is not clear. I estimate an *upper* limit to the supernova rate in the central arcminute ($\sim$1.5 kpc) of Maffei of $\sim$0.05 yr^{-1}. This is the same value as adopted by Ishiguro *et al.* (1989) in their explanation of the expanding molecular ring observed in Maffei 2, although they don't explain in detail how they arrived at their value.

The supernova rate in Orion is $\sim$20–50 supernovae over the last $\sim$ 2 $\times 10^7$ yr (Bally 1989). If Maffei 2 can be represented by a superposition of 2 $\times 10^4$ Orions, this leads to a supernova rate of 0.02–0.05 yr^{-1}, consistent with the above estimate. A further estimate of the supernova rate may be made from the non-thermal radio continuum emission, if it is assumed that this originates in supernovae and their remnants. Condon & Yin (1990) give an empirical relation between the type II supernova rate, $\nu_{\rm SN}$, and the non-thermal radio luminosity, $L_{\rm NT}$, based on the observed ratio in the Milky Way

of $L_{\rm NT}$ and the production rate of radio-emitting supernovae:

$$L_{\rm NT}\ ({\rm W\ Hz^{-1}}) = 1.3 \times\ 10^{23}\ \left(\frac{\nu}{1{\rm GHz}}\right)^{-0.8}\ \nu_{\rm SN}\ ({\rm yr^{-1}}). \qquad (5.10)$$

(Condon & Yin argue that previous theoretical predictions underestimate the radio flux from a supernova by considering only the $\sim 10^4$-yr adiabatic expansion phase, and hence overestimate the supernova rate producing a given radio flux.) Maffei 2 has been mapped in the radio by Seaquist *et al.* (1976) at 11.1 and 3.7 cm, and by Ho & Turner at 6 cm (Ho *et al.* 1989). The 3.7- and 6-cm maps show only the compact, non-thermal multiple component in the central $\sim 15''$. The 11-cm map consists of three components – a $\sim 1'$ central structure with a strong nuclear source superimposed, and extended disc emission following the morphology of the spiral arms. The 11-cm flux density of the whole map is 0.46 Jy, but unfortunately the fluxes of the individual components are not given. However, it is clear from Seaquist *et al.*'s contour maps that the bulk of the flux arises from the central arcminute region. The emission is non-thermal, so 0.46 Jy will be regarded as an upper limit to the non-thermal 11-cm supernova radio flux from the starburst region. The lower limit, taken to be the flux from the compact core region, is 50 mJy at 6 cm (from Ho *et al.* 1989). For a distance to Maffei 2 of 5 Mpc, then, applying equation (5.10) for 2.9 and 5 GHz gives a range of supernova rates of $0.004 \leq \nu_{\rm SN} \leq\ 0.02\ {\rm yr^{-1}}$. The upper end of this range is consistent with previous estimates of the supernova rate, described above.

Assuming, as an absolute upper limit, that a supernova rate of 0.05 $\rm yr^{-1}$ applies to a central 'nuclear disc' about 1.5 kpc in diameter and 80 pc thick (Sanders, Solomon & Scoville 1984), gives a supernova rate per unit volume of $\sim\ 3.5\ \times 10^{-10}$ supernovae $\rm pc^{-3}\ yr^{-1}$, or about 3500 times the Milky Way disc value. A smaller supernova rate (0.01 $\rm yr^{-1}$) over the same volume would give $\sim 7\ \times 10^{-11}\ \rm pc^{-3}\ yr^{-1}$, or 700 times the Milky Way value.

Thus a predicted supernova rate in Maffei 2 of $\sim$0.05 $\rm yr^{-1}$ can just sustain velocity dispersions of $\sim$70 km $\rm s^{-1}$, if the conversion efficiency of supernova energy to cloud kinetic energy is 3% or more. For lower conversion efficiencies, lower supernova rates, or the high velocity dispersions observed at near-nuclear positions, it becomes doubtful whether supernovae are sufficient to sustain the observed velocities.

The deduced cloud velocity dispersion and/or supernova rate is of course dependent

on the assumed cloud size, density, etc. The adoption of an ensemble of identical clouds is a simplification – in reality there will be a range of sizes, densities and masses. From equation (5.9), $S \propto N_{\rm cl}^2\, \sigma^3\, ma^2$, where $N_{\rm cl} \propto 1/m$ and $m \propto na^3$. Therefore $S \propto \sigma^3/na$, or $\sigma \propto (naS)^{1/3}$. So the supernova rate required to sustain a given velocity dispersion is a strong function of σ, depending more weakly on the adopted cloud size and density. Filling-factor arguments (Section 5.6.2) give 15–30 pc as an upper limit to the cloud size. If the clouds are on average smaller or less dense (and hence less massive) than the values adopted here, although an injection of energy to a particular cloud will give a greater velocity boost, the kinetic energy for a given supernova rate will be shared among a greater number of clouds. The clouds will also lose energy more quickly as the cloud–cloud collision rate goes up. The equilibrium velocity dispersion sustainable by supernovae will therefore decrease for smaller clouds, although only as the cube root of the cloud size.

Obviously, with such a simplistic treatment, there is room for error in terms of the assumptions made about the sizes and densities of clouds, the nature of the interstellar medium, the properties of supernova remnants and the fraction of energy transferred by them to the molecular gas, all of which may serve to alter the cloud velocity dispersion they are capable of producing. But if, after all, supernova explosions *cannot* produce the linewidths observed in Maffei 2 and other starburst galaxies, then what is the mechanism behind them? A possibility that should be considered is that Maffei 2 harbours some kind of active nucleus in addition to its prolific nuclear starburst – although the linewidths seen (~ 300 km s^{-1}) are far below those observed in typical AGN ($\sim 10^3$ km s^{-1}, Blanco 1991). Active nuclei can operate in tandem with starbursts, both feeding on the rich reserves of molecular gas [such as, for example, the Seyfert NGC 1068, where the active nucleus and a 3-kpc star-forming disc share the infrared output of a few $\times\ 10^{11}\ L_\odot$(Telesco *et al.* 1984; Lester *et al.* 1987)]. However, Maffei 2 is on a far smaller scale ($L_{\rm IR} \sim$ few $\times\ 10^9\ L_\odot$) than the 'ultraluminous' (usually interacting) infrared systems of $10^{11-12}\ L_\odot$ which may be powered by compact 'monsters' (e.g. Sanders *et al.* 1988). The presence of extended (~ 100 pc) 10 μm emission (implying heating by distributed sources), mid-infrared spectral features and [CII] emission from UV-illuminated HII-region/neutral-gas interfaces all point to prolific star formation as the dominant energy source in Maffei 2 (Ho *et al.* 1989; Stacey *et al.* 1991; Roche *et al.*

1991; Pat Roche, private communication). Near-infrared mapping, also, provides no evidence for a compact near-infrared central source as seen in some heavily obscured active nuclei such as Cygnus A (Fig 5.9, see also Blanco 1991; Djorgovski *et al.* 1991). It is unfortunate that Maffei 2's location, low down in the Galactic plane, and its consequent high extinction, have prevented any attempts at sensitive optical spectroscopy which could shed light on this issue.

5.6 Excitation of the molecular gas

Comparison of line strengths of different transitions and isotopes of CO is in principle a valuable diagnostic of the excitation of the gas. In practice, analysis of the observed ratios is far from straightforward. The simplest interpretation of CO rotational line emission comes from assuming that Local Thermodynamic Equilibrium (LTE) holds. In this situation, it is assumed that the density of the gas is such that excitation of CO is dominated by collisions with H_2 molecules, and that the relative populations of the rotational levels approach a Boltzmann distribution described by a single kinetic temperature T_k. The excitation temperature T_{ex}, which describes the actual level populations, is then equal to T_k, and is common to all isotopes and transitions. Under these conditions, it is then relatively straightforward, in principle, to derive such quantities as optical depth, excitation temperature and column density from observations of different isotopes and transitions (see Appendix C for derivation of the LTE equations used in this section). In practice, however, the path is strewn with traps for the unwary, in the form of temperature and abundance gradients, and various non-LTE effects.

5.6.1 LTE analysis of the CO data

Under the assumption of LTE, with the populations of the rotational levels described by a single excitation temperature T_{ex}, equations relating the relative strengths of the ^{12}CO and ^{13}CO J=1–0 and J=2–1 transitions can be derived (Appendix C). Some of the main results are summarized below.

The radiation temperature of a line at frequency ν is given by

$$T_r = [J_\nu(T_{ex}) - J_\nu(T_{bg})]\,(1 - e^{-\tau_\nu}), \tag{5.11}$$

with

$$J_\nu(T) = \frac{h\nu}{k}\,(\mathrm{e}^{h\nu/kT} - 1)^{-1}, \tag{5.12}$$

where $T_{\rm bg}$ is the background temperature (2.7 K), and τ_ν is the optical depth of the transition.

$T_{\rm r}$ will be equal to the observed main-beam brightness temperature ($T_{\rm mb}$) for a source which uniformly fills the beam (i.e. with filling factor unity). In the case of an extragalactic source, this will almost certainly not be the case, and the exact coupling of the beam to a clumpy source is impossible to evaluate. The advantage of using line ratios to probe excitation is that if the observations are made with the same beamsize, the unknown filling factor cancels out. In addition, if the observations are made at the same telescope, the problems of relative calibration and differing efficiencies between telescopes are avoided.

In the case of optically thick emission, equation (5.11) can be used to derive the excitation temperature. For the ^{12}CO J=2–1 line, rearranging gives

$$T_{\rm ex} = 11.09 \left[\ln\left(1 + \frac{11.09}{T_{\rm r} + 0.185}\right)\right]^{-1}. \tag{5.13}$$

This will be a lower limit to the excitation temperature since, for extragalactic sources, the filling factor will in general be $\ll$1.

Observations of one transition in both ^{12}CO and ^{13}CO can be used with equation (5.11) to derive the optical depths of ^{12}CO and ^{13}CO, if the same excitation temperature is assumed for both transitions:

$$\frac{T_{\rm mb}^{12}}{T_{\rm mb}^{13}} = \frac{(1 - \mathrm{e}^{-\tau_{12}})}{(1 - \mathrm{e}^{-\tau_{13}})}, \tag{5.14}$$

where $\tau_{12} = R\ \tau_{13}$, R being the [^{12}CO]:[^{13}CO] abundance ratio. The line ratio varies between 1 (both lines optically thick) and R (both optically thin). In the solar neighbourhood, R=89, while at the Galactic Centre it may be as low as 25 (Langer & Penzias 1990).

For a given isotope, then, $T_{\rm ex}$ can be determined directly from the ratio of the 2–1 and 1–0 main-beam brightness temperatures:

$$\frac{T_{\rm mb}^{21}}{T_{\rm mb}^{10}} = \frac{(1 - \mathrm{e}^{-\tau_{21}})}{(1 - \mathrm{e}^{-\tau_{10}})}\ \frac{[J_{21}(T_{\rm ex}) - J_{21}(T_{\rm bg})]}{[J_{10}(T_{\rm ex}) - J_{10}(T_{\rm bg})]}. \tag{5.15}$$

For optically thick 2–1 and 1–0, the brightness temperature ratio never exceeds 1, while for completely optically thin gas it can be approximated by

$$\frac{T_{\rm mb}^{21}}{T_{\rm mb}^{10}} \simeq 4\exp(-11.03/T_{\rm ex}). \tag{5.16}$$

For example, for $T_{\rm ex}$=40 K, the completely optically thin line ratio is ~3.

The peak ^{12}CO/^{13}CO J=1–0 and ^{12}CO/^{13}CO J=2–1 main-beam brightness temperature ratios, calculated using both our observations and the ^{12}CO J=1–0 data of Nakai *et al.* (in preparation) are presented in Tables 5.9 and 5.10. In Figs 5.22 and 5.23, the ^{12}CO and corresponding ^{13}CO spectra are plotted on the same axes, for comparison, and to show up any variation in line ratio across the profile which may point to differing excitation within a beam.

The ^{12}CO/^{13}CO J=1–0 ratio

The ^{13}CO spectra are quite noisy, so that it is difficult to tell if there is any trend of $T_{\rm mb}(^{12}{\rm CO})/T_{\rm mb}(^{13}{\rm CO})$ with velocity. Except at a few positions where the ^{13}CO line is barely detected, the ^{12}CO and ^{13}CO profiles are very similar in shape. At (–7.5,7.5) there is a suggestion that the ^{13}CO profile is double-peaked, with the two components corresponding in velocity with those of the ^{12}CO profile. There is no obvious trend in the peak line ratios away from the galaxy centre, although there are variations on scales of ~7″ (170 pc) with typical values being ~5–10.

The ^{12}CO/^{13}CO J=2–1 ratio

The signal-to-noise ratio of the ^{13}CO J=2–1 profiles is generally better than for ^{13}CO 1–0. The similarity in line profile between ^{12}CO and ^{13}CO at a given offset is very good, and the asymmetry of the profile shapes is generally what would be expected from the galaxy rotation curve (see Section 5.5). At offset (0,–7) the ^{13}CO profile has a distinct 'shoulder' at negative velocities which isn't seen in ^{12}CO. At (7,–7) ^{12}CO is strong and centrally peaked but the ^{13}CO displays a flattened profile.

The peak main-beam brightness temperature ratios show striking variations on scales of ~7″. One of the most dramatic examples of the rapid change of line ratio is shown in Fig. 5.24, for the offsets (14,7), (7,7), and (0,7), where the ratio varies from >100 to 3.3 in just 14″ (800 pc when corrected for galactic inclination). The

Table 5.9: Peak $^{12}CO/^{13}CO$ antenna temperature ratio for the J=1–0 transition.

Offset (arcsec)		T_{mb} (K) ^{12}CO [1]	^{13}CO	T_{mb} ratio [2]	$\tau(^{12}CO)$ [3]	$\tau(^{12}CO)$ [4]
0.0	0.0	1.04	0.16	6.5±1.6	10.0	4.9
+7.5	0.0	1.39	0.17	8.2±1.9	7.8	3.8
+15.0	0.0	1.34	0.13	10.3±2.4	6.1	2.9
+22.5	0.0	1.08	0.13	8.3±2.1	7.7	3.8
+30.0	0.0	0.62	0.12	5.2±1.7	12.9	6.4
− 7.5	0.0	1.44	0.15	9.6±2.2	6.6	3.2
−15.0	0.0	1.18	0.14	8.4±1.9	7.6	3.7
−22.5	0.0	1.18	0.19	6.2±1.5	10.5	5.2
−30.0	0.0	0.67	0.14	4.8±1.5	14.1	7.0
+ 7.5	+ 7.5	1.31	0.13	10.1±2.6	6.2	2.9
0.0	+ 7.5	1.10	0.12	9.2±2.4	6.9	3.3
− 7.5	+ 7.5	1.04	0.14	7.4±1.9	8.7	4.3
+ 7.5	− 7.5	0.76	0.11	6.9±1.9	9.4	4.6
0.0	− 7.5	0.82	0.12	6.8±1.7	9.5	4.7
− 7.5	− 7.5	1.04	0.11	9.5±3.1	6.7	3.2
0.0	+15.0	0.58	0.12	4.8±1.5	13.9	6.9
0.0	−15.0	0.52	0.08	6.5±2.1	10.0	4.9
+15.0	+ 7.5	1.02	0.10	10.2±3.0	6.2	2.9
−15.0	+ 7.5	0.96	0.15	6.4±1.6	10.2	5.1
+15.0	− 7.5	0.89	0.11	8.1±2.0	7.9	3.9
−15.0	− 7.5	0.73	0.16	4.6±1.2	14.8	7.4

(1) The ^{12}CO data are from Nakai *et al.*, in preparation. (2) Combination (in quadrature) of (i) rms noise of ^{12}CO and ^{13}CO and (ii) calibration uncertainties of ~15–20% for both transitions. (3) Calculated assuming LTE and R=[^{12}CO]:[^{13}CO] = 60. (4) As (3), but for R=30.

close agreement in profile shape and peak velocity over the map makes it unlikely that these line ratios can be attributed to poor pointing. Offset (14,7) was observed on two separate occasions during the run, and the non-detection at this position was confirmed.

The overall picture then is of a region of high $^{12}CO/^{13}CO$ J=2–1 ratio (weak or non-detected ^{13}CO) to the north-east of the nucleus, although this trend is not as pronounced in the J=1–0 data, possibly due to the lower signal-to-noise ratio of the ^{13}CO profiles.

The ^{12}CO 2–1/1–0 ratio

Since the ^{12}CO J=1–0 and J=2–1 data were taken with different telescopes, at different resolutions and on different grids, the original profiles cannot be directly compared. The

Table 5.10: Peak $^{12}CO/^{13}CO$ antenna temperature ratio for the J=2–1 transition

Offset (arcsec)		T_{mb} (K) ^{12}CO	^{13}CO	T_{mb} ratio [1]	$\tau(^{12}CO)$ [2]	$\tau(^{12}CO)$ [3]
+21	+21	0.80	<0.03	>27.0	–	–
+14	+21	0.95	0.09	10.6±4.2	5.9	2.8
+ 7	+14	1.39	0.18	7.7±1.9	8.3	4.1
0	+14	1.64	0.22	7.5±1.7	8.6	4.3
− 7	+14	0.58	<0.02	>29.0	–	–
+14	+ 7	2.00	<0.02	>100.0	–	–
+ 7	+ 7	2.89	0.19	15.2±3.6	4.0	1.6
0	+ 7	1.39	0.42	3.3±0.7	21.6	10.8
+ 7	0	2.35	0.19	12.4±2.9	5.0	2.3
0	0	2.19	0.33	6.6±1.5	9.8	4.9
− 7	0	0.97	0.26	3.7±0.9	18.7	9.4
+ 7	− 7	1.99	0.10	19.9±5.8	2.9	0.9
0	− 7	2.47	0.29	8.5±1.9	7.5	3.6
− 7	− 7	1.17	0.33	3.5±0.8	19.9	9.9
0	−14	1.52	0.22	6.9±1.8	9.4	4.6
− 7	−14	2.58	0.36	7.2±1.6	9.0	4.5
−14	−14	1.91	0.25	7.6±1.7	8.4	4.1
0	−21	1.44	0.07	20.6±9.9	2.8	0.8
− 7	−21	1.64	0.16	10.3±2.6	6.1	2.9
−14	−21	0.93	0.24	3.9±1.0	17.9	8.9

(1) Combination (in quadrature) of (i) rms noise of ^{12}CO and ^{13}CO and (ii) calibration uncertainties of ~15–20% for both transitions. (2) Calculated assuming LTE and R=[^{12}CO]:[^{13}CO] = 60. (3) As (2), but for R=30.

Nobeyama data reduction software was used to interpolate the ^{12}CO J=1–0 profiles (Nakai *et al.*, in preparation) on to the IRAM grid. The ^{12}CO J=2–1 data were then smoothed from 13″ to 17″ resolution, to match that of the Nobeyama data. This was done by merging neighbouring profiles channel by channel, weighted by a Gaussian of FWHM = $(17^2 - 13^2)^{1/2}$ = 10.9″. Before comparing line strengths from the two data sets, it is necessary to check whether, despite being on the same temperature scale (T_{mb}), the ratios are likely to be affected by differences in calibration between the Nobeyama and IRAM telescopes. The ^{12}CO J=1–0 transition in Maffei 2 was observed with IRAM by Weliachew *et al.* (1988), using a 23″ beam. Their observations were centred on RA(1950)=$02^h\ 38^m\ 08.5^s$, Dec(1950)=+59° 23′ 24″, 6″ south of the central position of the present observation. Their central profile is therefore only 1″

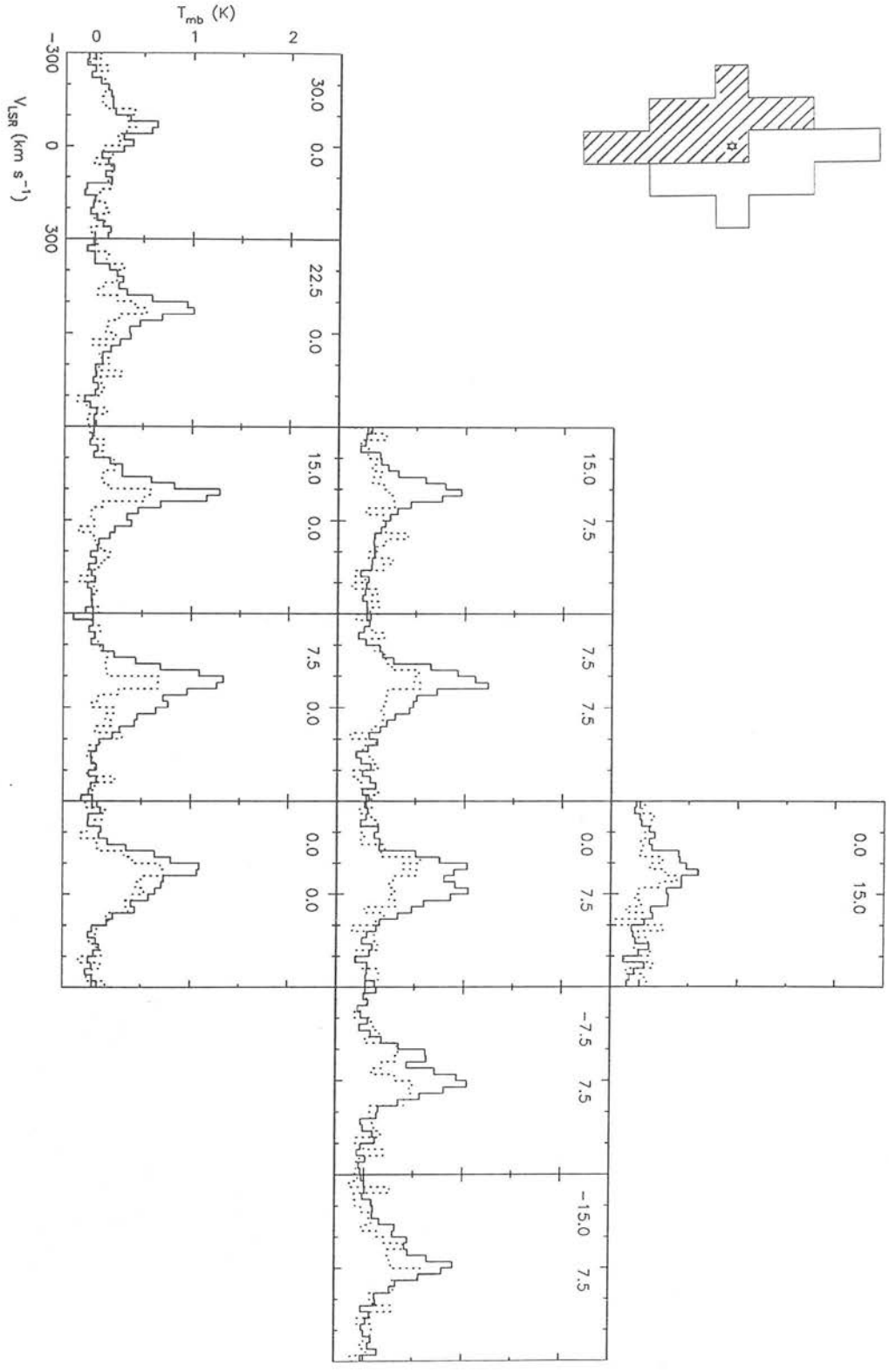

Figure 5.22: ^{12}CO and ^{13}CO J=1–0 profiles plotted on the same axes. The ^{12}CO data (solid lines) are from Nakai *et al.* (in preparation). The ^{13}CO profiles (dotted lines) have been scaled up by a factor of 5.

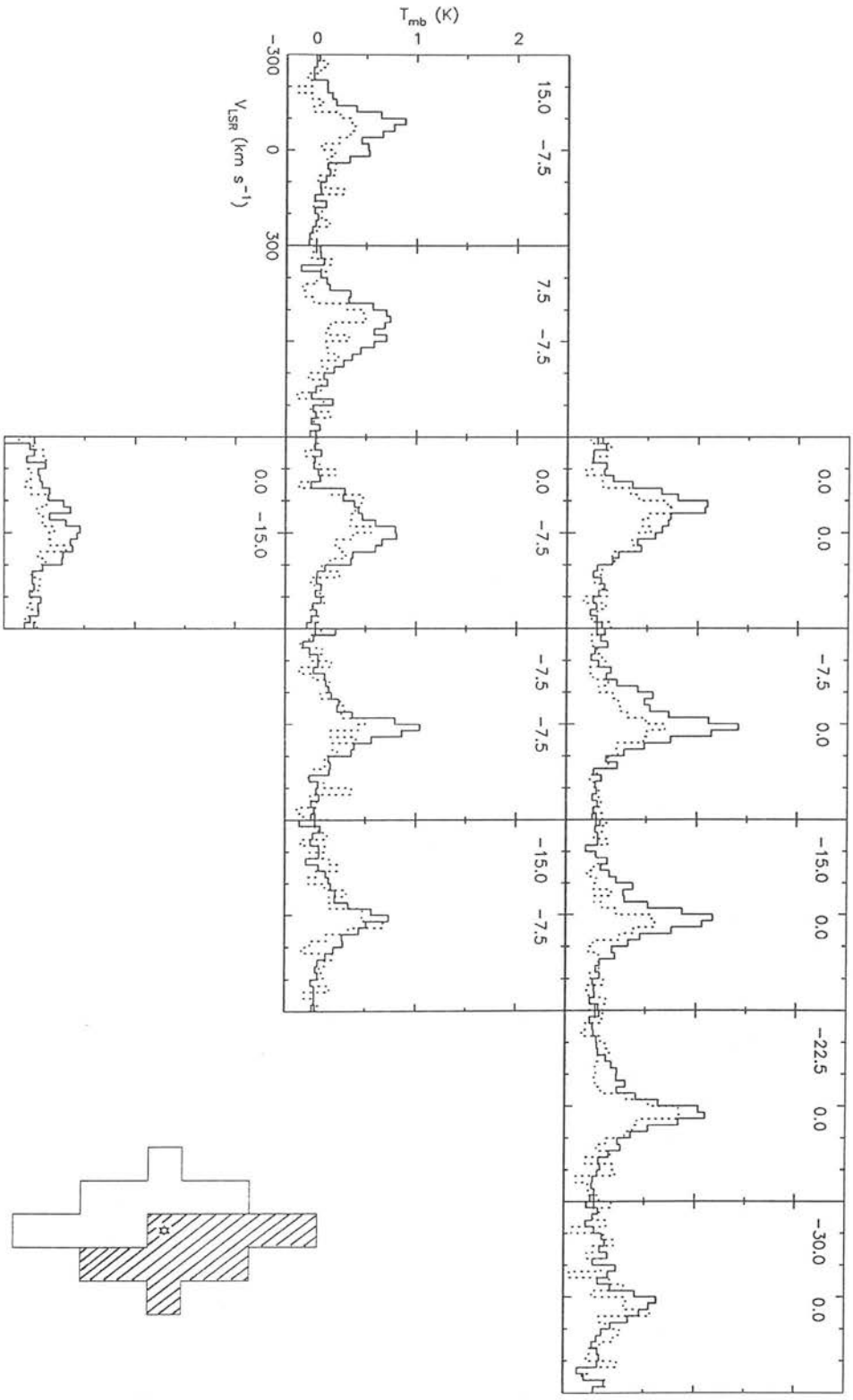

Figure 5.22 – continued

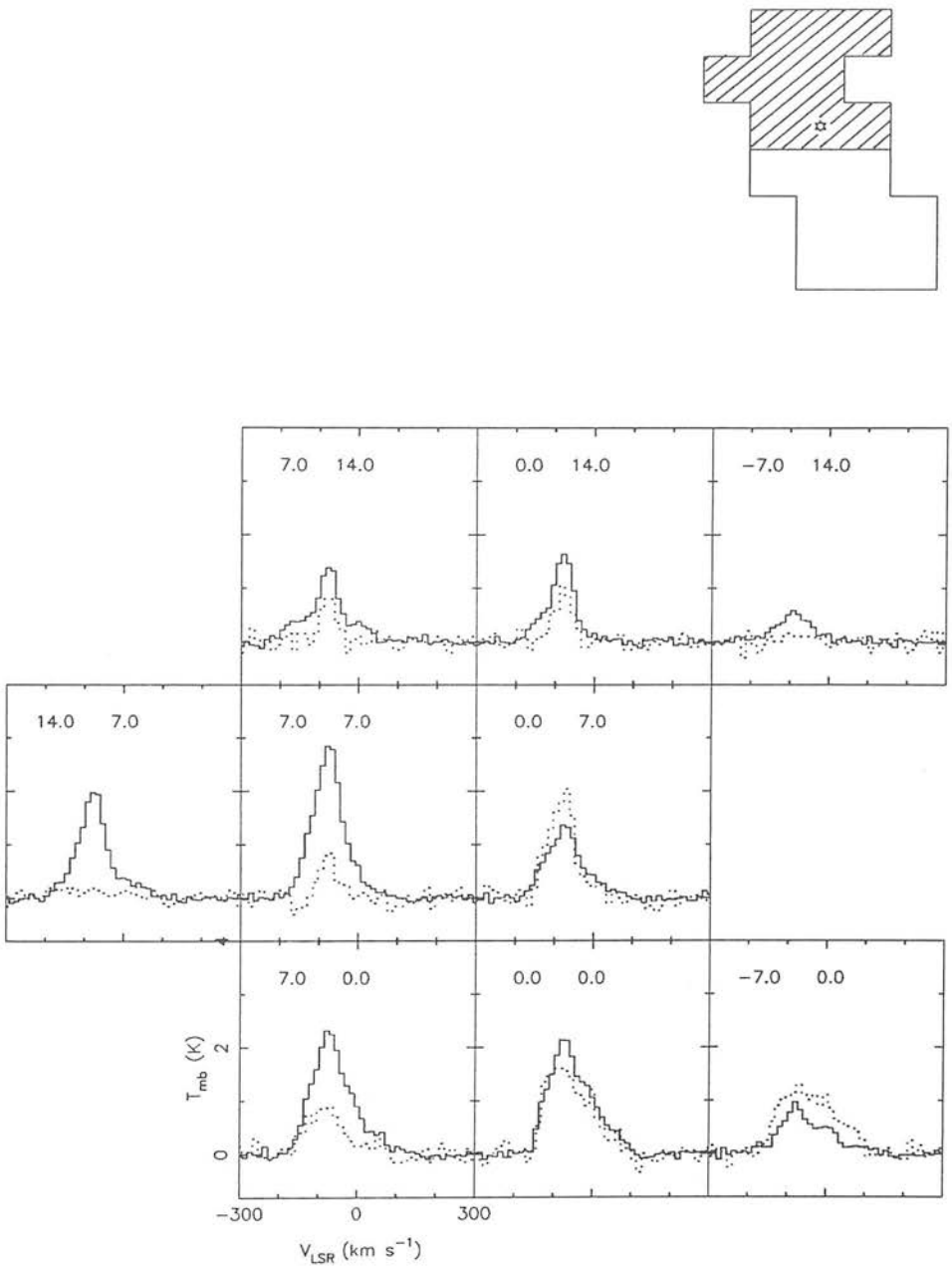

Figure 5.23: ^{12}CO and ^{13}CO J=2–1 profiles on the same axes. The ^{13}CO data (dotted lines) have been multiplied by a factor of 5 to ease comparison.

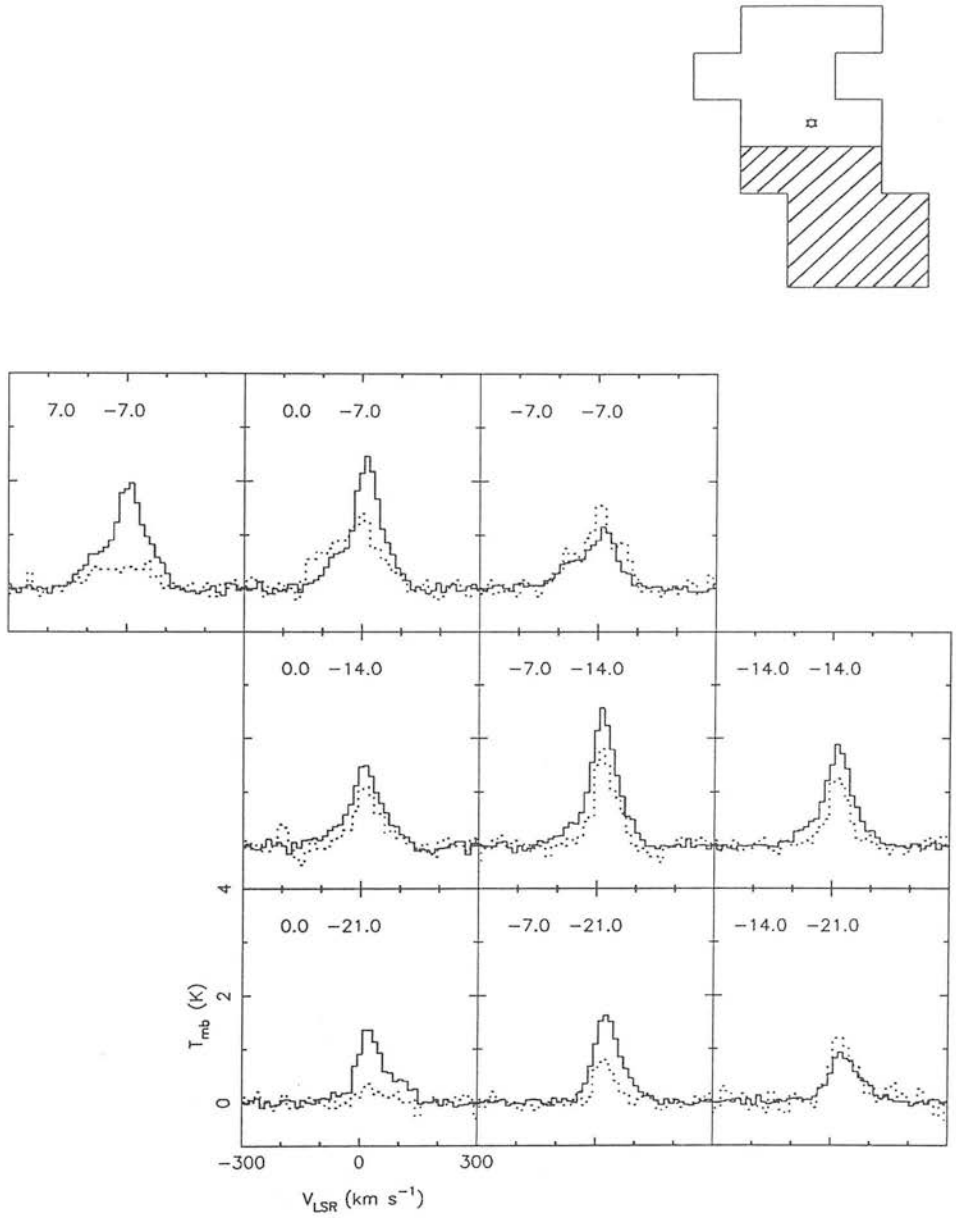

Figure 5.23 – continued

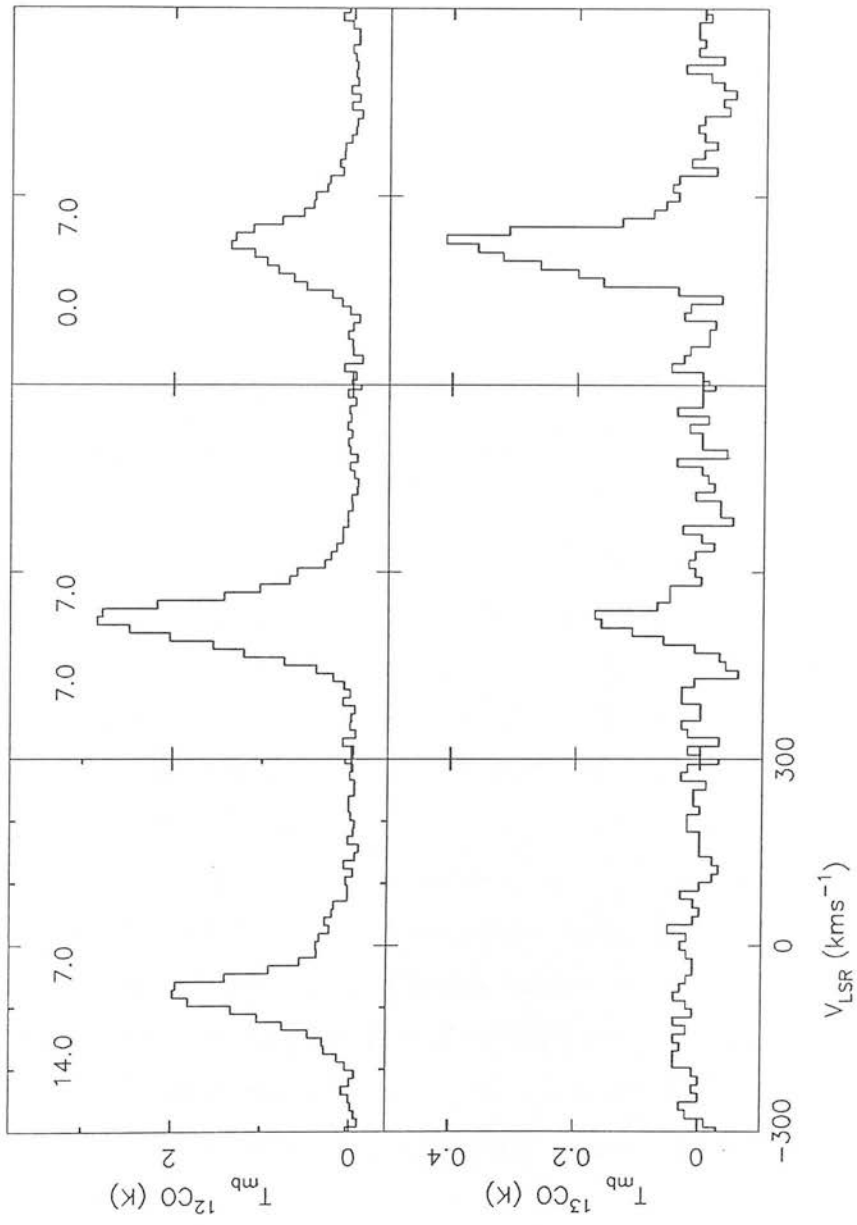

Figure 5.24: ^{12}CO and ^{13}CO J=2–1 profiles from three adjacent positions, at offsets (ΔRA,ΔDec.) = (14,7), (7,7) and (0,7) arcsec. Note the striking spatial variation of the line ratio, from >100 to ~3 in only ~20″.

from the (interpolated) Nobeyama spectrum at ΔRA=0.0, ΔDec=−7.0, an offset less than the pointing accuracy of the observations and much less than the beamsize.

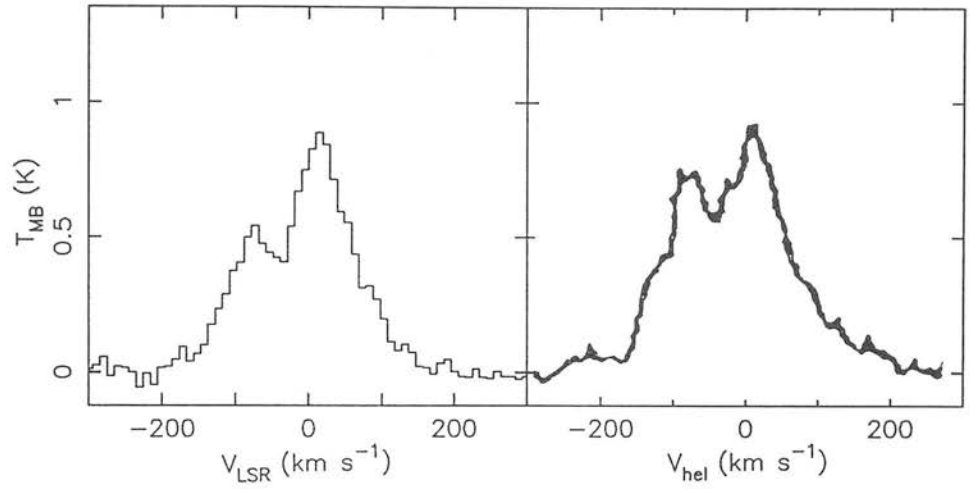

Figure 5.25: The central ^{12}CO J=1–0 profile from the NRO 45-m (Nakai *et al.*, in preparation) smoothed to a resolution of 23″, compared to the ^{12}CO 1–0 spectrum at the same position observed with IRAM by Weliachew *et al.* (1988). The similarity in line strengths and profile shape indicates that the pointing was satisfactory and the calibration of the two telescopes consistent with each other.

The Nobeyama profile was smoothed to a resolution of 23″ to match the IRAM observation. The two profiles are compared in Fig 5.25 and it can be seen that they are in good agreement. The peak antenna temperature of the IRAM profile is $T_{\rm mb} \simeq 0.9$ K (F.Combes, personal communication). The measured peak main-beam brightness temperature of the smoothed Nobeyama profile is $T_{\rm mb}$ = 0.89 K. In the following analysis it is assumed that the temperature scales of the Nobeyama 45-m and the IRAM 30-m are consistent and that there is no significant contribution to the errors in the 2–1/1–0 line ratios from differences in calibration between the two sets of data.

In Table 5.11 are presented the peak ^{12}CO J=2–1/J=1–0 main-beam brightness temperature ratios at positions where the J=2–1 transition was well detected. The individual line profiles are compared in Fig. 5.26, while a contour plot of the ratio is presented in Fig. 5.27.

From Fig. 5.26 it can be seen that the J=1–0 and 2–1 profile shapes and peak velocities are remarkably consistent, giving confidence in the accuracy of the pointing for the J=2–1 observations, as well as in the reliability of the smoothed and interpolated spectra. The peak 2–1/1–0 ratio varies across the map, as can be seen in Fig. 5.27.

Table 5.11: ^{12}CO 2–1/1–0 antenna temperature ratio.

Offset (arcsec) [1]		T_{mb} (K) J=1–0 [2]	T_{mb} J=2–1 [3]	Peak 2–1/1–0 T_{mb} Ratio [4]
+28	+35	0.53	0.53	1.00±0.28
+21	+35	0.47	0.47	1.00±0.30
+14	+35	0.37	0.37	1.00±0.44
+ 7	+35	0.47	0.23	0.49±0.19
+28	+28	0.47	0.67	1.43±0.38
+21	+28	0.50	0.73	1.46±0.43
+14	+28	0.60	0.67	1.12±0.33
+ 7	+28	0.40	0.47	1.20±0.48
0	+28	0.60	0.27	0.45±0.16
+28	+21	0.37	0.60	1.62±0.53
+21	+21	0.47	0.67	1.43±0.51
+14	+21	0.93	0.80	0.86±0.20
+ 7	+21	1.00	0.80	0.80±0.19
0	+21	0.80	0.57	0.71±0.18
− 7	+21	0.37	0.30	0.81±0.38
+28	+14	0.30	0.30	1.00±0.35
+21	+14	0.50	0.50	1.00±0.28
+14	+14	0.83	0.97	1.20±0.28
+ 7	+14	1.33	1.33	1.00±0.22
0	+14	1.07	1.07	1.00±0.22
− 7	+14	0.77	0.53	0.69±0.18
+28	+ 7	0.47	0.30	0.64±0.26
+21	+ 7	0.40	0.40	1.00±0.30
+14	+ 7	0.90	1.43	1.60±0.36
+ 7	+ 7	1.27	1.93	1.52±0.33
0	+ 7	1.27	1.47	1.16±0.25
− 7	+ 7	1.07	0.63	0.59±0.14
+21	0	0.46	0.30	0.65±0.22
+14	0	0.50	1.00	2.00±0.50
+ 7	0	0.65	1.70	2.62±0.59
0	0	1.13	1.50	1.33±0.30
− 7	0	1.00	0.63	0.63±0.15
+14	− 7	0.47	0.60	1.30±0.41
+ 7	− 7	0.80	1.27	1.59±0.36
0	− 7	1.27	1.60	1.26±0.27
− 7	− 7	1.30	1.30	1.00±0.22
−14	− 7	0.97	0.73	0.75±0.18
−21	− 7	0.63	0.33	0.52±0.16

Table 5.11: – continued.

Offset (arcsec) [1]		T_{mb} (K) J=1–0 [2]	T_{mb} (K) J=2–1 [3]	Peak 2–1/1–0 T_{mb} Ratio [4]
+14	−14	0.53	0.33	0.62±0.18
+ 7	−14	0.63	0.80	1.27±0.33
0	−14	0.80	1.47	1.84±0.44
− 7	−14	1.20	1.73	1.40±0.31
−14	−14	0.87	1.27	1.46±0.32
−21	−14	0.60	0.60	1.00±0.24
+14	−21	0.20	0.20	1.00±0.70
+ 7	−21	0.47	0.47	1.00±0.28
0	−21	0.63	1.03	1.63±0.40
− 7	−21	0.77	1.27	1.65±0.38
−14	−21	1.03	0.97	0.94±0.21
−21	−21	0.47	0.47	1.00±0.42
−28	−21	0.30	0.30	1.00±0.49
−14	−28	0.63	0.57	0.90±0.24
−21	−28	0.47	0.47	1.00±0.32
−28	−28	0.30	0.30	1.00±0.39
−21	−35	0.30	0.30	1.00±0.46
−28	−35	0.30	0.30	1.00±0.35

(1) On IRAM grid, i.e. in RA, Dec. from the map centre at RA (1950) = $02^h\ 38^m\ 08.5^s$, Dec. (1950) = $+59°\ 23'\ 30''$. (2) J=1–0 profiles from Nakai *et al.* (unpublished), interpolated onto the IRAM grid. (3) Smoothed to $17''$ resolution to match the J=1–0 data. (4) Errors are from the combination of rms noise and calibration uncertainty (about 15–20% for each transition).

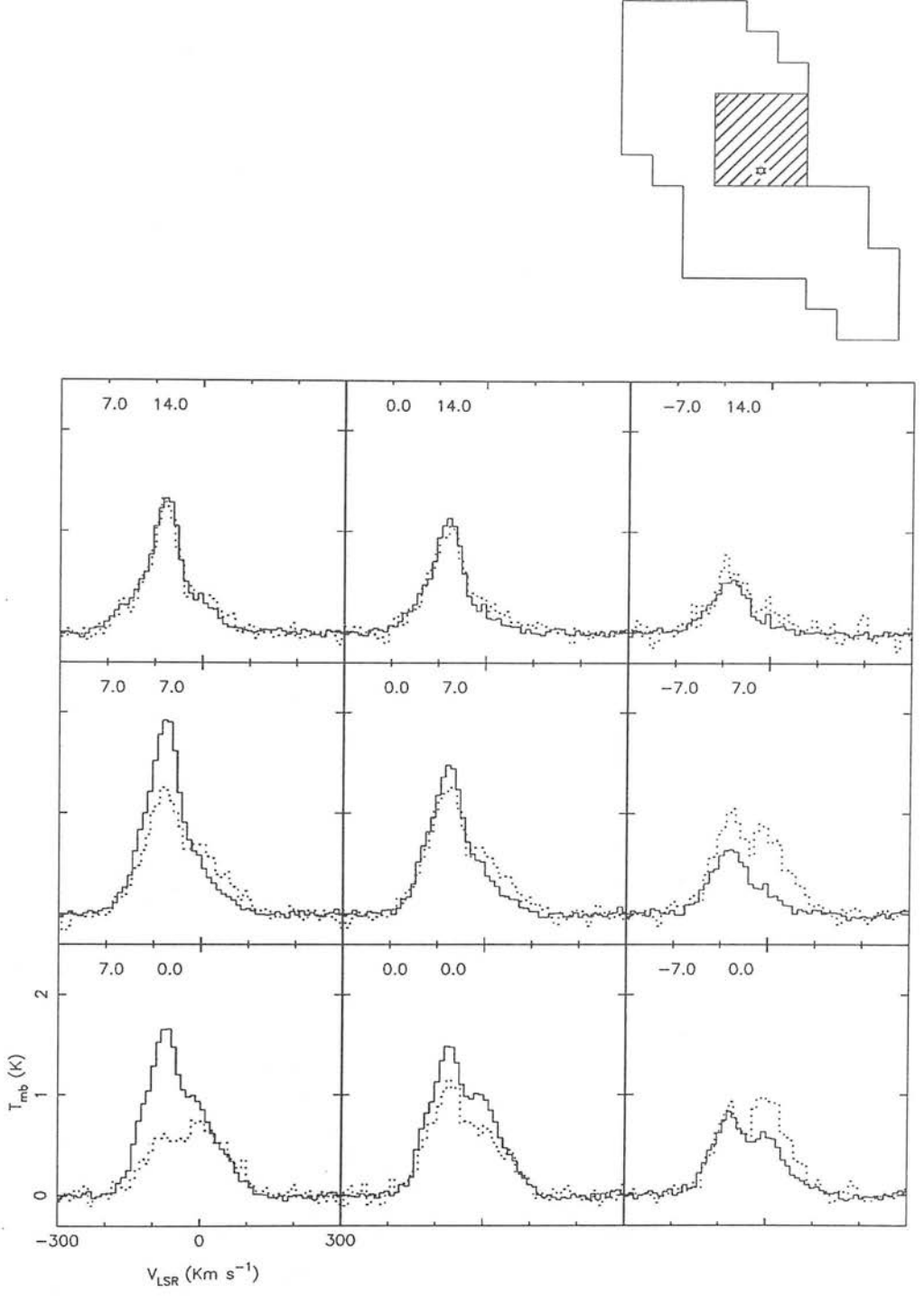

Figure 5.26: ^{12}CO J=1–0 and J=2–1 profiles from the central arcminute of Maffei 2, plotted on the same axes for comparison. The ^{12}CO J=1–0 profiles, taken with the NRO 45-m, are from Nakai *et al.* (in preparation), and have been interpolated on to the IRAM grid. The ^{12}CO J=2–1 profiles (this work) have been smoothed to 17″ resolution to match the 1–0 data. Solid line = 2–1, dotted line = 1–0 profiles.

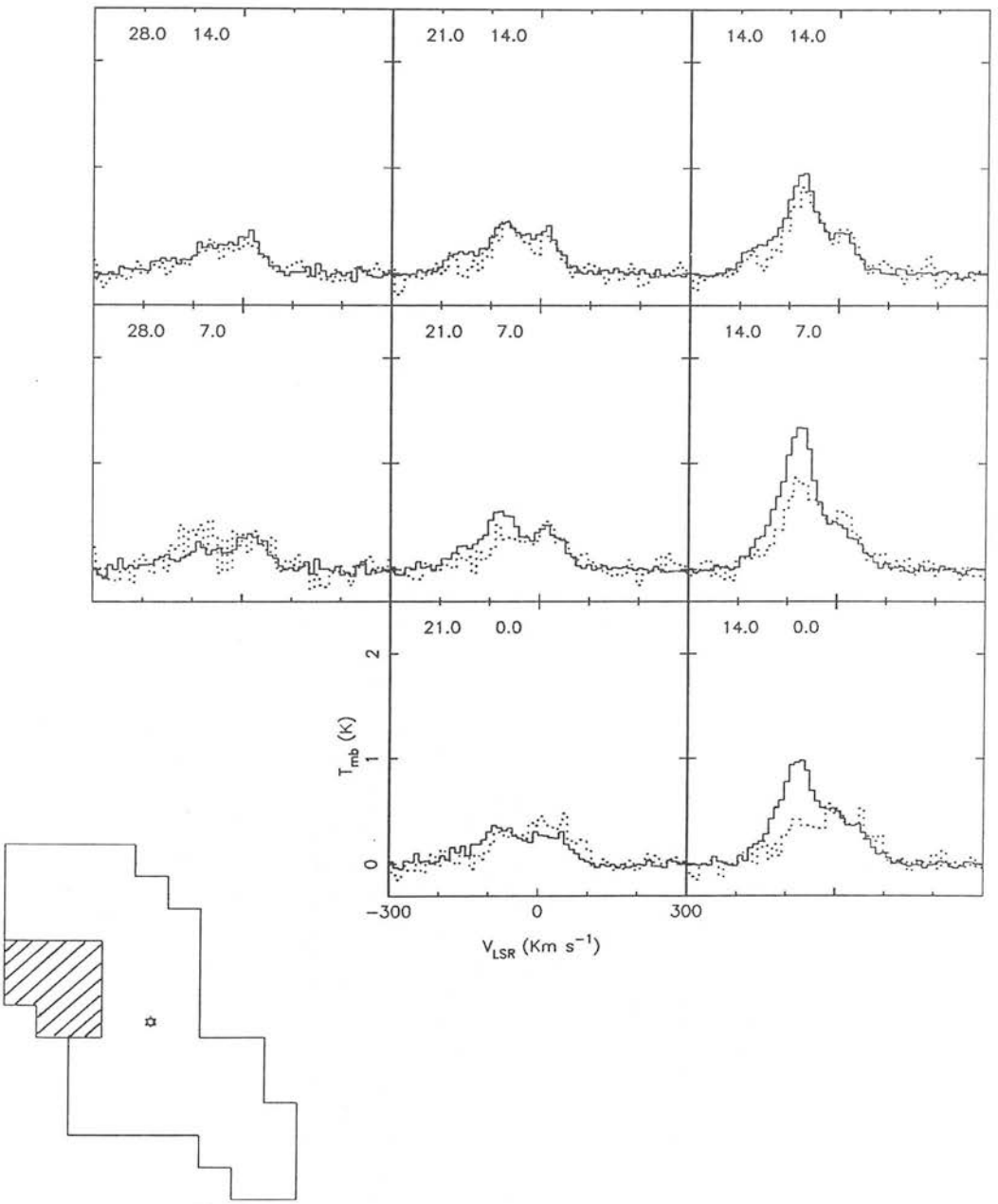

Figure 5.26 – continued

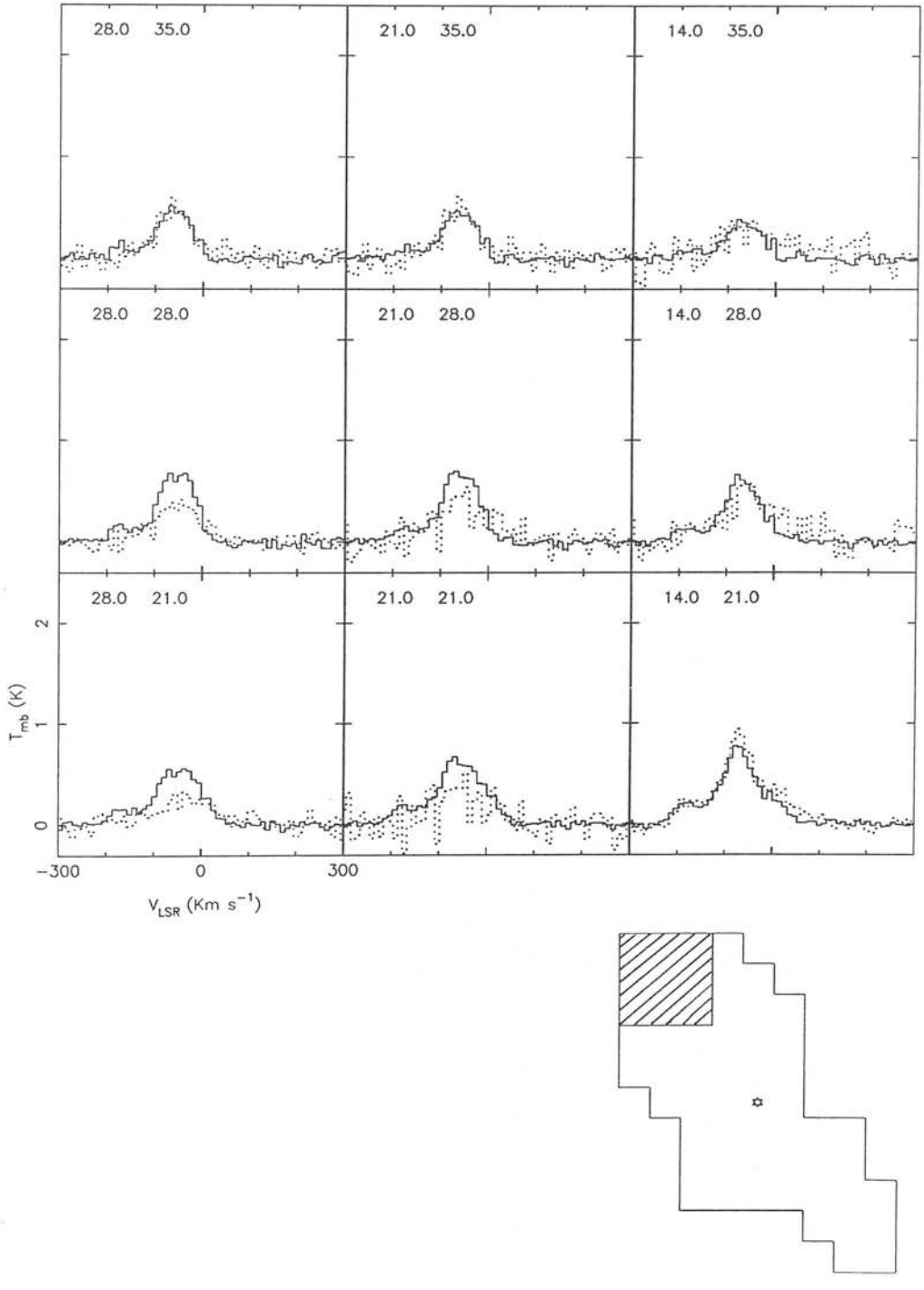

Figure 5.26 – continued

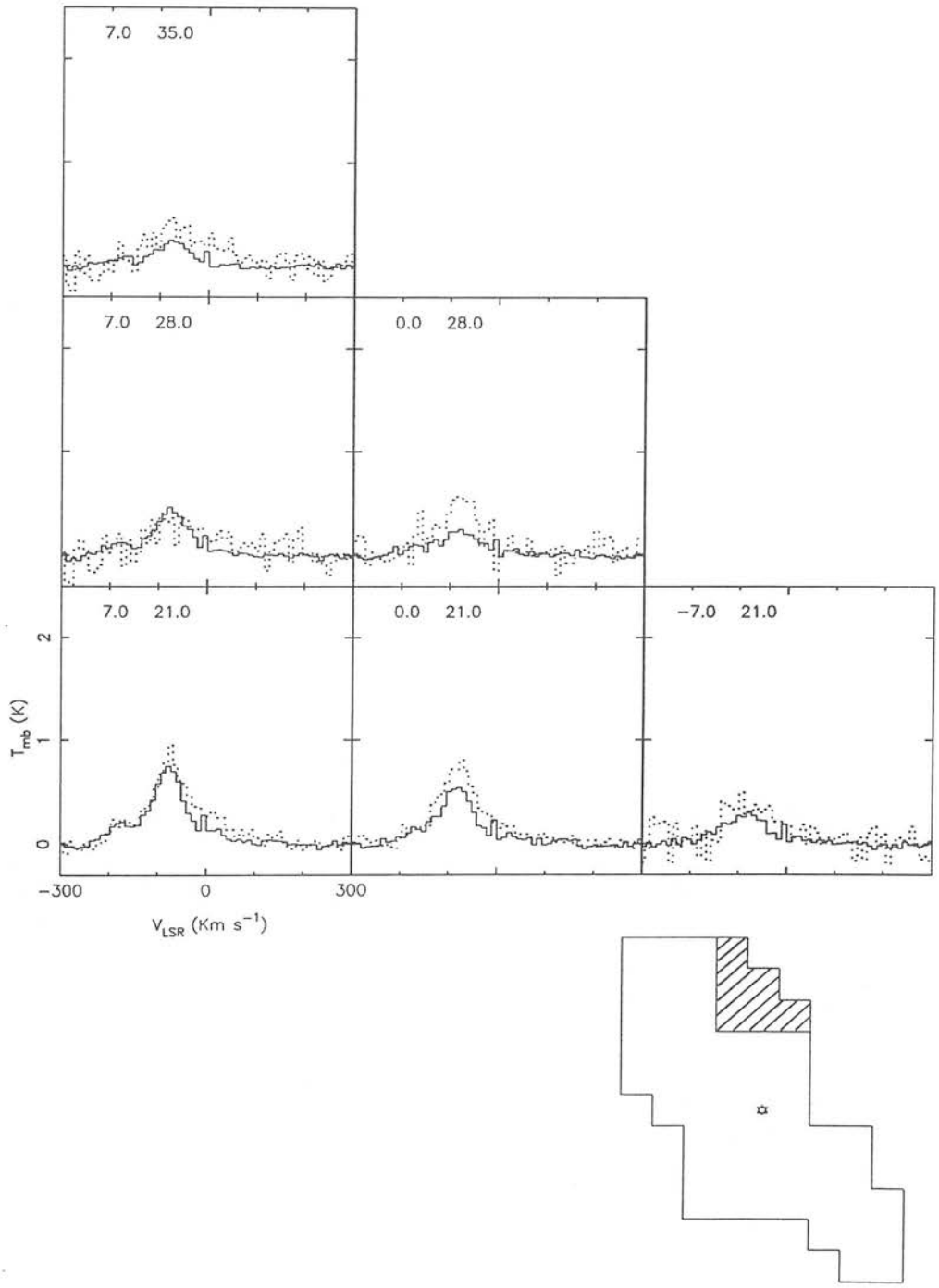

Figure 5.26 – continued

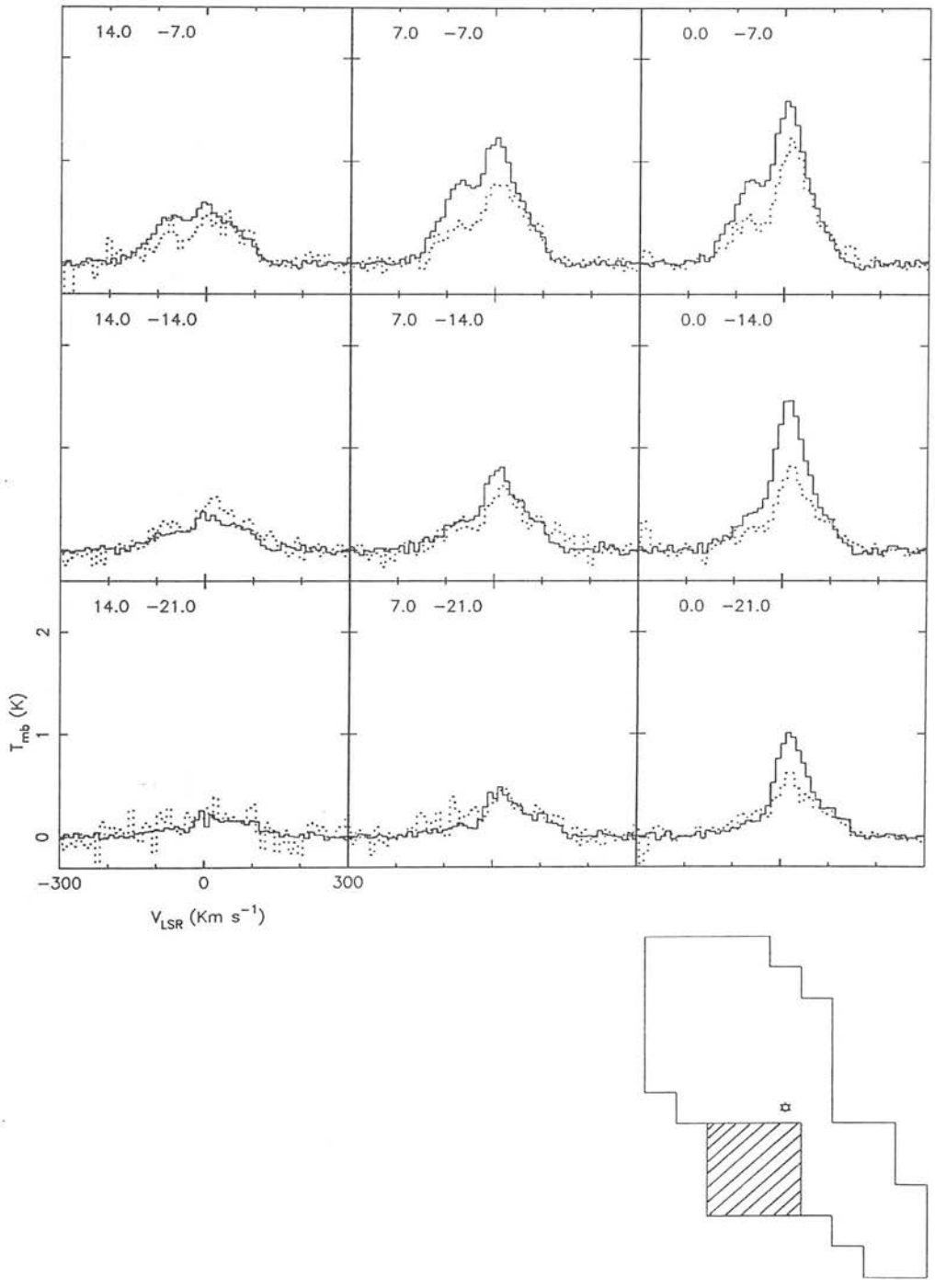

Figure 5.26 – continued

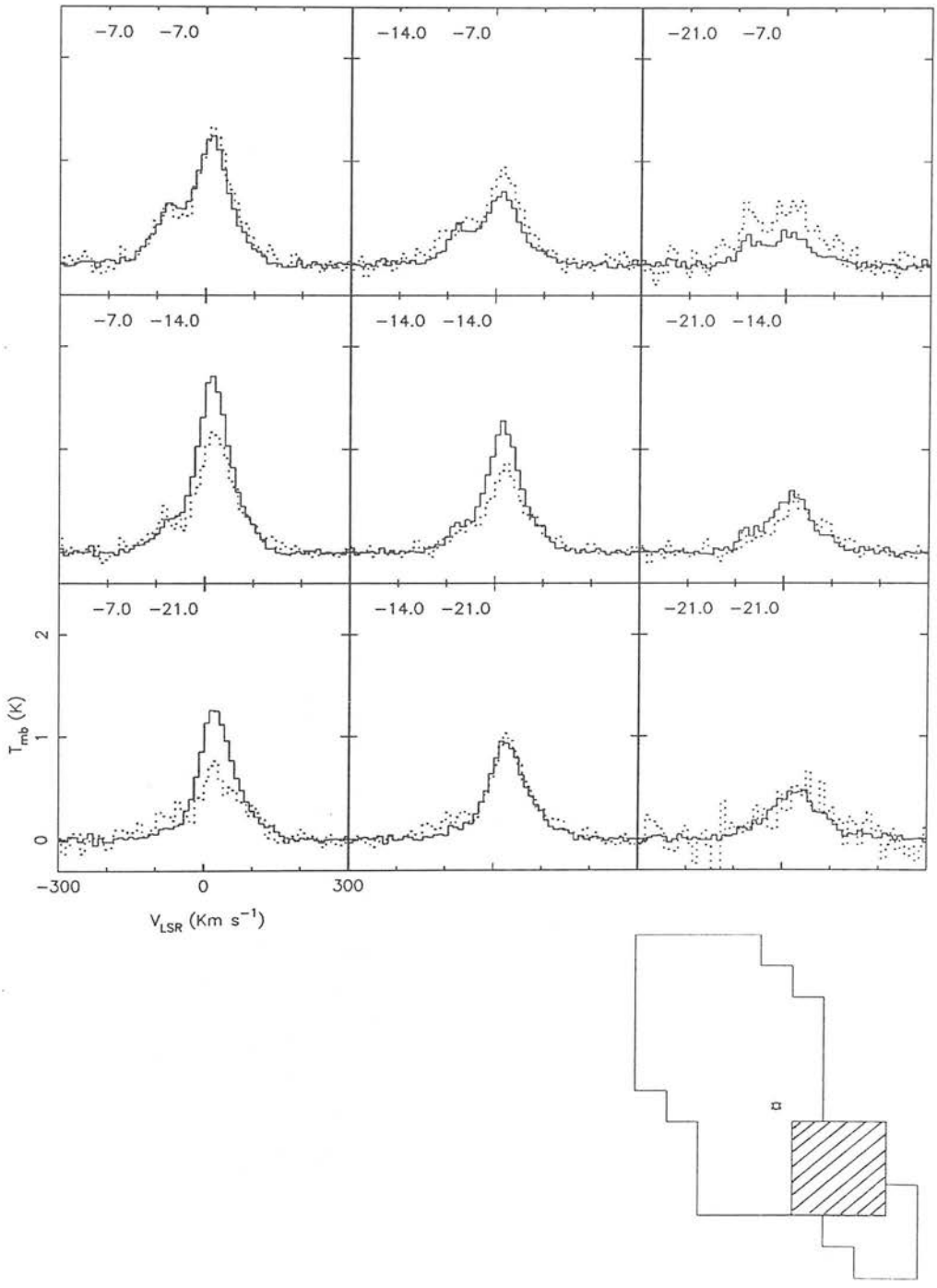

Figure 5.26 – continued

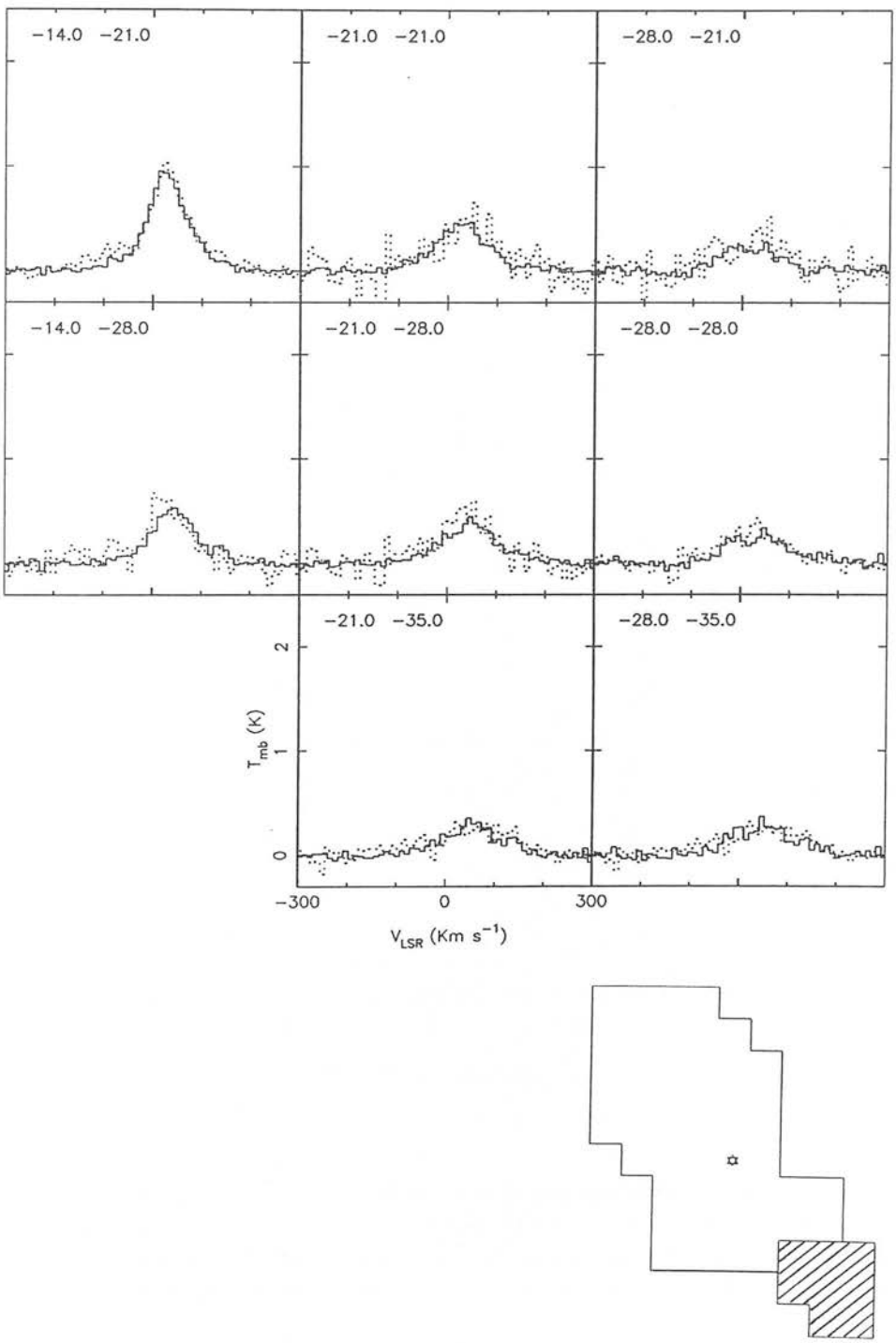

Figure 5.26 – continued

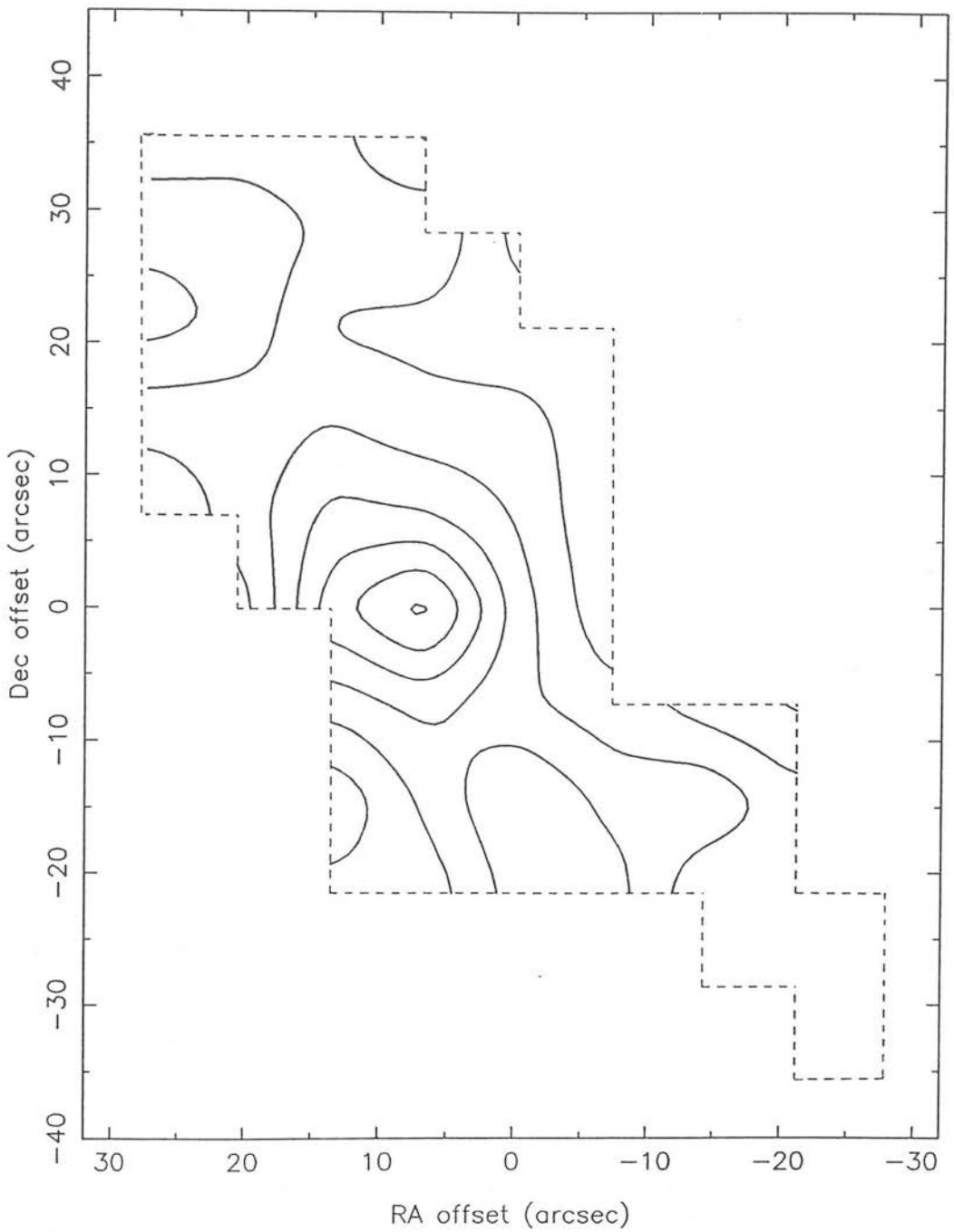

Figure 5.27: The peak ^{12}CO J=2–1/J=1–0 main beam brightness temperature ratio. The contour interval is 0.3 from a base level of 0.6. The ^{12}CO J=2–1 profiles have been smoothed into a 17″ beam and the J=1–0 data interpolated on to the grid of the IRAM observations. Note that the highest ratios ($\geq$2) are seen to the north-east of the galaxy nucleus.

$T_{\rm mb}$(2–1) exceeds $T_{\rm mb}$(1–0) only in the central regions of the galaxy – away from the nucleus $T_{\rm mb}$(2–1)/$T_{\rm mb}$(1–0)$\leq$1, getting as low as 0.5 at some positions. At two offsets north-east of the nucleus, (7,0) and (14,0), $T_{\rm mb}$(2–1)/$T_{\rm mb}$(1–0) exceeds 2, while south-west of the nucleus it reaches 1.5. The region of high 2–1/1–0 ratio is fairly well spatially correlated with the region of high ^{12}CO/^{13}CO J=2–1 ratio, although there are exceptions to this – for example the offsets (21,21),(–7,14) and (14,7) where $T_{\rm mb}(^{12}{\rm CO})/T_{\rm mb}(^{13}{\rm CO})$ >27–100, yet $T_{\rm mb}$(2–1)/$T_{\rm mb}$(1–0) is only 0.7–1.6. Low values of $T_{\rm mb}$(2–1)/$T_{\rm mb}$(1–0) (<1) are generally associated with low values of ^{12}CO/^{13}CO J=2–1.

There is a tendency in the central regions for the line ratio to vary across the profile, being higher at negative velocities. This probably just reflects the higher ratio in the north-east (approaching) side of the galaxy. There is no discernible tendency for the 2–1/1–0 ratio to increase in the line wings, as is often observed in Galactic sources (signifying a lower optical depth at high velocities), but, since we are looking not at a single source but at an ensemble of moving clouds, this is perhaps not surprising.

LTE interpretation of the line ratios

The ^{12}CO/^{13}CO J=2–1 and 1–0 peak line ratios can be used to calculate ^{12}CO and ^{13}CO peak optical depths, from equation (5.14), assuming a [^{12}CO]:[^{13}CO] abundance ratio R, and the same excitation temperature for both transitions. Columns 5 and 6 of Tables 5.9 and 5.10 present optical depths calculated for R=60 (near solar) and R=25 [as has been reported for the centre of the Milky Way (Güsten, Henkel & Batrla 1985; Langer & Penzias 1990)].

For R=60, the ^{12}CO is very optically thick over the whole starburst region, in both the 2–1 and 1–0 transitions. τ^{12}(1–0) varies from 6–15, while τ^{12}(2–1) ranges from 2–20. For R=25, the optical depths are much smaller (0.5–9) but still >1 over much of the map.

The assumption of a single-component, LTE interstellar medium runs into difficulties when one tries to use 2–1/1–0 ratios in conjunction with ^{13}CO data to deduce excitation temperatures. The ^{12}CO/^{13}CO ratio is consistent with quite optically thick gas. As can be seen from Fig. C.1 (Appendix C), for optically thick gas, the ratio of ^{12}CO 2–1/1–0 can never exceed 1. Yet, in the centre of Maffei 2, ^{12}CO/^{13}CO 'optically

thick' ratios of 5–15 are accompanied by ^{12}CO 2–1/1–0 ratios of ~1.5–2. High J=2–1/1–0 ratios (>2) have been observed previously in Maffei 2 (Sargent *et al.* 1985), as well as in M82 (Knapp *et al.* 1980), and have been interpreted as arising in optically thin gas. For a single-component ISM, the low ^{12}CO/^{13}CO ratios are not consistent with optically thin gas. However, to achieve 2–1/1–0 >1 in LTE, there must be a component of optically thin gas present. It is very unlikely that the gas is totally optically thin, since a ^{12}CO 2–1/1–0 ratio of ~2 then implies an excitation temperature of only ~12 K (Fig. C.1) which is inconsistent with the high *IRAS* dust temperatures (25–40 K) and evidence of active star formation in Maffei 2. The ratio of the J=2–1 and 1–0 transitions for the ^{13}CO isotope sheds no light on the problem. Fig. 5.28 shows the ^{12}CO J=1–0 and 2–1, ^{13}CO J=1–0 and 2–1 profiles at the centre of Maffei 2. Due to the small number of ^{13}CO profiles observed, it is not possible either to interpolate the ^{13}CO 1–0 spectra on to the IRAM grid, or to smooth the J=2–1 data to the resolution of the J=1–0 lines. However, at (0,0) it can be deduced that $T_{\rm mb}$ (2–1)/$T_{\rm mb}$ (1–0) $\leq$ 2.1 – the upper limit allowing for the effect of beam dilution on the ^{13}CO J=1–0 data. This low ratio for two presumably optically thin lines would seem to indicate cool (~12 K) gas.

A possible explanation of such anomalous ratios, which was proposed by Levreault (1988), is that the gas is warm, and the ^{12}CO J=2–1 transition has 'just' become optically thick (since the 2–1 line will saturate before the 1–0). In this case, the ratio will have started to drop away from the optically thin, high-temperature limit of 4, but has not yet reached the optically thick limit of $\leq$1. If a ratio of less than 4 but greater than 1 is then interpreted as arising from optically thin gas, a low excitation temperature will be deduced. In Fig. 5.29 [adapted from Levreault (1988)], the ^{12}CO J=2–1/1–0 ratio is plotted as a function of $T_{\rm ex}$ and τ_{10}. It can be seen that for excitation temperatures of 30–40 K, antenna temperature ratios of 1.1–1.2 can be achieved for J=1–0 optical depths of 1–2. Low ^{12}CO optical depths are however not consistent with the low observed ^{12}CO/^{13}CO ratios, unless the ^{13}CO is subject to considerable enhancement, with [^{12}CO]:[^{13}CO] $\ll$ 25. For example, for a ^{12}CO/^{13}CO antenna temperature ratio of 7 and ^{12}CO optical depth of 1.5, an abundance ratio of 13 is required – a marked enhancement even over the Galactic Centre value of ~25 (Langer & Penzias 1990). Neither is this picture consistent with the low observed ratio of ^{13}CO J=2–1/1–0 – if

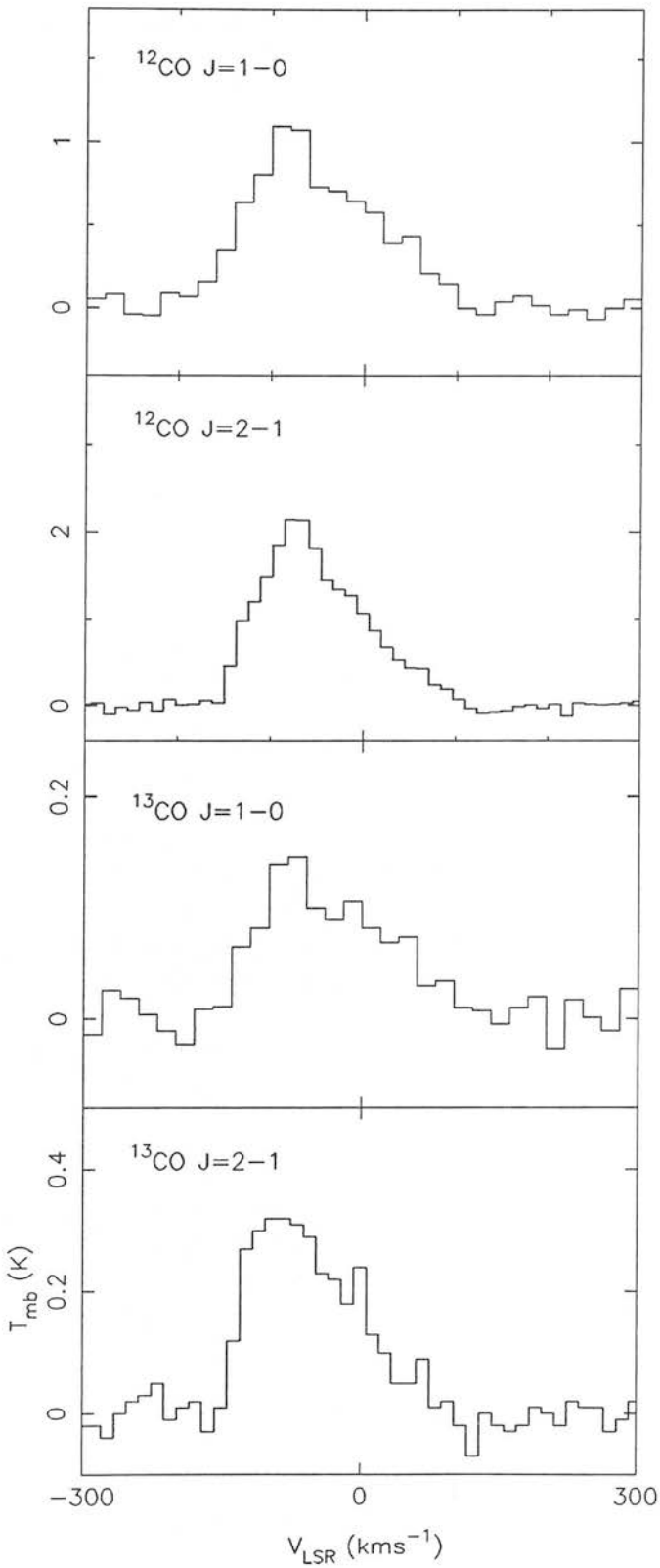

Figure 5.28: Line profiles of the ^{12}CO J=1–0, ^{12}CO J=2–1, ^{13}CO J=1–0 and ^{13}CO J=2–1 transitions from the central position of Maffei 2. The profile shapes are in good agreement, indicating that pointing errors have not badly affected the data.

the ^{12}CO is 'just' optically thick, then the ^{13}CO will certainly be optically thin, and for excitation temperatures of 30–40 K should produce a 2–1/1–0 ratio of ∼3. It is clear from the above discussion that a single-component LTE analysis cannot explain the line ratios observed at the centre of Maffei 2.

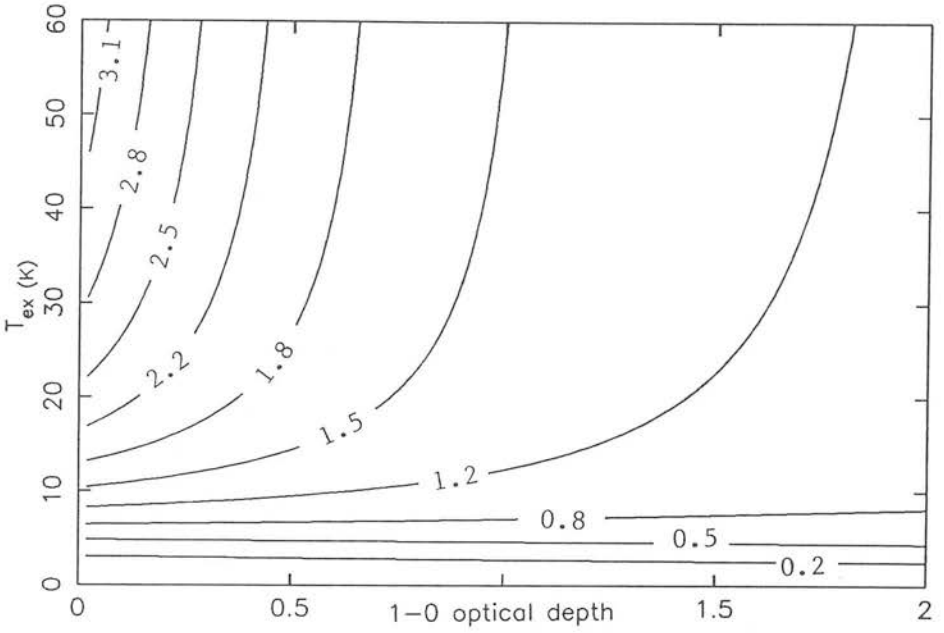

Figure 5.29: The theoretical ^{12}CO J=2–1/1–0 antenna temperature ratio, as a function of excitation temperature and ^{12}CO J=1–0 optical depth, in a one-component LTE analysis (adapted from Levreault 1988). When the gas 'just' optically thick, ratios similar to those observed (∼ 1.2) can occur for warm (30–40 K) gas. As the optical depth increases, the ratio starts to drop away from its 'optically thin' value of ∼2–4. For optical depths ≥4, ratios of ≤1 occur even for warm (≥30 K) gas.

In the outer regions of the galaxy, the ^{12}CO 2–1/1–0 ratio falls to ∼1, indicating warm (>20 K), optically thick gas, consistent with the low ^{12}CO/^{13}CO line ratios. J=2–1/1–0 ratios of ∼0.5 imply quite cool (∼10 K), optically thick gas, also consistent with the low observed ^{12}CO/^{13}CO ratios. In principle, it should be possible to deduce excitation temperatures from the ^{12}CO J=2–1/1–0 ratio, if LTE holds. Unfortunately, as can be seen from Fig. C.1 (Appendix C), the 2–1/1–0 ratio is rather insensitive to excitation temperatures T_{ex}>20 K in the optically thick case [for example, for excitation temperature increasing from 25 to 60 K, T_{mb}(2–1)/T_{mb}(1–0) increases from 0.91 to 0.96]. The calibration errors of ∼20% are far too large to discriminate between different values of T_{ex} when the 2–1/1–0 ratio is close to unity. Even for optically thin gas, the 2–1/1–0 ratio is best suited to tracing excitation temperatures <30 K – for the higher

temperatures expected in an active star formation region, observations of the J=3–2 or even higher transitions are desirable. If the dust and gas temperatures are coupled via collisions with hydrogen, then excitation temperatures of 30 K or more are quite plausible, while the observational signatures of photodissociation regions imply that a large fraction of the neutral interstellar medium may be warm.

Assuming a one-component, single-temperature, LTE interstellar medium is of course a gross simplification. In the environment of a starburst (a clumpy medium, swept up into small clouds and filaments by the combined effect of HII regions, stellar winds and supernovae), the surface area to volume ratio of a molecular cloud will be quite large, and much of the heating of the cloud is likely to arise from the outside. Such externally heated clouds will then possess temperature gradients with temperature decreasing inwards, which will distort the observed line ratios. Specifically, the more optically thick ^{12}CO and J=2–1 transitions will arise in the warmer outer layers of a cloud, artificially enhancing the ^{12}CO/^{13}CO and ^{12}CO 2–1/1–0 line ratios (Young & Scoville 1984; Cantó, Rodríguez & Anglada 1987; Maloney & Black 1988). Not only could this produce 2–1/1–0 line ratios of >1 in optically thick gas, such as is seen at the centre of Maffei 2, but the true ^{12}CO optical depth could be even higher than is deduced from the ^{12}CO/^{13}CO ratio by assuming the same T_{ex} for the two transitions. Externally heated clouds may also explain the low observed ^{13}CO J=2–1/1–0 line ratios. In this scenario, if the optically thin ^{13}CO transitions are arising from the cooler interior of the clouds, rather than the warm, UV-illuminated outer layers from which the optically thick ^{12}CO line originates, the ^{13}CO J=2–1/1–0 ratio will reflect this. The two isotopes would then trace quite different components of the molecular gas. Such a picture is qualitatively consistent with the significant component of cool gas implied by the dust observations in Chapter 4.

A similar effect can be produced by line trapping. If a transition is very optically thick, a photon emitted by one molecule will very quickly be absorbed by another, changing the relative populations of the levels in such a way as to increase T_{ex}. The result of this is that the excitation temperature of a very optically thick transition can approach the kinetic temperature – i.e. the line can become thermalized – at a lower density than the 'critical density'. Thus the ^{12}CO may be thermalized while the ^{13}CO isn't, and the two transitions may have very different excitation temperatures. It is

possible to underestimate markedly the true optical depth in this way – for example, if $T_{ex}(^{12}CO)$ exceeds $T_{ex}(^{13}CO)$ by 50%, the $^{12}CO/^{13}CO$ line ratio can underestimate $\tau(^{12}CO)$ by a factor of $\sim$2.

Table 5.12: Critical densities for CO transitions – from Wild (1990).

Transition	n_{crit} (H_2) (cm^{-3})
^{12}CO J=1–0	2.2×10^3
^{12}CO J=2–1	1.4×10^4
^{13}CO J=1–0	1.9×10^3
^{13}CO J=2–1	1.3×10^4

Table 5.12 (from Wild 1990) summarizes the critical densities for the ^{12}CO and ^{13}CO J=2–1 and 1–0 transitions. Since the J=2 level is more quickly spontaneously depopulated than the J=1 level ($A_{21} \simeq 10\ A_{10}$), its critical density for thermalization is higher. It is therefore possible, at gas densities $n(H_2) \sim$ few $\times\ 10^3$ cm^{-3}, that the J=2–1 transition will be subthermally excited, and $T_{ex}(2\text{–}1) < T_{ex}(1\text{–}0)$. Although this is probably not significant for ^{12}CO [since if $\tau(^{12}CO) \gg 1$, line trapping will produce thermalization even at $n < n_{crit}$], subthermal excitation of the ^{13}CO J=2–1 line may be an important factor contributing to the low ^{13}CO J=2–1/1–0 ratio.

Apart from the non-LTE 2–1/1–0 and $^{12}CO/^{13}CO$ line ratios, a striking aspect of the data is the marked variation of $^{12}CO/^{13}CO$ ratio from position to position within the galaxy for the J=2–1 transition (e.g. Fig. 5.23). Such variations point to changes in the global properties of cloud ensembles, resulting in variations in optical depth and/or [^{12}CO]:[^{13}CO] abundance ratio throughout the galaxy. There are a number of factors that can affect the [^{12}CO]:[^{13}CO] abundance ratio. Stellar processing results in an enhanced abundance of ^{13}C, which is then returned to the ISM via mass loss and supernovae (Audouze, Lequeux & Vigroux 1975). ^{13}CO can be depleted by selective photodestruction in intense UV fields – the more abundant ^{12}CO molecule is self-shielded to the dissociating UV transitions as they become optically thick, while the rarer isotope does not have the benefit of self-shielding and is selectively dissociated (Bally & Langer 1982; Glassgold, Huggins & Langer 1985). The [^{12}CO]:[^{13}CO] abundance ratio is therefore influenced by the competing processes of stellar evolution enhancing the ^{13}CO and photodissociation depleting it. In the Galactic Centre, the

relative abundance of ^{13}CO is markedly enhanced ([^{12}CO]:[^{13}CO]$\sim$25) over the solar neighbourhood value of 89 (Güsten *et al.* 1985; Langer & Penzias 1990). Variations on $\sim 7''$ scales of the ^{13}CO abundance may partially explain the striking variation in ^{12}CO/^{13}CO line ratio for the J=2–1 data – for example, at (14,7) where ^{12}CO is strong but ^{13}CO not detected (Fig. 5.24), the ^{13}CO may have been selectively destroyed in the intense UV fields associated with a region of young massive stars.

A contribution to the line ratios from optically thin gas?

Another possible cause of the anomalous line ratios described in the previous subsections is a mixture of optically thin and thick emission within the beam, whereby the optically thin component enhances the 2–1/1–0 line ratio without requiring that the gas be completely optically thin and therefore cool. The fraction of optically thin gas necessary to produce the observed ^{12}CO J=2–1/1–0 line ratios can be studied by following the method outlined by Wiklind *et al.* (1990).

Consider an ensemble of clouds consisting of two components : a fraction f being optically thin [$\tau(^{12}\mathrm{CO}) \ll 1$], and a fraction $(1-f)$ having $\tau(^{12}\mathrm{CO}) \gg 1$. The global beam filling factor is F. If the excitation temperature $T_{\rm ex}$ is assumed constant for both transitions and cloud populations, then the observed antenna temperatures are given by

$$T_{\rm mb} = F\,[(1-f)\,T_{\rm r}(\tau > 1) + f\,T_{\rm r}(\tau < 1)], \tag{5.17}$$

where $T_{\rm r}$ is defined as in equation (5.11), and F is the global beam filling factor.
For the optically thick component, $1\text{–}e^{-\tau} \simeq 1$. Then the observed line ratio $R_{\rm obs}$ is given by

$$R_{\rm obs} = R_0\,\frac{(1 - f e^{\,p\tau_{10}})}{(1 - f e^{-\tau_{10}})} \tag{5.18}$$

(Wiklind *et al.* 1990), where

$$R_0 = [J_{21}(T_{\rm ex}) - J_{21}(2.7\,\mathrm{K})]/[J_{10}(T_{\rm ex}) - J_{10}(2.7\,\mathrm{K})] \tag{5.19}$$

(J being defined as in equation 5.12), and

$$p = \frac{\tau_{21}}{\tau_{10}} = \frac{2(1 - e^{-h\nu_{21}/kT_{\rm ex}})}{(e^{h\nu_{10}/kT_{\rm ex}} - 1)}$$

is the ratio of optical depths for the optically thin component.

In Fig. 5.30 contours of constant f are plotted, as a function of τ_{10} and $T_{\rm ex}$, for $R_{\rm obs}$ = 1.5, 2.0 and 2.5. Also plotted are contours of constant f when the excitation temperature of the optically thick component is held constant at 20 or 40 K.

It can be seen from Fig. 5.30 that the higher the observed temperature ratio, the more restricted the range of $T_{\rm ex}$ and τ_{10}, and the higher the fraction of optically thin emission needed to reproduce the observed 2–1/1–0 ratio. For example, for a ^{12}CO 2–1/1–0 ratio of 2.5, excitation temperatures >25 K and ^{12}CO optical depths <0.2 are required, and the filling factor of the optically thin cloud population is at least 0.9. For antenna temperature ratios of 1.6–2.0, the range of acceptable $T_{\rm ex}$, τ_{10} and f is much greater, but the filling factor of optically thin gas is always greater than 0.45 for excitation temperatures less than 60 K. If the gas excitation temperature for Maffei 2 is 30–40 K, then Fig. 5.30 shows that, if the observed line ratios are due to a mixture of optically thick and thin emission, the minimum fraction of optically thin gas in the beam needs to be ~70% for $R_{\rm obs}$=1.6, and ~85% for $R_{\rm obs}$ = 2.0.

What effect would such a mixture of clouds have on the other diagnostic line ratio, ^{12}CO/^{13}CO? Once more, consider the emission coming from two cloud populations: (i) $\tau(^{12}{\rm CO}) \ll 1$ and filling factor f, and (ii) $\tau(^{12}{\rm CO}) \gg 1$ and filling factor (1–f). For each component, the ^{13}CO optical depth is given by

$$\tau(^{13}{\rm CO}) = \tau(^{12}{\rm CO})/R, \tag{5.20}$$

where R is the [^{12}CO]:[^{13}CO] abundance ratio. Then (for $h\nu \ll kT_{\rm ex}$ and $T_{\rm ex} \gg 2.7$ K)

$$\begin{aligned} T_{\rm mb}^{12} &= {\rm F}\, f\, T_{\rm ex}\, (1 - {\rm e}^{-\tau_{\rm thin}^{12}}) + (1-f)\, F\, T_{\rm ex}\, (1 - {\rm e}^{-\tau_{\rm thick}^{12}}), \\ T_{\rm mb}^{13} &= {\rm F}\, f\, T_{\rm ex}\, (1 - {\rm e}^{-\tau_{\rm thin}^{13}}) + (1-f)\, F\, T_{\rm ex}\, (1 - {\rm e}^{-\tau_{\rm thick}^{13}}), \end{aligned}$$

and, for the J=2–1 transition, it follows that

$$\frac{T_{\rm mb}^{12}}{T_{\rm mb}^{13}} = \frac{1 - f\, {\rm e}^{-p\tau_{10}}}{1 - f\, {\rm e}^{-p\tau_{10}/R} + A(f-1)}, \tag{5.21}$$

where p is defined above, τ_{10} is the ^{12}CO J=1–0 optical depth of the optically thin component, and A=${\rm e}^{-\tau_{\rm thick}^{13}}$ = ${\rm e}^{-\tau_{\rm thick}^{12}/R}$. So, for example, if $T_{\rm ex}$ = 35 K, the 2–1/1–0

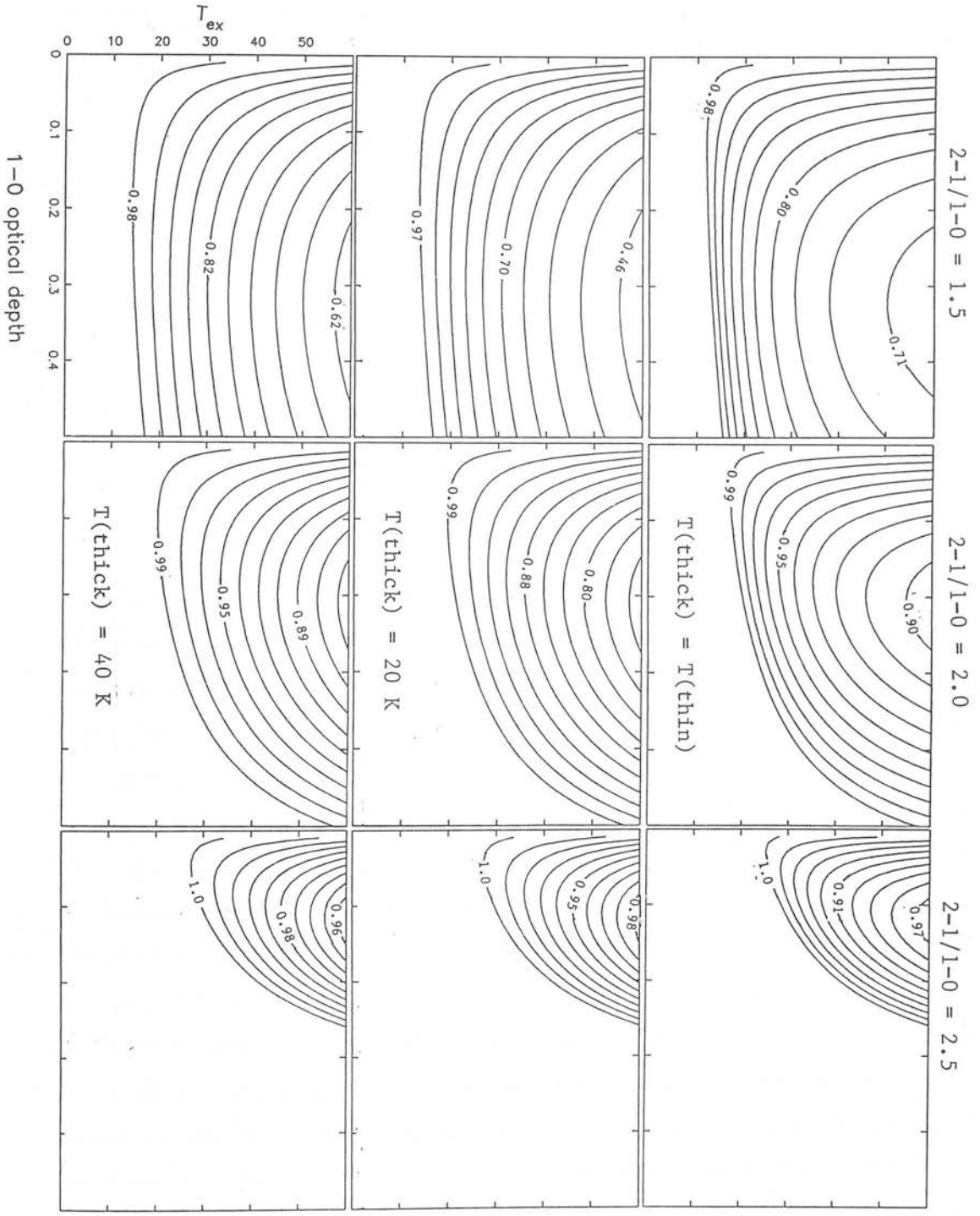

Figure 5.30: A simple two-component model of optically thin and optically thick gas, showing the fraction of optically thin emission, as a function of excitation temperature, that would be needed to push the ^{12}CO 2–1/1–0 ratio to 1.5, 2 or 2.5. Three scenarios are shown: $T_{\rm thick} = T_{\rm thin}$, and $T_{\rm thick}$ held constant at 20 or 40 K. This approach was outlined in Wiklind *et al.* (1990).

ratio is 1.6 and $\tau_{10} = 0.3$ (and therefore from Fig. 5.30, $f = 0.8$), then $T_{\rm mb}^{12}/T_{\rm mb}^{13} = 0.69/(0.23 - 0.2A)$ for a [^{12}CO]:[^{13}CO] abundance ratio of 30. Whereas, for a 2–1/1–0 ratio of 2.0 under the same conditions ($f \simeq 0.95$), then $T_{\rm mb}^{12}/T_{\rm mb}^{13} = 0.64/(0.08 - 0.05A)$. If the optically thick component has ^{12}CO J=2–1 optical depths of ~5–30, this will give ^{12}CO/^{13}CO J=2–1 line ratios of 5–18, quite similar to those actually observed.

Although the above line ratio predictions may seem somewhat contrived, they do demonstrate that, even without excitation temperature gradients, line trapping, sub-thermal excitation and other non–LTE effects, it is possible to produce, by invoking a simple mixture of optically thin and thick clouds, ^{12}CO 2–1/1–0 and ^{12}CO/^{13}CO line ratios that would be very misleading if interpreted assuming a single-component interstellar medium.

5.6.2 Non-LTE modelling

From the discussion in Section 5.6.1, it is clear that there are a number of effects, such as line trapping, multiple temperature/opacity components, etc., that can make reliable interpretation of CO line ratios very difficult. The ideal solution would obviously be a full radiative transfer treatment of the line emission from an ensemble of unresolved, independently moving clouds. As well as needing vast amounts of computing time, such a model would require a wide array of input parameters – cloud size, density and temperature distributions and gradients, velocity dispersions (both internal and cloud–cloud), large-scale motions (rotation, infall, outflow), etc. With many of these quantities not certain even in our own Milky Way, let alone in external systems, the problems of finding a unique solution to observed data are obvious.

However, much work has been done over the last few years on simplified versions of the ideal model, from which useful constraints on physical conditions can still be obtained. One of the most comprehensive of recent published non-LTE models of extragalactic molecular line data is that of Eckart *et al.* (1990), who observe ^{12}CO, ^{13}CO and C^{18}O J=2–1 and J=1–0 emission from IC342 – a nearby, almost face-on spiral lying at approximately the same distance as Maffei 2, and only ~11° away in the sky.

Eckart *et al.* (1990) observe in IC342 line ratios quite similar to those in Maffei 2 – ^{12}CO 2–1/1–0 ratios of 0.5–1.3, ^{13}CO 2–1/1–0 ratios of 0.8–1.3 (i.e. much less than the

optically thin, warm value of ~4), and $^{12}CO/^{13}CO$ ratios of ~11, indicating optically thick gas. They do not observe ^{12}CO 2–1/1–0 ratios as high as the values of >2 that are present at some positions in Maffei 2, and deduce, from LTE considerations, that the gas in IC342 is generally optically thick and warm, although, as we found also for Maffei 2, the ^{13}CO 2–1/1–0 ratios are inconsistent with optically thin LTE emission from warm gas. Further from the nucleus of IC342, the line ratios drop to ~0.7, again similar to Maffei 2.

To attempt a non-LTE analysis of the CO emission from IC342, Eckart *et al.* (1990) assume that emission from all isotopes and transitions arises from regions with the same physical conditions. They then use a 'clumpy cloud' model to calculate the ^{12}CO and ^{13}CO J=2–1/1–0 line ratios expected from an ensemble of unresolved clouds, as a function of H_2 column and number density, and gas kinetic temperature. This is a 'single-component' model and does not allow for density and temperature gradients, or for radiative interaction between clumps, although it does take into account line trapping and filling-factor effects. Using this model, Eckart *et al.* explain their observed 2–1/1–0 ratios of ~1 at the centre of IC342 as arising from warm (>20 K), dense (2×10^3 cm^{-3}) optically thick gas. In one region of their map, the line ratios reach ~1.3, implying hot (>40 K), partially optically thin gas, while ratios of 0.5–0.75 are interpreted as cooler gas with kinetic temperatures $\simeq$ 10–20 K. Although this model as presented in Eckart *et al.* is specifically for the IC342 data, if we accept the principal assumption that all the lines arise in the same gas, at any one position, then the line ratio predictions made by the model can also be applied to Maffei 2. Unfortunately, it is impossible to evaluate accurately the ^{13}CO 2–1/1–0 ratio in Maffei 2, as the ^{13}CO observations were made on different grids, with different beamsizes, and too few points were observed to attempt any kind of smoothing or interpolation. At (0,0), the ratio is $\leq$2.1, and this seems to be fairly typical of the central $\simeq$15″. An H_2 column density of $\sim 1.5 \times 10^{22}$ cm^{-2} (see next section) then implies (with Eckart *et al.*'s abundance ratio of $[^{12}CO]:[H_2]=8 \times 10^{-5}$) that $N(^{12}CO) \sim 1.2 \times 10^{18}$ cm^{-2}. In Fig. 5.31 are shown the predictions of their model for $N(^{12}CO)=1.3 \times 10^{18}$ cm^{-2}, plotting ^{12}CO and ^{13}CO 2–1/1–0 line ratios as a function of $n(H_2)$ and T_k. A ^{12}CO 2–1/1–0 ratio of $\geq$1.8 implies kinetic temperatures of >60 K – the assumption of a one-component, single-temperature ISM, however, is not very realistic, and, as has already been discussed,

multicomponent gas and temperature gradients can easily distort the observed line ratios. For a ^{12}CO 2–1/1–0 line ratio of 1.3–1.6, and ^{13}CO 2–1/1–0 ratio of <2, Fig. 5.31 implies that T_k = 30–50 K, with $n(H_2)\simeq 2$–5×10^3 cm^{-3}. For a slightly higher ^{12}CO column density of 4×10^{18} cm^{-2}, the same constraints lead to T_k >35 K, $n(H_2)\simeq$ 1–3 $\times$ 10^3 cm^{-3}. Thus very simple non-LTE modelling techniques indicate that the molecular gas in Maffei 2 is warm and dense, and support our previous assumptions that the J=1–0 transitions of both ^{12}CO and ^{13}CO are probably thermalized, while the ^{13}CO J=2–1 line may well be subthermal. Temperature gradients, and the contribution from an optically thin component of gas, may conspire to push the ^{12}CO 2–1/1–0 ratio above ~1.8 at some positions.

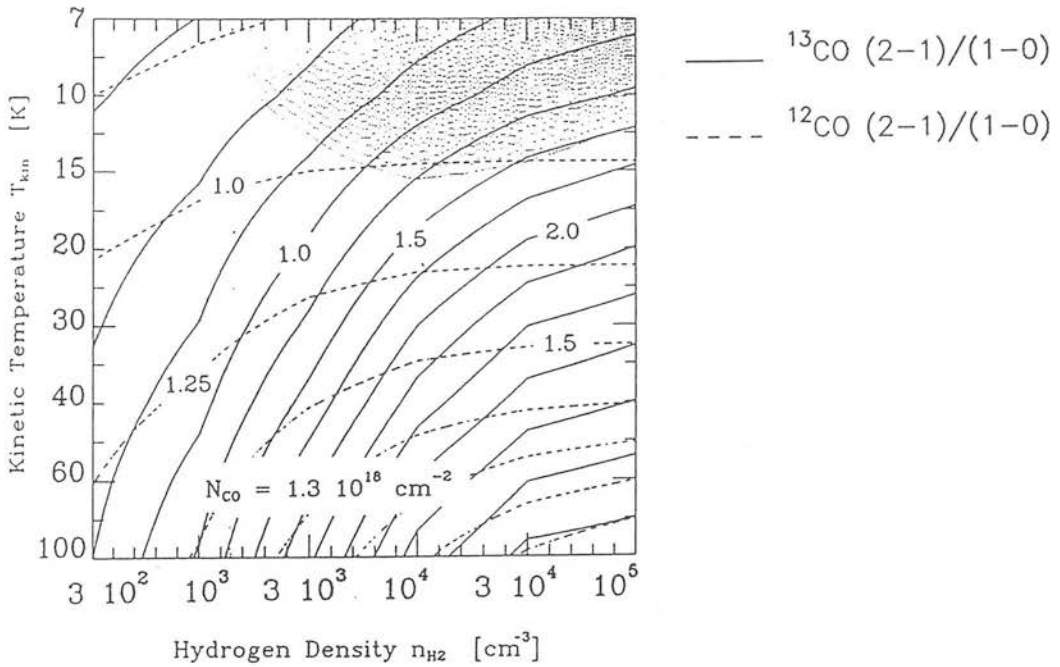

Figure 5.31: Predicted ^{12}CO and ^{13}CO J=2–1/1–0 ratios as a function of gas kinetic temperature and number density, from the non-LTE, clumpy-cloud model of Eckart *et al.* (1990), developed for their IC342 data. The line ratios observed in the centre of Maffei 2 are consistent with warm ($\geq$30 K), moderately dense ($\sim 3 \times 10^3$ cm^{-3}) gas.

5.6.3 Column density and mass of molecular gas

The column density, and hence mass, of molecular hydrogen, is typically calculated from CO data in one of two ways.

(i) If the CO emission is optically thin, then by assuming LTE and adopting an

excitation temperature T_{ex}, the column density of CO is given, e.g. for the ^{13}CO J=2–1 transition, by

$$N^{13} = 1.20 \times 10^{14}\, e^{5.3/T_{ex}} \frac{\int T_{mb}\, dv\, (\mathrm{K\,km\,s^{-1}})}{(1 - e^{-10.6/T_{ex}})}\, \mathrm{cm^{-2}}, \tag{5.22}$$

while for the J=1–0 line,

$$N^{13} = 2.41 \times 10^{14} \frac{\int T_{mb}\, dv\, (\mathrm{K\,km\,s^{-1}})}{(1 - e^{-5.3/T_{ex}})}\, \mathrm{cm^{-2}}. \tag{5.23}$$

The column density of H_2, $N(H_2)$, then follows directly by adopting an appropriate abundance ratio – e.g. $[H_2]$:$[^{13}CO]$=5×10^5 (Dickman 1978). The accuracy of this method is of course dependent on the validity of the LTE assumption, and the reliability of the assumed values of T_{ex} and $[H_2]$:$[^{13}CO]$. As was discussed in the previous sections and in Chapter 1, all of these assumptions are somewhat risky.

(ii) An alternative method has been extensively applied to CO observations of external galaxies, and relies on the assumptions that ^{12}CO is very optically thick, as in the Milky Way, and that the clouds are virialized. In this case, I_{CO} is simply 'counting the number of clouds in the beam', and is directly proportional to $N(H_2)$. From observations of a wide range of Galactic objects, the constant of proportionality has been deduced (see Chapter 1):

$$N(H_2)/I_{CO} = 2.6 \times 10^{20}\, \mathrm{cm^{-2}}\, (\mathrm{K\,km\,s^{-1}})^{-1} \tag{5.24}$$

(Young & Scoville 1982; Wild 1990). There is a growing body of evidence, however, to suggest that, while the 'constant conversion factor' may reliably give $N(H_2)$ in the discs of spiral galaxies, it is far from reliable in galactic nuclei and starbursts (e.g. Maloney & Black 1988; Maloney 1990a; Chapter 1).

The line profiles of ^{12}CO J=1–0 and 2–1 are very similar in shape and intensity, and $T_{mb}(2\text{–}1) \simeq T_{mb}(1\text{–}0)$ over most of the galaxy. Hence application of the Galactic conversion factor for the 1–0 transition will give approximate values of $N(H_2)$, possibly in error by factors of $\leq$2 either way (assuming the conversion factor to be valid). The ^{13}CO J=2–1 data can also be used to estimate $N(H_2)$, by adopting appropriate values of T_{ex} and $[H_2]$:$[^{13}CO]$. As discussed in Section 5.6.1, it is very difficult to deduce T_{ex} from the observed line ratios, although a variety of observational evidence suggests that a value of between 20 and 45 K is reasonable. $N(H_2)$ was therefore calculated for T_{ex}

= 20 and 40 K. The higher temperature is likely to be more appropriate for the central starburst region, and the lower temperature for the outer regions of the ^{12}CO 2–1 map. An [H_2]:[^{13}CO] abundance ratio of 5×10^5 (Dickman 1978) is adopted. In Table 5.13, the values of $N(H_2)$ derived using both methods are compared.

Table 5.13: Column density of H_2 from ^{12}CO and ^{13}CO J=2–1 data.

Offset (arcsec)		$I(^{12}CO)$ [1] (K km s^{-1})	$I(^{13}CO)$ [1] (K km s^{-1})	$N(H_2)$ [2] 10^{22} cm^{-2}	$N(H_2)$ [3] 10^{22} cm^{-2}	$N(H_2)$ [4] 10^{22} cm^{-2}	Ratio [5]
+14	+21	99.63	7.61	2.59	0.14	0.22	12–19
+ 7	+14	138.72	8.29	3.61	0.16	0.24	15–23
0	+14	129.36	10.79	3.36	0.21	0.32	11–16
+ 7	+ 7	281.54	8.17	7.32	0.16	0.24	31–46
0	+ 7	151.10	32.24	3.93	0.61	0.95	4–6.4
+ 7	0	270.95	20.82	7.04	0.40	0.61	12–17.5
0	0	266.49	42.24	6.93	0.80	1.24	5.5–9
− 7	0	115.91	42.45	3.01	0.81	1.25	2.4–3.7
+ 7	− 7	225.19	14.88	5.85	0.28	0.44	13–21
0	− 7	239.64	38.59	6.23	0.73	1.13	5.5–8.5
− 7	− 7	133.15	34.05	3.46	0.65	1.00	3.5–5.3
0	−14	153.55	19.01	3.99	0.36	0.56	7–11
− 7	−14	224.29	23.83	5.83	0.45	0.70	8.3–13
−14	−14	175.95	18.03	4.57	0.34	0.53	9–13.4
0	−21	129.99	4.12	3.38	0.08	0.12	28–42
− 7	−21	143.84	10.68	3.74	0.20	0.31	12–19
−14	−21	92.68	20.13	2.41	0.38	0.59	4–6.3

(1) Error in I_{CO} of $\simeq$15–20% . (2) Calculated from the ^{12}CO J=2–1 data assuming $\tau \gg 1$ and $N(H_2)/I_{CO} = 2.6 \times 10^{20}$ cm^{-2} (K kms^{-1})$^{-1}$ (Wild 1990) which is appropriate for IRAM data. Estimated errors of up to a factor of 2 either way. (3) Calculated from the ^{13}CO J=2–1 data by adopting T_{ex} = 20 K, [H_2]:[^{13}CO] = 5×10^5 (Dickman 1978), and assuming optically thin ^{13}CO emission. (4) As for (3) but with T_{ex} = 40 K. (5) Ratio of column densities derived using ^{12}CO and ^{13}CO integrated intensities.

It can be seen from Table 5.13 that $N(H_2)$ as derived from the 'constant conversion factor' exceeds that derived from optically thin ^{13}CO by factors of ~2–20. If the ^{13}CO J=2–1 transition is subthermally excited (Section 5.6.1), then $N(H_2)$ will be underestimated. In Table 5.14, the ^{13}CO J=1–0 line, which has a critical density 10 times less than that of ^{13}CO J=2–1, is used for an independent calculation of $N(H_2)$, and compared to $N(H_2)$ calculated from the ^{12}CO J=1–0 data (Nakai *et al.*, in preparation) using the Galactic conversion factor. The values of $N(H_2)$ derived from

^{13}CO J=2–1 are slightly less than those obtained from ^{13}CO J=1–0, consistent with subthermal excitation of ^{13}CO J=2–1 and unequal excitation temperatures for the two transitions. Yet even for the thermalized J=1–0 transition, $N(H_2)$ calculated using the constant conversion factor exceeds that obtained from ^{13}CO data by factors of 4–12.

Table 5.14: Column density of H_2 from ^{12}CO and ^{13}CO J=1–0 data.

Offset (arcsec)		$I(^{12}CO)$ [1] (K km s^{-1})	$I(^{13}CO)$ [2] (K km s^{-1})	$N(H_2)$ [3] 10^{22} cm^{-2}	$N(H_2)$ [4] 10^{22} cm^{-2}	$N(H_2)$ [5] 10^{22} cm^{-2}	Ratio [6]
0.0	0.0	168.0	20.39	4.37	1.06	1.98	2.2–4.1
+ 7.5	0.0	191.5	11.14	4.98	0.58	1.08	4.6–8.6
+15.0	0.0	137.5	8.31	3.56	0.43	0.81	4.4–8.3
+22.5	0.0	126.5	12.67	3.29	0.66	1.23	2.7–4.9
+30.0	0.0	77.8	12.62	2.02	0.65	1.22	1.7–3.1
- 7.5	0.0	170.4	14.87	4.43	0.77	1.44	3.1–5.8
−15.0	0.0	136.2	8.48	3.54	0.44	0.82	4.3–8.0
−22.5	0.0	136.5	15.75	3.55	0.82	1.53	2.3–4.3
−30.0	0.0	71.9	8.92	5.42	0.46	0.87	6.2–11.8
+ 7.5	+ 7.5	144.2	14.52	3.75	0.75	1.41	2.7–5.0
0.0	+ 7.5	177.8	12.80	4.62	0.66	1.24	3.7–7.0
- 7.5	+ 7.5	136.0	14.79	3.54	0.77	1.44	2.5–4.6
+ 7.5	- 7.5	137.2	8.55	3.56	0.44	0.83	4.3–8.1
0.0	- 7.5	123.7	17.09	3.22	0.88	1.66	1.9–3.7
- 7.5	- 7.5	113.4	12.09	2.95	0.63	1.17	2.5–4.7
0.0	+15.0	77.9	4.18	2.03	0.22	0.41	5.0–9.2
0.0	−15.0	76.8	5.31	1.99	0.27	0.52	3.8–7.4
+15.0	+ 7.5	114.0	10.36	2.96	0.54	1.00	2.9–5.5
−15.0	+ 7.5	117.7	14.66	3.06	0.76	1.42	2.2–4.0
+15.0	- 7.5	126.4	9.87	3.29	0.51	0.96	3.4–6.5
−15.0	- 7.5	86.1	11.18	2.24	0.58	1.09	2.1–3.9

(1) The ^{12}CO data are from Nakai *et al.* (in preparation). (2) Error in I_{CO} of $\simeq$15–20% . (3) Calculated from the ^{12}CO J=1–0 data assuming $\tau \gg 1$ and $N(H_2)/I_{CO} = 2.6 \times 10^{20}$ cm^{-2} (K km s^{-1})$^{-1}$ (Wild 1990). (4) Calculated from the ^{13}CO J=1–0 data by adopting T_{ex} = 20 K, [H_2]:[^{13}CO] = 5×10^5 (Dickman 1978), and assuming optically thin ^{13}CO emission. (5) As for (4) but with T_{ex} = 40 K. (6) Ratio of column densities derived using ^{12}CO and ^{13}CO integrated intensities.

The ^{12}CO J=2–1 map can be used to estimate an upper limit to the total molecular hydrogen mass in the central region of Maffei 2. The total integrated intensity in the map is 1640 K km s^{-1} . If it is assumed that $\tau(^{12}CO) \gg 1$, that $I_{CO}(2-1) \simeq I_{CO}(1-0)$ (to within a factor 2), and that the Galactic 'constant conversion factor' holds, then the total molecular hydrogen mass in the central 1.2 kpc diameter region of Maffei 2 is

1–4 $\times 10^8$ $M_\odot$.

From the galactic rotation curve, derived from peak CO velocities, the total dynamical mass within a radius of 600 pc (25″) is 3.7 $\times$ 10^8 $M_\odot$ (Section 5.5.1). This in turn implies that the mass of molecular hydrogen in the starburst region of Maffei 2 comprises 30–100% of the dynamical mass of the galaxy. Similar results were found from high-resolution CO observations of three Seyfert galaxies (Meixner *et al.* 1990) and in the case of the starburst galaxy M82, where the molecular gas mass in the central kiloparsec comprises about 30% of the total dynamical mass in that region (Sofue 1988). It is usually assumed that the gravitational potential of a spiral galaxy is dominated not by molecular gas, but by the underlying stellar population in the galactic disc and bulge. In the Milky Way, molecular clouds make up a few per cent of the dynamical mass of the central kiloparsec. It is likely that in a star-forming galaxy, the molecular component will contribute more to the total mass than in the disc of a 'normal' spiral such as the Milky Way. However, even a star-forming galaxy should hold a considerable proportion of its mass in the form of stars, both the old, red population and the young, hot starburst component. K-band IRCAM images of Maffei 2 (Fig. 5.9) show a prominent near-infrared continuum peak, representing the old stellar population, consistent with the position of the CO dynamical centre.

The peak hydrogen column density deduced from ^{12}CO observations is $\sim$6 $\times 10^{22}$ cm^{-2}, which translates to a peak mass surface density of 900 $M_\odot$ pc^{-2}. This compares to a typical value for the central $\sim$1 kpc of the Milky Way of $\sim$100 $M_\odot$ pc^{-2} (Sanders *et al.* 1984). Using ^{13}CO J=1–0 gives a mass surface density of 150 $M_\odot$ pc^{-2}.

Size of clouds in Maffei 2

Filling-factor arguments can be used to estimate the characteristic size of the molecular clouds in Maffei 2.

The peak observed main-beam brightness temperature of J=2–1 emission is related to the gas excitation temperature via

$$T_{\rm r} = f_{\rm a}\,[J_\nu(T_{\rm ex}) - J_\nu(T_{\rm bg})]\,(1 - {\rm e}^{-\tau_\nu}), \qquad (5.25)$$

where $f_{\rm a}$ is the area filling factor of the molecular clouds, and the other quantities are defined as in Section 5.6.1. Hence for optically thick emission and $f_{\rm a}$=1, the excitation

temperature is given by equation (5.13).

The peak observed main-beam brightness temperature in the smoothed ^{12}CO J=2–1 map is ~2 K. This then corresponds, from equation (5.13), to a 'beam-diluted excitation temperature' T'_{ex} = 6.1 K (i.e., the excitation temperature averaged over the beam, where the filling factor is in reality $\ll$1). Considering that the beam covers an area nearly 300 pc in diameter at the distance of Maffei 2, this is quite a high value.

If the true excitation temperature is $\simeq$ 40 K, then the expected main-beam brightness temperature for a filling factor of 1 would be 34.5 K. From the observed $T_{mb}\simeq$2 K, then, the surface filling factor of molecular clouds, $f_a, \simeq$ 0.06. For an excitation temperature of 30 K, the corresponding value of f_a is 0.08.

To estimate the volume filling factor, H_2 column densities derived from ^{13}CO 1–0 data (which are less likely to suffer from subthermal excitation than the 2–1) can be used. The average H_2 column density for the central few hundred parsecs is $N(H_2)$ $\simeq$1.0 $\times10^{22}$ cm^{-2}. For a face-on path length of ~80 pc through the galactic disc (e.g. Sanders *et al.* 1984), and a disc inclination of 65°, this corresponds to an average (beam-diluted) H_2 number density $n(H_2)$~17.5 cm^{-3}. This is much lower than the critical density for thermalization of the ^{13}CO J=1–0 transition, (n_{crit}=1.9 $\times$ 10^3 cm^{-3} – Wild 1990), therefore if the gas is thermalized it must also be highly clumped. Assuming that the true cloud-averaged number density is greater than n_{crit} (i.e. the transition is thermalized) then gives an estimate of the volume filling factor, $f_v \leq 9 \times10^{-3}$. Non-LTE modelling (Section 5.6.2) suggests that $n(H_2) \simeq$ 2–5 $\times10^3$ cm^{-3}, hence $f_v \simeq$ 3.5–9 $\times10^{-3}$.

For an ensemble of clouds of diameter a, the cloud size is related to the volume and surface filling factors via

$$a = \frac{3 f_v l}{2 f_s} \tag{5.26}$$

(Nakai *et al.* 1987), where l is the path length through the emitting region. For $f_v \simeq$3.5–9 $\times10^{-3}$ and $f_s \sim$ 0.07, this gives a cloud diameter a ~14–35 pc. For comparison, the typical scale for a Milky Way GMC complex is $\sim$ 40–100 pc (Sanders *et al.* 1985). It is quite reasonable to expect that clouds in vigorous nuclear star-forming regions, subjected to the combined effects of stellar winds, supernovae and intense radiation fields, may be smaller than typical disc GMCs. The above result relies on the assumption of

optically thick ^{12}CO J=1–0. If the ^{12}CO is in reality partly optically thin (e.g. Section 5.6.1) then from equation (5.25), for a given excitation temperature and observed main-beam brightness temperature, the deduced surface filling factor will be larger [since $(1-e^{-\tau}) \simeq \tau \ll 1$]. Hence the derived cloud diameter is likely to be an upper limit.

5.7 Summary of main conclusions

The chapter presented high-resolution observations of the ^{12}CO and ^{13}CO J=1–0 and J=2–1 transitions from a nearby star-forming galaxy, Maffei 2. The molecular gas is concentrated in the central $\sim 30'' \times 40''$, elongated along the galaxy's major axis. The ^{12}CO J=2–1 integrated intensity peaks to the north-east of the nucleus, possibly indicative of enhanced excitation and/or gas column in this region. The major and minor axis extents are consistent with a thin disc at the assumed galactic inclination of 65° – the narrow bar and ring seen in interferometer data are not resolved.

The velocity field as derived from the CO peak velocities is typical of spiral galaxies, with a steep gradient in the central few hundred parsecs, implying a massive, compact, rigidly rotating core. The systemic velocity is estimated to be –29 km s^{-1}, consistent with previous determinations, giving a dynamical centre $\sim 3''$ south-west of the map centre and spatially coincident with the peak of the stellar mass distribution as traced by the 2 μm continuum emission. The isovelocity contours are inclined to the minor axis, suggesting that radial gas motions are superimposed on the orbital velocities. The dynamical mass of the central kiloparsec is about 4×10^8 $M_\odot$.

The CO lines are very wide, exceeding 70 km s^{-1} (FWHM) over the whole of the mapped region and reaching 160 km s^{-1} at some near-nuclear positions. A very simple model, of a rotating inclined disc observed with a Gaussian beam, shows that only a small part of the observed linewidths can be explained by the steep rotation curve. Cloud velocity dispersions of $\geq$100 km s^{-1} are required to explain the linewidths in the central regions. Such large velocity dispersions have also been deduced for other starburst nuclei, such as IC342 and M83. The usual explanation is frequent supernova explosions – however, the loss of cloud kinetic energy by inelastic cloud–cloud collisions is usually neglected. Adopting the approach of McKee & Ostriker (1977) of balancing energy gain from supernovae with energy loss from collisions, it was deduced that a su-

pernova rate $\geq 10^3$ times that in the solar neighbourhood is needed to sustain a velocity dispersion of 100 km s^{-1}, if $\geq 3\%$ of the supernova energy goes to cloud kinetic energy. This translates to ~ 0.05 supernovae yr^{-1} for a typical starburst region of kiloparsec dimensions. From comparison of the [CII] and *IRAS* fluxes of Maffei 2 with those of M82, and from consideration of the non-thermal radio continuum emission, we estimate a supernova rate of 0.01–0.05 yr^{-1} in the starburst region, implying that dispersions of 100 km s^{-1} can just be sustained. For a lower supernova rate, lower conversion efficiency or higher velocity dispersions, other mechanisms may well be needed. It is possible that the starburst in Maffei 2 may be combined with a mild form of active galactic nucleus, as in the case of the Seyfert galaxy NGC 1068, which could produce the very wide emission lines. Discriminating observations are difficult, however, because of the large extinction to Maffei 2 – more observations at infrared and longer wavelengths would be valuable.

The high resolution and spatial coverage of the observations were exploited to investigate the variation in cloud properties across the central star-forming region. The $^{12}CO/^{13}CO$ main-beam brightness temperature ratios imply that the gas is quite optically thick. Striking variations of the $^{12}CO/^{13}CO$ J=2–1 ratio on scales of 7″ may indicate that the [^{12}CO]:[^{13}CO] abundance ratio is being altered as a result of processes connected with the starburst. In particular, non-detection of ^{13}CO J=2–1 north-east of the nucleus may be the result of selective photodestruction of ^{13}CO in the intense UV fields associated with a region of massive star formation. Increased gas excitation north-east of the nucleus is also suggested by the peak in ^{12}CO 2–1 integrated intensity, by particularly high ^{12}CO 2–1/1–0 ratios (>2), higher than average $^{12}CO/^{13}CO$ line ratios (>10) and extended Hα line emission in this region.

The assumption of a single-component, LTE interstellar medium runs into severe difficulties when trying to reconcile optically thick $^{12}CO/^{13}CO$ with ^{12}CO 2–1/1–0 ratios of >1 over most of the central region, exceeding 2 in the north-east region. Low observed ^{13}CO 2–1/1–0 ratios are also difficult to interpret in terms of a warm, star formation dominated ISM. High 2–1/1–0 ratios are usually interpreted (as in the case of M82) as arising from optically thin gas, but this is not consistent with the observed isotopic ratios, even for an enhanced [^{12}CO]:[^{13}CO] abundance ratio such as might be expected in galactic nuclei. In the environment of a starburst, with a clumpy ISM

swept up by the action of HII regions, supernovae and stellar winds into small clouds and filaments, much of the cloud heating may arise from the outside. External heating of clouds may explain many of the observed line-ratio characteristics, artificially enhancing the ^{12}CO 2–1/1–0 ratio while producing low ^{13}CO 2–1/1–0 ratios as the optically thin lines probe the cooler cloud interior. Line trapping, subthermal excitation, or a mixture of optically thin and thick gas may also contribute to the anomalous line ratios. Single-temperature, non-LTE clumpy-cloud modelling can, for kinetic temperatures of 30–50 K, explain ^{12}CO 2–1/1–0 line ratios of up to about 1.8.

The ^{12}CO and ^{13}CO data were used to estimate the molecular hydrogen column density. $N(H_2)$ as calculated from the ^{12}CO data and 'constant conversion factor' is typically 5–10 times higher than that calculated from the ^{13}CO transition assuming LTE and an excitation temperature of 20–40 K. An upper limit to the molecular gas mass in the central kpc of 1–4 $\times$ 10^8 $M_\odot$ – 30–100% of the dynamical mass – is derived from the ^{12}CO 2–1 map using the constant conversion factor. From filling-factor arguments, it was deduced that the molecular gas is highly clumped, with typical cloud sizes $\leq$20–30 pc, smaller than typical Galactic GMCs (40–100 pc) but not as extreme as in M82, where cloud sizes of only a few parsecs have been claimed. It seems that Maffei 2 is a scaled-down version of the M82 starburst.

5.7.1 CO as a mass tracer in star-forming galaxies

What are the implications of these findings for the use of CO as a mass tracer in extragalactic environments? The overall picture obtained of the Maffei 2 starburst is of two distinct cloud populations. At distances greater than 500 pc from the nucleus, the gas is optically thick and fairly cool (10–20 K), as indicated by the 2–1/1–0 line ratios of $\leq$1, and probably quite similar to Galactic disc GMCs. In these outer regions the H_2 content may be reliably traced by the CO. In the central kiloparsec, on the other hand, and particularly in the region of increased excitation north-east of the nucleus, the situation is considerably more complex. ^{12}CO 2–1/1–0 ratios of 1.5–2.5 cannot be explained by a simple, single-temperature, LTE, optically thick interstellar medium. Non-LTE modelling with gas temperatures 30–50 K can explain line ratios of up to about 1.8, and temperature gradients in optically thick UV-illuminated clouds, or a component of optically thin gas, may also make a significant contribution to push

the line ratios towards 2. Temperature gradients are to be expected, given the highly clumped nature of the gas disrupted by the processes of massive star formation. It is evident that vigorous star formation has resulted in a cloud population substantially different to that in the relatively quiescent disc of the Milky Way. It seems likely that, under such circumstances, the CO emission may be tracing a complicated combination of gas mass and excitation. Further non-LTE, multicomponent modelling is needed to investigate the detailed correspondence between the CO emission and the mass and distribution of H_2 molecules with which the CO is mixed. The effects on the observed emission of optical depth, temperature gradients and abundance variations, resulting from photodestruction or stellar processing, should not be ignored. Observation of higher J transitions, as well as of other molecules and isotopic species, will undoubtedly have an important role to play.

Chapter 6

Conclusions

In this concluding section, I summarize the main results from each of the preceding chapters, and discuss the implications of these results for our knowledge of the interstellar medium in star-forming galaxies and the use of dust continuum and CO lines as tracers of the extragalactic molecular gas in such environments. Finally, I briefly discuss some possible directions that research in this subject may take.

6.1 450 μm mapping of M82

One of the new generation of large-aperture millimetre-wave telescopes, the JCMT on Mauna Kea, was used to make possibly the first ever 450 μm map of an extragalactic source, the well-known starburst galaxy M82. Comparison of these 13″-resolution data, presented in Chapter 2, with existing ^{12}CO line data revealed striking spatial dissimilarities, implying that the two data sets could not both be representing the molecular interstellar medium in this galaxy. The initial 450 μm map and a later, diffraction-limited 450 μm slice presented in Chapter 3 were more spatially consistent with the distribution of the optically thin ^{13}CO and C^{18}O J=2–1 isotopes than with the ^{12}CO J=1–0 data. This suggests that optical depth effects may be a significant contributor to the differing morphologies, with the optically thin dust and ^{13}CO emission both tracing molecular gas not seen in ^{12}CO because of high optical depth. It is also possible that enhanced dust temperature in the extensive south-western star-forming region may be 'swamping' a dusty ring, although there is no conclusive evidence of a global dust temperature gradient large enough to cause such an effect.

The CO emission may be significantly affected by the harsh environment of a star-forming interstellar medium quite unlike that found in the disc of the Milky Way. The effects of active star formation, in the form of stellar winds, supernovae and intense UV fields, will conspire to produce a population of small, warm, dense, fast-moving clouds. Indeed, a wealth of observational evidence including CO ratios, far-infrared [CII] lines from photodissociated gas, and the detection of species such as HCO^+, CS and HCN point to the existence of significant quantities of warm, dense, clumpy gas in the interstellar media of galaxies such as M82. Under such circumstances, it is likely that molecular line data may be tracing a complex combination of gas excitation and mass, casting doubt upon the reliability of the Galactic 'constant conversion factor' which assumes cool, optically thick gas in giant molecular clouds, and maybe also contributing to the differing CO and dust morphologies.

6.2 Dust continuum observations of IR-bright spirals

In Chapter 4, the programme of submillimetre mapping of infrared-bright galaxies was extended to include the three nearby starbursts M83, Maffei 2 and IC342, all of which have previously been studied in transitions of CO. Each galaxy was mapped at 800 μm with 13″–16″ resolution (comparable to that of existing CO data), and photometry at 450–1100 μm was also performed. All three galaxies turned out to possess strong submillimetre continuum emission (with peak 800 μm flux densities of 0.4–0.6 Jy beam^{-1}), their 800 μm morphologies extended in at least one direction with respect to the telescope beam. Comparison with other star-formation diagnostics, such as radio continuum emission, revealed the 800 μm continuum to be spatially consistent with emission at other wavelengths. The resolution of the maps was not sufficient to permit detailed comparison with the CO morphology – however, the 800 μm emission appeared in general less extended than the CO, perhaps as a result of decreasing dust temperature or gas density away from the galaxy nuclei.

The 450, 800 and 1100 μm photometry fills an important gap in the long-wavelength spectra of these objects. Knowledge of the continuum emission spectrum is essential as a first step towards deriving dust temperatures, optical depths and gas masses. The simplest picture of the emission, that of dust at a single temperature, can fit the ob-

served 450–1100 μm fluxes only for a dust temperature of $\sim$ 45 K and an emissivity spectral index β=1, constant all the way to 1100 μm. Although 45 K is a plausible temperature for dust exposed to the high UV fields resulting from vigorous star formation, it is likely that in a composite object such as a galaxy, multiple dust components will exist. A two-temperature fit implied, rather surprisingly given the galactic nuclear environment, that over 90% of the dust is cool (20–25 K), dominating the emission at submillimetre wavelengths, and quite distinct from the dust that is producing the far-infrared fluxes. A possible explanation for this involves a population of small, externally heated clouds resulting from disruption by the processes of the nuclear starburst. In this scenario, the far-infrared fluxes (and the optically thick ^{12}CO emission) arise from the warmer 'outer skin' of the clouds, while the submillimetre emission (and the optically thin ^{13}CO isotopic lines) originate from the cooler cloud interior. Alternatively, the $\sim$10% of warm dust may be associated with star-forming HII-region/molecular-cloud complexes, with the cooler dust heated by the general interstellar radiation field – although, in a vigorous nuclear starburst, modelling suggests that even this may be capable of heating dust to $\sim$40 K. The implied presence of such a large fraction of cool dust, 'unseen' by previous far-infrared observations, has a significant effect on the derived dust and gas masses, increasing by factors of $\leq$10 the column densities and masses calculated using far-infrared-emitting, 45-K dust alone. The value of measuring submillimetre/millimetre fluxes is further emphasized by the fact that, when such fluxes are included in the spectrum fitting, even a simplistic single-temperature fit 'misses' less of the cool dust than do previous studies which employed far-infrared data only. It should be borne in mind, however, that the dust temperature and hence gas masses derived are critically dependent on the adopted form of β, and this is poorly constrained by both observation and theory.

6.3 CO observations of Maffei 2

Observational and theoretical evidence suggests that the ^{12}CO J=1–0 transition may by itself be an unreliable tracer of molecular hydrogen in extreme extragalactic environments. In an attempt to overcome this, Chapter 5 presented observations of the gas-rich spiral Maffei 2 in the ^{12}CO J=2–1 and ^{13}CO J=2–1, 1–0 lines. As well

as permitting a point-by-point comparison of the brightness temperatures of different isotopes and transitions, to study any large-scale gas excitation variations across the starburst region, the long wavelength and high velocity resolution of the data provide an extinction-free probe of the nuclear kinematics of this heavily extinguished galaxy.

The morphology of the ^{12}CO J=2–1 emission shows gas concentrated in the central $30'' \times 40''$, with a peak offset to the north-east of the assumed (near-infrared) galactic nucleus, superimposed on lower level emission. This offset-peak morphology may be due to increased gas column or excitation north-east of the nucleus, perhaps associated with a region of massive star formation. The J=2–1 emission is generally spatially coincident with single-dish ^{12}CO and interferometer ^{13}CO J=1–0 maps, and with other star-formation/interstellar-medium diagnostics such as radio continuum and recombination line emission. The major-to-minor axis ratio is consistent with a disc seen at the adopted galactic inclination of 65°.

The CO peak velocities along the major axis were used to construct a rotation curve for Maffei 2. As has been observed in other gas-rich spirals, the rotation curve exhibits a steeply rising inner few hundred parsecs (indicative of rigid rotation), with flatter, differential rotation in the outer regions. This kinematic morphology is repeated in the velocity contours. Here, however, misalignment of the kinematic and galactic minor axes suggests non-circular motions (e.g. inflow or outflow) near the nucleus. These have been interpreted, together with the double-peaked morphology seen in high-resolution data, as indicating an expanding molecular ring created by the nuclear starburst.

One of the most striking features of the CO profiles is their width – the linewidths exceed 70 km s^{-1} FWHM over the whole of the mapped region, reaching 160 km s^{-1} at some near-nuclear positions. A very simple model of a rotating disc observed with a Gaussian beam shows that only a small part of the observed linewidths could be produced by beam smearing of the steep rotation curve, leaving cloud velocity dispersions of $\sim$100 km s^{-1} to be explained. Such large dispersions, consistent with those deduced for other starburst nuclei, are usually explained in terms of frequent supernova explosions associated with the star formation. Adopting a simple approach, of balancing energy input via supernovae and energy loss from cloud–cloud collisions, it was found that a supernova rate $\sim 10^3$ times that in the solar neighbourhood, or $\sim$0.05 yr^{-1} in the central kiloparsec, would be required. Consideration of the *IRAS*, [CII]

and radio continuum fluxes lead to an estimate for the supernova rate in the starburst region of Maffei 2 of $\sim$0.01–0.05 yr^{-1}, implying that the observed linewidths could just be sustained. However, for lower supernova rates, higher near-nuclear velocity dispersions or a lower supernova energy conversion efficiency, other mechanisms may well be needed. A possible energy source may be some sort of mild nuclear activity, as is often seen in tandem with starburst phenomena, although the Maffei 2 linewidths are considerably less than those traditionally associated with active nuclei. The high extinction to Maffei 2 makes discriminating observations difficult.

^{12}CO and ^{13}CO J=1–0 and 2–1 line ratios were used to study any variation in bulk cloud properties across the starburst region. The ^{12}CO/^{13}CO ratios imply that the gas is quite optically thick, even for enhanced [^{13}CO]:[^{12}CO] abundance ratios such as may prevail in spiral nuclei. Variation of the ^{12}CO/^{13}CO 2–1 ratio on 7″ scales suggest that the abundance ratio is being affected by the starburst. There is evidence, from the ^{12}CO morphology, line ratios and Hα emission, of increased gas excitation north-east of the nucleus, perhaps associated with a region of particularly vigorous star formation.

The assumption of a single-component, LTE interstellar medium encounters serious problems when attempting to reconcile 'optically thick' ^{12}CO/^{13}CO ratios of $\sim$5–15 with 'optically thin' ^{12}CO 2–1/1–0 ratios of $\leq$2.5. Low observed ^{13}CO 2–1/1–0 ratios, also, are difficult to explain in terms of a warm starburst medium. A possible scenario to explain qualitatively the observed ratios involves clumpy externally heated molecular clouds, the optically thick ^{12}CO transitions arising from the warmer outer layers and the optically thin ^{13}CO line tracing the cooler cloud interior. Such a picture is also consistent with the large fraction of cool dust implied by the long-wavelength continuum spectrum. Line trapping, subthermal excitation or a multicomponent medium may also conspire to make single-component, LTE interpretations of CO data quite hazardous. Simple non-LTE 'clumpy cloud' models can predict ^{12}CO 2–1/1–0 line ratios of $\leq$1.8 for gas temperatures of $\sim$30–50 K.

The column density of molecular hydrogen, $N(H_2)$, as calculated from the ^{12}CO assuming a constant conversion factor, exceeds that calculated from ^{13}CO by factors of $\sim$5–10. An upper limit to the total gas mass of 1–4 $\times$ 10^8 $M_\odot$ (30–100% of the dynamical mass) can be deduced. Filling factor arguments suggest that the gas is very clumpy, putting the typical cloud size at $\leq$20–30 pc, smaller than typical Galactic

GMCs but less extreme than in the nucleus of M82, where cloud sizes of only a few parsecs have been estimated. Maffei 2 may represent a scaled-down version of the M82 starburst.

The overall picture of the interstellar medium of Maffei 2 is that of two distinct cloud populations. At distances >500 pc from the nucleus, the gas is optically thick and quite cool, probably similar to Galactic disc GMCs. In contrast, in the central kiloparsec the gas may be warm, clumpy and disturbed, particularly in the region north-east of the nucleus, with energy input from massive star formation and frequent supernovae resulting in a population of warm, dense, fast-moving and externally heated clouds, substantially different to that in the relatively quiescent disc of the Milky Way.

6.4 CO and dust tracers of the star-forming interstellar medium: the direction of future research

What are the implications of the results presented in this thesis for the use of CO and dust observations in tracing star-forming molecular gas?

The CO molecule appears at first sight to be an ideal probe of molecular clouds, being both abundant and easily detectable. However, CO emission is very sensitive to physical and excitation conditions in the clouds; therefore, the common practice of applying a global, Milky Way derived, 'constant conversion factor' to extragalactic sources is dependent for its accuracy on conditions in extragalactic clouds being the same as in GMCs of the Milky Way. The CO observations presented in this thesis add to the mounting evidence that this is not the case in actively star-forming galaxies, the near-nuclear gas being located in warm, dense, clumpy, fast-moving clouds, possibly with external heating, temperature gradients and an optically thin component also. This is a far cry from the cool (~10 K), optically thick giant molecular clouds which populate the disc of the Milky Way and upon which the 'constant conversion factor' is based.

Clearly, much more work needs to be done, both theoretically and observationally, on evaluating the effect of an extragalactic star-forming environment on the reliability of CO as an H_2 tracer. Promising developments on the observational side have come with the new generation of large millimetre-wave telescopes such as the JCMT, IRAM

and Nobeyama, and ever-improving receiver technology, enabling high-resolution observations not only of the low-J transitions of ^{12}CO, but of high-J CO lines, rare CO isotopes (C^{18}O, C^{17}O) and other molecular species such as CS, HCN and HCO$^+$. Such data are invaluable as they probe regimes of temperature and density to which the low-lying ^{12}CO transitions are not sensitive. The rare isotopes of CO are also useful for tracing the morphology of gas not well represented by optically thick ^{12}CO emission.

It is also clear, from attempts to interpret the CO line ratios, that the often-adopted picture of a single-component medium in LTE is almost certainly invalid in such a complex environment, and that, ideally, multicomponent non-LTE cloud models are needed if CO data are to be reliably interpreted. Several groups, notably that based at the Max Planck Institute and using the IRAM 30-m telescope (Eckart, Mauersberger and others) are beginning to obtain useful and important results from their (albeit simple) non-LTE multitransition modelling of molecular line data.

Dust continuum observations are invaluable as an independent tracer of the quantity and distribution of molecular gas. Unlike ^{12}CO, long-wavelength continuum emission is always optically thin, and so all the material is sampled. The interpretation of the data is relatively straightforward, and the dust grains are less sensitive to the effects of UV fields and the excitation of the interstellar medium than is the complex CO molecule. The above should not, however, hide the fact that there are still problems with this method that translate directly into uncertainties in derived gas masses and distributions. Perhaps the most significant of these comes from the necessity of fitting a modified blackbody spectrum, characterized by values of $T_{\rm dust}$ and β, to the long-wavelength data. As was demonstrated in Chapter 4, assumption of a particular value of β, and adoption of a single- or multi-component dust temperature, can have dramatic effects on derived column densities and masses, particularly when far-infrared data only are used. When making large-beam observations of galaxies, multiple dust components within a single beam are to be expected, yet there is considerable disagreement in the literature over whether a multicomponent fit to the data is needed at all. Although considerable progress has been made in modelling the long-wavelength Milky Way disc emission in terms of different components of the ISM, little theoretical work has yet been done on the long-wavelength continuum emission from star-forming galactic nuclei. The value of β and its variation with wavelength have been studied

both observationally and theoretically, yet are still very poorly constrained, and this translates directly into uncertainty in the derived dust temperature as well as in the value of the conversion factor $N(H_2)/\tau(\nu)$, which may have been calibrated at a different wavelength from that being observed. The conversion factor itself was initially derived in the Milky Way, although the relative insensitivity of grain parameters to gas excitation means that the Galactic dust conversion factor may produce more accurate results, when applied to extragalactic clouds, than the equivalent CO conversion factor. In addition to these problems, observations at submillimetre wavelengths are technically difficult, and problems arising from differing beamsizes, lack of calibration sources, rapidly varying atmospheric opacities and the time required to map faint extended sources all contribute to large uncertainties in derived submillimetre fluxes. It is clear from Chapter 4, however, that despite these drawbacks, submillimetre and millimetre data are invaluable for constraining the shape of the long-wavelength spectrum, and may significantly reduce the amount of cool dust that is 'missed' when only far-infrared fluxes are used to derive dust and gas masses.

However, the field is still young, and it is to be hoped that improvements in submillimetre instrumentation (e.g. SCUBA) and observing practice (e.g. the establishment of a reliable calibration data base and the implementation of sky dips on the JCMT) will eventually result in the ability to perform fast, accurate and extensive photometry and mapping of sources in this important wavelength range. In the future, then, high-resolution, multiwavelength continuum data may be combined with improved grain emission models to investigate the spatial and spectral distribution of emission across a galaxy's starburst nucleus, with the ultimate aim of reliably tracing the quantity, distribution and excitation of its star-forming molecular fuel.

References

Allen, R.J. & Raimond, E., 1972. *Astr. Astrophys.*, **19**, 317.

Andreasian, N.K. & Khachikian, E.Ye., 1987. *Observational Evidence of Activity in Galaxies, IAU Symp. No. 121,* p. 541, eds Khachikian, E. Ye., Fricke, K.J. & Melnick, J., Reidel, Dordrecht.

Audouze, J., Lequeux, J. & Vigroux, L., 1975. *Astr. Astrophys.*, **43**, 71.

Baan, W.A., Henkel, C., Schilke, P., Mauersberger, R. & Güsten, R., 1990. *Astrophys. J.*, **353**, 132.

Bally, J., 1989. In: *Proc. ESO Workshop on Low Mass Star Formation and Pre-Main Sequence Objects*, p. 1, ed. Reipurth, B., ESO, Garching.

Bally, J. & Langer, W.D., 1982. *Astrophys. J.*, **255**, 143.

Balzano, V.A., 1983. *Astrophys. J.*, **268**, 602.

Bartel, N., Ratner, M.I., Rogers, A.E.E., Shapiro, I.I., Bonometti, R.J., Cohen, N.L., Gorenstein, M.V., Marcaide, J.M. & Preston, R.A., 1987. *Astrophys. J.*, **323**, 505.

Becklin, E.E. & Wynn-Williams, C.G., 1987. In: *Star Formation in Galaxies*, p. 643, ed. Lonsdale-Persson, C.J., NASA CP-2466.

Becklin, E.E., Gatley, I., Matthews, K., Neugebauer, G., Sellgren, K., Werner, M.W. & Wynn-Williams, C.G., 1980. *Astrophys. J.*, **236**, 441.

Bevington, P.R., 1969. *Data Reduction and Error Analysis for the Physical Sciences,* McGraw-Hill.

Blanco, P.R., 1991. *PhD thesis*, University of Edinburgh.

Blitz, L., Bloemen, J.B.G.M., Hermsen, W. & Bania, T.M., 1985. *Astr. Astrophys.*, **143**, 267.

Bloemen, J.B.G.M., Strong, A.W., Blitz, L., Cohen, R.S., Dame, T.M., Grabelsky, D.A., Hermsen, W., Lebrun, F., Mayer-Hassalwander, H.A. & Thaddeus, P., 1986. *Astr. Astrophys.*, **154**, 25.

Bohlin, R.C., Savage, B.D. & Drake, J.F., 1978. *Astrophys. J.*, **224**, 132.

Bottinelli, L., Chamaraux, P., Gérard, E., Gouguenheim, L., Heidmann, J., Kazès, I. & Lauqué, R., 1971. *Astr. Astrophys.*, **12**, 264.

Cantó, J., Rodríguez, L.F. & Anglada, G., 1987. *Astrophys. J.*, **321**, 877.

Carlstrom, J.E., 1988. In: *Galactic and Extragalactic Star Formation*, p. 157, eds Pudritz, R. & Fich, M., Kluwer, Dordrecht.

Carlstrom, J.E. & Kronberg, P.P., 1991. *Astrophys. J.*, **366**, 422.

Chandler, C.J., 1990. *PhD thesis*, University of Edinburgh.

Chini, R., Kreysa, E., Krügel, E. & Mezger, P.G., 1986. *Astr. Astrophys.*, **166**, L8.

Condon, J.J. & Yin, Q.F., 1990. *Astrophys. J.*, **357**, 97.

Condon, J.J., Condon, M.A., Gisler, G. & Puschell, J.J., 1982. *Astrophys. J.*, **252**, 102.

Condon, J.J., Huang, Z.-P., Yin, Q.F. & Thuan, T.X., 1991. *Astrophys. J.*, **378**, 65.

Combes, F., 1988. In: *Galactic and Extragalactic Star Formation*, p. 475, eds Pudritz, R.E. & Fich, M., Kluwer, Dordrecht.

Comte, G., 1981. *Astr. Astrophys. Suppl.*, **44**, 441.

Courvoisier, T.J.-L., Reichen, M., Blecha, A., Golay, M. & Huguenin, D., 1990. *Astr. Astrophys.*, **238**, 63.

Cowan, J.J. & Branch, D., 1985. *Astrophys. J.*, **293**, 400.

Cox, P. & Mezger, P.G., 1989. *Astr. Astrophys. Rev.*, **1**, 49.

Crawford, M.K., Genzel, R., Townes, C.H. & Watson, D.M., 1985. *Astrophys. J.*, **291**, 755.

Cunningham, C.R. & Gear, W.K., 1990. In: *Proc. SPIE Symp. Astronomical Telescopes and Instrumentation*, February 1990.

Danver, C.G., 1942. *Ann. Obs. Lund*, No. 10, 1.

de Jong, T., Klein, U., Wielebinski, R. & Wunderlich, E., 1985. *Astr. Astrophys.*, **147**, L6.

DePoy, D.L., Becklin, E.E. & Geballe, T.R., 1987. *Astrophys. J. Lett.*, **316**, L63.

de Vaucouleurs, G., 1979. *Astr. J.*, **84**, 1270.

de Vaucouleurs, G., Pence, W.D. & Davoust, E., 1983. *Astrophys. J. Suppl.*, **53**, 17.

Devereux, N., 1987. *Astrophys. J.*, **323**, 91.

Devereux, N. & Young, J.S., 1990. *Astrophys. J.*, **359**, 42.

Dickman, R.L., 1978. *Astrophys. J. Suppl.*, **37**, 407.

Dickman, R.L., Snell, R.L. & Schloerb, F.P., 1986. *Astrophys. J.*, **309**, 326.

Dietz, R.D., Gehrz, R.D., Jones, T.J., Grasdalen, G.L., Smith, J., Gullixson, C. & Hackwell, J.A., 1989. *Astr. J.*, **98**, 1260.

Djorgovski, S., Wier, N., Matthews, K. & Graham, J.R., 1991. *Astrophys. J. Lett.*, **372**, L67.

Downes, D., 1989. In: *Diffraction-Limited Imaging with Very Large Telescopes*, p. 53, eds Alloin, D.M. & Mariotti, J.-M., Kluwer, Dordrecht.

Draine, B.T., 1990. In: *The Interstellar Medium in Galaxies*, p. 483, eds Thronson, H.A. & Shull, J.M., Kluwer, Dordrecht.

Draine, B.T. & Lee, H.M., 1984. *Astrophys. J.*, **285**, 89.

Duncan, W.D., Robson, E.I., Ade, P.A.R., Griffin, M.J. & Sandell, G., 1990. *Mon. Not. R. astr. Soc.*, **243**, 126.

Eales, S.A., Wynn-Williams, C.G. & Duncan, W.D., 1989. *Astrophys. J.*, **339**, 859.

Eckart, A., Downes, D., Genzel, R., Harris, A.I., Jaffe, D.T. & Wild, W., 1990. *Astrophys. J.*, **348**, 434.

Elias, J.H., Ennis, D.J., Gezari, D.Y., Hauser, M.G., Houck, J.R., Lo, K.Y., Matthews, K., Nadeau, D., Neugebauer, G., Werner, M.W. & Westbrook, W.E., 1978. *Astrophys. J.*, **220**, 25.

Encrenaz, P.J., Stark, A.A., Combes, F. & Wilson, R.W., 1979. *Astr. Astrophys.*, **78**, L1.

Falgarone, E. & Puget, J.L., 1988. In: *Galactic and Extragalactic Star Formation*, p. 195, eds Pudritz, R.E. & Fich, M., Kluwer, Dordrecht.

Frerking, M.A., Langer, W.D. & Wilson, R.W., 1982. *Astrophys. J.*, **262**, 590.

Gear, W.K., 1988. In: *Millimetre and Submillimetre Astronomy*, p. 307, eds Wolstencroft, R.D. & Burton, W.B., Kluwer, Dordrecht.

Gear, W.K., Gee, G., Robson, E.I., Ade, P.A.R. & Duncan, W.D., 1986. *Mon. Not. R. astr. Soc.*, **219**, 835.

Glassgold, A.E., Huggins, P.J. & Langer, W.D., 1985. *Astrophys. J.*, **290**, 615.

Gräve, R. & Beck, R., 1988. *Astr. Astrophys.*, **192**, 66.

Griffin, M.J., Ade, P.A.R., Orton, G.S., Robson, E.I., Gear, W.K., Nolt, I.G. & Radostitz, J.V., 1986. *Icarus*, **65**, 244.

Guilloteau, S. & Lucas, R., 1988. IRAM internal publication.

Güsten, R., Henkel, C. & Batrla, W., 1985. *Astr. Astrophys.*, **149**, 195.

Handa, T., Nakai, N., Sofue, Y., Hayashi, M. & Fujimoto, M., 1990. *Publs astr. Soc. Japan.*, **42**, 1.

Harris, A.I., Hills, R.E., Stutzki, J., Graf, U.U., Russell, A.P.G. & Genzel, R., 1991. *Astrophys. J.*, submitted.

Harris, A.I., Wild, W., Stutzki, J., Jaffe, D.T., Jackson, J.M., Eckart, A., Lugten, J.B. & Genzel, R., 1989. *Bull. Am. astr. Soc.*, **21**, 1188.

Haslam, C.G.T., 1974. *Astr. Astrophys. Suppl.*, **15**, 333.

Heckman, T.M., 1991. In: *Massive Stars in Starbursts*, eds Leitherer, C., Walborn, N.R., Heckman, T.M. & Norman, C.A., Cambridge University Press, Cambridge.

Heckman, T.M., Armus, L., McCarthy, P., van Breugel, W. & Miley, G.K., 1987. In: *Star Formation in Galaxies*, p. 461, ed. Lonsdale-Persson, C.J., NASA CP-2466.

Helou, G., 1989. *Interstellar Dust, IAU Symp. No. 135,* p.285, eds Allamandola, L.J. & Tielens, A.G.G.M., Kluwer, Dordrecht.

Helou, G., Soifer, B.T. & Rowan-Robinson, M., 1985. *Astrophys. J. Lett.*, **298**, L7.

Henkel, C., Mauersberger, R. & Schilke, P., 1988. *Astr. Astrophys.*, **201**, L23.

Henkel, C., Baan, W.A. & Mauersberger, R., 1991. *Astr. Astrophys. Rev.*, **3**, 47.

Hildebrand, R.H., 1983. *Q. J. R. astr. Soc.*, **24**, 267.

Hildebrand, R.H., Whitcomb, S.E., Winston, R., Steining, R.F., Harper, D.A. & Moseley, S.H., 1977. *Astrophys. J.*, **216**, 698.

Ho, P.T.P., Beck, S.C. & Turner, J.L., 1990a. *Astrophys. J.*, **349**, 57.

Ho. P.T.P., Martin, R.N., Turner, J.L. & Jackson, J.M., 1990b. *Astrophys. J. Lett.*, **355**, L19.

Ho, P.T.P., Turner, J.L., Fazio, G.G. & Willner, S.P., 1989. *Astrophys. J.*, **344**, 135.

Hughes, D.H., Gear, W.K. & Robson, E.I., 1990. *Mon. Not. R. astr. Soc.*, **244**, 759.

Hummel, E., 1981. *Astr. Astrophys.*, **93**, 93.

Hummel, E. & Gräve, R., 1990. *Astr. Astrophys.*, **228**, 315.

Hurt, R.L. & Turner, J.L., 1991. *Astrophys. J.*, **377**, 434.

Ishiguro, M., Kawabe, R., Morita, K.-I., Okumura, S.K., Chikada, Y., Kasuga, T., Kanzawa, T., Iwashita, H., Handa, K., Takahashi, T., Kobayashi, H., Murata, Y., Ishizuki, S. & Nakai, N., 1989. *Astrophys. J.*, **344**, 763.

Ishizuki, S., Kawabe, R., Ishiguro, M., Okumura, S.K., Morita, K.-I., Chikada, Y. & Kasuga, T., 1990. *Nature*, **344**, 224.

Israel, F.P., 1988. In: *Millimetre and Submillimetre Astronomy*, p. 281, eds Wolstencroft, R.D. & Burton, W.B., Kluwer, Dordrecht.

Israel, F.P. & Burton, W.B., 1986. *Astr. Astrophys.*, **168**, 369.

Israel, F.P., de Graauw, Th., van der Stadt, H. & de Vries, C.P., 1986. *Astrophys. J.*, **303**, 186.

Jaffe, D.T., Becklin, E.E. & Hildebrand, R.H., 1984a. *Astrophys. J. Lett.*, **285**, L31.

Jaffe, D.T., Hildebrand, R.H., Keene, J., Harper, D.A., Loewenstein, R.F. & Moran, J.M., 1984b. *Astrophys. J.*, **281**, 225.

Jog, C.J. & Ostriker, J.P., 1988. *Astrophys. J.*, **328**, 404.

Joseph, R.D., 1990. In: *Dynamics and Interactions of Galaxies*, p. 132, ed. Wielen, R., Springer-Verlag, Berlin.

Joseph, R.D., 1991. In: *Massive Stars in Starbursts*, eds Leitherer, C., Walborn, N.R., Heckman, T.M. & Norman, C.A., Cambridge University Press, Cambridge.

Joseph, R.D. & Wright, G.S., 1985. *Mon. Not. R. astr. Soc.*, **214**, 87.

Joy, M., Lester, D.F. & Harvey, P.M., 1987. *Astrophys. J.*, **319**, 314.

Keene, J., Hildebrand, R.H. & Whitcomb, S.E., 1982. *Astrophys. J. Lett.*, **252**, L11.

Kennicutt, R.C., 1990. In: *The Interstellar Medium in Galaxies*, p. 405, eds Thronson, H.A. & Shull, J.M., Kluwer, Dordrecht.

Klein, U., Wielebinski, R. & Morsi, H.W., 1988. *Astr. Astrophys.*, **190**, 41.

Knapp, G.R., Phillips, T.G., Huggins, P.J., Leighton, R.B. & Wannier, P.G., 1980. *Astrophys. J.*, **240**, 60.

Kronberg, P.P., 1988. In: *Galactic and Extragalactic Star Formation*, p. 391, eds Pudritz, R.E. & Fich, M., Kluwer, Dordrecht.

Kronberg, P.P. & Wilkinson, P.N., 1975. *Astrophys. J.*, **200**, 430.

Kronberg, P.P., Biermann, P. & Schwab, F.R., 1981. *Astrophys. J.*, **246**, 751.

Kronberg, P.P., Biermann, P. & Schwab, F.R., 1985. *Astrophys. J.*, **291**, 693.

Krügel, E., Chini, R., Klein, U., Lemke, R., Wielebinski, R. & Zylka, R., 1990. *Astr. Astrophys.*, **240**, 232.

Kutner, M.L. & Leung, C.M., 1985. *Astrophys. J.*, **291**, 188.

Lada, C.J., 1985. *Ann. Rev. Astr. Astrophys.*, **23**, 267.

Lada, 1988. In: *Galactic and Extragalactic Star Formation*, eds Pudritz, R.E. & Fich, M., Kluwer, Dordrecht.

Langer, W.D. & Penzias, A.A., 1990. *Astrophys. J.*, **357**, 477.

Leger, A. & Puget, J.L., 1984. Astr. Astrophys., **137**, L5.

Lesch, H., Biermann, P.L., Crusius, A., Reuter, H.P., Dahlem, M., Barteldrees, A. & Wielebinski, R., 1990. *Mon. Not. R. astr. Soc.*, **242**, 194.

Lester, D.F., Joy, M., Harvey, P.M., Ellis Jr, H.B. & Parmar, P.S., 1987. *Astrophys. J.*, **321**, 755.

Lester, D.F., Carr, J.S., Joy, M. & Gaffney, N., 1990. *Astrophys. J.*, **352**, 544.

Levreault, R.M., 1988. *Astrophys. J. Suppl.*, **67**, 283.

Lo, K.Y., Berge, G.L., Claussen, M.J., Heiligman, G.M., Leighton, R.B., Masson, C.R., Moffet, A.T., Phillips, T.G., Sargent, A.I., Scott, S.L., Wannier, P.G. & Woody, D.P., 1984. *Astrophys. J. Lett.*, **282**, L59.

Lo, K.Y., Cheung, K.W., Masson, C.R., Phillips, T.G., Scott, S.L. & Woody, D.P., 1987. *Astrophys. J.*, **312**, 574.

Loiseau, N., Reuter, H.-P., Wielebinski, R. & Klein, U., 1988. *Astr. Astrophys.*, **200**, L1.

Loiseau, N., Nakai, N., Sofue, Y., Wielebinski, R., Reuter, H.-P. & Klein, U., 1990. *Astr. Astrophys.*, **228**, 331.

Love, R., 1972. *Nature Phys. Sci.*, **235**, 53.

Lugten, J.B., Watson, D.M., Crawford, M.K. & Genzel, R., 1986. *Astrophys. J. Lett.*, **311**, L51.

Lynds, C.R. & Sandage, A.R., 1963. *Astrophys. J.*, **137**, 1005.

Maffei, P., 1968. *Publs astr. Soc. Pacif.*, **80**, 618.

Maloney, P., 1990a. In: *The Interstellar Medium in Galaxies*, p. 493, eds Thronson, H.A. & Shull, J.M., Kluwer, Dordrecht.

Maloney, P., 1990b. *Astrophys. J. Lett.*, **348**, L9.

Maloney, P. & Black, J.H., 1988. *Astrophys. J.*, **325**, 389.

Martin, R.N. & Ho, P.T.P., 1986. *Astrophys. J. Lett.*, **308**, L7.

Mathis, J.S., Rumpl, W. & Nordsieck, K.H., 1977. *Astrophys. J.*, **217**, 425.

Mathis, J.S., Mezger, P.G. & Panagia, N., 1983. *Astr. Astrophys.*, **128**, 212.

Mauersberger, R. & Henkel, C., 1989. *Astr. Astrophys.*, **223**, 79.

Mauersberger, R. & Henkel, C., 1991. *Astr. Astrophys.*, **245**, 457.

Mauersberger, R., Henkel, C., Wilson, T.L. & Walmsley, C.M., 1986. *Astr. Astrophys.*, **162**, 199.

Mauersberger, R., Henkel, C., Wilson, T.L. & Harju, J., 1989, *Astr. Astrophys.*, **226**, L5.

Mauersberger, R., Henkel, C., Walmsley, C.M., Sage, L.J. & Wiklind, T., 1991. *Astr. Astrophys.*, **247**, 307.

Mauersberger, R., Guélin, M., Martin-Pintado, J., Thum, C., Cernicharo, J., Hein, H. & Navarro, S., 1988. IRAM internal document.

McCarthy, P.J., Heckman, T. & van Breugel, W., 1987. *Astr. J.*, **92**, 264.

McKee, C.F. & Ostriker, J.P., 1977. *Astrophys. J.*, **218**, 148.

Meixner, M., Puchalsky, R., Blitz, L., Wright, M. & Heckman, T., 1990. *Astrophys. J.*, **354**, 158.

Mezger, P.G., 1990, In: *Physics and Composition of the Interstellar Matter*, p. 97, eds Krelowski, J. & Papaj, J., Nicolaus Copernicus University, Torun, in press.

Moore, T.J.T., 1989. *PhD thesis*, University of Edinburgh.

Morris, M., Polish, N., Zuckerman, B. & Kaifu, N., 1983. *Astr. J.*, **88**, 1228.

Nakai, N., Hayashi, M., Handa, T., Sofue, Y., Hasegawa, T. & Sasaki, M., 1987. *Publs astr. Soc. Japan.*, **39**, 685.

Neugebauer, G., Elias, J.H., Matthews, K., McGill, J., Scoville, N.Z. & Soifer, B.T., 1987. *Astr. J.*, **93**, 1057.

Neugebauer, G., Habing, H.J., van Duinen, R., Aumann, H.H., Baud, B., Beichman, C.A., Beintema, D.A., Boggess, N., Clegg, P.E., de Jong, T., Emerson, J.P., Gautier, T.N., Gillett, F.C., Harris, S., Hauser, M.G., Houck, J.R., Jennings, R.E., Low, F.-J., Marsden, P.L., Miley, G., Olnon, F.M., Pottasch, S.R., Raimond, E., Rowan-Robinson, M., Soifer, B.T., Walker, R.G., Wesselius, P.R. & Young, E., 1984. *Astrophys. J. Lett.*, **278**, L1.

Nguyen-Q-Rieu, Nakai, N. & Jackson, J.M., 1989. *Astr. Astrophys.*, **220**, 57.

Nguyen-Q-Rieu, Henkel, C., Jackson, J.M. & Mauersberger, R., 1990, *Astr. Astrophys.*, preprint.

Nilson, P., 1973. *Uppsala astr. Obs. Ann.*, **6**.

Norris, R.P., 1985. *Mon. Not. R. astr. Soc.*, **216**, 701.

O'Connell, R.W. & Mangano, J.J., 1978. *Astrophys. J.*, **221**, 62.

Olofsson, H. & Rydbeck, G., 1984. *Astr. Astrophys.*, **136**, 17.

Ondrechen, M.P., 1985. *Astr. J.*, **90**, 1474.

Ostriker, J.P., 1990. In: *The Interstellar Medium in Galaxies*, p. 543, eds Thronson, H.A. & Shull, J.M., Kluwer, Dordrecht.

Padman, R., 1991. SPECX *Users' Manual.*

Pajot, F., Gispert, R., Lamarre, J.M., Pomerantz, M.A., Puget, J.-L. & Serra, G., 1989. *Astr. Astrophys.*, **223**, 107.

Panagia, N., 1973. *Astr. J.*, **78**, 929.

Pipher, J.L., Moneti, A., Forrest, W.J., Woodward, C.E. & Shure, M.A., 1987. In: *Infrared Astronomy with Arrays*, p. 326, eds Wynn-Williams, C.G. & Becklin, E.E., University of Hawaii, Honolulu.

Puxley, P.J., 1988. *PhD thesis*, University of Edinburgh.

Puxley, P.J., 1991. *Mon. Not. R. astr. Soc.*, **249**, 11P.

Puxley, P.J., Brand, P.W.J.L., Moore, T.J.T., Mountain, C.M. & Nakai, N., 1991. *Mon. Not. R. astr. Soc.*, **248**, 585.

Puxley, P.J., Brand, P.W.J.L., Moore, T.J.T., Mountain, C.M., Nakai, N. & Yamashita, T., 1989. *Astrophys. J.*, **345**, 163.

Rengarajan, T.N., 1984. *Astr. Astrophys.*, **140**, 213.

Rickard, L.J. & Harvey, P.M., 1983. *Astrophys. J. Lett.*, **268**, L7.

Rickard, L.J. & Harvey, P.M., 1984. *Astr. J.*, **89**, 1520.

Rickard, L.J. & Blitz, L., 1985. *Astrophys. J. Lett.*, **292**, L57.

Rickard, L.J., Turner, B.E. & Palmer, P., 1977a. *Astrophys. J. Lett.*, **218**, L51.

Rickard, L.J., Palmer, P., Morris, M., Turner, B.E. & Zuckerman, B., 1977b. *Astrophys. J.*, **213**, 673.

Rieke, G.H., 1976. *Astrophys. J. Lett.*, **206**, L15.

Rieke, G.H. & Lebofsky, M.J., 1985. *Astrophys. J.*, **288**, 618.

Rieke, G.H., Lebofsky, M.J., Thompson, R.I., Low, F.J. & Tokunaga, A.T., 1980. *Astrophys. J.*, **238**, 24.

Rieke, G.H., Cutri, R.M., Black, J.H., Kailey, W.F., McAlary, C.W., Lebofsky, M.J. & Elston, R., 1985. *Astrophys. J.*, **290**, 116.

Roche, P.F., Aitken, D.K., Smith, C.H. & Ward, M.J., 1991. *Mon. Not. R. astr. Soc.*, **248**, 606.

Rowan-Robinson, M., 1986. *Mon. Not. R. astr. Soc.*, **219**, 737.

Rowan-Robinson, M., 1990. In: *The Interstellar Medium in Galaxies,*, p.121, eds Thronson, H.A. & Shull, J.M., Kluwer, Dordrecht.

Rumstay, K.S. & Kaufman, M., 1983. *Astrophys. J.*, **274**, 611.

Russell, R.W., Melnick, G., Gull, G.E. & Harwit, M., 1980. *Astrophys. J. Lett.*, **240**, L99.

Sandage, A. & Tammann, G.A., 1975. *Astrophys. J.*, **196**, 313.

Sandage, A. & Tammann, G.A., 1981. *A Revised Shapley-Ames Catalog of Bright Galaxies*, Carnegie Institute of Washington, Washington DC.

Sargent, A.I., Sutton, E.C., Masson, C.R., Lo, K.Y. & Phillips, T.G., 1985. *Astrophys. J.*, **289**, 150.

Sanders, D.B., Solomon, P.M. & Scoville, N.Z., 1984. *Astrophys. J.*, **276**, 182.

Sanders, D.B., Scoville, N.Z. & Solomon, P.M., 1985. *Astrophys. J.*, **289**, 373.

Sanders, D.B., Soifer, B.T., Elias, J.H., Madore, B.F., Matthews, K., Neugebauer, G. & Scoville, N.Z., 1988. *Astrophys. J.*, **325**, 74.

Scalo, J., 1990. In: *Windows on Galaxies*, p. 125, eds Fabbiano, G. *et al.*, Kluwer, Dordrecht.

Scoville, N.Z., 1990. In: *Submillimetre Astronomy*, p. 197, eds Watt, G.D. & Webster, A.S., Kluwer, Dordrecht.

Scoville, N.Z., Yun, M.S., Clemens, D.P., Sanders, D.B. & Waller, W.H., 1987. *Astrophys. J. Suppl.*, **63**, 821.

Seaquist, E.R., Pfund, J. & Bignell, R.C., 1976. *Astr. Astrophys.*, **48**, 413.

Seaquist, E.R., Bell, M.B. & Bignell, R.C., 1985. *Astrophys. J.*, **294**, 546.

Sellgren, K., Werner, M. & Gatley, I., 1978. *Bull. Am. astr. Soc.*, **10**, 422.

Shostak, G.S. & Weliachew, L., 1971. *Astrophys. J. Lett.*, **169**, L71.

Smith, B.J., Lester, D.F. & Harvey, P.M., 1990. In: *The Interstellar Medium in External Galaxies: Summary of Contributed Papers*, p.84, eds Hollenbach, D.J. & Thronson, H.A., NASA CP-3084.

Sofue, Y., 1988. In: *Galactic and Extragalactic Star Formation,* p. 409, eds Pudritz, R. & Fich, M., Kluwer, Dordrecht

Sofue, Y., Handa, T., Hayashi, M. & Nakai, N., 1987. In: *Star Formation in Galaxies*, p. 179, ed. Lonsdale-Persson, C.J., NASA CP-2466.

Soifer, B.T., Houck, J.R. & Neugebauer, G., 1987. *Ann. Rev. Astr. Astrophys.*, **25**, 187.

Solomon, P.M. & Sanders, D.B., 1979. In: *Giant Molecular Clouds in the Galaxy,* eds Solomon, P.M. & Edmunds, M., Pergamon, Oxford.

Solomon, P.M., Sanders, D.B. & Scoville, N.Z., 1979. *The Large Scale Characteristics of the Galaxy, IAU Symp. No. 84,* p.35, ed. Burton, W.B., Reidel, Dordrecht.

Solomon, P.M., Rivolo, A.R., Barrett, J. & Yahil, A., 1987. *Astrophys. J.,* **319**, 730.

Spinrad, H., Bahcall, J., Becklin, E.E., Gunn, J.E., Kristian, J., Neugebauer, G., Sargent, W.L.W. & Smith, H., 1973. *Astrophys. J.,* **180**, 351.

Stacey, G.J., Geis, N., Genzel, R., Lugten, J.B., Poglitsch, A., Sternberg, A. & Townes, C.H., 1991. *Astrophys. J.,* **373**, 423.

Stark, A.A., 1984. *Astrophys. J.,* **281**, 624.

Stark, A.A. & Carlson, E.R., 1984. *Astrophys. J.,* **279**, 122.

Steppe, H., Mauersberger, R., Schulz, A. & Baars, J.W.M., 1990. *Astr. Astrophys.,* **233**, 410.

Strong, A.W., Bloemen, J.B.G.M., Dame, T.M., Grenier, I.A., Hermsen, W., Lebrun, F., Nyman, L.-Å., Pollock, A.M.T. & Thaddeus, P., 1988. *Astr. Astrophys.,* **207**, 1.

Sukumar, S., Klein, U. & Gräve, R., 1987. *Astr. Astrophys.,* **184**, 71.

Sutton, E.C., Masson, C.R. & Phillips, T.G., 1983. *Astrophys. J. Lett.,* **275**, L49.

Sutton, E.C., Blake, G.A., Masson, C.R. & Phillips, T.G., 1984. *Astrophys. J. Lett.,* **283**, L41.

Tammann, G.A. & Sandage, A.R., 1968. *Astrophys. J.,* **151**, 825.

Telesco, C.M., 1988. *Ann. Rev. Astr. Astrophys.,* **26**, 343.

Telesco, C.M. & Harper, D.A., 1980. *Astrophys. J.,* **235**, 392.

Telesco, C.M. & Gatley, I., 1981. *Astrophys. J. Lett.,* **247**, L11.

Telesco, C.M., Decher, R. & Joy, M., 1989. *Astrophys. J. Lett.,* **343**, L13.

Telesco, C.M., Becklin, E.E., Wynn-Williams, C.G. & Harper, D.A., 1984. *Astrophys. J.,* **282**, 427.

Telesco, C.M., Decher, R., Ramsey, B.D., Wolstencroft, R.D. & Leggett, S.G., 1987. In: *Star Formation in Galaxies*, p. 497, ed. Lonsdale-Persson, C.J., NASA CP-2466.

Telesco, C.M., Campins, H., Joy, M., Dietz, K. & Decher, R., 1991. *Astrophys. J.,* **369**, 135.

Terlevich, R., 1990. In: *Windows on Galaxies*, p. 87, eds Fabbiano, G. *et al.*, Kluwer, Dordrecht.

Thronson, H.A., 1988. In: *Galactic and Extragalactic Star Formation,* p. 621, eds Pudritz, R. & Fich, M., Kluwer, Dordrecht.

Thronson, H.A., Walker, C.K., Walker, C.E. & Maloney, P., 1987. *Astrophys. J.,* **318**, 645.

Thronson, H.A., Walker, C.K., Walker, C.E. & Maloney, P., 1989. *Astr. Astrophys.,* **214**, 29.

Tielens, A.G.G.M. & Hollenbach, D., 1985. *Astrophys. J.,* **291**, 722.

Tilanus, R.P.J., Tacconi, L.J., Sutton, E.C., Zhou, S., Sanders, D.B., Wynn-Williams, C.G., Lo, K.Y. & Stephens, S.A., 1991. *Astrophys. J.,* **376**, 500.

Townes, C.H. & Schawlow, A.L., 1955. *Microwave Spectroscopy*, McGraw-Hill, New York.

Tully, R.B., 1988. *Nearby Galaxies Catalog,* Cambridge University Press, Cambridge.

Turner, J.L. & Ho, P.T.P., 1983. *Astrophys. J. Lett.,* **268**, L79.

Turner, J.L., Ho, P.T.P. & Beck, S.C., 1987. *Astrophys. J.,* **313**, 644.

Turner, J.L., Martin, R.N. & Ho, P.T.P., 1991. *Astrophys. J.,* **367**, 677.

van der Kruit, P.C. & Allen, R.J., 1976. *Ann. Rev. Astr. Astrophys.,* **14**, 417.

van Dishoeck, E.F. & Black, J.H., 1986. In: *Physical Processes in Interstellar Clouds*, p. 241, eds Morfill, G.E. & Scholer, M., Reidel, Dordrecht.

Verter, F. & Rickard, L.J., 1989. *Astr. Astrophys.,* **225**, 27.

Wall, W.F. & Jaffe, D.T., 1990. *Astrophys. J. Lett.,* **361**, L45.

Wannier, P.G., 1980. *Ann. Rev. Astr. Astrophys.*, **18**, 399.

Watson, M.G., Stanger, V. & Griffiths, R.E., 1984. *Astrophys. J.,* **286**, 144.

Weliachew, L., Fomalont, E.B. & Greisen, E.W., 1984. *Astr. Astrophys.,* **137**, 335.

Weliachew, L., Casoli, F. & Combes, F., 1988. *Astr. Astrophys.,* **199**, 29.

Whitcomb, S.E., Gatley, I., Hildebrand, R.H., Keene, J., Sellgren, K. & Werner, M.W., 1981. *Astrophys. J.,* **246**, 416.

Wiklind, T., Rydbeck, G., Hjalmarson, Å & Bergman, P., 1990. *Astr. Astrophys.,* **232**, L11.

Wild, W., 1990. *PhD thesis,* Ludwig-Maximilians-Universität.

Willner, S.P., Soifer, B.T., Russell, R.W., Joyce, R.R. & Gillett, F.C., 1977. *Astrophys. J. Lett.,* **217**, L121.

Wilson, T.L. & Walmsley, C.M., 1989. *Astr. Astrophys. Rev.,* **1**, 141.

Wolfire, M.G., Hollenbach, D. & Tielens, A.G.G.M., 1989. *Astrophys. J.,* **344**, 770.

Wolfire, M.G., Tielens, A.G.G.M. & Hollenbach, D.J, 1990. *Astrophys. J.,* **358**, 116.

Wright, G.S., Joseph, R.D., Robertson, N.A., James, P.A. & Meikle, W.P.S., 1988. *Mon. Not. R. astr. Soc.,* **233**, 1.

Wright, M.C.H. & Seielstad, G.A., 1973. *Astrophys. Lett.,* **13**, 1.

Wynn-Williams, C.G., 1987. In: *Star Formation in Galaxies*, p. 125, ed. Lonsdale-Persson, C.J., NASA CP-2466.

Young, J.S., 1990. In: *The Interstellar Medium in Galaxies*, p. 67, eds Thronson, H.A. & Shull, J.M., Kluwer, Dordrecht.

Young, J.S. & Scoville, N.Z., 1982. *Astrophys. J.,* **258**, 467.

Young, J.S. & Scoville, N.Z., 1984. *Astrophys. J.,* **287**, 153.

Young, J.S. & Scoville, N.Z., 1991. *Ann. Rev. Astr. Astrophys.,* **29**, 581.

Appendix A

Submillimetre continuum observing techniques

The region of the electromagnetic spectrum between near/mid-infrared and centimetre–radio wavelengths is one of the most scientifically productive for studies of star formation in (our own and other) galaxies. It is also one of the last to be opened up for study. As in the infrared, submillimetre observations are hampered chiefly by water vapour absorption in the Earth's atmosphere, which permits ground-based observations, from high and dry sites, only through a few relatively narrow windows, at approximately 350, 450, 600, 750, 800 and >1100 μm (Fig. A.1). Even at 4200 m, the altitude of Mauna Kea, observations at 350 and 450 μm are difficult. Shortward of $\sim$300 μm, balloons, satellites, or facilities such as the Kuiper Airborne Observatory flying at an altitude of $\sim$15 km, are the only option.

Additional considerations at submillimetre wavelengths include the possibility of rapid ($\sim$1 hr) variations in sky opacity over the course of a night, the technological difficulties of building large antennae of high surface accuracy, and the scarcity of reliable submillimetre calibration sources.

Submillimetre and millimetre continuum observations on the JCMT are performed with the ^{3}He-cooled bolometer UKT14 (Duncan *et al.* 1990). Some characteristics of the detector and telescope are summarized in Table A.1. The sensivity of UKT14 at various wavelengths is described by the Noise Equivalent Flux Density, or NEFD, given in Table A.1. This is the flux density which would give a signal-to-noise ratio of one, in one second of integration. Table A.1 demonstrates how sensitive to atmospheric conditions short-wavelength (<800 μm) observations are. For example, in good sky conditions (extinction $a \simeq 1$) at the zenith, the NEFD at 450 μm is $\sim$4 Jy. In contrast,

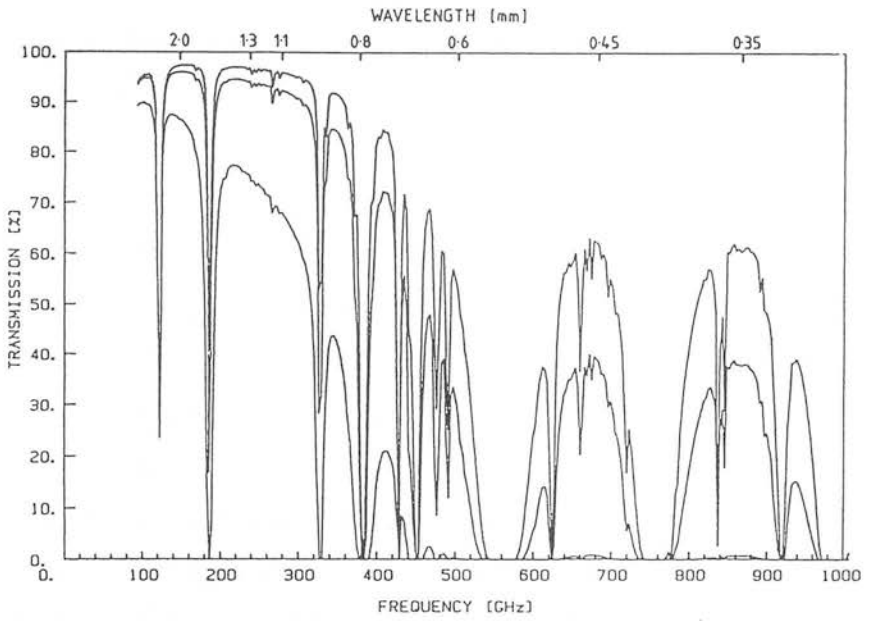

Figure A.1: Representation of the atmospheric transmission at the JCMT, for varying amounts of water vapour, taken from Duncan *et al.* (1990). The UKT14 atmospheric 'windows' between 350 and 1100 μm can be clearly seen, and the difficulty of observing at wavelengths shortward of 800 μm is apparent.

in poor conditions ($a \simeq 5$) at a more typical zenith distance of $\sim$40°, the NEFD at 450 μm is $\sim$1000 Jy! In fact, only about 30% of all nights are suitable for short-wavelength work.

Careful planning of the observing programme, including frequent calibration, focus and pointing observations, and sensible selection of calibrators, pointing sources and extinction monitors, are essential to obtain scientifically useful results in this exciting yet technically difficult wavelength region.

A.1 Calibration

Calibration at submillimetre wavelengths is difficult, and frequent observations of calibrator sources are essential, as the sky opacity in this region is continually varying.

The ideal calibration sources are bright, point-like, non-varying and with accurately known fluxes. The objects which come closest to meeting these criteria in the submil-

limetre are planets, particularly Jupiter and Mars, but even these are frequently of an angular size comparable to the beamwidth, making the observed flux density dependent on pointing accuracy. In addition, planets are often available for only part of the observing shift. A programme has been underway since the JCMT was commissioned to establish a set of reliable secondary calibrators with well-known fluxes (G. Sandell, JCMT internal memo). These include evolved stars such as CRL618 and IRC10216 (which although slowly varying, is still used as it is strong in the submillimetre and fills a gap in RA when other bright calibrators are scarce). Compact HII regions [e.g. W3(OH)] or embedded pre-main-sequence objects (OMC1) are also commonly used. At present, reliable fluxes of secondary calibrators are only available for the most commonly used 800 and 1100 μm filters, and, less accurately, at 450 μm also. Despite these efforts, it is still frequently the case that well-determined primary or secondary calibrator sources are only available for part of the observing shift.

The signal measured by UKT14 in millivolts, $m(\nu)$, is related to the true flux density of the source, $F(\nu)$, by

$$m(\nu) = \frac{F(\nu)}{C(\nu)}\, \mathrm{e}^{-a(\nu)\mathrm{sec}z}, \tag{A.1}$$

where $a(\nu)$ is the atmospheric extinction at frequency ν, sec$z$ is the airmass through which the object is being observed, and $C(\nu)$ is a conversion factor in Jy/mV. In stable conditions, frequent observation of a bright source at several airmasses [far enough apart that the difference in signal is much greater than the observational noise, but not so far apart that $a(\nu)$ changes between the observations] will give the variation of $a(\nu)$ with time, via

$$a(\nu) = \ln\left[\frac{m_1(\nu)}{m_2(\nu)}\right]\, (\mathrm{sec}z_2 - \mathrm{sec}z_1)^{-1}, \tag{A.2}$$

and this can be used, with observation of a calibrator of accurately known flux, to determine $C(\nu)$ and hence calibrate the data. The extinction monitor can be an established calibration source itself, but under ideal conditions, it is not necessary to know its absolute flux, therefore objects such as 3C273 and 3C279, which due to their variability are unsuitable as secondary calibrators, can be used as extinction monitors.

Unfortunately, the atmosphere is rarely stable enough to determine $a(\nu)$ and $C(\nu)$ in this way – even with frequent calibration (every hour), the opacity often changes

sufficiently to make the output from equation (A.2) meaningless. The usual method of extinction correction is therefore directly from observations of calibrator sources, via

$$a(\nu) = \frac{1}{\sec z} \ln \left[\frac{F(\nu)}{C(\nu)\, m(\nu)} \right]. \qquad (A.3)$$

In this case, it is necessary to assume a value of $C(\nu)$ to calculate $a(\nu)$. The most recent published values of $C(\nu)$ date from June 1988. However, UKT14 is a stable instrument and, in the absence of major changes to the telescope or detector, $C(\nu)$ should remain fairly constant (G. Sandell, JCMT User Note). If there are no well-calibrated sources available for part of the shift, and objects such as 3C273 are being used, these will themselves have to be calibrated at the beginning or end of the shift, before they can be used as extinction monitors during the remainder of the night.

Once factors such as sensitivity and extinction uncertainties have been taken into account, the typical calibration error on submillimetre observations is ~10–15% .

An additional source of error at short (<800 μm) wavelengths is the fact that the beam profile, despite the high surface accuracy of the JCMT, is poorly known and probably non-Gaussian. The error beam can therefore pick up a non-negligible fraction of the emission from an extended source, and the beam–source coupling will be very different for a point source (e.g. CRL618), disc (e.g. Mars) or extended source (e.g. Maffei 2). This may contribute additional errors of ~30% at 450 μm . The beam–source coupling is impossible to estimate for an extended object such as a galaxy, unless the beam and true source profiles are accurately known, which is rarely the case. It is usual to assume that both source and beam can be represented by Gaussian functions, since this is mathematically convenient and physically fairly plausible, for the beam at least and probably for many sources as well.

Future developments for the calibration of JCMT continuum observations include the use of skydips (measuring sky emission as a function of airmass) as an extinction monitor, and a chopper-wheel calibration system (comparing the emission from the sky with that from an ambient load and a liquid nitrogen cooled load).

A.2 Pointing

As well as calibration, frequent pointing checks should be performed using bright point sources (such as quasars or evolved stars), preferably in the same part of the sky as

UKT14 filter	1100 μm	800 μm	450 μm
Effective [1] wavelength (μm)	1128	781	440
Bandpass (μm)	310	205	54
Beamsize:			
(65-mm aperture)	18.5″	15.8″	17.7″ [2]
(47-mm aperture)	–	13.5″	13″
(27-mm aperture)	–	–	7″
Sensitivity (Jy/mV) [3]	11.8	8.5 (65 mm) 11.1 (47 mm)	15.5 (65 mm)
Typical Extinction	0.1 (good) 0.3 (poor)	0.3 (good) 1.5 (poor)	1.0 (good) 5.0 (poor)
NEFD [4,5] (1σ 1s)	350 mJy	500 mJy	~4 Jy

Notes. (1) The effective wavelength depends on atmospheric conditions, source spectral index and dish accuracy (Duncan *et al.* 1990), although in practice the variation is only a few per cent for typical conditions. (2) Non-Gaussian beam. (3) June 1988 (G. Sandell, JCMT User Note). (4) In good conditions at the zenith. (5) Flux density (outside the atmosphere) which would give a signal-to-noise of one in one second of integration time.

Table A.1: Characteristics of UKT14.

the target. Pointing checks are carried out by means of fitting a Gaussian function to a 'five-point scan' of a bright source to determine the pointing offsets in azimuth and elevation.

A.3 'Spikes' in the stored data

A UKT14 integration is split into a number of cycles, each cycle consisting of an 'on' (source) and an 'off' (emission-free reference position) integration of typically ~5–20 seconds. These are stored as a sequence of on–off–off–on–on–off–off–on.....For each of i cycles, the quantity x_i = ('on' – 'off') is calculated, and the mean and standard error of the observation (N cycles) are then given by

$$\overline{x} = \sum_i \frac{x_i}{N}, \tag{A.4}$$

$$\sigma_{\overline{x}} = \frac{\sigma_x}{\sqrt{N}}, \tag{A.5}$$

σ_x being the standard deviation of x_i. The signal-to-noise ratio $R = \overline{x}/\sigma_{\overline{x}}$ is then governed by the scatter of the individual on–off pairs about the mean. If a 'spike' occurs (i.e. an individual 'object–ref' that is much higher or lower than the mean) it can have the effect of markedly increasing the standard error while leaving the mean little changed. The effect of such spikes can be guarded against by searching for and removing any individual on–off pairs that are, say, more than five standard errors from the mean. This generally results in a negligible change in $\overline{x}$, but can improve σ. This procedure is only practical for fairly long (5–10 min) integrations, such as the point-to-point mapping of M83 and IC342 (Chapter 4). For raster-scanned maps such as the 800 μm map of Maffei 2 (Chapter 4) or the 450 μm map of M82 (Chapter 2) where each integration may consist of only 2–4 cycles, it is not possible to remove spikes in this way, if they occur.

Another unexpected result of spikes which occurs occasionally is the generation of two adjacent numbers in the stored on–off–off–on–on– sequence that are identical, following which the data reduction software appears to get out of step calculating the on–off pairs, resulting in a meaningless value of $\overline{x}$. At the time of the final JCMT

observing run described in this thesis, in May 1990, this apparent bug had not been traced or corrected for.

Appendix B

Contamination of dust continuum fluxes by molecular line emission

The flux density at frequency ν from a spectral line of peak main-beam brightness temperature $T_{\rm mb}$ in a beam of solid angle $\Omega_{\rm b}$ is (Downes 1989):

$$S(\nu)_{\rm line} = I(\nu)_{\rm line}\ \Omega_{\rm b}\ {\rm Wm^{-2}\ Hz^{-1}}, \tag{B.1}$$

where

$$I(\nu)_{\rm line} = \frac{2\nu^2}{c^2}\ kT_{\rm mb}\ {\rm Wm^{-2}\ Hz^{-1}\ sr^{-1}}. \tag{B.2}$$

The flux from the line is therefore given by the integration of equation (B.2) over frequency,

$$F(\nu)_{\rm line} = \Omega_{\rm b} \int I(\nu)_{\rm line}\, d\nu = I(\nu)_{\rm line}\ \Omega_{\rm b}\ \Delta\nu_{1/2}\ {\rm Wm^{-2}}, \tag{B.3}$$

where the half-width of the line, $\Delta\nu_{1/2}$, can be expressed as a FWHM velocity width:

$$\Delta\nu_{1/2} = \nu\ \frac{\Delta V_{1/2}}{c}. \tag{B.4}$$

This energy is emitted into the UKT14 filter, bandpass B(Hz). The contribution to the dust continuum flux density is therefore

$$S(\nu)_{\rm cont} = I(\nu)_{\rm line}\ \Omega_{\rm b}\ \frac{\Delta\nu_{1/2}}{B}\ {\rm Wm^{-2}\ Hz^{-1}},$$

or

$$S(\nu)_{\rm cont} = 2\ \left(\frac{\nu}{c}\right)^3\ \frac{k\Omega_{\rm b}}{B} \int T_{\rm mb}\, dV\ {\rm Wm^{-2}\ Hz^{-1}}. \tag{B.5}$$

Appendix C

Derivation of equations used in the LTE analysis of molecular line data

Much of this sequence of derivations was compiled from the literature by C.J. Chandler (personal communication) and appears in Chandler (1990).

The absorption coefficient for a pure rotational transition between two molecular states $J = j \rightarrow i\,(j = i + 1)$ is

$$\kappa(\nu_{ji}) = \frac{h\nu_{ji}}{4\pi}\left(n_i B_{ij} - n_j B_{ji}\right)\,\phi(\nu_{ji}),$$

where n_i and n_j are the populations of levels i and j, B_{ij} and B_{ji} the Einstein coefficients for stimulated absorption and emission, respectively, ν_{ji} the frequency and $\phi(\nu_{ji})$ the line profile function of the transition. Therefore

$$\kappa(\nu_{ji}) = \frac{h\nu_{ji}}{4\pi} n_i B_{ij}\left(1 - \frac{n_j B_{ji}}{n_i B_{ij}}\right)\,\phi(\nu_{ji}).$$

If Local Thermodynamic Equilibrium (LTE) is assumed (i.e. the gas is dense enough that collisions dominate), the level populations are described by the Boltzmann equation

$$\frac{n_j}{n_i} = \frac{g_j}{g_i}\exp(-h\nu_{ji}/kT_{\rm ex}),$$

where g_j and g_i are the statistical weights of the two levels, and $T_{\rm ex}$ is the excitation temperature characterizing the actual level populations (and is equal to the kinetic

temperature $T_{\rm kin}$). Since $g_i B_{ij} = g_j B_{ji}$, $\kappa(\nu_{ji})$ can then be written:

$$\begin{aligned}\kappa(\nu_{ji}) &= \frac{h\nu_{ji}}{4\pi} n_i B_{ij} \left(1 - \frac{n_j g_i}{n_i g_j}\right) \phi(\nu_{ji}) \\ &= \frac{h\nu_{ji}}{4\pi} n_i B_{ij} \left(1 - \mathrm{e}^{-h\nu_{ji}/kT_{\rm ex}}\right) \phi(\nu_{ji}).\end{aligned}$$

The Einstein A and B coefficients are related by

$$A_{ji} = \frac{2h\nu_{ji}^3}{c^2} B_{ji} = \frac{g_i}{g_j} B_{ij} \frac{2h\nu_{ji}^3}{c^2},$$

and hence

$$\kappa(\nu_{ji}) = \frac{h\nu_{ji}}{4\pi} n_i \frac{g_j}{g_i} \frac{c^2}{2h\nu_{ji}^3} A_{ji} \left(1 - \mathrm{e}^{-h\nu_{ji}/kT_{\rm ex}}\right) \phi(\nu_{ji}) \tag{C.1}$$

$$= \frac{c^2}{8\pi} \frac{g_j}{g_i} n_i \frac{A_{ji}}{\nu_{ji}^2} \left(1 - \mathrm{e}^{-h\nu_{ji}/kT_{\rm ex}}\right) \phi(\nu_{ji}). \tag{C.2}$$

The total number of particles in all levels, n, is related to the number of particles in a level i by

$$\frac{n_i}{n} = \frac{g_i}{Z} \mathrm{e}^{-h\nu_{i0}/kT_{\rm ex}}, \tag{C.3}$$

where Z is the partition function, given by

$$Z = \sum_{i=0}^{\infty} (2i+1) \exp\left[\frac{-hBi(i+1)}{kT_{\rm ex}}\right],$$

and $\nu_{i0} = Bi(i+1)$ is the energy above the ground state of level i. B is the rotation constant of the molecule, given by $B = h/8\pi^2 I$, where I is its moment of inertia.

For $hB \ll kT_{\rm ex}$, and assuming that $T_{\rm ex}$ is the same for all transitions (a requirement of LTE), the expression for Z can be approximated by an integral over i, the solution of which is given by

$$Z \simeq \frac{kT_{\rm ex}}{hB}. \tag{C.4}$$

From equations (C.3) and (C.4), then

$$n_i \frac{g_j}{g_i} = \frac{g_j}{g_i} \frac{g_i}{Z} n \mathrm{e}^{-h\nu_{i0}/kT_{\rm ex}} = g_j \frac{hB}{kT_{\rm ex}} n \mathrm{e}^{-h\nu_{i0}/kT_{\rm ex}},$$

which is substituted into equation (C.2) to give an expression for $\kappa(\nu_{ji})$:

$$\kappa(\nu_{ji}) = \frac{c^2}{8\pi} g_j \frac{hB}{kT_{\rm ex}} \mathrm{e}^{-h\nu_{i0}/kT_{\rm ex}} \frac{A_{ji}}{{\nu_{ji}}^2} \left(1 - \mathrm{e}^{-h\nu_{ji}/kT_{\rm ex}}\right) n\phi(\nu_{ji}).$$

The optical depth of the gas to radiation at frequency ν is given by the integral of the absorption coefficient along the line of sight through the gas:

$$\begin{aligned} d\tau(\nu) &= \kappa(\nu)dx, \\ \tau(\nu) &= \int \kappa(\nu)dx \simeq \kappa(\nu)L, \end{aligned}$$

where L is the extent of the emission region along the line of sight. Therefore

$$\tau(\nu_{ji}) \simeq \frac{c^2}{8\pi} g_j \frac{hB}{kT_{\rm ex}} \mathrm{e}^{-h\nu_{i0}/kT_{\rm ex}} \frac{A_{ji}}{\nu_{ji}^2} \left(1 - \mathrm{e}^{-h\nu_{ji}/kT_{\rm ex}}\right) \phi(\nu_{ji}) N,$$

where $N = nL$ is the column density of material in the line of sight. Substituting $g_j = 2j+1$ and $\nu_{i0} = Bi(i+1)$ into the above equation, then

$$\tau(\nu_{ji}) = \frac{c^2}{8\pi}(2j+1) \frac{hB}{kT_{\rm ex}} \mathrm{e}^{-hBi(i+1)/kT_{\rm ex}} \frac{A_{ji}}{\nu_{ji}^2} \left(1 - \mathrm{e}^{-h\nu_{ji}/kT_{\rm ex}}\right) \phi(\nu_{ji}) N. \qquad \text{(C.5)}$$

The Einstein coefficient A_{ji} for a spontaneous downward transition from j to i, with $j = i + 1$, is given by

$$A_{ji} = \frac{16\pi^3}{3\epsilon_0 hc^3} \nu_{ji}^3 \mu^2 \frac{j}{2j+1},$$

(Townes & Schawlow 1955), μ being the dipole moment of the molecule (0.112 Debye for ^{12}CO). Then

$$\tau(\nu_{ji}) = \frac{2\pi^2}{3\epsilon_0 hc} \frac{hB}{kT_{\rm ex}} \nu_{ji} \, \mu^2 j \mathrm{e}^{-hBi(i+1)/kT_{\rm ex}} \left(1 - \mathrm{e}^{-h\nu_{ji}/kT_{\rm ex}}\right) \phi(\nu_{ji}) N. \qquad \text{(C.6)}$$

Now the integral of optical depth over frequency, $\int \tau(\nu)d\nu = \tau_0 \Delta\nu$, where τ_0 is the peak optical depth and $\Delta\nu$ is related to the FWHM of the line via

$$\Delta\nu = (\pi/4\ln 2)^{1/2} \, \nu_{1/2} = 1.064 \, \nu_{1/2}$$

for a Gaussian line profile. For a velocity-broadened line, $\Delta\nu \simeq \nu_{1/2} = \nu_{ij}\Delta V/c$ where ΔV is the velocity width of the line (FWHM).

For two adjacent optically thin transitions of the same species, the ratio of peak line optical depths can be calculated. From equation (C.6), and remembering that $\int \phi(\nu)d\nu = 1$:

$$\begin{aligned} \tau(j+1, j) &= \frac{2\pi^2}{3\epsilon_0 hc} \frac{hB}{kT_{\rm ex}} \frac{c}{\Delta V} \mu^2 (j+1) \, \mathrm{e}^{-hBj(j+1)/kT_{\rm ex}} \left[1 - \mathrm{e}^{-2hB(j+1)/kT_{\rm ex}}\right] N, \\ \tau(j, j-1) &= \frac{2\pi^2}{3\epsilon_0 hc} \frac{hB}{kT_{\rm ex}} \frac{c}{\Delta V} \mu^2 j \, \mathrm{e}^{-hBj(j-1)/kT_{\rm ex}} \left[1 - \mathrm{e}^{-2hBj/kT_{\rm ex}}\right] N, \end{aligned}$$

giving the ratio of peak line optical depths:

$$\frac{\tau(j+1,j)}{\tau(j,j-1)} = \frac{j+1}{j}\frac{\left[1-\mathrm{e}^{-2hB(j+1)/kT_{\rm ex}}\right]}{\left[\mathrm{e}^{2hBj/kT_{\rm ex}}-1\right]}. \tag{C.7}$$

Now the observed radiation temperature $T_{\rm r}$ is *defined* as a Rayleigh–Jeans brightness temperature, given by

$$T_{\rm r} = \frac{c^2}{2k\nu^2}(I_\nu - I_{\rm bg})[1-\mathrm{e}^{-\tau(\nu)}],$$

where the filling factor of the emitting gas has been assumed to be unity, $I_{\rm bg}$ is the intensity of the microwave background at the frequency of the line, and

$$I_\nu = \frac{2h\nu^3}{c^2}\frac{1}{(\mathrm{e}^{h\nu/kT_{\rm ex}}-1)}.$$

Hence

$$T_{\rm r} = \frac{h\nu}{k}\left[\frac{1}{(\mathrm{e}^{h\nu/kT_{\rm ex}}-1)} - \frac{1}{(\mathrm{e}^{h\nu/kT_{\rm bg}}-1)}\right][1-\mathrm{e}^{-\tau(\nu)}], \tag{C.8}$$

where $T_{\rm bg}$=2.7 K is the microwave background temperature. For $\tau(\nu) \ll 1$, $h\nu \ll kT_{\rm ex}$ and $T_{\rm ex} \gg T_{\rm bg}$, this becomes

$$T_{\rm r} \simeq \tau(\nu)T_{\rm ex}\ , \tag{C.9}$$

while in the optically thick limit,

$$T_{\rm r} \simeq T_{\rm ex}\ . \tag{C.10}$$

For optically thick emission, equation (C.8) can be used for an estimate of the excitation temperature. For example, for the ^{12}CO J=2–1 line:

$$T_{\rm ex} = 11.09\left[\ln\left(1+\frac{11.09}{T_{\rm r}+0.185}\right)\right]^{-1}. \tag{C.11}$$

Note that this assumes that the filling factor of the emission is unity – i.e. that the source fills the beam completely. In practice, this will not be the case, particularly for extragalactic observations where the measured antenna temperatures rarely exceed a few K, and the beam–source coupling is unknown. The value of $T_{\rm ex}$ derived from equation (C.11) will therefore always be a lower limit to the true excitation temperature.

In the optically thin limit, equation (C.8) can be used to find the antenna temperature ratio for two adjacent transitions, since, assuming the same excitation temperature

for both,

$$\frac{T_{\rm r}(j+1,j)}{T_{\rm r}(j,j-1)} \simeq \frac{\tau(j+1,j)}{\tau(j,j-1)} \simeq \frac{(j+1)}{j}\frac{(1-{\rm e}^{-2hB(j+1)/kT_{\rm ex}})}{({\rm e}^{2hBj/kT_{\rm ex}}-1)}$$

(see Fig. C.1). In the optically thin, high-temperature limit, this becomes

$$\frac{T_{\rm r}(j+1,j)}{T_{\rm r}(j,j-1)} \simeq \left(\frac{j+1}{j}\right)^2. \tag{C.12}$$

Equation (C.8) can also be used to relate the antenna temperature ratio for a given transition of two isotopes to their respective optical depths, if $h\nu \ll kT_{\rm ex}$ and $T_{\rm ex} \gg T_{\rm bg}$. For example:

$$\frac{T_{\rm r}(^{12}{\rm CO})}{T_{\rm r}(^{13}{\rm CO})} \simeq \frac{[1-{\rm e}^{-\tau^{12}(\nu)}]}{[1-{\rm e}^{-\tau^{13}(\nu)}]} \tag{C.13}$$

(Fig. C.1), where $\tau^{12}(\nu) = R\tau^{13}(\nu)$, R being the ^{12}CO:^{13}CO abundance ratio. Equation (C.13) can be used to calculate optical depths if an abundance ratio is assumed.

From equation (C.5), for optically thin transitions, it is possible to derive the column density of emitting gas in terms of the observed line temperature $T_{\rm r}$. The column density of molecules derived from a transition j to i is given by

$$N = \frac{8\pi}{(2j+1)c^2}\frac{kT_{\rm ex}}{hB}{\rm e}^{hBi(i+1)/kT_{\rm ex}}\frac{\nu_{ji}^2}{A_{ji}}\left(1-{\rm e}^{-h\nu_{ji}/kT_{\rm ex}}\right)^{-1}\int\tau(\nu_{ji})d\nu,$$

and since, from above,

$$\int\tau(\nu)d\nu \simeq \frac{1}{T_{\rm ex}}\int T_{\rm r}(\nu)d\nu = \frac{\nu}{cT_{\rm ex}}\int T_{\rm r}(V)dV,$$

the gas column density is given by

$$N = \frac{8\pi}{(2j+1)}\frac{\nu_{ji}^3}{c^3}\frac{k}{hB}{\rm e}^{hBi(i+1)/kT_{\rm ex}}\frac{1}{A_{ji}}\frac{\int T_{\rm r}(V)dV}{\left(1-{\rm e}^{-h\nu_{ji}/kT_{\rm ex}}\right)}. \tag{C.14}$$

Note that, for beam filling factors <1, i.e. for all extragalactic observations, this will be a beam-diluted column density and will in general be less than the true column density. Additional errors will be introduced by departures from LTE and the resulting inaccuracy of the assumed partition function, i.e. if not all the levels can be described by a single excitation temperature.

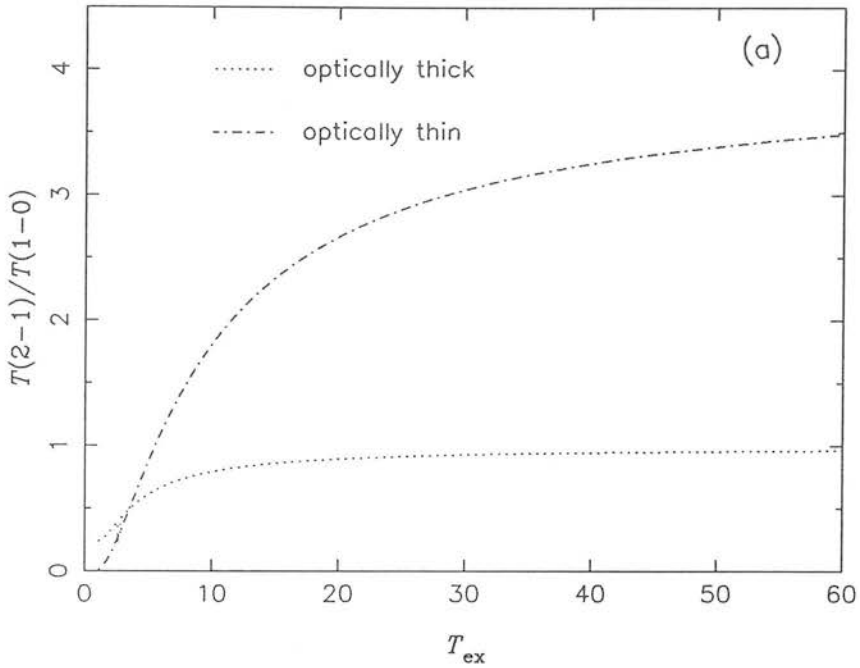

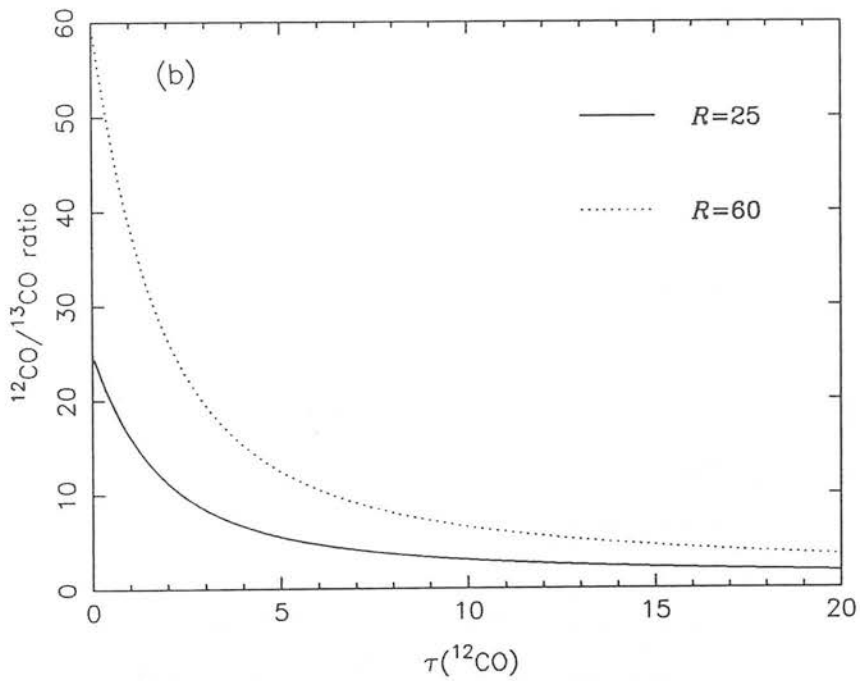

Figure C.1: (a) The ^{12}CO J=2–1/J=1–0 antenna temperature ratio as a function of excitation temperature for optically thick (dotted line) and optically thin (dot–dashed line) gas. (b) The ^{12}CO/^{13}CO antenna temperature ratio as a function of τ for values of R=25 and 60.

Appendix D

A model of extragalactic CO line profiles

This appendix describes a very simple model of a rotating disc galaxy which will enable, for a given rotation curve, the prediction of linewidths to be expected purely from the broadening effects of rotation and a finite beamsize.

The galaxy is modelled as a thin rotating disc inclined at an angle i to the line of sight, with the inclination angle and the equation of the galaxy rotation curve specified. The galaxy is then 'observed' with a Gaussian beam. Beam offsets are measured, with respect to the dynamical centre, along the apparent major and minor axes of the galaxy. The y-coordinate is deprojected from the galactic inclination (Fig. D.1), via

$$y_{\rm true} = y/\cos i. \tag{D.1}$$

The beam area on the galaxy is divided into a grid of several hundred pixels, with the size of the grid chosen such that the Gaussian beam weighting at the edge is very small. Thus it is ensured that most of the 'emission' is sampled. For each pixel in the grid, the true (inclination-corrected) distance from the dynamical centre of the galaxy is calculated. The input rotation curve then gives the rotational velocity for that pixel. This can be transformed to the velocity along the line of sight, via:

$$V_{\rm LSR}({\rm observed}) = V_{\rm rot}\,\sin i\,\cos\alpha, \tag{D.2}$$

where α is the angle between the direction of motion and the line of sight projected into the plane of the galaxy (Fig. D.1) Each pixel as a whole also has a spatial Gaussian weighting according to its position in the beam:

$$B \propto {\rm e}^{-4\ln 2\,(x_{\rm off}^2+y_{\rm off}^2)/\theta^2}, \tag{D.3}$$

where θ is the beam FWHM and $x_{\rm off}$, $y_{\rm off}$ the offsets of the pixel from the centre of the beam.

The results for each beam offset, from summing up all the weighted velocity contributions from all the pixels, are then plotted as a histogram of 'flux' against velocity in 5 km s^{-1} velocity bins (where the 'flux' is the number of pixels possessing velocities within each range). This is the 'line profile'.

As well as a specified rotational velocity around the galactic centre, each pixel may have assigned to it a 'velocity dispersion' intended to represent the internal velocity dispersion of a 'cloud' or 'cloud complex'. Each pixel is then considered to possess a Gaussian distribution of velocities about its galactic rotation velocity. This can be expressed as a Gaussian weighting:

$$f(v) = {\rm e}^{-4\ln 2\,(v-V_{\rm rot})^2/w^2}, \tag{D.4}$$

where w is the FWHM of the velocity dispersion, and $V_{\rm rot}$ is the rotational velocity (Fig. D.2) In this case, each pixel contributes flux in a range of velocity bins, with a weighting given by the above equation.

For a heavily obscured galaxy such as Maffei 2, where optical observations are very difficult, it is possible that the inclination of the disc will not be very accurately known. This will introduce an error into the modelled linewidths. To check the significance of this source of uncertainty, the model presented in Chapter 5 (involving an inclination of 65°) was rerun with an inclination of 85°, i.e. almost edge-on. This made very little difference to the resultant line profiles. From the derivation presented in this Appendix, it can be seen that increasing the disc inclination will have several competing effects, which may partially cancel out.

(i) The true minor axis extent covered by a beam will increase as $1/\cos i$, from equation (D.1). This will introduce a small contribution, at large minor axis offsets, from the steeply rising central portion of the rotation curve. Likewise, near-nuclear positions will include, within the beam, regions on the flat outer rotation curve.

(ii) From equation (D.2), $\sin i$ will increase, thus increasing the component of the rotational velocity in the line of sight. At the same time, as $y_{\rm true}$ increases (equation D.1), the angle α will increase, leading to smaller $\cos\alpha$ and partially cancelling out the effects of increased $\sin i$.

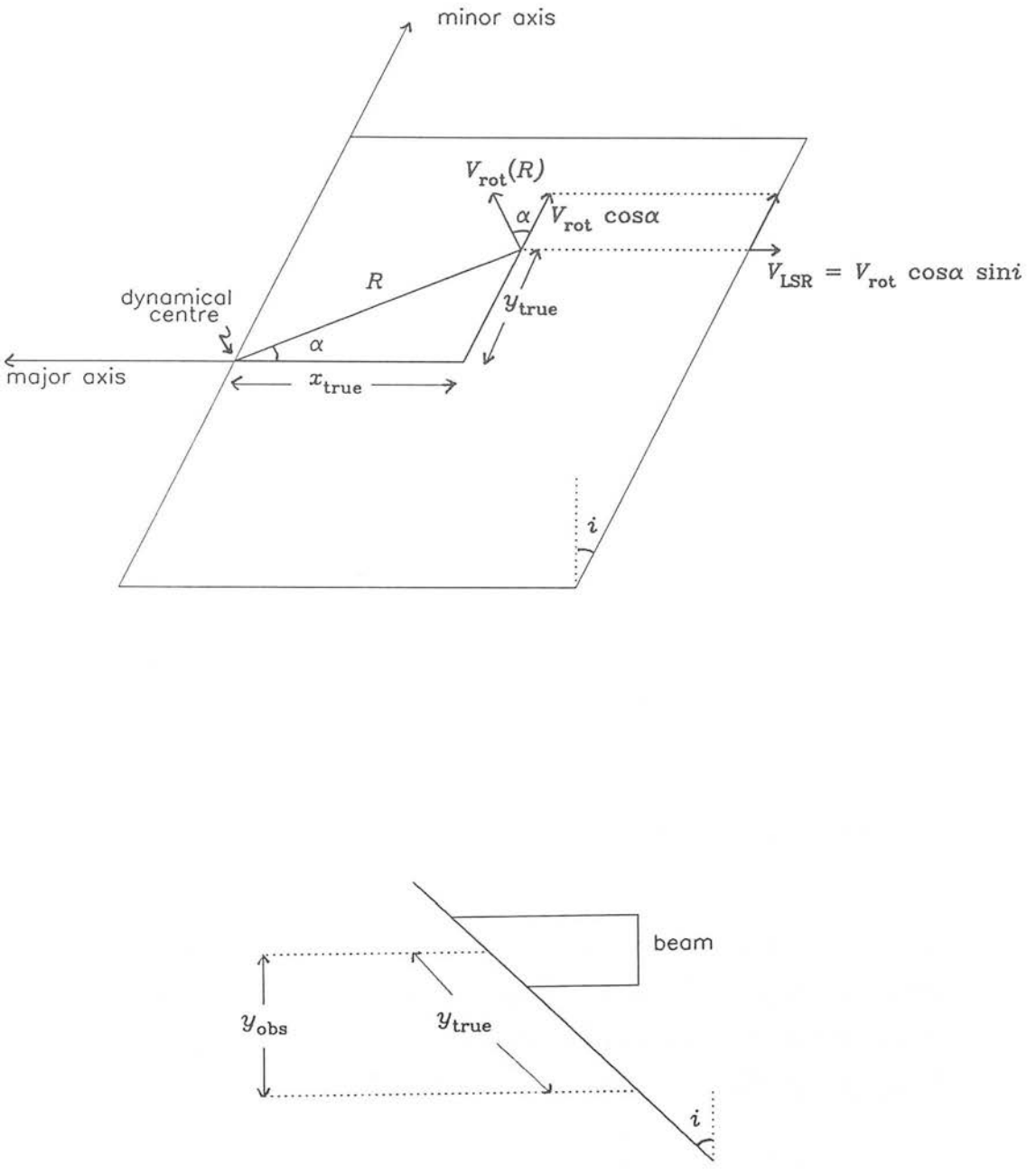

Figure D.1: Schematic illustration of the mathematical set-up for the rotating disc model of CO line profiles.

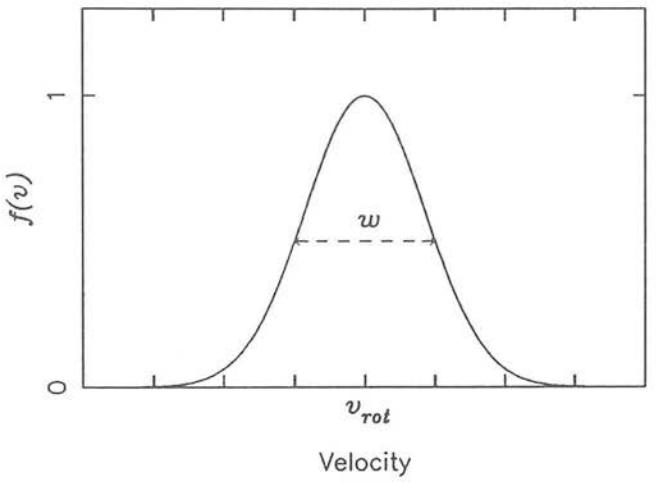

Figure D.2: Diagram illustrating a Gaussian distribution of velocities about the galactic rotation velocity.

In Chapter 5, the effect of uncertain inclination on the model results will be ignored. Consideration of the large-scale CO morphology (Section 5.3), as well as the appearance of a distinct spiral arm-like feature in red light and radio continuum (Spinrad *et al.* 1973; Seaquist, Pfund & Bignell 1976) suggest that the inclination has not been underestimated.

Appendix E

The rotation curve of a spherically symmetric massive core and low-density halo

Consider a galaxy composed of a constant-density, spherically symmetric core, and a spherically symmetric, much less dense halo, with density varying as some power-law function of radius. Let r_c = radius of core, ρ_c = density of core, and $\rho(r) = \rho_0(\frac{r}{r_0})^{-2}$ = density of halo. At any radius r, the velocity of a test particle, $v(r)$, is obtained by equating the gravitational and centrifugal forces:

$$\frac{GM(r)}{r} = v(r)^2, \tag{E.1}$$

where $M(r)$ is the mass contained within r. $M(r)$ is determined by dividing the galaxy into concentric shells of radius r and thickness dr. Then the mass within a shell is given by

$$dM(r) = 4\pi\, r^2\, \rho(r)\, dr,$$

and the total mass is obtained by integrating over all the shells.

(i) For $r < r_c$:

$$M(r) = \int_0^r dM(r) = \int_0^r 4\pi\, r^2 \rho_c\, dr = \frac{4\pi}{3}\, \rho_c\, r^3.$$

Hence

$$v(r) = \left(\frac{4\pi}{3}\, \rho_c\right)^{1/2} (G)^{1/2}\ r, \tag{E.2}$$

This is rigid, solid-body rotation [$v(r) \propto r$], as is observed in the centre of Maffei 2 and many other spiral galaxies (e.g. Nakai *et al.* 1987; Chapter 5).

(ii) For $r > r_c$:

$$\begin{aligned} M(r) &= \int_0^r dM(r) = \int_0^{r_c} 4\pi\, r^2 \underbrace{\rho_c}\, dr + \int_{r_c}^r 4\pi\, r^2\, \rho_0\, r_0^{\alpha}\, r^{-\alpha}\, dr \\ &= \frac{4\pi}{3}\, r_c^3\, \rho_c + \frac{4\pi\, \rho_0\, r_0^{\alpha}}{3-\alpha}\, (r^{3-\alpha} - r_c^{3-\alpha}). \end{aligned}$$

Letting $A = 3\,\rho_0\, r_0^{\alpha}/(3-\alpha)$, one has

$$v(r)^2 = \frac{G\,M(r)}{r} = \frac{4\pi}{3}\, G\, r_c^3\, (\rho_c - A\, r_c^{-\alpha})\, \frac{1}{r} + \frac{4\pi}{3}\, A\, G\, r^{2-\alpha},$$

or

$$\frac{v(r)^2\, r}{G} = \frac{4\pi}{3}\, r_c^3\, (\rho_c - \mathrm{A}\, r_c^{-\alpha}) + \frac{4\pi}{3}\, A\, r^{3-\alpha}. \qquad \text{(E.3)}$$

For any given value of α, this equation is linear in r and so in principle one can use the method of least-squares fitting (minimization of χ^2) to fit the data and solve for r_c, ρ_c, α and A. In practice, however, the data were too few and the errors too large to constrain a fit to four parameters. The values of r_c, ρ_c and α were therefore fixed (Section 5.5), and A fitted.

Appendix F

Published Papers

Copies of the following papers are included here:

Smith, P.A., Brand, P.W.J.L., Puxley, P.J., Mountain, C.M. & Nakai, N., 1990. *Mon. Not. R. astr. Soc.*, **243**, 97.

Smith, P.A., Brand, P.W.J.L., Mountain, C.M., Puxley, P.J. & Nakai, N., 1991. *Mon. Not. R. astr. Soc.*, **252**, 6P.

The material included in Chapter 2 has also been published in the following conference proceedings:

Smith *et al.* 1990. *The Interstellar Medium in External Galaxies*, p. 81, eds Hollenbach, D.J. & Thronson, H.A., NASA CP-3084.

Smith 1989. *The XXII YERAC Conference, Kharkov* (abstract).

In addition, the following paper has been submitted for publication in *Mon. Not. R. astr. Soc.*,, including JCMT data taken by Tim Hawarden during my December 1988 observing run, reduced and partially interpreted by myself:

Hawarden, T., Sandell, G., Matthews, H.E., Friberg, P., Watt, G.D. & Smith, P.A., 1992. *Mon. Not. R. astr. Soc.*, submitted.

Mon. Not. R. astr. Soc. (1990) 243, 97–102

A 450-μm continuum map of M82: comparison with the CO emission

R. A. Smith, P. W. J. L. Brand and P. J. Puxley*
University of Edinburgh, Department of Astronomy, Blackford Hill, Edinburgh EH9 3HJ

C. M. Mountain
Royal Observatory, Blackford Hill, Edinburgh EH9 3HJ

N. Nakai
Nobeyama Radio Observatory, Nobeyama, Minamisaku Nagano 384-13, Japan

Accepted 1989 August 23. Received 1989 August 23; in original form 1989 April 13

SUMMARY

We have mapped the 450-μm dust continuum emission from the central 40×40 arcsec region of M82, and find that the total mass of gas in this region is $\simeq 2 \times 10^8$ $M_\odot$. The 450-μm map has one peak, in contrast to existing ^{12}CO maps which show two distinct peaks. The difference in structure between the two maps is probably due to the sensitivity of CO and dust emission to the physical and excitation conditions in molecular clouds. In particular, ^{12}CO and ^{13}CO observations suggest significant optical depth variations across the galaxy, and the intense UV field in the central 'starburst' region implies the existence of photodissociation regions from which the CO emission may originate. We conclude that the ^{12}CO and sub-millimetre emission cannot both be reliable tracers of molecular hydrogen in the extreme environments of starburst galaxies, and advise caution when using conversion factors determined in the Milky Way to find the H_2 mass in extragalactic molecular clouds.

INTRODUCTION

An important step towards an understanding of the global processes of star formation in galaxies is the ability to determine accurately the mass of available material in molecular clouds. Unfortunately the major constituent, H_2, is difficult to detect directly, and so it is necessary to observe a tracer to calculate the molecular hydrogen column density $N(H_2)$. The $J=1-0$ rotational line of ^{12}CO is commonly employed. Under the assumption that the ^{12}CO emission is optically thick, as is nearly always the case in galactic clouds (e.g. Lada 1985), and with excitation temperature $T_{ex} \simeq 10$ K, $N(H_2)$ follows from the ^{12}CO integrated intensity via $N(H_2)$ $(cm^{-2}) = 4 \times 10^{20}$ I_{CO} (K km s^{-1}) (Young & Scoville 1982). However, doubts have arisen over the constancy of this conversion factor, particularly in so-called 'starburst' galaxies where the presence of large numbers of hot young stars may invalidate the principal assumptions of optically thick ^{12}CO and $T_{ex} \simeq 10$ K. An alternative method of H_2 mass determination is to observe the sub-millimetre continuum emission due to re-radiation by dust grains, at characteristic temperatures $\sim 20-50$ K, of the stellar UV, and convert to gas mass via the ratio $N(H_2)/\tau(\nu)$ where $\tau(\nu)$ is the continuum optical depth. The method has been discussed in detail by Hildebrand (1983) and Gear (1988). The sub-millimetre emission is usually optically thin, and so all the dust is sampled.

To study the applicability of these two methods to extragalactic star-forming regions, we have mapped the sub-millimetre dust continuum of M82, a nearby galaxy already extensively observed in CO. M82 is a 'classic' starburst galaxy, the bulk of its energy output being in the IR, with a far-IR luminosity of 3×10^{10} $L_\odot$ (Telesco & Harper 1980). The multiwavelength observations are consistent with an intense episode of star formation in the central 1 kpc, which started some 5×10^7 yr ago (Rieke *et al.* 1980). Radio observations reveal numerous supernova remnants within 300 pc of the nucleus (Kronberg, Biermann & Schwab 1985). Hα filaments and X-ray emission extend several kpc perpendicular to the galactic plane (Lynds & Sandage 1963; Watson, Stanger & Griffiths 1984; Kronberg *et al.* 1985). CO and H I maps show a double-lobed structure, which is interpreted as a rotating molecular ring, 400 pc in diameter, enclosing the central starburst, with molecular and ionized gas being driven out of the galactic plane by the associated stellar winds and supernovae (Weliachew, Fomalont & Greisen 1984; Lo *et al.* 1987; Nakai *et al.* 1987). In contrast to galactic molecular clouds, ^{12}CO $J=2-1/J=1-0$ antenna temperature ratios and ^{12}CO $J=1-0/^{13}$CO $J=1-0$ integrated intensity ratios suggest that the CO in the central

*Present address: Institute for Astronomy, University of Hawaii, 2680 Woodlawn Drive, Honolulu, Hawaii 96822, USA.

regions of M82 is optically thin, perhaps in the form of small (few pc) hot (40 K), $6 \times 10^3\ M_\odot$ clouds, quite unlike the giant molecular clouds (40 pc, 10 K, $5 \times 10^5\ M_\odot$) in the Milky Way (Knapp *et al.* 1980; Sofue 1988; Stark & Carlson 1982; Young & Scoville 1984; Nakai *et al.* 1987).

2 OBSERVATIONS

The central 40×40 arcsec of M82 was mapped at 450 μm in the dust continuum on the night of 1988 March 20, using the James Clerk Maxwell Telescope (JCMT) on Mauna Kea, Hawaii, and the common-user bolometer system UKT14 (filter width $\Delta\lambda \simeq 54$ μm at 450 μm). The beamsize at 450 μm was 13 arcsec (not diffraction limited, owing to the lower dish quality and pointing precision then available on the recently commissioned JCMT). We mapped a fully sampled 7×7 grid, spaced at 6.5 arcsec and oriented along the major axis which lies at position angle PA = 65° (Nilson 1973). Using observations of the 450-μm peak at two different airmasses, the data were transformed out of the atmosphere with a zenith extinction coefficient $\tau(\mathrm{atm}) = 1.5$, taking account of the variation in airmass over the maps, which were then reduced and co-added using the continuum reduction software package NOD2 (Haslam 1974). The central pixel of the map was determined by peaking up on M82 at 800 μm. The 800-μm continuum peak is within 5 arcsec of the 2.2-μm peak (Hughes, Gear & Robson, in preparation), at RA(1950) = $09^h51^m43\overset{s}{.}47$, Dec(1950) = 69° 55′ 00″.3 (Pipher *et al.* 1987). Pointing was checked by means of five-point scans before and after each map. It was found that the second map was shifted by $\simeq 7$ arcsec with respect to the first, along the minor axis, and this offset was corrected before the maps were added. The estimated positional uncertainty of the map is therefore 7 arcsec. 450-μm photometry of M82 from the night of 1988 February 6 (Hughes *et al.*, in preparation) was used to scale up the integrated flux from our map. In a 13-arcsec beam centred at the peak, the 450-μm flux density is 15.5 ± 5 Jy.

3 RESULTS

The 450-μm map is presented in Fig. 1(a). Fig. 1(b), to the same scale, shows the ^{12}CO $J = 1$–0 interferometer map of Lo *et al.* (1987). It is immediately obvious that there is a morphological difference between the two maps. While in the CO map there are two distinct peaks, 25 arcsec apart, situated asymmetrically either side of the dynamical (and 2-μm) nucleus, our 450-μm map has only one peak, to the south-west of the nucleus, with an extension to the north-east. Before considering physical reasons for the apparent absence of a second peak, it is necessary to check the telescope pointing – could we have missed the second peak entirely? This seems unlikely. Both 100- and 40-μm profiles along the major axis (Joy, Lester & Harvey 1987) and a new 800-μm map (Hughes *et al.*, in preparation) show similar, single-peak structures. The centre of our map – the 800-μm peak – is within 5 arcsec of the 2.2-μm nucleus. The positional accuracy of our map is $\simeq 7$ arcsec, and there was good agreement between our two maps in the position on the major axis of the 450-μm peak. From physical considerations – at 450- and 800-μm we are approaching the Rayleigh–Jeans tail for characteristic dust temperatures

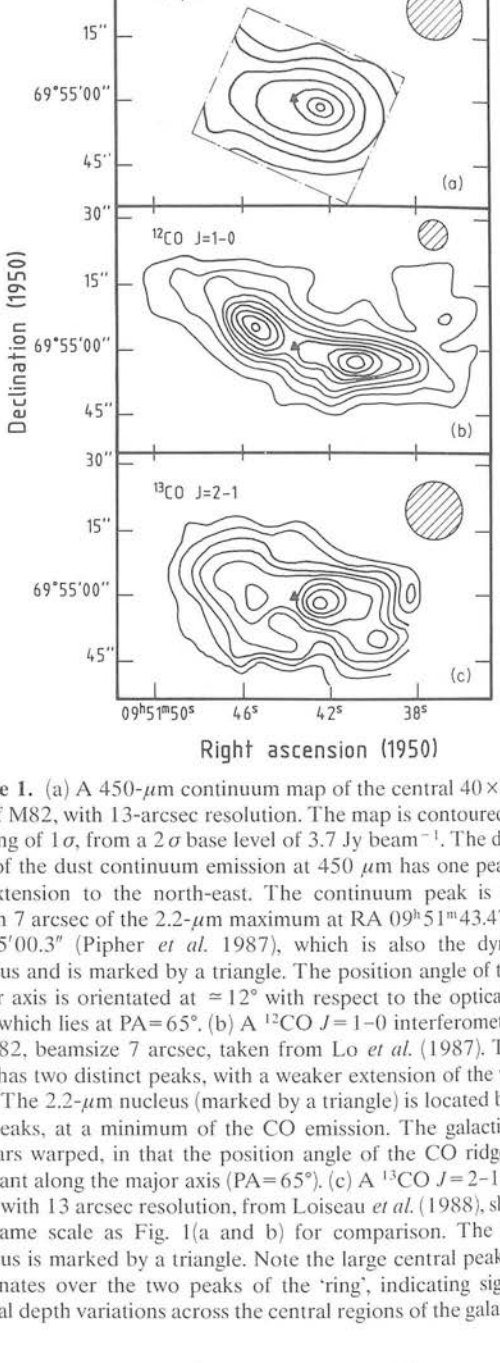

Figure 1. (a) A 450-μm continuum map of the central 40×40 arcsec of M82, with 13-arcsec resolution. The map is contoured with a spacing of 1σ, from a 2σ base level of 3.7 Jy beam^{-1}. The distribution of the dust continuum emission at 450 μm has one peak, with an extension to the north-east. The continuum peak is located within 7 arcsec of the 2.2-μm maximum at RA $09^h51^m43.47^s$, Dec. 69°55′00.3″ (Pipher *et al.* 1987), which is also the dynamical nucleus and is marked by a triangle. The position angle of the dust major axis is orientated at $\simeq 12°$ with respect to the optical major axis, which lies at PA = 65°. (b) A ^{12}CO $J = 1$–0 interferometer map of M82, beamsize 7 arcsec, taken from Lo *et al.* (1987). The CO map has two distinct peaks, with a weaker extension of the western lobe. The 2.2-μm nucleus (marked by a triangle) is located between the peaks, at a minimum of the CO emission. The galactic plane appears warped, in that the position angle of the CO ridge is not constant along the major axis (PA = 65°). (c) A ^{13}CO $J = 2$–1 map of M82 with 13 arcsec resolution, from Loiseau *et al.* (1988), shown to the same scale as Fig. 1(a and b) for comparison. The 2.2-μm nucleus is marked by a triangle. Note the large central peak, which dominates over the two peaks of the 'ring', indicating significant optical depth variations across the central regions of the galaxy.

($\simeq 30$–45 K, see below) – it seems reasonable to assume that the emission at the two wavelengths comes from similar material. For these reasons, we place the peak of our map within $\simeq 7$ arcsec of the 2.2-μm peak – i.e. interior to the CO ring. It is also unlikely that we are seeing two unresolved peaks. Our resolution is comparable to that of the IRAM ^{12}CO $J = 2$–1 map (13 arcsec at 230 GHz – Loiseau *et al.* 1990), and better than that of the ^{12}CO $J = 1$–0 Nobeyama map (16 arcsec – Nakai *et al.* 1987), in which two maxima are clearly seen. If there are two continuum peaks, we should expect to resolve them.

The position angle of the dust major axis is orientated at $\simeq 12°$ to the optical major axis, as has also been observed in

...e ^{12}CO $J=1-0$ maps of Olofsson & Rydbeck (1984) and ...kai *et al.* (1987).

Integrating up the emission from our calibrated map gives ... total flux density of $F(450\ \mu m)=49\pm21$ Jy over our ...)×40 arcsec grid, where the quoted error is due to uncer...inty in the 450-μm photometry and in the relative locations ...f the 450-μm photometric aperture and map peak. Neither ...nchrotron (*cf.* Klein, Wielebinski & Morsi 1988) nor ...remsstrahlung [$S(450\ \mu m)\sim0.5$ Jy, Puxley *et al.* 1989] pro...sses contribute significantly to the integrated emission at ...is wavelength.

...1 Gas mass

...he physics of emission from dust grains has been discussed ...detail by Hildebrand (1983), and the advantages of using ...b-millimetre observations to derive gas masses convinc...gly argued by Thronson (1987). Gear (1988) points out ...at, rather than assuming a uniform source brightness dis...ibution and top hat beam profile, as Hildebrand does, it is ...ore realistic to assume Gaussian source and beam profiles, ...us introducing a correction into Hildebrand's formulae. We ...ill use Gear's equations in this paper.

The dust continuum optical depth is given by

$$...(\nu)=5.42\times10^{-16}[(\theta_s^2+\theta_b^2)/\theta_s^2\theta_b^2][S(\nu)/B(\nu,T)], \qquad (1)$$

...here θ_s and θ_b are the FWHM (arcsec) of the source and ...eam profiles, respectively, $S(\nu)$ is the flux density into a ...eam centred on the peak of the source (Jy per beam), and ...ν, T) is the blackbody intensity at frequency ν and dust ...mperature T.

The determination of a reliable dust temperature depends ...n being able to fit the far-IR spectrum of the source to a ...odified blackbody function of the form $\nu^\beta B(\nu, T)$ (assum...g optically thin emission), where β is the frequency ...pendence of the dust emissivity. The value of β is believed ...increase from $\simeq1$ at 50 $\mu m\leq\lambda\leq250$ μm to $\beta\geq2$ by $\lambda\sim$ ...000 μm (Hildebrand 1983), but its exact variation with fre...uency is not well known. Clearly, the derived dust ...mperature depends on the value of β adopted. In general, β ...rying between 1 and 2 leads to an uncertainty of ~30 per ...nt in the dust temperature (Thronson *et al.* 1989). In addi...on, it is not normally possible to fit the whole far-IR spec...um to a single temperature – usually only the long ...avelength end can be fitted, while there is an excess of emis...on at the shorter wavelengths indicative of hotter regions ...ithin the source (Gear 1988). It must be borne in mind that, ...r a composite object such as a galaxy, any derived tempera...re will only be an average over the system (Thronson *et al.* ...987).

Telesco & Harper (1980) and Klein *et al.* (1988) both fit a ...$^{1.5}$ $B(\nu, T)$ function to the far-IR spectrum of M82, for ...≥30–40 μm, deducing a dust temperature of 45 K. Simi...rly, Hughes *et al.* (1989) obtain a best-fit to the 40–1300 ...m spectrum, including new data at 800 and 1100 μm, of ...=1.5 and $T=47$ K, while Thronson *et al.* (1987) adopt a ...mperature of 30±10 K from a $\beta=2$ fit to the far-IR data. ...e will use here a $\beta=1.5$ emissivity law, and a correspond...g dust temperature of 47 K, from the work of Hughes *et al.*, ...though a fit to $\nu^{1.5}$ $B(\nu, T)$ could be mimicked by an emis...ivity law varying smoothly from $\beta=1-2$ towards longer ...avelengths (Gear *et al.* 1986). Our data are not of sufficient signal-to-noise to attempt an accurate temperature profile, although the similarity of our map to the 100-μm slice of Joy *et al.* (1987), and direct ratioing of the 100- and 40-μm profiles lead us to conclude that the temperature does not vary by more than about ±5 K over the central regions of the galaxy.

The hydrogen column density can be calculated from

$$N(H+H_2)=1.2\times10^{25}[750/\nu]^\beta\tau(\nu)\ \text{atoms cm}^{-2} \qquad (2)$$

(Hildebrand 1983), where ν is in GHz. The total mass of gas in the source is then

$$M_g=M(H+H_2)=2.7\times10^{-19}N(H+H_2)(\theta_s D)^2\ M_\odot, \qquad (3)$$

where D is the distance to the source in Mpc. Equation (3) includes a factor $\simeq1.36$ to allow for helium and other heavy elements (Hildebrand 1983). In the case of M82, molecular hydrogen dominates over atomic hydrogen in the central 1 kpc (e.g. Lugten *et al.* 1986) and so M_g closely approximates the mass of molecular hydrogen in the inner regions of the Galaxy.

The main sources of uncertainty in deriving the mass can now be clearly seen, namely, the assumed values of dust temperature and $N(H+H_2)/\tau(\nu)$. We have adopted the value of $N(H+H_2)/\tau(\nu)$ given by Hildebrand (1983), of 1.2×10^{25} atoms cm^{-2} at 400 μm, which is derived from the work of Whitcomb *et al.* (1981) on the far-IR properties of dust grains. The reliability of this number reflects the accuracy to which gas and dust parameters are known, which Thronson *et al.* (1987) estimate to be a factor of ~5 in the galactic disc. Thronson (1987) plots a number of theoretically and experimentally derived values of the ratio and finds it to be constant, within a factor of $\simeq3$, for a variety of galactic objects, although it may scale inversely with metallicity (Thronson *et al.* 1988).

The dust optical depth, hydrogen column density and total gas mass can now be calculated. Fitting a two-dimensional Gaussian profile to our data gives a map FWHM (beam convolved with source) of 28×16 arcsec. Then, using the 450-μm flux density of 15.5±5 Jy in a 13-arcsec beam and taking $T=47$ K, equation (1) gives a value for the dust optical depth of 0.02 at 450 μm, consistent with our initial assumption that the sub-millimetre emission is optically thin. Adopting $\beta=1.5$ gives a hydrogen column density $N(H+H_2)=2.6\times10^{23}$ atoms cm^{-2} from equation (2). We take the distance to M82 to be 3.25 Mpc (Tammann & Sandage 1968), leading finally to a total gas mass $M_g=(2.0\pm0.8)\times10^8\ M_\odot$, where the quoted error reflects the uncertainties in the 450-μm flux density and fitted source size. Adoption of a ν^2 emissivity law and corresponding temperature of 30 K would increase the derived mass by a factor of 2.1 to $(4.2\pm1.8)\times10^8\ M_\odot$. Of this total gas mass, atomic hydrogen contributes only about $0.1\times10^8\ M_\odot$ in the central 1 kpc (Weliachew *et al.* 1984).

Our derived mass is consistent, within the accuracy of the technique, with previous estimates from sub-millimetre data. Thronson *et al.* (1988) calculate a mass of $3\times10^8\ M_\odot$ from a 1.3 mm flux of 0.9 Jy and an adopted dust temperature of 30 K. They propose that this mass is perhaps a factor of 3 too high, suggesting that the analysis of O'Connell & Mangano (1978) indicates a metallicity in M82 two to three times that in the solar neighbourhood. However, other work has suggested values of heavy element abundances which are close

to solar (Willner *et al.* 1977, Puxley *et al.* 1989). Jaffe, Becklin & Hildebrand (1984a) calculate a mass of 8×10^7 $M_\odot$ from a large-beam 400-μm flux of 30 Jy and dust temperature of 45 K. Olofsson & Rydbeck (1984) and Lo *et al.* (1987) both obtain an H_2 mass of 6×10^7 $M_\odot$ from ^{12}CO $J=1-0$ data, assuming optically thin emission. Under the same assumption, Nakai *et al.* (1987) derive a mass of 1.1×10^8 $M_\odot$ in the central 1.5 arcmin from their ^{12}CO $J=1-0$ map. Assumption of optically thick CO and application of a 'constant conversion factor' leads to a mass an order of magnitude higher than in the optically thin case (Nakai *et al.* 1987).

4 DISCUSSION

The difference in structure between the Co and sub-millimetre maps is surprising if, as is commonly assumed, the CO and dust continuum are both reliable tracers of the molecular hydrogen. As molecular hydrogen forms on dust grains, we can expect to find dust mixed with the H_2. On the other hand, the association of H_2 with CO is one of the cornerstones of the CO technique of mass determination. Our 450-μm map is similar in its morphology to both the 100- and 800-μm data, and intermediate-resolution radio observations, while the double-lobed structure of CO is repeated in H I, HCN and HCO^+ maps (Seaquist, Bell & Bignell 1985; Weliachew *et al.* 1984; Carlstrom 1988).

The peak of the 100-μm emission coincides with a region of particularly vigorous star formation ~10 arcsec south-west of the nucleus, displaying recombination lines from H II regions, OH masers, and a bright, non-thermal radio source associated with the supernova remnant 41.9+58 (Weliachew *et al.* 1984; Seaquist *et al.* 1985; Kronberg, Biermann & Schwab 1981, 1985; Joy *et al.* 1987). A weak ^{12}CO 1–0 feature is seen in the interferometer map between the nucleus and the western lobe, and an extension of the western peak of H I, as well as peaks of the HCN and ^{13}CO $J=2-1$ emission are coincident with this area, leading to speculation on the presence of a 'giant molecular clump' in the vicinity of the star formation region (Weliachew *et al.* 1984; Lo *et al.* 1987; Carlstrom 1988; Loiseau *et al.* 1988).

A possible explanation of the differing structures then, is that the two lobes are present in dust but are 'swamped' by sub-millimetre emission from the giant star-forming region. The blackbody flux from a population of N spherical dust grains, radius a, at distance D, is given by

$$F(\nu)=N\pi(a/D)^2\,Q(\nu)\,B(\nu,T) \qquad (4)$$

(Hildebrand 1983), where $Q(\nu)$ is the emissivity of the grains at frequency ν. Thus flux density is proportional to the number of grains, which is equivalent to the amount of H_2 assuming a constant gas–dust ratio, and varies with temperature; for $\lambda\sim450$ μm, $B(\nu,T)$ can be approximated by $B(\nu,T)\propto T^{1.6}$, to within an accuracy of 10 per cent, for $T=20-60$ K (e.g. Jaffe *et al.* 1984b). An increase in temperature by approximately a factor of 1.5 from 47 K, or a two-fold increase in dust column density would be needed to 'fill in' the central depression suggested by the CO map of Lo *et al.* (1987). As stated before, we infer no temperature variations of this magnitude across M82, and since the emission is optically thin, we are seeing all the dust. We therefore believe it likely that the sub-millimetre emission from M82 is tracing predominantly column density variations across the central regions of the galaxy.

If the sub-millimetre emission can be assumed to be accurately following the column density of H_2 across M82, then it is apparent that some process must be enhancing the ^{12}CO emission in the lobes or depressing it in the interior regions. The CO emission from M82 is highly complex. Although the double-lobed structure apparent in ^{12}CO $J=1-0$ and $J=2-1$ maps (Lo *et al.* 1987; Nakai *et al.* 1987; Loiseau *et al.* 1989) has been widely interpreted as representing a rotating molecular ring, the velocity structure of the CO is disturbed, and, it has been argued, not consistent with a simply rotating disc or torus. The structural minor axis is not aligned with the axis of rotation, and the galactic plane appears warped (Lo *et al.* 1987).

The integrated intensity of CO emission, I_{CO}, is highly sensitive to changes in the physical and excitation conditions of molecular clouds, such as gas number density, metallicity, optical depth and excitation temperature, and such variations must be taken into account when deriving H_2 masses by this method.

(i) Gas number density, n: for optically thick ^{12}CO emission, Maloney & Black (1988) find that $I_{CO}\propto n^{1/2}$, thus application of a 'constant' conversion factor to extragalactic molecular clouds will not give a reliable indication of the H_2 mass if those clouds differ from the ($n\simeq200\mathrm{cm}^{-3}$) norm.

(ii) Heavy element abundance: I_{CO} increases with increasing metallicity, although, as stated earlier, the heavy element abundance in M82 may not differ significantly from solar neighbourhood values.

(iii) Optical depth: ^{12}CO $J=1-0$ emission is almost always optically thick in galactic molecular clouds (e.g. Lada 1985). In the case of M82, however, large-beam observations give ^{12}CO $J=2-1/J=1-0$ antenna temperature ratios of $\simeq2-3.5$, and ^{12}CO $J=1-0/^{13}$CO $J=1-0$ integrated intensity ratios of $\simeq20-30$ suggest that the ^{12}CO in the central regions is at least partially optically thin (Knapp *et al.* 1980; Sofue 1988; Young & Scoville 1984; Stark & Carlson 1982). If the ^{12}CO emission was optically thin throughout the central region of M82, then we would be seeing all the gas, the ^{12}CO emission, like the dust, would be tracing molecular hydrogen column density, and the sub-millimetre and ^{12}CO maps should show similar structure. Clearly this is not the case. The recently published ^{13}CO $J=2-1$ map (Fig. 1c) of Loiseau *et al.* (1988) shows a large central peak, coincident in position and velocity with the active south-western star-forming region, which dominates over the two peaks of the 'ring'. As ^{13}CO $J=2-1$ emission is nearly always optically thin, the ^{12}CO $J=2-1/^{13}$CO $J=2-1$ antenna temperature ratio is a good tracer of changes in ^{12}CO optical depth. The ratio at the central peak of the ^{13}CO $J=2-1$ map is 6.8, compared to 9–25 over the rest of the map, implying that the ^{12}CO optical depth varies across the central regions of M82 (Loiseau *et al.* 1988). We must therefore consider ^{12}CO optical depth variations as a likely cause of the differing CO and sub-millimetre structures, although other effects may also contribute.

(iv) Excitation temperature, T_{ex}: for optically thick CO emission, $I_{CO}\propto T_{ex}$ (Maloney & Black 1988), while in the optically thin case, for $h\nu\ll kT_{ex}$, $I_{CO}\propto1/T_{ex}$ (Jaffe *et al.* 1984b). In addition, antenna temperature ratios in regions

with an excitation temperature gradient can be very different from those resulting from a region at uniform temperature (Cantó, Rodríguez & Anglada 1987). Knowledge of the gas excitation temperature and optical depth is therefore vital for correct interpretation of CO data and line ratios. One factor, which could have a marked effect on the gas temperature and hence the CO emission, is the presence of intense UV radiation fields. Recent H53α measurements of the central region of M82 imply an ionization rate of 1.1×10^{54} Lyman continuum photons per second (Puxley *et al.* 1989). Assuming that these photons are produced by B0 stars with an effective temperature $\simeq 31\,000$ K, this translates to $\simeq 5 \times 10^6$ B0 stars in the central region of M82 (Panagia 1973), with a resulting UV field $\geq 10^3$ times that in the solar neighbourhood (Maloney & Black 1988). In such intense UV fields, the CO emission may originate from the warm (100 K), dense (10^3 cm^{-3}) photodissociation regions at the boundary between H II regions and molecular clouds, which have been extensively modelled by Tielens & Hollenbach (1985). In these regions, illuminated either from within by embedded stars or from outside by galactic UV fields, grain photoelectric ejection is the dominant heating mechanism, and the gas temperature far exceeds the dust temperature. The dust emission, on the other hand, is largely independent of the UV field strength (Thronson 1988). The existence of photodissociation regions in M82 is implied by the detection of the 158-μm [C II] line which arises in such interface zones, and has the same spatial distribution and velocity structure as the ^{12}CO $J = 1-0$ line (Crawford *et al.* 1985). Maloney & Black (1988) suggest further that the anomalously high ^{12}CO $J = 2-1/J = 1-0$ antenna temperature ratios can be explained in terms of emission from photodissociation regions.

5 CONCLUSIONS

We have presented new high-resolution observations of M82 at 450 μm in the dust continuum. Our map of the central 40×40 arcsec shows distinct structural differences from the CO maps of the same region. Whereas the CO maps show a double-peaked structure believed to represent a 200 pc nuclear molecular ring, our 450-μm observations show one peak only. We believe that the difference is real, and not a result of insufficient resolution or poor pointing. We place the 450-μm peak within 7 arcsec of the 2.2-μm nucleus – interior to the CO 'ring'. The 450-μm emission is optically thin, and the integrated flux density over the map is 49 ± 21 Jy. Adoption of a dust temperature of 47 K results in a derived H_2 mass of 2.0×10^8 $M_\odot$, which increases by a factor of 2.1 if a lower dust temperature (30 K) is used. This is similar to previous estimates from sub-millimetre and CO observations, although assumption of optically thick ^{12}CO and corresponding 'constant conversion factor' leads to a somewhat higher derived mass.

The sub-millimetre and CO data cannot both be considered to be reliable tracers of molecular hydrogen. It is possible that a double-peaked dust structure is being 'swamped' by enhanced emission from a large star formation region south-west of the nucleus. However, due to the similarity of our 450-μm map to the 100-μm slice, and by direct comparison of the 100- and 40-μm profiles, we conclude that there are no large dust temperature gradients across M82; hence we expect the dust emission to trace column density variations only. We therefore consider it more likely that some effect is enhancing the CO emission in the lobes or depressing it in the inner regions. The CO emission in M82 is very complex and the integrated intensity is sensitive to changes in gas number density, metallicity, optical depth and excitation temperature. Although data on heavy element abundances suggest that the metallicity of M82 is close to solar, gas number density variations may render unreliable the standard $N(H_2)/I_{CO}$ conversion factor as applied to extragalactic molecular clouds. In addition, we consider it likely that a combination of optical depth variations and excitation temperature gradients are a major cause of the differing structures. Observations of the ^{13}CO $J = 2-1$ transition, a reliable tracer of the ^{12}CO optical depth, indicate significant variations of $\tau(^{12}CO)$ across the Galaxy. The intense UV flux in the central starburst region of M82 ($\geq 10^3 \times$ solar neighbourhood value) and the detection of [C II] 158-μm emission lead us to believe that the CO may originate in warm, dense photodissociation regions at the interface between H II regions and molecular clouds, where the gas temperature greatly exceeds the dust temperature.

We therefore believe that CO data must be treated with caution when applied to the extreme environments of vigorous extragalactic star formation regions, and that the effects on the CO emission of such parameters as optical depth and excitation temperature must be thoroughly investigated if CO lines are to be reliably used to trace the molecular gas content of extragalactic systems.

ACKNOWLEDGMENTS

We thank the staff of the Joint Astronomy Centre in Hilo for their technical support both during and after our observing run, and PATT for the allocation of JCMT telescope time. David Hughes kindly supplied us with the 800-μm peak position and 450-μm flux, and let us see the unpublished 800-μm map. We are grateful to Bill Dent and Walter Gear for helpful discussions and comments on the manuscript. Marjorie Fretwell drew the diagrams. PAS and PJP acknowledge SERC studentships.

The James Clerk Maxwell Telescope is operated by the Royal Observatory Edinburgh, on behalf of the Science and Engineering Research Council of the United Kingdom, the Netherlands Organization for Scientific Research and the National Research Council of Canada.

REFERENCES

Cantó, J., Rodríguez, L. F. & Anglada, G., 1987. *Astrophys. J.*, **321**, 877.

Carlstrom, J. E., 1988. *Galactic and Extragalactic Star Formation*, p. 571, eds Pudritz, R. E. & Fich, M., Kluwer, Dordrecht.

Crawford, M. K., Genzel, R., Townes, C. H. & Watson, D. M., 1985. *Astrophys. J.*, **291**, 755.

Gear, W. K., 1988. *Millimetre and Submillimetre Astronomy*, p. 307, eds Wolstencroft, R. D. & Burton, W. B., Kluwer, Dordrecht.

Gear, W. K., Gee, G., Robson, E. I., Ade, P. A. R. & Duncan, W. D., 1986. *Mon. Not. R. astr. Soc.*, **219**, 835.

Haslam, C. G. T., 1974. *Astr. Astrophys. Suppl.*, **15**, 333.

Hildebrand, R. H., 1983. *Q. Jl R. astr. Soc.*, **24**, 267.

Jaffe, D. T., Becklin, E. E. & Hildebrand, R. H., 1984a. *Astrophys. J.*, **285**, L31.

Jaffe, D. T., Hildebrand, R. H., Keene, J., Harper, D. A., Loewenstein, R. F. & Moran, J. M., 1984b. *Astrophys. J.*, **281,** 225.
Joy, M., Lester, D. F. & Harvey, P. M., 1987. *Astrophys. J.*, **319,** 314.
Klein, U., Wielebinski, R. & Morsi, H. W., 1988. *Astr. Astrophys.*, **190,** 41.
Knapp, G. R., Phillips, T. G., Huggins, P. J., Leighton, R. B. & Wannier, P. G., 1980. *Astrophys. J.*, **240,** 60.
Kronberg, P. P., Biermann, P. & Schwab, F. R., 1981. *Astrophys. J.*, **246,** 751.
Kronberg, P. P., Biermann, P. & Schwab, F. R., 1985. *Astrophys. J.*, **291,** 693.
Lada, C. J., 1985. *Ann. Rev. Astr. Astrophys.*, **23,** 267.
Lo, K. Y., Cheung, K. W., Masson, C. R., Phillips, T. G., Scott, S. L. & Woody, D. P., 1987. *Astrophys. J.*, **312,** 574.
Loiseau, N., Reuter, H.-P., Wielebinski, R. & Klein, U., 1988. *Astr. Astrophys.*, **200,** L1.
Loiseau, N., Nakai, N., Sofue, Y., Wielebinski, R., Reuter, H.-P. & Klein, U., 1990. *Astr. Astrophys.*, submitted.
Lugten, J. B., Watson, D. M., Crawford, M. K. & Genzel, R., 1986. *Astrophys. J.*, **311,** L51.
Lynds, C. R. & Sandage, A. R., 1963. *Astrophys. J.*, **137,** 1005.
Maloney, P. & Black, J. H., 1988. *Astrophys. J.*, **325,** 38.
Nakai, N., Hayashi, M., Handa, T., Sofue, Y., Hasegawa, T. & Sasaki, M., 1987. *Publs astr. Soc. Japan*, **39,** 685.
Nilson, P., 1973, *Uppsala astr. Obs. Ann.*, **6**.
O'Connell, R. W. & Mangano, J. J., 1978. *Astrophys. J.*, **221,** 62.
Olofsson, H. & Rydbeck, G., 1984. *Astr. Astrophys.*, **136,** 17.
Panagia, N., 1973. *Astr. J.*, **78,** 929.
Pipher, J. L., Moneti, A., Forrest, W. J., Woodward, C. E. & Shure, M. A., 1987. In: *Infrared Astronomy with Arrays*, p. 326, eds Wynn-Williams, C. G. & Becklin, E. E., Univ. Hawaii, Honolulu.
Puxley, P. J., Brand, P. W. J. L., Moore, T. J. T., Mountain, C. M., Nakai, N. & Yamashita, T., 1989. *Astrophys. J.*, **345,** 163.
Rieke, G. H., Lebofsky, M. J., Thompson, R. I., Low, F. J. & Tokunaga, A. T., 1980. *Astrophys. J.*, **238,** 24.
Seaquist, E. R., Bell, M. B. & Bignell, R. C., 1985. *Astrophys. J.*, **294,** 546.
Sofue, Y., 1988. *Galactic and Extragalactic Star Formation*, p. 409, Whistler, eds Pudritz, R. E. & Fich, M., Kluwer, Dordrecht.
Stark, A. A. & Carlson, E. R., 1982. *Astrophys. J.*, **279,** 122.
Tammann, G. A. & Sandage, A. R., 1968. *Astrophys. J.*, **151,** 825.
Telesco, C. M. & Harper, D. A., 1980. *Astrophys. J.*, **235,** 392.
Thronson, H. A., 1988. *Galactic and Extragalactic Star Formation*, p. 621, eds Pudritz, R. E. & Fich, M., Kluwer, Dordrecht.
Thronson, H. A., Walker, C. K., Walker, C. E. & Maloney, P., 1987. *Astrophys. J.*, **318,** 645.
Thronson, H. A., Walker, C. K., Walker, C. E. & Maloney, P., 1989. *Astr. Astrophys.*, **214,** 29.
Tielens, A. G. G. M. & Hollenbach, D., 1985. *Astrophys. J.*, **291,** 722.
Watson, M. G., Stanger, V. & Griffiths, R. E., 1984. *Astrophys. J.*, **286,** 144.
Weliachew, L., Fomalont, E. B. & Greisen, E. W., 1984. *Astr. Astrophys.*, **137,** 335.
Whitcomb, S. E., Gatley, I., Hildebrand, R. H., Keene, J., Sellgren, K. & Werner, M. W., 1981. *Astrophys. J.*, **246,** 416.
Willner, S. P., Soifer, B. T., Russell, R. W., Joyce, R. R. & Gillett, F. C., 1977. *Astrophys. J.*, **217,** L121.
Young, J. S. & Scoville, N. Z., 1982. *Astrophys. J.*, **258,** 467.
Young, J. S. & Scoville, N. Z., 1984. *Astrophys. J.*, **287,** 153.

Mon. Not. R. astr. Soc. (1991) **252**, *Short Communication*, 6P–11P

The ^{12}CO to H_2 ratio in the centre of M82

P. A. Smith,[1] P. W. J. L. Brand,[1] C. M. Mountain,[2] P. J. Puxley[2]★ and N. Nakai[3]

[1]*University of Edinburgh, Department of Astronomy, Blackford Hill, Edinburgh EH9 3HJ*
[2]*Royal Observatory, Blackford Hill, Edinburgh EH9 3HJ*
[3]*Nobeyama Radio Observatory, Nobeyama, Minamisaku, Nagano 384-13, Japan*

Accepted 1991 June 19. Received 1991 April 15

SUMMARY

We present 450-μm continuum observations of M82 at high signal-to-noise and spatial resolution. Our 1′ scan along the major axis shows a main peak SW of the nucleus with a secondary peak to the NW. This morphology differs from that of ^{12}CO $J=1-0$ at the same resolution, but is quite similar to that of optically thin ^{13}CO and $C^{18}O$. We use our 450-μm data to evaluate the CO to H_2 conversion factor, $N(H_2)/I_{CO}$, and find that it varies along the major axis and is up to a factor of 3 lower than the Milky Way value, suggesting that the galactic conversion factor may overestimate $N(H_2)$ in 'starburst' galaxies. Recent multitransition observations of CO and other molecules in M82 point towards a clumpy, disturbed interstellar medium subject to intense UV fields, in which it is unlikely that the ^{12}CO reliably traces molecular hydrogen. Dust continuum observations, on the other hand, offer a far more direct and straightforward tracer of H_2, that does not depend so critically on the excitation and chemistry of the interstellar medium.

1 INTRODUCTION

The advent of sensitive millimetre wave telescopes has encouraged the study of molecular gas in galaxies using the relatively easily detected ^{12}CO $J=1-0$ transition as a tracer of molecular hydrogen. However, it is becoming increasingly doubtful whether ^{12}CO is a reliable probe of either the total mass or spatial distribution of H_2 in regions of vigorous star formation, where numerous massive young stars greatly influence conditions in the clouds (e.g. Maloney & Black 1988). An alternative tracer is submillimetre continuum emission from 30–50 K dust mixed with the molecular gas, and heated by the UV from young stars. It has been argued by several authors that the continuum emission is a more reliable tracer of H_2 than the CO line, having both low optical depth and relative insensitivity to such parameters as temperature and UV field strength (e.g. Thronson 1987).

In an earlier paper (Smith *et al.* 1990 – Paper I) we presented 450-μm continuum mapping of the nearby starburst galaxy M82 with the James Clerk Maxwell Telescope, for a direct comparison with the CO emission. Our 450-μm map, made with a 13″ beam, showed a strikingly different morphology to ^{12}CO maps of the same region and at the same spatial resolution. While ^{12}CO $J=1-0$ and $J=2-1$ observations reveal a double-peaked structure, interpreted as a rotating, 400-pc diameter ring enclosing the nuclear starburst (Nakai *et al.* 1987; Lo *et al.* 1987; Loiseau *et al.* 1990), our 450-μm map had only one peak, inside the CO ring (Paper I). Such a morphological difference is inconsistent with both the CO and the dust reliably tracing H_2. We could find no strong evidence, from far-IR data (Joy, Lester & Harvey 1987), of dust temperature variations sufficient to explain the discrepancy. The 450-μm map closely resembles a ^{13}CO $J=2-1$ map of the central region which, unlike the ^{12}CO, is centrally peaked (Loiseau *et al.* 1988). Furthermore, detection of [C II] 158 μm and H53α emission from M82 implies the existence of a highly disturbed nuclear region with the molecular clouds bathed in the radiation of $\sim 10^6$ hot young stars and the CO intensity perhaps governed more by the UV field than by the molecular mass (Crawford *et al.* 1985; Puxley *et al.* 1989). It seemed, therefore, that our 450-μm observations were tracing a concentration of molecular gas not seen in ^{12}CO, and that line optical depth and excitation effects may be a significant cause of the differing morphologies. Our data added to the growing evidence that ^{12}CO is *not* a reliable tracer of H_2 in regions of vigorous star formation.

However, our observations were limited by the then lower quality dish surface and pointing precision of the recently commissioned JCMT which prevented us mapping at diffraction-limited resolution and introduced fairly large ($\sim 7''$) pointing uncertainties. Since our original observations, the dish surface and pointing have improved to such an extent that diffraction-limited (7″) observations are now feasible. The value of such data is clear – the opportunity to verify our previous results with high pointing accuracy and a resolution sufficient for a direct comparison with CO interferometer

★Present address: Joint Astronomy Centre, 665 Komohana St, Hilo, Hawaii 96720, USA.

data that shows the double-peaked structure very clearly (Lo *et al.* 1987).

2 OBSERVATIONS

The observations were made on the night of 1989 December 18–19, using the James Clerk Maxwell Telescope on Mauna Kea, Hawaii. We observed M82 at 450 μm in the continuum with the common user ^{3}He-cooled bolometer UKT14 (Duncan *et al.* 1990), and the aperture set to 27 mm, resulting in a (diffraction-limited) beamsize of 7″. The filter width of UKT14 at 450 μm is 56 μm.

A 19-point scan was made along the major axis of M82, oriented at a position angle of 76° (E from N) and centred at RA(1950) = 09^{h}51^{m}43^s.53, Dec(1950) = 69°55′00″.7 (Dietz *et al.* 1986). The scan direction is consistent with the apparent CO and dust major axes, which are offset from the optical major axis of M82 (Paper I, Nakai *et al.* 1987). The data were fully sampled at 3″ spacing with an integration time ~2 min per point, leading to signal-to-noise ratios ranging from ~4σ at the edge to ~27σ at the centre of the scan. We chopped 150″ away in azimuth to get good sky cancellation.

When working at the diffraction limit of the telescope, accurate pointing becomes very important. Pointing and focus checks were performed on the bright, evolved stars IRC10216 and CRL618, and on Mars. Over the whole night, the rms pointing error was ~1.6″ in azimuth and ~3.6″ in elevation. However, five-point scans carried out immediately before and after the M82 observation showed that the pointing was accurate to ≤2″ over this period. These five-points were carried out using IRC10216, which at RA(1950) = 09^{h}45^{m}14^s.8, Dec(1950) = +13°30′41″ is the closest bright sub-mm pointing source to M82.

Frequent calibration observations are essential at sub-mm wavelengths, because of the possibility of rapid (~1 hr) variations in atmospheric opacity. We observed CRL618 and OMC-1, both reasonably bright and well-calibrated at 450 μm, and Mars. We adopted 450-μm fluxes (in a 19″ beam) for CRL618 and OMC-1 of 11±1 Jy and 770±120 Jy respectively (G. Sandell, personal communication). For Mars, a brightness temperature of 215.1 K (Griffin *et al.* 1986) and 450-μm flux of 788.3 Jy were adopted. Using our calibrator observations, we transformed the M82 data out of the atmosphere with a sky extinction at 450 μm of 0.7±0.1 (virtually constant throughout the night) and UKT14 sensitivity at 450 μm of 41±3 Jy mV^{-1}. The accuracy of calibration is affected by the dependence of the 450-μm filter effective frequency on both source spectral index and atmospheric water vapour content. A major source of uncertainty when making diffraction-limited observations at 450 μm is the fact that, despite the high surface accuracy of the JCMT, the beam shape is poorly known (and probably not Gaussian), and the error beam non-negligible. The beam-source coupling will therefore differ for a point source (CRL618), disc (Mars) or extended object (M82). From these considerations, we estimate that the overall calibration uncertainty may be as high as 30 per cent. The weather prevented us making a beam map during our run. However, our derived fluxes agree very well with previous photometry (Hughes, Gear & Robson 1990). Using data from Wild (1990), we were also able to estimate the contribution to the 450-μm continuum flux of the ^{12}CO J=6–5 line at 434 μm, which was found to be ≤0.3 Jy beam^{-1} and therefore negligible.

3 RESULTS

In Fig. 1 we present our data, together with slices from the ^{12}CO J=1–0 interferometer observations of Lo *et al.* (1987) and the ^{13}CO J=2–1 IRAM data of Loiseau *et al.* (1988) taken along the same scan direction, for comparison. The 450-μm flux density at each observed position is given in Table 1.

It can be seen from Fig. 1 that our 450-μm scan has two peaks ~18″ apart. The position of the larger south-west (SW) peak is coincident, within the pointing errors, with the peak of our original 450-μm map and that of the ^{13}CO J=2–1 data (Loiseau *et al.* 1988). The north-east (NE) peak is approximately coincident with the NE maximum of the ^{12}CO (Lo *et al.* 1987), and a secondary peak in the ^{13}CO map. Note, however, that there is *no* feature in our slice to correspond with the main SW ^{12}CO peak of Lo *et al.* The ^{12}CO maximum is offset by ~6″ from our data – an offset too large to be explained by our pointing errors of ≤2″.

To compare our new data with the previous 450-μm map, we smoothed our scan with a Gaussian filter to a resolution of 13″. Lack of knowledge of minor axis fluxes will not introduce large errors in the case of M82, as the sub-mm emission is nearly unresolved along the minor axis (extent ~9″, Paper I). The results of this smoothing are presented in Fig. 2. It can be seen that, at 13″ resolution, the two peaks blend into one, ~8″ SW of the nucleus, with a plateau extending to the NE, similar to our original map. The peak is rather less sharply defined than in the original 13″ map, although this is perhaps in part due to the non-Gaussian beam shape of the high resolution data and the errors introduced by smoothing the 1D slice. However, the flux into a 13″ beam at the peak is calculated to be 14.5±4.4 Jy, and the integrated flux from the slice is 42 Jy, in very good agreement with the original 450-μm photometry and 13″ map flux (Hughes *et al.* 1990; Paper I). This gives us confidence in the accuracy of our calibration and demonstrates that our new data is essentially consistent with our previous results at lower resolution.

4 DISCUSSION

Since our original map was published, a number of new observations have appeared in the literature which throw more light on the nature of the interstellar medium in M82. Improving receiver technology has enabled the detection, and in some cases, mapping, of rare isotopes and higher frequency transitions of CO, as well as observations of other molecular species such as CS, HCN and HCO$^+$ (Nguyen-Q-Rieu, Nakai & Jackson 1989; Wild 1990; Tilanus *et al.* 1990; Turner, Martin & Ho 1991; Baan *et al.* 1990; Harris *et al.* 1990; Mauersberger & Henkel 1989). The advantage of observing other transitions, isotopes and species is that they probe regimes of temperature and density to which the low-J lines of ^{12}CO are not sensitive, and allow for more sophisticated modelling of the excitation of the molecular gas. High resolution continuum mapping at wavelengths from 10 μm to 3.3 mm has also been reported (Telesco, Decher & Joy 1989; Telesco *et al.* 1991; Dietz *et al.* 1989; Krügel *et al.* 1990; Carlstrom & Kronberg 1991). In Paper I we attributed

the differing CO and dust morphologies to optical depth or excitation effects, although we could not completely rule out an enhanced dust temperature in the star forming region SW of the nucleus. We can now re-examine this conclusion in the light of the new data.

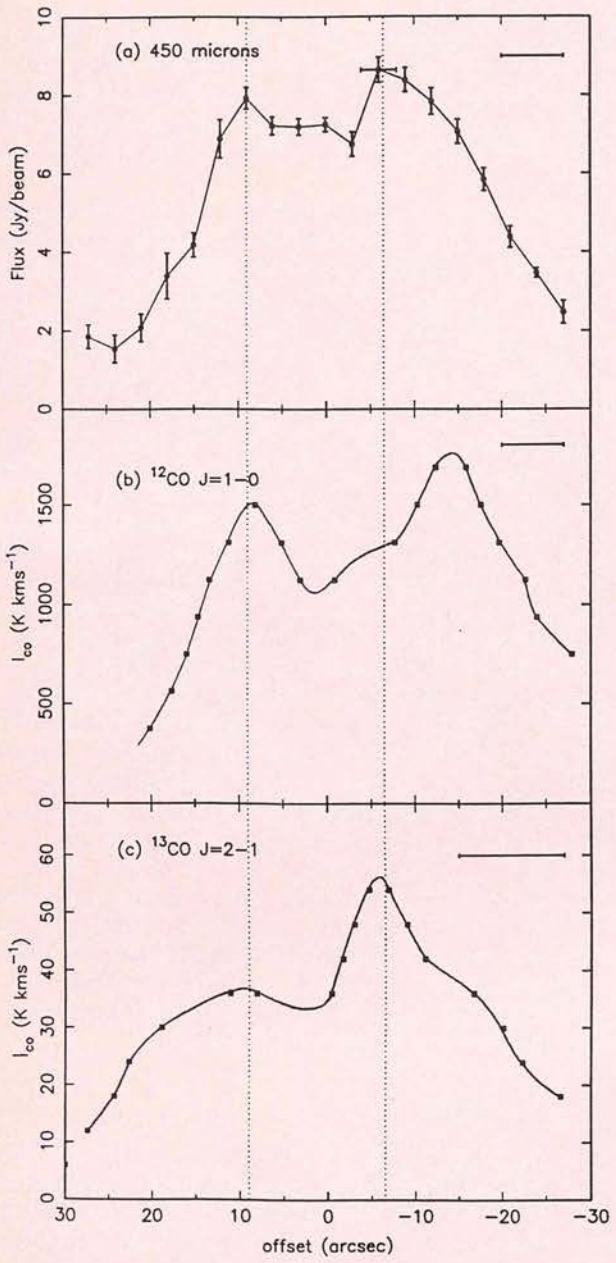

Figure 1. Scans along the major axis of M82, in ^{12}CO $J=1$–0, ^{13}CO $J=2$–1, and 450-μm dust continuum. In each case, the scan direction was at position angle 76° (E from N), and the central position was at RA(1950) = 09^{h}51^{m}43^s.53, Dec(1950) = 69°55′00″.7. The CO scans were produced by interpolating between the contour levels (indicated by filled squares) of the published maps. The beam-width is represented by a horizontal line. (a) Continuum observations at 450 μm with 7″ resolution (this work). The vertical error bars represent observational signal-to-noise – there is an additional overall calibration error of ≤30 per cent. The horizontal error bar on the data point at offset −3″ represents the pointing uncertainty of ≤2″. Note that this is much smaller than the offset between the south-western CO and dust peaks. (b) ^{12}CO $J=1$–0 interferometer observations from Lo *et al.* (1987), with 7″ resolution. (c) ^{13}CO $J=2$–1 observations, from Loiseau *et al.* (1988), at 12″ resolution.

4.1 Interpretation of molecular line data

^{12}CO 2–1/1–0 antenna temperature ratios of ≥2 in M82 have been interpreted as arising from warm, optically thin gas, quite unlike galactic molecular clouds (Loiseau *et al.* 1990; Olofsson & Rydbeck 1984; Knapp *et al.* 1980). However, M82 seems to be unique among galaxies in having a large 2–1/1–0 ratio (e.g. Verter & Rickard 1989), and the ^{12}CO/^{13}CO $J=2$–1 ratio appears more consistent with optically thick ^{12}CO (Loiseau *et al.* 1988, 1990). Maps of the 1–0, 2–1 and 3–2 transitions of ^{12}CO all show the double-peaked 'ring' structure (Lo *et al.* 1987; Nakai *et al.* 1987; Loiseau *et al.* 1990; Tilanus *et al.* 1990), while observations of the much optically thinner ^{13}CO and C^{18}O isotopes display a large central maximum (Loiseau *et al.* 1988; Wild 1990).

An idea of the optical depth of the emission comes from comparing the ^{12}CO and ^{13}CO $J=2$–1 lines (Loiseau *et al.* 1988, 1990). By assuming the same excitation temperature for both isotopes [local thermodynamic equilibrium (LTE)] and adopting a [^{12}CO]/[^{13}CO] abundance ratio R, the ^{12}CO and ^{13}CO optical depths can be calculated from the antenna temperature ratio via

$$\frac{T(^{12}CO)}{T(^{13}CO)} = \frac{[1-e^{-\tau(12)}]}{[1-e^{-\tau(13)}]}, \qquad (1)$$

where $\tau(12) = R\tau(13)$.

From their $J=2$–1 observations, and by adopting $R=60$ (Wannier 1980), Loiseau *et al.* (1988) derive ^{12}CO optical depths of 2–10. The highest optical depths are found in

Table 1. Flux density at 450 μm along major axis of M82 (7″ beam).

Position[a] (arcsec)	Flux Density (Jy/beam)	Error[b] (Jy/beam)
-27.0	2.46	0.29
-24.0	3.46	0.12
-21.0	4.38	0.27
-18.0	5.84	0.29
-15.0	7.06	0.31
-12.0	7.83	0.34
-9.0	8.38	0.31
-6.0	8.64	0.32
-3.0	6.74	0.31
0.0	7.24	0.18
3.0	7.18	0.21
6.0	7.21	0.23
9.0	7.92	0.28
12.0	6.87	0.49
15.0	4.18	0.31
18.0	3.39	0.58
21.0	2.08	0.35
24.0	1.54	0.35
27.0	1.85	0.30

[a]With respect to the central position RA(1950) = 09^{h}51^{m}43^s.53, Dec(1950) = 69°55′00″.7, along a line inclined at position angle 76° E of N. [b]Statistical errors only. There is an overall calibration error of ≤30 per cent.

between the ^{12}CO lobes, where the ^{13}CO peaks. There is some evidence that the $[^{12}CO]/[^{13}CO]$ abundance ratio R varies from its solar neighbourhood value throughout the Milky Way, and may be as low as 24–30 at the Galactic Centre (e.g. Langer & Penzias 1990). In this case, the ^{12}CO optical depths resulting from equation 1 are quite low (~ 1) at some positions in M82, but still reach values of >4 at the ^{13}CO peak. If external heating of the clouds is significant (Young & Scoville 1984; Maloney & Black 1988), then the apparent $^{12}CO/^{13}CO$ ratio may be artificially high, reflecting the fact that the optically thicker ^{12}CO line will arise in the warmer outer layers of a cloud. The true ratio may thus be lower than observed, and the ^{12}CO optical depth even higher. *Thus, as we concluded in Paper I, our 450-μm observations and the rare CO isotopes may simply be tracing molecular gas not seen in ^{12}CO because of high optical depth.*

The above analysis is very simple and relies on the validity of the assumption of LTE. However, attempts at more detailed multitransition analysis have met with only limited success because of the complexity of the interstellar medium in M82. Wild (1990) applies a one-component, non-LTE radiative transfer model to observations of ^{12}CO, ^{13}CO and $C^{18}O$ and finds his data to be consistent with a high ^{12}CO optical depth, but Tilanus *et al.* (1990) cannot explain their observed line ratios by any simple one-component model.

The detection of the $J=6$–5 and $J=7$–6 transitions of ^{12}CO, as well as CS, HCN, HCO^+ and even the rare isotopes $C^{34}S$ and $H^{13}CN$, all suggest large amounts of warm (>40 K), dense ($n>10^4$ cm^{-3}), clumpy gas in the interstellar medium of M82 (Wild 1990; Baan *et al.* 1990; Nguyen-Q-Rieu *et al.* 1989; Harris *et al.* 1990; Mauersberger & Henkel 1989). Wolfire, Tielens & Hollenbach (1990) model the central kiloparsec of M82 in terms of an ensemble of photodissociation regions (PDRs), consisting of $\sim 3\times10^5$ small (~ 1 pc), dense clouds irradiated by a UV field $\sim 10^4$ times

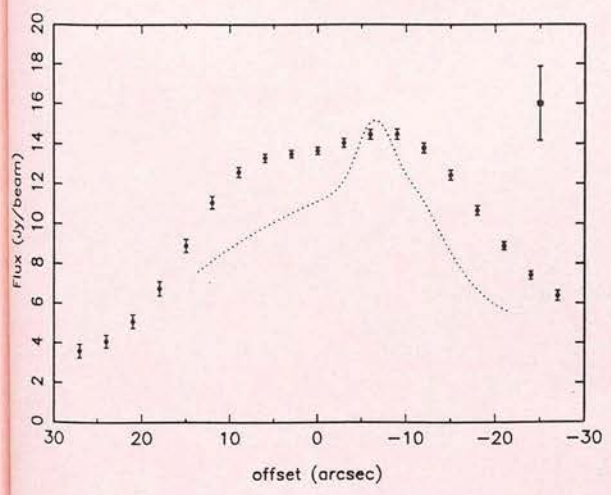

Figure 2. The 450-μm continuum fluxes smoothed into a 13″ Gaussian beam, for comparison with our previous data, which is represented by a dotted line (Paper I). Scan direction and central position are as for Fig. 1. The errors on the smoothed data points are statistical – in addition there are global calibration uncertainties of ≤30 per cent. The large vertical error bar shows the typical uncertainty in the fluxes of the original data (Paper I).

that in the solar neighbourhood. A picture emerges of a highly disturbed interstellar medium in which the molecular clouds have been swept up by stellar winds, supernovae and H II regions into small, dense, warm clumps or filaments, embedded in low density ionized gas and bathed in UV from $\sim 10^6$ hot young O and B stars.

Interpretation of CO data is highly dependent on the physical, excitation and chemical state of the interstellar medium (e.g. Maloney & Black 1988). It is therefore unsurprising that simple one-component models appear not to work in a region as complex and disturbed as the centre of M82. The validity of the commonly applied method of using a galactic conversion factor to obtain $N(H_2)$ from observations of ^{12}CO $J=1$–0 depends on the assumption that extragalactic molecular clouds have similar physical conditions as those in the disc of the Milky Way (i.e. $n\sim200$ cm^{-3}, $T\sim10$ K, $\tau\gg1$). In the nuclei of actively star-forming galaxies this is not necessarily true. Maloney & Black (1988) predict that it is possible to overestimate $N(H_2)$ by factors of up to 5 in starburst nuclei.

Wild (1990) uses optically thin $C^{18}O$ data to deduce $N(H_2)$ and hence calculate the conversion factor $N(H_2)/I_{CO}$ along the major axis of M82. He finds that not only is the conversion factor ~ 3 times lower than the accepted Milky Way value of 4×10^{20} cm^{-2} (K km s^{-1})$^{-1}$ (Young & Scoville 1982), but that it varies by a factor of ~ 2 along the major axis. It is possible that $C^{18}O$ is subject, to a lesser extent, to the same excitation and abundance effects as ^{12}CO. We have used our 450-μm data for an independent calculation of $N(H_2)/I_{CO}$ in M82.

The column density of H_2 can be derived in a straightforward way from the submillimetre flux using the method outlined by Hildebrand (1983) and modified by Gear (1988) for Gaussian source and beam profiles.

The dust continuum optical depth is given by

$$\tau(\nu)=5.42\times10^{-16}[(\theta_s^2+\theta_b^2)/\theta_s^2\theta_b^2][S(\nu)/B(\nu,T)], \qquad (2)$$

where θ_s and θ_b are the FWHM (arcsec) of the source and beam profiles, respectively, $S(\nu)$ is the flux density from the source (Jy per beam), and $B(\nu, T)$ is the blackbody intensity at frequency ν and dust temperature T.

The hydrogen column density is then

$$N(H_2)=6.0\times10^{24}[750/\nu(\mathrm{GHz})]^{\beta}\tau(\nu)\,\mathrm{cm}^{-2}, \qquad (3)$$

where β is the frequency dependence of the dust emissivity, and we have adopted the value of $N(H+H_2)/\tau(\nu)$ given by Hildebrand (1983), assuming that the neutral hydrogen in the central region of M82 is predominantly molecular (Weliachew, Fomalont & Greisen 1984). We adopt a dust temperature of 47 K and $\beta=1.5$ as derived from the 40–1300 μm spectrum (Hughes *et al.* 1990). A discussion of the possible sources of error of this method was given in Paper I and is outlined briefly in the next section. For the purposes of the calculation we have decomposed the major axis scan into two Gaussians of FWHM 22.5″ and 11.9″ (beam convolved with source) at major axis offsets of −8.5″ and 9.4″ respectively. Values of I_{CO} were taken from the 7″ resolution interferometer map of Lo *et al.* (1987). The results are plotted in Fig. 3, together with those of Wild (1990) for comparison. We find, as does Wild, that the derived $N(H_2)/I_{CO}$ ratio is up to three times lower in M82 than the accepted Milky Way value, consistent with the prediction by Maloney

& Black (1988) that $N(H_2)$ may be overestimated in the centres of starburst galaxies if the galactic conversion factor is applied. We also observe a variation of the ratio across M82 (up to a factor of 2), although the detailed structure differs from that inferred by Wild (1990), which may in part be due to the effects of excitation or abundance on the $C^{18}O$ data, or of dust temperature on the 450-μm emission.

4.2 Dust continuum emission from galaxies

The submillimetre/millimetre continuum provides an independent tracer of molecular hydrogen that is free of the complex excitation and cloud chemistry effects that plague the interpretation of CO data. The dust emission is optically thin, so all the dust, and hence the H_2, is sampled. CO emission is very sensitive to high UV fields, as the molecule is easily dissociated. Indeed, it is believed that much of the ^{12}CO $J=1-0$ emission in galaxies such as M82 may arise from the warm (>50 K) C II/C/CO transition zones in photodissociation regions, at the boundaries between H II regions and molecular clouds (e.g. Crawford *et al.* 1985). In these circumstances, the CO may be tracing UV field strength rather than H_2 column density. In contrast, dust grains are not easily destroyed by high UV fields and respond only via a very slow increase in temperature. The submillimetre flux, and hence derived $N(H_2)$, has an approximately linear dependence on dust temperature [$S(\nu) \propto T_d^{1.6}$ at 450 μm – Paper I]. The dust temperature itself is relatively straightforward to determine from the IR-mm data by fitting a modified blackbody function [$\nu^\beta B(\nu, T)$] to the spectrum.

The relative simplicity of the technique does not make it free from error, however. Even for small beams, a galaxy is very much a composite object, and the IR-mm spectrum will be composed of emission from dust at a range of different temperatures. The derived dust optical depth, and hence $N(H_2)$, is dependent on the dust temperature adopted. Long wavelength ($\lambda > 300$ μm) observations are particularly valuable, as they are more sensitive to the cool (≤ 30 K) dust that is easily missed if only far-IR fluxes are used, and reduce the inevitable errors that follow from trying to fit several temperature components to a small number of data points. Apart from the pitfalls of spectrum fitting, the largest source of error lies with the conversion factor $N(H_2)/\tau(\nu)$. As in the case of CO, the conversion factor in use has been derived from observations within the Milky Way, and is then assumed also to be valid in other galaxies. Although it may be as accurate as ± 50–100 per cent in the Milky Way (Mezger 1990), its possible variation in extragalactic environments is not well understood. However, the value of the conversion factor is not critically dependent on the details of gas excitation, as is the case for CO, but on grain parameters. These might perhaps not be expected to vary drastically both between and within most galaxies, given the relative insensitivity, compared to CO, of both H_2 and grains to such factors as increased UV field. It therefore seems likely that our knowledge of $N(H_2)/\tau(\nu)$ is no less accurate than that of $N(H_2)/I_{CO}$, and is probably better, although further theoretical modelling such as has already been carried out for the Milky Way (e.g. Cox & Mezger 1989) is clearly needed.

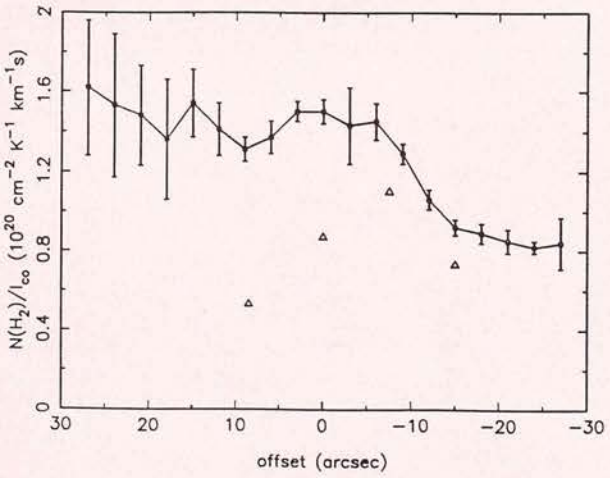

Figure 3. The CO to H_2 conversion factor, $N(H_2)/I_{CO}$, along the major axis of M82. The filled circles represent the conversion factor calculated from our 450-μm observations as described in the text. The open triangles represent values calculated by Wild (1990), using $C^{18}O$ observations. Note that both data sets give values of $N(H_2)/I_{CO}$ considerably below the accepted galactic value of $\simeq 4\times10^{20}$ cm^{-2} (K km s^{-1})$^{-1}$.

5 CONCLUSIONS

We have observed M82 at 450 μm in the dust continuum, with $7''$ resolution. Because of the small minor axis extent of the galaxy at 450 μm ($\sim 9''$), our 1D slice along the major axis loses very little flux, and may therefore be considered representative of the flux distribution from the entire nuclear region. The data are consistent, both in flux and morphology, with our earlier observations at lower resolution.

The scan has a main peak $\sim 8''$ SW of the nucleus of the galaxy, with a secondary peak to the NE. This morphology differs from that of ^{12}CO $J=1-0$ at the same high resolution – specifically, there is *no* feature in our map to correspond with the SW lobe of ^{12}CO, while the main peak of our scan is barely visible in CO. In contrast, the optically thin tracers of ^{13}CO and $C^{18}O$, as well as the 1.3-mm continuum, bear a strong resemblance to our 450-μm scan, all four peaking within the CO lobes.

Although ^{12}CO 2–1/1–0 ratios of >2 appear to indicate optically thin gas in M82, simple LTE analysis of the ^{12}CO and ^{13}CO $J=2-1$ lines suggests that the ^{12}CO is quite optically thick at the centre of the galaxy, even for the low $^{12}CO/^{13}CO$ abundance ratios of ~ 25 that may apply to the centres of galaxies. Thus our observations could simply be tracing molecular gas not seen in the ^{12}CO line because of high optical depth. However, recent attempts at sophisticated non-LTE modelling by several authors have led to contradictory conclusions, and a wealth of multi-transition observations of isotopes of CO, CS and other molecules all point to an interstellar medium so complex and disturbed that it seems highly likely that CO, with its sensitivity to excitation, cloud chemistry etc, is an unreliable tracer of the bulk of the molecular material. Indeed, our 450-μm data imply that the CO to H_2 conversion factor, $N(H_2)/I_{CO}$, varies along the major axis and is up to three times lower than the Milky Way value, supporting the growing body of evidence that blind application of a 'constant conversion factor' can lead to serious overestimates of $N(H_2)$ in many 'active' galaxies.

The submillimetre dust continuum, on the other hand, would seem to provide a far more direct, straightforward method of tracing molecular hydrogen column density, free from the complex dependence on UV field and excitation, and the necessity for sophisticated radiative transfer modelling, that plagues interpretation of molecular line data. Although not without pitfalls, chiefly the accuracy of the conversion factor $N(H_2)/\tau(\nu)$, the simplicity of the method, coupled with the low optical depth of submillimetre emission, means that observation of the dust continuum is an important tool in the investigation of the interstellar medium in external galaxies. Further theoretical modelling of dust emission from galactic nuclei, such as has already been performed for the disc of the Milky Way, would be very welcome.

ACKNOWLEDGMENTS

We thank the PATT for awarding us telescope time for this project, and the staff of the Joint Astronomy Centre in Hilo for their technical support – particularly our telescope operator, Thomas Walker, without whose expertise we would not have obtained the data during the limited period that the weather cooperated.

We are grateful to Claire Chandler for comments on the manuscript, and Wolfgang Wild for letting us see material from his PhD thesis. PAS and PJP acknowledge financial support from the SERC. The James Clerk Maxwell Telescope is operated by the Royal Observatory, Edinburgh, on behalf of the Science and Engineering Research Council of the United Kingdom, the Netherlands Organisation for Scientific Research, and the National Research Council of Canada.

REFERENCES

Baan, W. A., Henkel, C., Schilke, P., Mauersberger, R. & Güsten, R., 1990. *Astrophys. J.*, **353,** 132.

Carlstrom, J. E. & Kronberg, P. P., 1991. *Astrophys. J.*, **366,** 422.

Cox, P. & Mezger, P. G., 1989. *Astr. Astrophys. Rev.*, **1,** 49.

Crawford, M. K., Genzel, R., Townes, C. H. & Watson, D. M., 1985. *Astrophys. J.*, **291,** 755.

Dietz, R. D., Gehrz, R. D., Jones, T. J., Grasdalen, G. L., Smith, J., Gullixson, C. & Hackwell, J. A., 1989. *Astr. J.*, **98,** 1260.

Dietz, R. D., Smith, J., Hackwell, J. A., Gehrz, R. D. & Grasdalen, G. L., 1986. *Astr. J.*, **91,** 758.

Duncan, W. D., Robson, E. I., Ade, P. A. R., Griffin, M. J. & Sandell, G., 1990. *Mon. Not. R. astr. Soc.*, **243,** 126.

Gear, W. K., 1988. *Proceedings of the Summer School on Millimetre and Submillimetre Astronomy, Stirling*, p. 307, eds Wolstencroft, R. D. & Burton, W. B., Kluwer, Dordrecht.

Griffin, M. J., Ade, P. A. R., Orton, G. S., Robson, E. I., Gear, W. K., Nolt, I. G. & Radostitz, J. V., 1986. *Icarus*, **65,** 244.

Harris, A. I., Wild, W., Stutzki, J., Jaffe, D. T., Jackson, J. M., Eckart, A., Lugten, J. B. & Genzel, R., 1990. Preprint.

Hildebrand, R. H., 1983. *Q. J. R. astr. Soc.*, **24,** 267.

Hughes, D. H., Gear, W. K. & Robson, E. I., 1990. *Mon. Not. R. astr. Soc.*, **244,** 759.

Joy, M., Lester, D. F. & Harvey, P. M., 1987. *Astrophys. J.*, **319,** 314.

Knapp, G. R., Phillips, T. G., Huggins, P. J., Leighton, R. B. & Wannier, P. G., 1980. *Astrophys. J.*, **240,** 60.

Krügel, E., Chini, R., Klein, U., Lemke, R., Wielebinski, R. & Zylka, R., 1990. Preprint. Max-Planck-Institut für Radioastronomie, Bonn.

Langer, W. D. & Penzias, A. A., 1990. *Astrophys. J.*, **357,** 477.

Lo, K. Y., Cheung, K. W., Masson, C. R., Phillips, T. G., Scott, S. L. & Woody, D. P., 1987. *Astrophys. J.*, **312,** 574.

Loiseau, N., Reuter, H.-P., Wielebinski, R. & Klein, U., 1988. *Astr. Astrophys.*, **200,** L1.

Loiseau, N., Nakai, N., Sofue, Y., Wielebinski, R., Reuter, H.-P. & Klein, U., 1990. *Astr. Astrophys.*, **228,** 331.

Maloney, P. & Black, J. H., 1988. *Astrophys. J.*, **325,** 38.

Mauersberger, R. & Henkel, C., 1989. *Astr. Astrophys.*, **223,** 79.

Mezger, P. G., 1990. In: *Physics and Composition of the Interstellar Matter*, p. 97, eds Krelowski, J. & Papaj, J., Nicolaus Copernicus University, Torun.

Nakai, N., Hayashi, M., Handa, T., Sofue, Y. & Hasegawa, T., 1987. *Publs astr. Soc. Japan.*, **39,** 685.

Nguyen-Q-Rieu, Nakai, N. & Jackson, J. M., 1989. *Astr. Astrophys.*, **220,** 57.

Olofsson, H. & Rydbeck, G., 1984. *Astr. Astrophys.*, **136,** 17.

Puxley, P. J., Brand, P. W. J. L., Moore, T. J. T., Mountain, C. M., Nakai, N. & Yamashita, T., 1989. *Astrophys. J.*, **345,** 163.

Smith, P. A., Brand, P. W. J. L., Puxley, P. J., Mountain, C. M. & Nakai, N., 1990. *Mon. Not. R. astr. Soc.*, **243,** 97 (Paper I).

Telesco, C. M., Decher, R. & Joy, M., 1989. *Astrophys. J. Lett.*, **343,** L13.

Telesco, C. M., Campins, H., Joy, M., Dietz, K. & Decher, R., 1991. *Astrophys. J.*, **369,** 135.

Thronson, H. A., 1988. *NATO Advanced Study Institute on Galactic & Extragalactic Star Formation, Whistler*, p. 621, eds Pudritz, R. & Fich, M., Kluwer, Dordrecht.

Tilanus, R. P. J., Tacconi, L. J., Zhou, S., Sanders, D. B., Sutton, E. C., Lo, K. Y., Stephens, S. A. & Wynn-Williams, C. G., 1990. Preprint. Institute for Astronomy, University of Hawaii.

Turner, J. L., Martin, R. N. & Ho, P. T. P., 1991. *Astrophys. J.*, **367,** 677.

Verter, F. & Rickard, L. J., 1989. *Astr. Astrophys.*, **225,** 27.

Wannier, P. G., 1980. *Ann. Rev. Astr. Astrophys.*, **18,** 399.

Weliachew, L., Fomalont, E. B. & Greisen, E. W., 1984. *Astr. Astrophys.*, **137,** 335.

Wild, W., 1990. *PhD Thesis*, Ludwig-Maximilians-Universität.

Wolfire, M. G., Tielens, A. G. G. M. & Hollenbach, D., 1990. *Astrophys. J.*, **358,** 116.

Young, J. S. & Scoville, N. Z., 1982. *Astrophys. J.*, **258,** 467.

Young, J. S. & Scoville, N. Z., 1984. *Astrophys. J.*, **287,** 153.